Numerical and experimental methodologies for understanding and predicting the hydroplaning phenomenon of tires by numerical coupled SPH-Finite Elements simulations and PIV measurements

Arbia Ben Khodja

THÈSE DE DOCTORAT DE

L'ÉCOLE CENTRALE DE NANTES

ÉCOLE DOCTORALE N° 602
Sciences pour l'Ingénieur
Spécialité : *Mécanique des Milieux Fluides*

Par

Arbia BEN KHODJA

Méthodologies numériques et expérimentales pour la compréhension et la prédiction du phénomène d'hydroplanage des pneumatiques par simulations numériques couplées SPH-Eléments Finis et mesures PIV

Thèse présentée et soutenue à l'École Centrale de Nantes, le 16 novembre 2022
Unité de recherche : UMR 6598, Laboratoire de Recherche en Hydrodynamique, Energétique et Environnement Atmosphérique (LHEEA)

Rapporteurs avant soutenance :

Jean-Bernard BLAISOT	Professeur des universités, Université de Rouen Normandie
Damien VIOLEAU	Ingénieur de recherche, HDR, EDF, Chatou

Composition du Jury :

Président :	Antonio SOUTO-IGLESIAS	Professor, Universidad Politécnica de Madrid, Espagne
Examinateurs :	Marc MICHARD	Ingénieur de recherche, École Centrale de Lyon
	Laurent DAVID	Professeur des universités, Université de Poitiers
	Violaine TODOROFF	Ingénieure de recherche, MICHELIN Cébazat
Dir. de thèse :	Guillaume OGER	Ingénieur de recherche, HDR, École Centrale de Nantes
Co-dir. de thèse :	Serge SIMOËNS	Directeur de Recherche CNRS, École Centrale de Lyon

ACKNOWLEDGEMENT

First, I would like to thank the members of my PhD defense committee, not only for their time and dedication but also for their intellectual contributions.

To my research director, Guillaume OGER, I would like to thank him for his encouragement, insightful suggestions, and guidance during these 3 years. His friendliness and good spirit were most welcome in tough hours. He was an example of scientific rigor and high human values. I am also deeply grateful to my academic supervisors Marc MICHARD, Serge SIMOËNS, and David LE TOUZÉ. They have played a leading role in pushing me to become a better scientist. Their interrogations and curiosity sharpened my critical sense, and I finally grasped the true worth of our long-lasting conversations. I admired their willingness and great interest in my work despite their intense schedule and multiple students to oversee. Their genuine involvement only increased my respect for them.

My acknowledgments are also addressed to my supervisors at Michelin, Corentin HERMANGE, and Violaine TODOROFF. They kindly welcomed me into the grip team, and quickly gave me the needed autonomy that helped me build my confidence. Their experience was much valuable, and being doctors themselves, they taught me the importance of balance between academic research and industrial expectation. Their objectivity and professional pragmatism constantly redirected this thesis to stay the course. A special thanks to Corentin HERMANGE who bore with me all the numerical not-so-pleasant surprises with patience and philosophy. I extend my sincere thanks to all the present and former colleagues from the grip team in Ladoux, especially to Clément PONCET, Simon NUYTTEN and Fabien LAUPRETRE for their esteemed friendliness. My thanks go also to Yohan LE CHENADEC, Philippe BADEAU, and Frédéric BIESSE for their most helpful guidance. I would also like to thank Laurent PATARY, Fabien CORDONNIER and Rudy AUBLANT for their patience during the late hours of PIV sessions. And I am very much thankful to Nathalie GROSJEAN for her valuable help during the TR-PIV tests in the LMFA.

I would also like to thank Matheus who shared with me the daily life of a PhD student in Michelin (obrigada!), and Théo, Maxime, and Gaspard who kindly welcomed me to the LHEEA.

To my parents Hager and Ouahib and my grandmother Emna, who raised me and cared for me more than for themselves, I would like to express my most profound gratitude. Without them, I would never have become the person I am today. I would also like to thank my sister Nour for her unwavering belief in me. As C.Rossetti said, "*For there is no friend like a sister, In calm or stormy weather; To cheer one on the tedious way, To fetch one if one goes astray, To lift one if one totters down, To strengthen whilst one stands*". And to my husband Romain, for just being incredibly supportive from day one, I am so grateful. By relentlessly reminding me that the journey was worth the trouble, he embodied best the wisdom and patience I sometimes lacked.

Finally, I thank Arij, Soumaya, and Sofiane for being such inspiring friends from childhood. I am proud of who you became, I hope you are proud of me too.

If you are irritated by every rub, how will your mirror be polished?

Rumi

Résumé

Cette thèse est dédiée à l'étude locale du phénomène d'hydroplanage et ceci à partir d'un travail numérique s'appuyant sur des simulations couplées SPH-FE (Smoothed Particle Hydrodynamics-Éléments Finis) et d'un travail expérimental se basant sur la méthode de la r-PIV (refracted Particle Image Velocimetry). L'hydroplanage est bien connu des conducteurs d'automobile et des manufacturiers de pneumatiques. C'est un phénomène pour lequel il peut y avoir une perte de contrôle du véhicule et cela représente donc un danger potentiel pour le conducteur et ses passagers. L'hydroplanage total se produit lorsqu'un film d'eau se crée entre le pneu et la route, lubrifiant le contact et empêchant la transmission d'efforts. Cela se produit au-delà d'un vitesse critique dite vitesse d'hydroplanage en raison de l'incapacité du pneu et des rugosités du sol à drainer ce film d'eau. Dans cette thèse, nous nous limitons à l'hydroplanage partiel, i.e. la vitesse du véhicule est inférieure à la vitesse d'hydroplanage et il n'y a donc pas de perte totale de contact entre le pneu et le sol. Différents paramètres influencent l'initiation et l'établissement de ce phénomène complexe, telles que l'épaisseur du film d'eau, la géométrie de la sculpture du pneu et sa hauteur, la vitesse du véhicule. L'étude est ainsi basée sur les résultats numériques et expérimentaux tout en faisant varier certains de ces paramètres influents. Différentes géométries de sculpture de pneumatiques sont considérées, allant de la plus simple (sans sillons) à la plus complexe (sculptures directionnelles). Différents outils d'analyse sont ainsi développés afin de correspondre au mieux aux spécificités de chaque cas étudié. L'objectif est de mieux comprendre l'hydroplanage afin de proposer des critères de conception et ainsi à améliorer la performance des pneumatiques en sol mouillé. En effet, la comparaison expérimentale/numérique nous permet d'avoir une vision complémentaire du phénomène, de mettre en évidence la flexibilité mais aussi les limites de la stratégie adoptée, de poursuivre la validation de l'outil numérique, mais aussi de conforter le besoin d'amélioration de la métrologie utilisée pour une meilleure appréciation des phénomènes tridimensionnels de l'écoulement.

Dans le premier chapitre, on présente quelques généralités sur l'hydroplanage ainsi qu'une bibliographie sur les travaux de recherche effectués sur ce sujet sur les plans

numériques, expérimentaux et des modèles physiques existants. Tout d'abord, on définit brièvement l'hydroplanage. On considère alors un pneu roulant à une certaine vitesse sur une route mouillée/inondée. Au-dessous de la vitesse critique, l'effet combiné de la sculpture du pneumatique et des aspérités de la route réussit à évacuer assez d'eau devant le pneu pour que celui-ci garde contact avec le sol. Mais progressivement, en augmentant la vitesse du véhicule, cette capacité à drainer l'eau tend vers sa limite et une accumulation d'eau se produit devant le pneu avec une pression hydrodynamique qui augmente et qui déforme la paroi du pneumatique. L'aire de contact (AdC) entre le pneu et le sol est ainsi réduite progressivement. À partir de la vitesse d'hydroplanage, la pression hydrodynamique est telle qu'elle est comparable à la pression de gonflage du pneu, et la force de portance devient égale à la charge appliquée à celui-ci. Le pneu perd alors contact avec le sol.

Depuis les années 60 les scientifiques ont commencé à s'intéresser à ce phénomène en particulier dans le domaine de l'aéronautique. Les premiers modèles empiriques ont émergé reliant de manière simplifiée la pression de gonflage du pneumatique à la vitesse d'hydroplanage. Ces relations ont été largement acceptées et utilisées, puis améliorées afin de prendre en compte d'autres paramètres telles que la forme de l'AdC, la rugosité du sol ou encore, la profondeur de la sculpture. Plus tard, des méthodes expérimentales plus poussées ont été proposées, d'abord basées sur la mesure de la perte de surface en fonction de la vitesse du véhicule, puis en se basant sur des techniques optiques telles que la PIV, ouvrant l'accès à des grandeurs très locales, i.e. la vitesse du fluide dans la sculpture du pneu et dans le bourrelet (la zone devant le pneu). Sur le plan numérique, ce n'est qu'à la fin des années 90 que les premiers modèles ont commencé à voir le jour se basant sur le couplage fluide-structure et adoptant la formulation FVM-FEM (Volumes Finis-Éléments Finis). D'autres formulations ont été proposées plus tard telles que le couplage FEM-FEM ou encore FDM-FEM (Différences Finies-Éléments Finis) avec progressivement une modélisation plus complexe et donc plus fidèle du pneumatique en particulier au niveau de la sculpture. Mais ces méthodes maillées présentent des limites en particulier lors de l'étude de phénomènes tels que l'hydroplanage où les déformations du domaine fluide sont extrêmement importantes. C'est ainsi que des méthodes non-maillées tel que la méthode SPH ont été considérées comme des alternatives à fort potentiel afin de s'affranchir des limitations du maillage.

Dans cette thèse la stratégie numérique adoptée est le couplage entre la méthode des éléments finis pour la modélisation du pneu en formulation implicite, et la méthode SPH

pour la flaque d'eau en explicite. Quant aux tests expérimentaux, ils sont effectués grâce à la r-PIV.

Dans le deuxième chapitre, l'outil numérique est présenté. D'abord on introduit les fondamentaux de la méthode SPH, puis les développements effectués par le LHEEA (Laboratoire de recherche en Hydrodynamique, Énergétique et Environnement Atmosphérique) à l'École Centrale de Nantes lors des précédentes thèses afin d'aboutir à la version actuelle du code (collaboration entre le LHEEA et NextFlow Software actuellement Siemens). En effet, un travail très important a été fourni sur les conditions aux limites à la paroi, le raffinement particulaire, la stabilité du code, la réduction des temps de calcul ainsi que le couplage fluide-structure. Ensuite, plus brièvement, la méthode des éléments finis est introduite, pour aboutir finalement au couplage SPH-FE dans notre application actuelle.

Le troisième chapitre est dédié à la présentation de l'outil expérimental. La r-PIV a été développée dans le cadre d'une collaboration entre Michelin et le LMFA (Laboratoire de Mécanique des Fluides et d'Acoustique) à l'École Centrale de Lyon, et a été dédiée à l'application hydroplanage lors d'une précédente thèse. Le principe de ce type de mesures est d'enregistrer lors du passage du véhicule sur une flaque d'eau, deux images de la région, autour du pneu, illuminée par un laser et ensemencée avec des particules fluorescentes. L'illumination se fait par une première réfraction de la nappe laser à travers un hublot transparent placé à ras du sol, puis de multiples réflexions s'ensuivent dans la flaque d'eau. Le laser et la caméra sont situés au-dessous du niveau du sol. Ensuite, un algorithme de corrélation croisée calcule le déplacement des particules illuminées entre les deux images aboutissant ainsi à un champ de vitesse du fluide autour du pneu et dans les sillons situés dans l'AdC. Différentes méthodes de recalage des images enregistrées ont été proposées afin de pouvoir effectuer des moyennes d'ensemble sur plusieurs passages. Ces méthodes sont plus ou moins efficaces selon le type de sculptures étudiées.

L'analyse des champs de vitesse obtenus est proposée dans le quatrième chapitre où un pneu slick (sans sillons) est étudié. Malgré la simplicité de sa géométrie, le bourrelet d'eau devant de ce pneu présente différents phénomènes complexes. On a observé un écoulement principal dans le plan mais également un écoulement secondaire hors-plan dans la direction verticale au sol. Une étude paramétrique sur la vitesse du véhicule et sur la profondeur du film d'eau a mis en évidence l'existence de différents régimes en fonction

des paramètres d'influence. En effet, la part de l'eau drainée vers les côtés du pneu est modifiée quand la hauteur d'eau augmente. Nous proposons une analyse originale avec les bilans de masse ayant permis de quantifier la répartition entre l'écoulement latéral et l'écoulement vertical malgré un champ de vitesse 2D issu de la r-PIV. Une analyse de l'écoulement dans le bourrelet effectuée à l'aide de différents indicateurs, comme les lignes de courant en repère relatif, suggère l'existence de mouvements locaux hors-plan qui ne sont pas reproduits par les simulations numériques, mais dont l'origine physique n'est pas encore expliquée. Le modèle de fluide parfait utilisé dans notre code SPH semble être limitant pour que des effets aussi locaux puissent être reproduits. En revanche, les résultats concernant l'écoulement principal sont assez satisfaisants. Les effets dus à la largeur du pneu ont également été discutés, et toujours grâce à l'analyse avec les bilans de masse, on quantifie la différence entre les éjections latérales de 4 largeurs de pneus slick. Par exemple, le pneu le plus large voit son drainage vers les épaules diminuer de $\approx 40\%$ en comparaison avec le pneu le moins large dans la zone se situant entre 20% et 30% de la largeur totale. Enfin, des essais préliminaires de la TR-PIV (Time-Resolved r-PIV) ont été effectués sur le pneu slick. Malgré des images assez difficiles à analyser (météo très défavorable pendant la campagne de tests), les premiers résultats sont très prometteurs, et des informations sur le caractère stationnaire de l'écoulement ont pu être obtenues. Cette voie de recherche est certainement à approfondir dans le futur pour l'obtention d'un champ 3D-3C résolu temporellement et du champ de pression afin de pousser encore plus les comparaisons avec les simulations numériques.

Afin de s'approcher de géométries plus réalistes, un pneu à sculpture longitudinale, le MICHELIN Primacy 4 à l'état usé, est considéré dans le chapitre 5. Une étude de l'écoulement dans le sillon central et devant celui-ci a été effectuée en se basant sur les résultats numériques et expérimentaux. Si la structure globale de l'écoulement dans le sillon et dans le bourrelet est proche entre la simulation et les mesures r-PIV, c'est à l'arrière du sillon qu'apparaissent des différences notables. Un nouvel outil numérique a été mis en place, le Test-Bench, permettant de s'affranchir des longs temps de calcul des simulations couplées SPH-FE. Malgré les hypothèses simplificatrices du Test-Bench, il est possible non seulement d'évaluer notre choix concernant certains paramètres numériques tels que la vitesse du son et le ratio $R/\Delta x_{SPH}$, mais aussi de tester un nouveau modèle de détachement de jet permettant de reproduire les effets de succion à l'arrière du pneumatique observés expérimentalement. Ce nouveau traitement nous a permis d'obtenir numérique-

ment une vitesse proche de la vitesse expérimentale dans la zone arrière du sillon. Ceci a également amélioré les résultats dans le bourrelet, et la vitesse qui était auparavant surestimée est en bon accord avec celle mesurée en r-PIV. Ces améliorations devront être confirmées dans le futur en appliquant ce nouveau traitement aux simulations couplées et à d'autres types de sculptures.

Enfin, dans le sixième et dernier chapitre, des cas de sculptures plus complexes sont abordés, à savoir le MICHELIN Alpin 6 et le MICHELIN Cross Climate+. Ces pneus ont une sculpture directionnelle constituant un réseau de sillons reliés les uns aux autres, et leur étude a nécessité la mise en place de la méthode de segmentation, développée dans un travail de thèse précédent, afin d'accéder à une vitesse caractéristique longitudinale dans chaque segment des sillons. On met en évidence la corrélation entre la vitesse dans ces segments et leur position dans l'AdC, particulièrement pour le sillon central en zigzag et au niveau des épaules. On observe également un changement de régime au niveau des segments à l'épaule quand la vitesse du véhicule augmente. En effet, si à faibles vitesses on observe une aspiration de l'eau vers l'AdC à l'arrière puis une expulsion à l'approche du bourrelet, à plus hautes vitesses l'eau est expulsée tout le long de l'AdC. On a pu comparer ce résultat avec d'autres sculptures de pneumatiques; et l'ensemble des résultats obtenus montre que la connexion de ces segments d'épaule à d'autres sillons ou segments de sillons est nécessaire pour qu'il y ait aspiration de l'eau vers l'AdC à l'arrière. La comparaison avec les résultats numériques met en évidence la nécessité de prendre en compte les détails complets de la sculpture dans le modèle numérique dans le cas de sculptures complexes afin de pouvoir reproduire correctement la circulation de l'eau dans ce réseau de sillons.

Table of Contents

List of Figures

List of Tables

List of symbols and abbreviations

Mathematical symbols

Δt	The time step
δt	The time between two PIV frames
Δt_{FE}	The FE time step
Δt_{SPH}	The SPH time step
Δx_{SPH}	The distance between two particles
δ	The Dirac function
λ	The bulk viscosity (SPH), wavelength (r-PIV)
φ	The shape function
μ	The dynamic viscosity
ν	The kinematic viscosity
Ω	The fluid domain (SPH), The solid domain (FE)
γ_k	The polytropic constant of the fluid
ω	The volume of a particle
∂D	The contour of the kernel support
$\partial\Omega$	The boundary of the domain Ω
ρ	The density
ρ_e	The density of Riemann problem solution
σ	The stress tensor (SPH), the standard deviation (r-PIV)
C_0	The nominal sound speed at the free surface
D	The stiffness tensor (FE), The compact support (SPH)
d	The strain rate tensor
d_p	The seeding particle diameter
FAR	The ratio of footprint width on length
$\vec{F}_{f/s}$	The force applied by the fluid on the deformable body
$\vec{F}_{ext}$	The generalized force vector
$\vec{f}$	The volumic forces density
$\vec{g}$	The gravity

H_w	The water film depth
h	The height of the tread, the smoothing length (SPH)
I	Intensity profile
K	The solid stiffness matrix (FE)
k_{CFL}	The Courant number
L_x	The length of the CPA, the length of the water puddle (SPH)
L_y	The width of the water puddle (SPH)
M	The solid mass matrix (FE)
Ma	The Mach number
m	The mass of fluid
m_c	The child particle mass for APR
m_p	The parent particle mass for APR
N	The number of particles (SPH), the number of runs (r-PIV)
n	The refractive index
n_s	The number of segments defining each groove
P	The fluid pressure
P_0	The nominal pressure at the free surface
P_e	The pressure of the Riemann problem solution
P_k	The pressure on wet panel
P_{tire}	The tire inflation pressure
p	The ratio between the numbers of fluid and solid time steps
R	The kernel radius
R_c	The radius of a child particle
Re	The Reynolds number
R_p	The radius of a parent particle
S	The contact surface between the tire and the ground
S_0	The reference contact surface between the tire and the ground
SD	The ratio rotating speed of a wheel dry on wet
St	The Stokes number
TXD	The mean profile tread depth
TVR	The tread void ratio
$\vec{u}$	The displacement vector
V_0	The vehicle speed
V_h	The hydroplaning speed

$V_{u_{mean}}$	The mean longitudinal velocity inside a segment
$\vec{v}$	The velocity vector
$\vec{v}_e$	The velocity of Riemann problem solution
W	The kernel function
$\vec{x}$	The position vector

Abbreviations

ALE	Arbitrary Lagrangian Eulerian
APR	Adaptive Particle Refinement
A6	MICHELIN Alpin 6
CCP	MICHELIN Cross Climate+
CFA	Cut-Face Approach
CFL	Courant-Friedrich-Levy
CPA	The contact patch area
CPS	Conventional Parallel Staggered
EOS	Equation Of State
FDM	Finite Difference Method
FEM	Finite Elements Method, also denoted FE
FSI	Fluid Structure Interactions
FVM	Finite Volume Method
ISPH	Incompressible Smoothed Particle Hydrodynamics
IW	Interrogation window
LES	Large Eddy Simulations
MB	Mass budget
MISCL	Monotone Upstream-Centered Scheme for Conservative Laws
NFM	Normal Flux Method
PCY4	MICHELIN Primacy 4
PIV	Particle Image Velocimetry
P-PIV	Planar Particle Image Velocimetry
PST	Particle Shifting Technique
RANS	Reynold-averaged Navier-Stokes
r-PIV	refracted Particle Image Velocimetry
SPH	Smoothed Particle Hydrodynamics

TR-PIV	Time-Resolved refracted Particle Image Velocimetry
VLIF	Volume Laser Induced Fluorescence
WB	The water-bank
WCSPH	Weakly Compressible Smoothed Particle Hydrodynamics
WI	The wear indicator

Chapter 1

Overview on the hydroplaning phenomenon

1.1 Introduction and motivations

Hydroplaning is a hydrodynamic phenomenon that occurs when the amount of fluid encountered by a tire exceeds the combined drainage capacity of the tread pattern and the road texture when reaching a critical rolling speed. At this point, a water film builds between the road surface and the tire leading to a loss of contact between the tire and the ground. This phenomenon is well known by drivers and may lead to very hazardous situations due to the loss of the vehicle's control. Today, the European Union wet grip label is implemented to rate tires depending on their ability to stick to the road in wet conditions. Tires are rated from class A (the shortest braking distance) to class E (the longest braking distance). The difference in each category can mean an extra 3-6 meters on the stopping distance [21]. However, the wet braking labeling rates the performance of the tire in the new stage, and this performance degrades with the tire wear [122]. Therefore, tire manufacturers have been actively exploring ways to improve the performance of tires under wet conditions, and testing them in both new and worn states. Indeed, maintaining tire performance as long as possible is a major challenge for the tire industry, especially in today's ecological context.

Michelin, as one of the world's leading tire manufacturers, initiated the present research in collaboration with the LHEEA (Research Laboratory in Hydrodynamics, Energetics and Atmospheric Environment) in Ecole Centrale de Nantes in France for the numerical simulation part and with the LMFA (Fluid Mechanics and Acoustics Laboratory) in Ecole Centrale de Lyon for the experimental part. The present CIFRE thesis is expected to fit in an industrial framework and is a part of a large project that started years ago and involved previous PhD theses in collaboration with Nextflow Software (Siemens

Digital Industry Software), the LMFA, and the LHEEA. The proposed work is therefore an extension to the anterior advances and relies largely on the numerical and experimental tools already implemented (Hermange [51], Michel [84], Cabut [10]). The main objective is to push further our understanding of the hydroplaning phenomenon by analyzing the water flow drained by the tire in different testing configurations (water height, vehicle speed...). In addition, we aim to propose new analyzing tools and build parameters of interest in order to propose new leads to enhance the performance of the tire tread pattern. The present study is based on both numerical and experimental analysis and introduces a novel local comparison between the related results, which has very scarcely been done in the past. Different tread types are studied from the geometrically simple smooth treads to the complex directional treads, bringing to light not only the flexibility of the adopted numerical/experimental strategy but also its limits.

In this first chapter, we introduce the mechanism of hydroplaning detailing the leading parameters involved in this phenomenon along with the different means to quantify the establishment of a hydroplaning situation. Afterward, a state-of-the-art concerning the study of wet grip loss with a particular interest in the existing numerical and experimental tools is presented. Several interrogations are raised, highlighting the ongoing developments and shortcomings. Finally, the strategy adopted to investigate the hydroplaning phenomenon is detailed. The difference between the studied treads requires a different investigation approach for each tread type and a focus on a specific region of the water flow.

1.2 Specific vocabulary and presentation of the phenomenon

1.2.1 Some definitions

We give below some definitions that we will use throughout this study, the reader may refer to Fig.1.1:

— Rib: a strip of rubber that wraps around the circumference of a tire. There are several ribs molded into each tread pattern.

— Groove: the space between each rib is called a groove. The water is channeled inside these grooves when the tire rolls over a puddle.

— Shoulder: the outer edge of the tread that wraps into the sidewall area.

— CPA (Contact Patch Area): the region where the tire is in contact with the ground.

— WB (Water-bank): the region in front of the tire where the fluid is pushed and its velocity is at its highest.

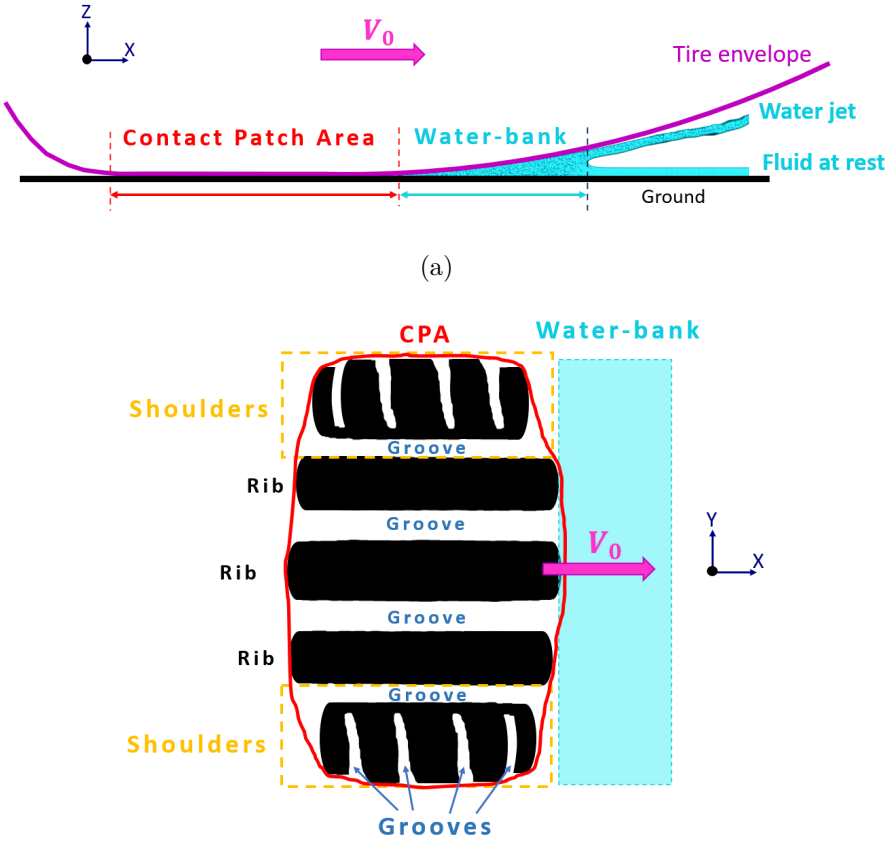

Figure 1.1 – Scheme of an XZ view of a tire rolling over a water puddle (a) and an example of a tire footprint with region definition (b). The CPA contour is traced with a red line. The rolling direction is indicated with a pink arrow V_0 in both figures.

1.2.2 The hydroplaning phenomenon

The situation of hydroplaning happens progressively. When the vehicle velocity increases, the contact surface between the tire and the wet road decreases due to the tire deformation under the hydrodynamic pressure [55] (Fig.1.2 points A to D). When reaching a critical speed, called the hydroplaning speed V_h, the fluid pressure, proportional to

the uplift force developed in the water film, exceeds the tire inflation pressure and a full loss of contact is witnessed (Fig.1.2 point E). The contact area between the tire and the

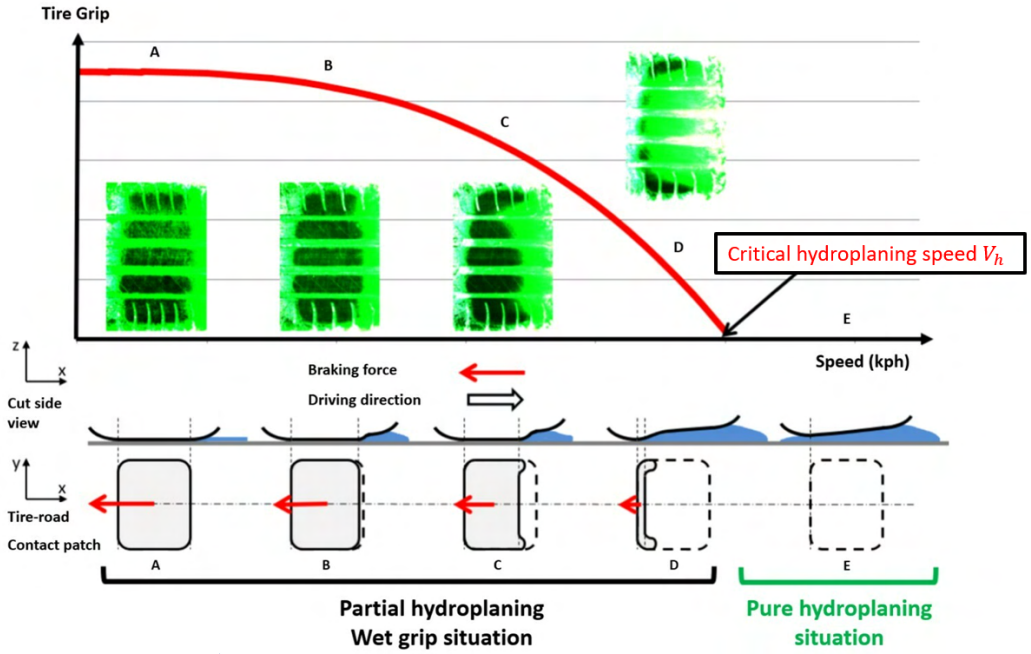

Figure 1.2 – Evolution of the contact patch area with the vehicle speed in the hydroplaning phenomenon (image extracted from Hermange et al. [50]).

road is subject to complex and different phenomena. It has been subdivided into three zones by Moore [89] and Allbert [2] (see Fig.1.3) :

— Hydrodynamic zone or bulk zone

— Viscodynamic zone (the transition zone between the first and third zones)

— Dry contact zone

In region A or bulk zone, the development of hydrodynamic pressure in the water wedge (or water-bank) results from the impact of the tire on the fluid at rest, and this pressure evolves nearly proportionally to the square of the speed of the vehicle. This is known as the NASA equation (Horne and Dreher [55]) and it directly links the inflation pressure of the tire with the hydroplaning speed (Eq. (1.3)).
In region B, a thin water film (few μ-meters) exists between the tire and the road surface. The thickness of this water film decreases progressively from the end of zone A to the beginning of the contact patch area (C). There is actually nearly zero relative motion

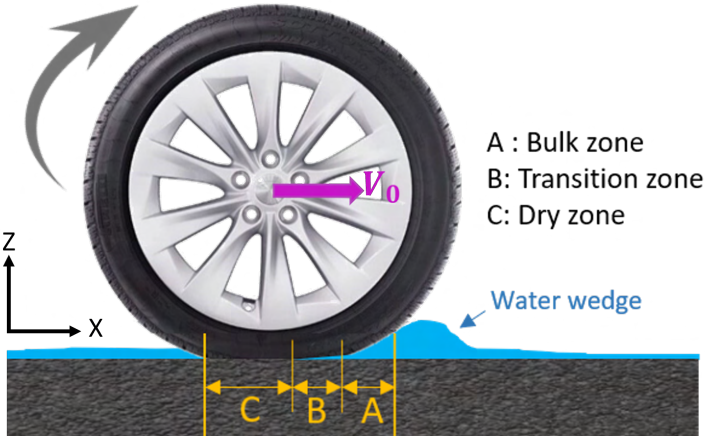

Figure 1.3 – The three-zone concept in hydroplaning. The tire rolling direction is indicated by the V_0 arrow. The width of the three zones is arbitrarily chosen and is not necessarily representative of a real situation.

between the tire and the ground in this area, the rubber blocks are laid down on the road surface in the same way we put our feet on the ground as we walk (Fig.1.4). If the vehicle speed is not high enough, the film of water gets stored inside each tire groove before the groove itself travels the full length of contact. If we increase the vehicle speed, at some point the water storage inside the grooves, which depends on the geometry of the tread elements, the thickness and viscosity of the water film, and the surface texture, will not happen because the grooves already left the contact area. Therefore, a thin water film remains and compressibility questions arise.

In region C, the tread elements have made, for the most part, contact with the road surface by removing nearly all the water towards the shoulders or the rear of the tire. This region is defined as the contact patch area (CPA). Although almost all the skid resistance is developed in this zone, small pockets of water still remain between the asperities of the road surface (Fig.1.5). The molecular adhesion is therefore inoperative between the tread and the road since it requires a perfectly dry and clean surface for van der Waals bonds to develop. Indeed, the tire grip is developed as a result of the frequency of excitation of the rubber when sliding on the ground. In this situation, two friction mechanisms intervene: i) the indentation caused by the crashing of the rubber block against the road asperities, and ii) the adhesion which results from the viscous behavior of rubber and therefore the deformation of the rubber blocks resisting the slipping (Hall et al. [45]). The first mechanism remains when the road is wet, whereas the adhesion cannot operate. For

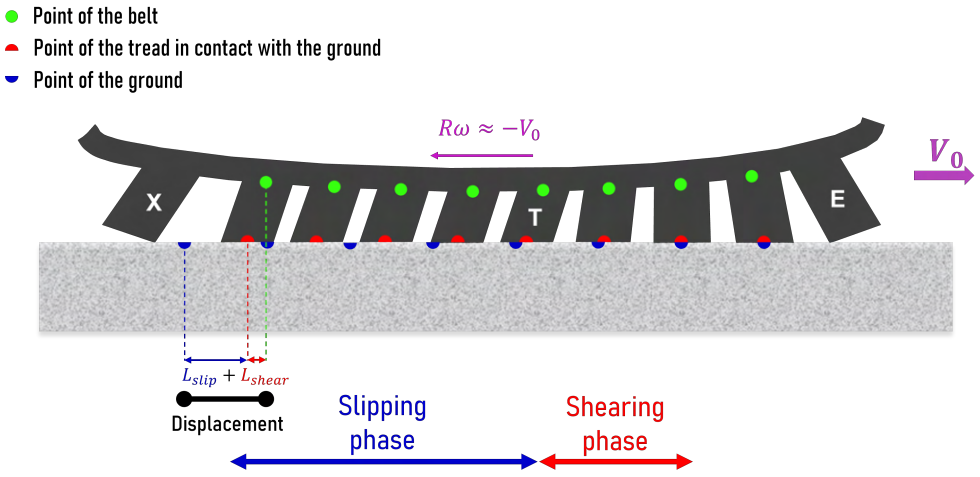

Figure 1.4 – Contact between tire blocks and dry ground during the braking phase. The tire is moving to the right (V_0), and the tire rotation is indicated with the $R\omega$ arrow. The tread block E is entering the contact region while block X is leaving it. Starting from block T, the blocks are slipping since the maximum shearing is reached.

more details about the rubber contact, we refer the reader to Persson [104].

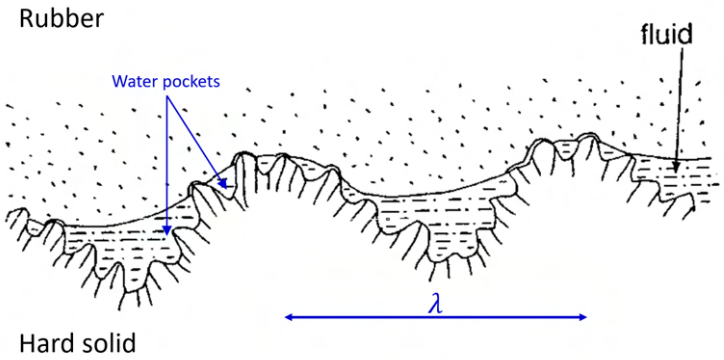

Figure 1.5 – The trapped liquid inhibits the rubber to get squeezed into the small-sized surface cavities. The distance between the macro asperities λ is between $10^{-6}m$ and $10^{-2}m$. Image extracted from Persson [104], the text in blue has been added.

As mentioned previously, multiple parameters are involved during the hydroplaning impacting directly the length of these three zones and in particular on dry zone C, which plays a major role in the tire grip. In the following section, we introduce these influencing parameters.

1.2.3 Influencing parameters

Various parameters are involved during a hydroplaning situation, and emphasizing their impact on the loss of contact surface between the tire and the wet ground is very important. The work of Horne and Dreher [55] already started establishing a list of the leading parameters contributing to the hydroplaning:

- Fluid parameters: fluid film thickness. It is important to notice that even a very thin water film (in the order of magnitude of the ground asperities i.e. less than $0.7mm$) in which the surface is called damp and not wet, impacts the grip performance. However, in the current study, we focus on the hydroplaning phenomenon, happening on a wet surface, meaning that the water film exceeds the average surface texture ($0.7mm$ to $0.8mm$). The density and the viscosity have also an impact, but usually, these parameters are supposed constants during a hydroplaning study.
- Tire parameters: tread pattern, tread depth, tire width, inflation pressure, tire materials, and internal architecture.
- Vehicle parameters: the vehicle speed and weight.
- Road parameters: the pavement roughness.

What has been already demonstrated in the literature and largely acknowledged is the following:

— Increasing the water film thickness reduces the hydroplaning speed since the volume of water to evacuate is increased and so is the hydrodynamic pressure. Furthermore, it has been observed that the higher the car speed, the higher the gap between the hydroplaning speed at low water depth and high water depth [50].

— Increasing the tire tread void increases the hydroplaning speed: The hydroplaning phenomenon seems dependent on a combination of the volume of water to evacuate from the road to the void volume of the tread. This is called the water-absorption capability of the tire and is noted γ. Sinnamon [115] proposed the following expression that has also been used by Spitzhüttl et al. [116]:

$$\gamma = \frac{\text{Volume of tread void}}{\text{Volume of water}} = \frac{TVR \times h}{H_w} \tag{1.1}$$

where TVR is the tread void ratio, h is the tread depth and H_w is the water depth. They stated that if $\gamma > 1$ then all the fluid is evacuated easily, and on the contrary, if $\gamma < 1$ some water remains and exerts on the tire an important hydrodynamic

pressure. Hermange et al. [50] extended this parameter in the case of worn tires taking into consideration the modification in the tread geometry due to the buffing operation and proposed the following equation:

$$\gamma = \frac{TVR(h) \times h}{H_w} \tag{1.2}$$

— Increasing the tire inflation pressure increases the hydroplaning speed: The inflation pressure acts as a shield against the hydrodynamic pressure counteracting its effects. The higher the tire pressure, the more difficult the deformation of the tire and the detaching from the ground. Horne and Dreher [55] proposed the empirical NASA equation for airplanes, linking the tire inflation pressure P_{tire} with the critical hydroplaning speed V_h as the following:

$$V_h = 10.35\sqrt{P_{\text{tire}}} \tag{1.3}$$

where P_{tire} is expressed in *psi* and V_h in *mph*. However, this formula is still used in the automobile framework adapting the value of the constant. Eq (1.3)) has been obtained assuming that the lift component of the hydrodynamic pressure force F_V is proportional to the contact area between the tire and the ground A_G, the fluid density, and the square of the ground speed. The tire inflation pressure was then approximated by F_V/A_G.

— The more rounded the initial footprint, the higher the hydroplaning speed. This is known as the bow wave. Basically, a rounded object penetrates more easily in water than a square shape. Indeed, by applying the Bernoulli equation in front of a locked wheel:

$$P_M = \frac{1}{2}\rho\ (V_0.cos(\beta))^2 \tag{1.4}$$

where P_M is the pressure at point M, ρ is the water density, V_0 is the vehicle speed and β is the local angle between the horizontal and the direction of the flow (Fig.1.6). To reduce the hydrodynamic pressure P_M causing the tire deformation and contact patch loss, β should be increased. Therefore, the CPA should be sharper in the rolling direction.

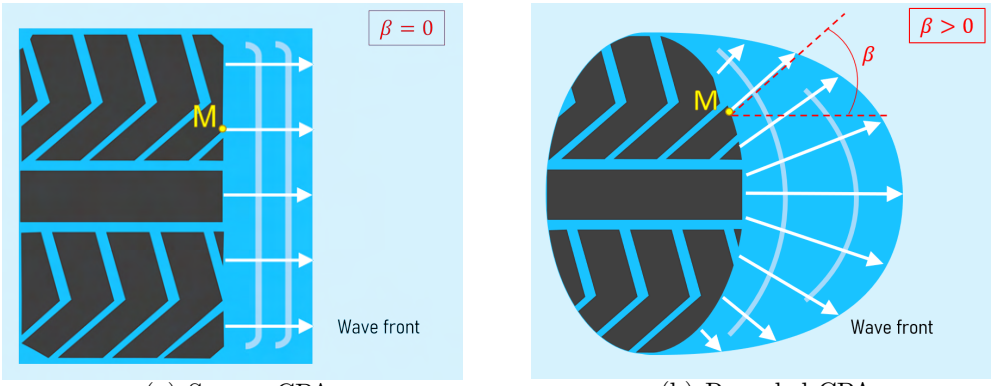

(a) Square CPA (b) Rounded CPA

Figure 1.6 – Schematic representation of respectively a square (a) and a rounded (b) CPA with a highlight on the water drainage in front of the tire.

1.2.4 Outputs quantities

The quantification of the hydroplaning is far from being a trivial matter. Some of the widely used parameters are:

- The relative remaining surface between the tire and the ground, expressed as (S/S_0), where S_0 is the reference contact surface (when the vehicle is at rest for example) and S is the actual contact surface at a given speed [50], [137] [27]. These works have all obtained such ratio as a function of specific tire design, leading to their own hydroplaning speed. Experimentally, in some smooth road conditions, the contact surface is usually determined using optical measurements.
- The contact patch length measurement has been used by Niskanen and Tuononen [91] comparing a longitudinal tire at different inflation pressure P_{tire}. Three accelerometers were attached to the inner liner of the tire to measure the distorted shape of the contact patch. By processing the longitudinal acceleration signal peaks, the phase of entering in contact with the fluid, the beginning of the viscous aquaplaning, and the end of the contact were determined. One of the interesting results was that the contact length of a tire with low P_{tire} is longer for low velocities than a tire with higher P_{tire}, but it reaches the full hydroplaning earlier.
- The hydrodynamic pressure distribution is also rather commonly used when the analysis is done via numerical tools [73]. They observed that the pressure inside longitudinal grooves is reduced in the case of a bionic tire (inspired by shark skin) against a smooth tire. They explained this difference with the reduction of flow

resistance and acceleration of the water drainage in the case of the bionic tire. This is one of the advantages of using a numerical model, giving the possibility to access the fluid pressure in very local regions in front of the tire and inside the grooves.

- In other studies, equations for the hydroplaning speed have been proposed based on the footprint aspect ratio and the inner tire pressure determination as proposed by Lim and Ku [71]:

$$V_h = 83.35 - 27.59FAR + 0.168P_{\text{tire}} \tag{1.5}$$

where FAR is the footprint aspect ratio (width divided by length), V_h is in km/h and P_{tire} in kPa. In this case, P_{tire} was fixed to $220kPa$. This links with the contact surface approach, it is just another way of expressing it.

- The skid resistance calculation was also adopted by some practitioners [108],[100]. The skid number expression involves the tire tread depth, the water depth, and the road surface texture. For example, Rose and Gallaway [108] proposed the following equation for skid resistance prediction:

$$SN = \frac{154}{V_0^{0.77}}\left(h^{0.05} + \frac{4.71\,TXD^{0.09}}{(25.4H_w + 2.5)^{0.09}}\right) \tag{1.6}$$

where SN is the skid number at a given speed and TXD is the average surface texture. All distances are in inches, V_0 in mph and $P_{\text{tire}} = 165.5kPa$.

- Lately, very local investigations inside the tread pattern have been introduced on both experimental [10] and numerical [49] levels opening the possibility to define new parameters built based on the fluid circulation inside the tread grooves and the water-bank.

1.2.5 Two-phase flow interrogations

The hydroplaning certainly raises a handful of interrogations considering the complexity of the problem and the actual state of the art regarding the comprehension of the phenomenon. Indeed, the more local information and resolved results in time and space about the flow circulation under and around the tire we are able to capture, the more demystified the physics of this phenomenon would get. Some new tools, either numerical or experimental, can deliver accurate local results, enabling not only a deeper understanding of the hydroplaning but also providing new observations and questions:

— Cabut [10], initiated the first r-PIV (refracted Particle Image Velocimetry) observations inside the grooves of a longitudinal tire tread. He confirmed Yeager's hypothesis about the existence of bubble columns which evolves with associated vortices depending on the tire wear state and groove's width. Cabut deduced from a cross-correlation model accounting for such bubble presence and a simulation of Taylor-Green vortices with or without bubbles what is really observed from in situ r-PIV tests (Michelin Ladoux) if a bubble column exists. He deduced what is the Z-level of the r-PIV measurements and that the velocity field showed indeed the presence of vortices. The masking effect of bubbles on the experimental measurements was pointed out in the case of a fluorescent particle present behind the bubble column. Indeed, the light emitted by this particle will not reach the camera sensor and the particle will not be seen on the PIV recorded image. In 1974, Yeager [136] first made the hypothesis of the flow inside a longitudinal groove with the presence of two vortices formed at the leading edge of the CPA (Fig.1.7). He also suggested that the viscosity is of minor importance because of the steadiness of these vortices in the case of a free-rolling tire. Indeed, their size is constant through the CPA as a function of time. These observations were made at a driving speed of less than $65km/h$ and a water film depth of $2mm$. These vortices have been observed through numer-

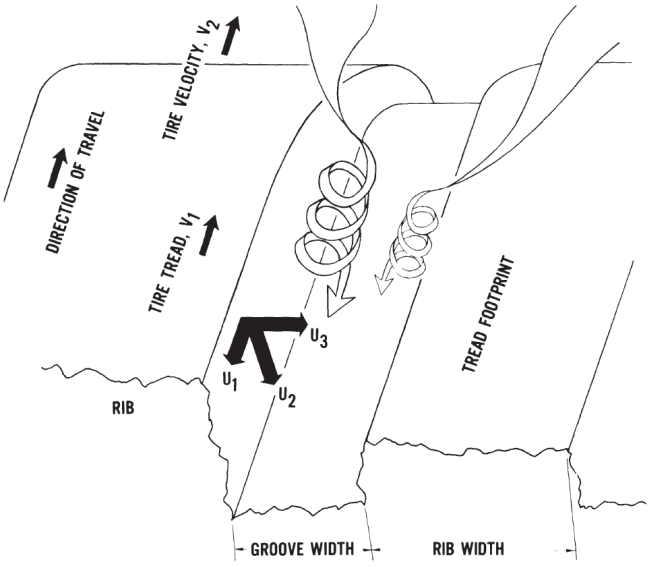

Figure 1.7 – Highlight of the twin vortices inside a longitudinal groove from Yeager [136].

ical analysis by Hermange et al. [49] as well. In the present work, bubble columns do appear inside the tire grooves in some r-PIV images, but their effect will not be

further discussed.

— The effect of multi-phase flow is also another aspect of the hydroplaning rather scarcely looked upon, yet it can have an influence on the flow circulation. Vincent et al. [131] suggested a hydroplaning simulation where a 3D air-water flow interacts with a moving tire. Other numerical strategies like the Finite Volumes-Finite Elements (FVM-FEM) coupling [111] [98] consider a simplified two-phase fluid model where the rest of the fluid domain not occupied by water is treated as void. Gillard [39] stated that the introduction of an air phase is computationally very expensive and that the airflow surrounding the tire is of no interest in the hydroplaning analysis. We do think that such a phenomenon has to be accounted for to determine correctly the water evacuation by the grooves but this could be a clear hypothesis to infirm or confirm for future research studies. It is true that lots of difficulties still exist when modeling turbulence and multi-phase flows in addition to the difficulty to model accurately the tread geometry in order to capture such effects. On the experimental side, the multi-phase flow is considered a source of bias in some measurements and is also a source of prohibition to providing measurements above the bubble column inside grooves [10]. In the r-PIV images we can see that in some regions, a two-phase flow exists, e.g., behind the tire. Turbulence effects may also appear inside new tire grooves where $Re \approx 17000$ ($V_0 = 50km/h$ and the velocity in the rear is around $0.1V_0$, groove width=$12mm$). In the rear zone of tires and regions close to the shoulders, the two phase-flow prohibits any kind of r-PIV measurements due to very high noise. In such zones, it is difficult to apply any mask to capture only valid measurements. No analysis was thus possible from the r-PIV measurements from Cabut's work. It has to be noted that it is the same for the present work. On the numerical side, introducing a gas phase in the SPH sub-domain goes beyond the scope of the present work for its very high computational costs.

1.2.6 Fluid-structure interaction accounting

Suction effects can appear due to the tire rubber block deformation as mentioned in Cabut's PhD work [10]. The relaxation of these blocks when the tire leaves the ground re-opens the grooves and the surrounding water flow is affected. To capture this phenomenon numerically is a challenge and very little research has been dedicated to it. In the SPH method, some treatments are usually added to the solver to induce the detachment of

particles from a body. However, the suction phenomenon requires that the particles stay attached to the solid. Michel [84] (Chapter 4) introduced an SPH model of jet detachment compatible with the suction effects. In the current work, tests are conducted using these developments in order to capture more accurately the flow circulation in some particular regions of the CPA. It highlighted the importance of this phenomenon in our numerical model. This will be discussed in Chapter 5.

1.2.7 Wear indicators influence

As mentioned at the beginning of this chapter, testing tires in both new and worn states are of interest to tire manufacturers. The commonly known difference between a worn and a new tire is the reduction of the tread depth, yet other geometrical modifications may appear when the tread is buffed (appearance/disappearances of sipes, blockage of grooves' connections, modification in the grooves' width...). These changes in the tread geometry are usually thoroughly controlled upstream of the designing phase. They contribute to maintaining the tire performance, e.g., wet and dry grip, even at a worn stage. Wear indicators (WI) are used to warn the vehicle's user that the tire needs replacement when the tread depth reaches a legal limit. WI are placed all around the tire at different points to measure how evenly the tread is worn down (Fig.1.8(a)). Michelin's testing protocol establishes that the worn stage is obtained by buffing a new tire until $h = 2mm$, at this point the tread nearly reaches the level of the wear bars. This results in the appearance of the WI in some of our r-PIV images as depicted in Fig.1.8. Their effect on the water circulation inside the longitudinal grooves has been discussed in Cabut [10]. The streamwise velocity inside the groove is affected depending on the position of the WI in the CPA. In the current work, no further analysis of the correlation between the WI position and the velocity inside the tread grooves is studied. Nevertheless, we choose the r-PIV images where no WI appears in the CPA to post-process, limiting the variability introduced by these wear bars.

1.2.8 Pavement texture

The surface texture of the road has already been cited as one of the influencing parameters of hydroplaning. Indeed, when we defined this phenomenon at the beginning of this chapter, we emphasized that it is the combined effect of the tread pattern and the road texture that defines the drainage capacity when rolling on a wet surface. In the

(a) (b)

Figure 1.8 – On the left is an image of the MICHELIN Primacy4 at a new state with a highlight of the wear indicators. And on the right an r-PIV image of the same tire in a worn state, the wear indicators are highlighted in red.

early 70s, Yager et al. [135] proved experimentally that when the average texture depth of the pavement increases, the wet stopping distance of aircraft decreases. Both asphalt and concrete surfaces were tested with an average texture depth varying from $0.1mm$ to $0.4mm$. Moreover, according to Hoerner [53], 70% of the wet weather crashes are preventable with improved texture or friction on pavement surfaces. Hoerner stated that the road macrotexture (longitudinal wavelengths of $0.5mm$ to $51mm$ and vertical amplitude ranging between $0.1mm$ and $20mm$) provides adequate friction in wet conditions and at high speeds. On the other hand, an effective microtexture provides adequate surface friction on dry pavements at all speeds and on wet pavements at slower speeds (Fig.1.9). In addition, Ahammed and Tighe [1] measured the skid resistance SN from nine asphalt concrete surface types and concluded that the quality of the aggregate is the predominant factor for SN. Ribbed tire skid resistance was shown to increase with an increase in coarse aggregate whereas the voids in mineral aggregate showed no correlation with SN. Last but not least, Dehnad and Khodaii [24] showed that by increasing the pavement texture by $0.5mm$, the hydroplaning occurrence frequency increases by 33%.

Nevertheless, the study of the road texture effects outreaches the present thesis scope. A smooth road is considered all along this study on both experimental and numerical levels though working with a rough ground is technically possible [48]. This will be further discussed in Section 2.4.3.

We now propose to develop the different works to date in the different possible approaches: experiments, numerical simulations, and models.

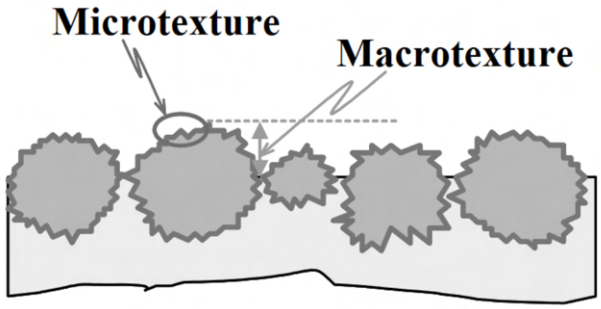

Figure 1.9 – Surface macrotexture and microtexture from Flintsch et al. [33].

1.3 Literature overview

In the literature, several studies have been conducted on the hydroplaning framework. More generally, experimental studies started in the early 60s but only for aerodynamic objectives, offering a first description of the flow around plane tires rolling on flat ground and describing the associated leading parameters. We will focus here only on studies concerning the hydroplaning problem. Recent optical measurement techniques offered the possibility to have a deeper analysis of the hydroplaning, accessing local data as shown below. Meanwhile, it was only in the mid-90s that the first numerical models emerged with the increasing interest in FSI (Fluid-Structure Interaction) problems. Different approaches have been proposed in which the tire is the solid sub-domain and the water is the fluid sub-domain. However, tire hydroplaning is a very challenging application due to the complexity of the tire (multiple materials, singular geometry, important deformation), the FSI coupling, the very large deformation of the fluid domain, the need for a fine discretization imposed by the tread elements' dimensions... We note that small tread geometry modifications can have a great impact on the phenomenon. Such fine resolution is therefore needed in industrial applications. For all these reasons, the early numerical methods considered simplified tire models rather far from reality [62], [101]. However with the increasing computational performances and the development of CFD (Computational fluid dynamics), more realistic models were proposed, on which tire manufacturers and academic researchers increasingly rely on.

1.3.1 From an experimental point of view

As stated before, the determination of the loss in the contact surface is one of the most spread tools to quantify a hydroplaning situation. Quantitative results to estimate the contact patch area have been proposed by Yeager [136] using the VLIF (Volume Laser Induced Fluorescence) technique. A fluorescein dye was introduced into the water puddle, then images of the tire footprint were recorded while a source of light illuminated the puddle through a glass plate. Then, based on the contrast difference between the region of tire/road contact (black portion) and the water around (illuminated portion), it was possible to measure the contact patch area. Two 2000W floodlights were used with a flash duration of 1/30000s and the images obtained had a good definition of tread geometry and allowed the determination of specific flow characteristics. More recently, Todoroff et al. [122] and Hermange et al. [50] adopted the same technique to measure the contact surface varying the vehicle velocity (from $50km/h$ to $90km/h$), the water depth (from $1mm$ to $8mm$), the tire type (summer/winter) and other parameters. An example of images taken using this technique are given in Figures 1.2 and 1.10 where a green fluorescent dye is used, and we can observe the black region of contact between the tire and the ground. In this case, the tire is rolling from the left to the right, and we can also notice the reduction in the contact surface mainly at the front of the tire when the vehicle velocity increases (point D in Fig.1.2). Numerical post-processing is required to determine the features of the surface which keeps contact with the ground using the black/green contrast (Fig.1.10).

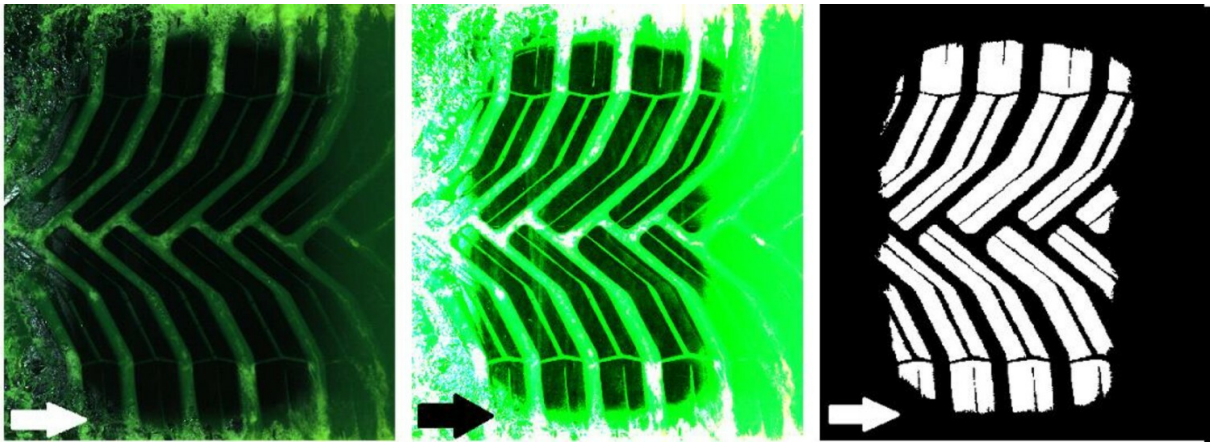

Figure 1.10 – Raw (left), post-processed (center) and final (right) images of the contact patch area at $50km/h$ and $8mm$ of water depth (extracted from Hermange et al. [50]). The arrows at the bottom indicate the rolling direction of the tire.

Donatellis et al. [27] used a similar technique to obtain images of the tire footprint at different vehicle speeds for the purpose of numerical validation.
Another method has been proposed by Tuononen and Hartikainen [123] [124] based on the measurement of the tire inner ring deformation (distance between the wheel and the inner ring) using an optical sensor. The tests were conducted on an $8mm$ water depth and at rather high speeds (most runs at $110km/h$). A comparison between the radial displacements at $80km/h$ and $110km/h$ was shown. The main advantages of this method are i) the possibility to incorporate the sensor inside the tire and therefore is applicable to nearly any tire, ii) no need for a specific in-situ track, iii) can easily test different road textures, and iv) offers a real-time estimation of the hydroplaning. However, the authors did not discuss the effect of the water height or the tire tread pattern.

Furthermore, Matilainen and Tuononen [79] introduced a contact length determination method based on the longitudinal acceleration signal of a tree-axial accelerometer attached to the inner liner of the tire. They quantified the reduction of the contact length as a function of the driving speed. Both new and worn tires were tested highlighting the importance of the tread depth parameter against the tire inflation pressure. Multiple water depths were considered from $2mm$ to $7mm$ depending on the track section. This method has the same advantages as the previous one.

Other practitioners adopted the skid number SN measurements to evaluate the hydroplaning. Mayora and Piña [81] pointed out that both wet and dry pavement crash rates present a decreasing trend as skid resistance values increase. Usually, the road texture is an important parameter to take into consideration when evaluating SN [108]. Zhang et al. [138] computed wet pavement skid resistance for porous and nonporous pavements. Three vehicle speeds were compared ($40km/h$, $60km/h$ and $80hm/h$) at three rainfall intensities ($60mm/h$, $150mm/h$ and $300mm/h$). They showed that the use of porous pavements resulted in a lower fluid uplift force, better tire–pavement contact, higher traction, and less tire deformation which are essential to developing a high SN.

Other methods based on velocity measurements of the water flow do exist as well, however, the literature is very sparse concerning these techniques. The first study was conducted by Suzuki and Fujikawa [119] and introduced a particle tracing measurement to build a velocity map of the water flow around a tire. The test facility consists of a

glass plate embedded in a water-filled road on which a car is rolling. A high-speed video camera and 500W tungsten lights were placed underground, oriented to the glass plate. Such a facility offered the possibility to visualize the contact area when using colored water. While for the velocity measurements, millet seeds of $1mm$ to $1.5mm$ of diameter were supplied in the water as tracer particles. The vehicle speed and the water depth were fixed at respectively $70km/h$ and $15mm$. This allowed them to obtain a Lagrangian trajectory from the seeding particles and its associated velocity map. The latter helped design an improved tread pattern with rearranged grooves parallel to the water flow. By doing so, the cornering force (lateral force generated by the tire slip during cornering) has been increased during a partial hydroplaning situation.
The second study concerning velocity measurements found in the literature was conducted by Cabut et al. [11] based on the r-PIV technique. The same test facility is used in the current work and is detailed in Chapter 3. The major advancements concern the measurements inside the grooves of some tire treads. Nevertheless, measurements in front of the tire were also conducted. Different vehicle speeds were tested in the case of a summer tire with longitudinal grooves. The water depth considered is $8mm$ in the case of a new tire and $1.5mm$ for a worn tire [10]. In front of the tire, the linear evolution of the water velocity with the vehicle speed was demonstrated. At high vehicle speeds, non-linear effects are highlighted and linked to the shape of the contact patch area. Moreover, a dependency between the location of the transverse grooves near the tire shoulder and the velocity inside these grooves is established. The potentiality of the r-PIV was demonstrated and is still to be developed but is not the aim of the present work. Nevertheless, some future work could lead to using the same principle to obtain 3D field adapting PTV (Particle Tracking Velocimetry) techniques. For the present work, we will just show the first trials with the Time-Resolved r-PIV (Chapter 4).

1.3.2 From a numerical point of view

On a numerical level, mesh-based methods have provided early hydroplaning models combining the Finite Elements (FEM) and the Finite volumes (FVM). Grogger and Weiss [43] initiated such a study by proposing a simplified model for a non-rotating tire. Based on symmetry considerations, only one-half of the problem was defined. The fluid method solves a free-surface flow on a rather coarse mesh ($\approx$ 25 000 cells) whereas a very simplified tire model was used ($\approx$ 2 700 solid elements). They compared the deformation of both a smooth and a grooved tire at different rolling speeds ($30km/h$, $60km/h$ and $90km/h$)

and water depths ($4mm$, $8mm$ and $12mm$). They compared as well the numerical results regarding the pressure distribution on the pavement with experimental results for the slick tire obtaining a rather good agreement for the three velocities. Moreover, Okano and Koishi [98] proposed also an FVM-FEM model combining a Lagrangian formulation for the tire and an Eulerian formulation for the fluid. To reduce computational costs, thin composite materials, such as the carcass and the belt are modeled using multi-layered shell elements, while the bead core is modeled with rigid elements. The other parts are modeled using 8-node continuum elements. The tire body portion and the tread portion are modeled separately first, and then combined with each other, by sticking them with a rigid connection. Also, a coupling algorithm enables the tire deformations to interact with the surrounding fluid by overlapping the fluid elements and the interface between Lagrangian and Eulerian elements is automatically updated. In these simulations, a water depth of $10mm$ is fixed and four analytical tread patterns are tested (longitudinal and V-shaped with some variations). The hydroplaning velocity of these models is confronted with experimental results. The numerical results are rather in good accordance with the tests in terms of ranking but the hydroplaning speed is over-estimated with the simulations. Other practitioners of the FVM-FEM coupling investigated the hydroplaning phenomenon. Cho et al. [18] proposed such coupling with some simplifications regarding the tire model (fiber-reinforced rubber parts modeled as composite shell, and the tire bead as rigid elements). However, they were able to generate a tire tread pattern more complex and realistic than the one presented in [98], and they compared it to a simple three-grooved pattern. This put into light the importance of the details in the tread design in particular the presence of directional grooves near the shoulders. To cite other studies using the FVM-FEM coupling for the hydroplaning application we can refer the reader to the work of Seta et al. [111] who compared a smooth tread and a grooved one adding some details to the pattern to improve the hydroplaning performance. They also highlighted the major difficulties in a hydroplaning simulation in the case of mesh-based methods (distortion of the fluid mesh and compatibility of the fluid mesh with a complex tread pattern). More recently, Gillard [39] proposed a new dynamic coupling scheme improving the numerical solution for tire hydroplaning and reducing the computing time, still under the FVM-FEM formulation. A solid predictor added to the GSS (generalized conventional serial staggered) algorithm and an adapted FSI time step size were introduced to optimize the accuracy and time efficiency of the simulation. The solid predictor replaces the solid displacement field at the interface transferred to the fluid. A more realistic longitudinal

tire was tested with $5mm$ of water layer thickness and the road/water ensemble was translated at $80km/h$. The 3D tire model was generated from the revolution of a 2D section inflated and mounted on a rim.

Another coupling strategy was proposed by Koishi et al. [62] where a FEM-FEM method was adopted to solve respectively the fluid and solid sub-domains. An analytical V-shaped tread was studied and compared to its reverse rotational direction. The rubber components of the tire were modeled with solid elements and the reinforcements with shell elements. A penalty-based Lagrangian-Eulerian coupling algorithm was developed to respect energy conservation and have a straightforward treatment of contact. A little later, Ong and Fwa [101] succeeded in simulating the sliding of a locked wheel over a flooded plane pavement surface taking into account the treatment of the tire/fluid/ground interactions. The tire tread was considered smooth simplifying significantly the problem. Therefore, in Fwa et al. [37], they studied in a theoretically derived analytical approach the effectiveness of rib tires. Later on, both Donatellis et al. [27] and Kumar et al. [63] used the FE formulation for solving the solid and fluid sub-domains in a unique software environment. The fluid behavior is described using an equation of state (EOS) for which mechanical properties of water are to be given. However, in [63] a smooth tire was considered for a range of tire inflation pressure and water depth conditions while in [27], a more realistic tire tread was studied with both longitudinal and directional grooves. They also confronted their results with experimental data regarding the evolution of the contact patch shape as a function of vehicle speed.

Furthermore, Oh et al. [97] proposed to use the Finite Difference Method (FDM) and the FEM strategy to simulate a hydroplaning problem. The FDM code solves the Navier-Stokes equation and results in the pressure distribution due to the water flow around the tire while the FE model of a tire is used to obtain the deformed shape of the solid part. Viscous effects of water were accounted and the film depth was taken between $5mm$ to $20mm$. A longitudinal tire was considered, and an asymptotic method was developed to estimate the pressure distribution in the regions of very shallow water (contact zone).

In 2011, Vincent et al. [131] developed a new solver to deal with unsteady multi-phase flows interacting with moving objects and they utilized it in a hydroplaning application. However, in this model, the effect of the flow on the tire deformation was not solved limit-

ing significantly the accuracy of the results. The study was rather about the macroscopic effects of water on the tire and the objective was to classify three tread topologies with respect to the magnitude of the total vertical normal forces exerted on the tire.

Recently, meshless methods have been adopted to model the fluid sub-domain in order to overcome the mesh limitations when simulating such complex problem as the hydroplaning. Let's recall that modeling this phenomenon presents many challenges due to i) the complexity of the tire geometry, ii) the large deformation of the tire mesh in the contact area, iii) the very important deformations of the fluid free-surface, iv) the non-linearity in the tire materials and v) the strong fluid-structure coupling. The Smoothed Particle Hydrodynamics (SPH) appeared as a reasonable approach for its good agreement with strong FSI problems and free surface flows with large deformations. The Lagrangian nature of this method offered rather simple handling of fluid-structure interface [35]. El-Sayegh and El-Gindy [109] adopted the SPH-FEM strategy in the case of truck tires. The master/slave contact concept was used for the interaction between the tire and the water film. They compared the hydroplaning speed for different inflation pressures with the NASA equation. The water depth effect was also examined stating that a decrease in the water film thickness between $20mm$ and $5mm$ leads to a 12% increase in the hydroplaning critical speed V_h.

Qu et al. [106] proposed an SPH-FEM model to simulate water spray generated by aircraft tires. The purpose of their study was not about the hydroplaning phenomenon in itself even if the footprint shapes were looked at, but it was about the comparison between the splashing angles and other spray contents for a rigid and an elastic tire. This study shows the efficiency of the SPH method to model such a phenomenon characterized by very large fluid deformations.

More recently, Hermange et al. [49] proposed a 3D fluid-structure SPH-FEM coupling strategy to study hydroplaning. The tire part was modeled using the FE method and the fluid using SPH. Both smooth and rough grounds were possible to model [51] and commercial tires were considered taking into account the complex grooves' geometry and the multiple materials constituting the several tire's layers. Several improvements were proposed in order to reduce the computational time while maintaining the accuracy and stability of the solution as the introduction of different time steps between the implicit

solid and the explicit fluid solvers. More details about this SPH-FEM coupling strategy are given in Chapter 2 as this work is in continuity to improve this numerical tool. To facilitate the comparison between the main existing computing hydroplaning models and the one adopted in the present research, we summarize in Table 1.3 the main features of these models.

Literature	**Formulation Fluid-Structure**	**Turbulence model/ Viscosity**	**Features and comments**
Grogger and Weiss [43] (1997)	FVM-FEM	$k-\varepsilon$	— $H_w \geqslant 4mm$ — Simplified tire model (smooth and longitudinal).
Seta et al. [111] (2000)	FVM-FEM	inviscid	— $H_w = 10mm$
Okano and Koishi [98] (2001)	FVM-FEM	(laminar flow)	— Compressible — $H_w = 10mm$ — Shell elements for carcass and belt. Rigid elements for the bead core.
Cho et al. [18] (2006)	FVM-FEM	inviscid	— $H_w = 10mm$ — Shell elements for the fiber-reinforced rubber.
Gillard [39] (2019)	FVM-FEM	-	— $H_w = 5mm$ — Membrane elements for the belts. The bead is modeled with 1D beam elements.

Koishi et al. [62] (2001)	FEM-FEM	-	— Compressible — $H_w = 10mm$ — Shell elements for reinforcements. Simple V-shaped tread.
Ong and Fwa [101] (2007)	FEM-FEM	$k-\varepsilon$	— $H_w = 7.62mm$ — Three components: the rim (rigid), the sidewalls, and the tread. Shell elements are adopted.
Donatellis et al. [27] (2009)	FEM-FEM	-	— $H_w = 7mm$ — The tread has a periodic symmetry.
Kumar et al. [63] (2012)	FEM-FEM	-	— $H_w \geqslant 7mm$ — Smooth tire tread. Three components: the rim (rigid), the sidewalls, and the tread.
Oh et al. [97] (2008)	FDM-FEM	-	— $H_w \geqslant 5mm$ — Straight-grooved tire.
Vincent et al. [131] (2011)	FVM-Analytic (no coupling)	LES	— $H_w = 8mm$ — No tire deformation due to the flow. Simple tread patterns.
Hermange et al. [49] (2022) and present work	SPH-FEM	inviscid	— Weakly-compressible SPH (explicit) — Implicit FE solver — $H_w \geqslant 1mm$

Table 1.3 – Review of numerical FSI approaches for tire hydroplaning

We can highlight that mesh-based methods are still the most widely adopted formulations in the case of hydroplaning simulation. The originality of our method is to work with a mesh-free method as the SPH. Moreover, most studies consider a water depth of at least $5mm$, while we initiated computations with $1mm$ of water depth. Such value of H_w is more representative of the daily use, i.e. about 99% of wet time the water depth is below or equal to $1mm$ (Biesse [9]). In addition, regarding the tire model, most studies simplify not only the geometry of the tire tread but also the internal tire structure (rigid bead core, shell elements for the belts), while in our case very realistic tire models are considered (commercial Michelin tires). It has no doubt advantages, especially for the experimental/numerical comparison although it also increases the computational costs. Finally, most models consider an incompressible fluid model while we work under the weakly-compressible hypothesis (further discussed in Section 2.1.7).

1.3.3 The physical models

Along with the experimental and numerical investigations regarding the hydroplaning phenomenon, some studies aimed at delivering physical models on either a simplified rubber/ground/water interaction or a macro tire/ground/water interaction. We have already introduced the NASA equation (1.3), a very simple yet extensively used model in the aviation and automobile industries. A little later, Horne et al. [56] proposed some improvements by including the initial tire footprint aspect ratio FAR into the first equation:

$$V_h = 7.95(P_{\text{tire}})^{0.5}\sqrt{\left(\frac{1}{FAR}\right)} \tag{1.7}$$

where P_{tire} is expressed in psi and V_h in mph. However, this model was limited to water film thickness superior to $10mm$ and for high pressure values. Ivey et al. [59] adapted Horne's equation, with empirical considerations in the case of heavy vehicles, and proved Horne's theory stating that lightly loaded truck tires do hydroplane (which was against the general assumption that trucks do not hydroplane) :

$$V_h = 23.3(P_{\text{tire}})^{0.21}\sqrt{\left(\frac{1.4}{FAR}\right)} \tag{1.8}$$

Other models were suggested taking into account other factors than tire pressure affecting the hydroplaning speed. For example, Gallaway et al. [38] proposed the introduction of

the road texture parameters and the tire tread depth based on empirical considerations:

$$V_h = SD^{0.04} \times P_{\text{tire}}^{0.3} \times (h+1)^{0.06} \times A \tag{1.9}$$

with

$$A = Max\left\{\frac{10.409}{H_w^{0.06}} + 3.507; \left(\frac{28.952}{H_w^{0.06}} - 7.817\right) \times TXD^{0.14}\right\}, \tag{1.10}$$

SD is the ratio between the rotating speed of the wheels on wet and dry pavement ($\approx 10\%$). P_{tire} is in psi, V_h in mph and TXD in mm.

Other models do exist in the literature including various parameters such as the drag coefficient (Cerezo et al. [14]) or the hydrodynamic lift coefficient for airplane tires (Van Es [128]).

Wies et al. [134] developed a rib sinkage model to determine the sinkage time of a given pattern. Indeed, if the water absorption into a pattern is prolonged the hydroplaning performance is improved. The idea of this study was to give simple rules of thumb for tread designers to improve the hydroplaning capacity of tires. However, this model was rather simple and included a single parameter to define the rib-type pattern :

$$K_p = \frac{(1-\Psi)^{3/2}}{1+n} \tag{1.11}$$

where n is the number of longitudinal grooves and Ψ is the void ratio.

Last but not least, we mention the contribution of Löwer et al. [74] as a more complex physical model to describe the contact between rubber and rough ground with water as an intermediate medium. Many parameters were taken into account as the tire pattern, the surface macro-roughness, and the rubber properties alongside the water film depth and the vehicle speed. Based on the Navier-Stokes equations and the Abbott-Firestone curve (an approximation for surface properties), the water squeeze out from a single tread block was considered thus calculating the contact area between the rubber and the ground. This model is valid for moderate water heights when no hydroplaning occurs and has been validated by the means of braking tests. Other models exist to describe rubber friction on wet surfaces, e.g, Persson et al. [103] taking into account viscous effects and validating the model through experimental and numerical results, and Kane et al. [61] approaching the hysteretic friction with a simplified visco-elastic contact. Nevertheless, we will not go into more details since in the present work we do not seek validation through these models but rather through the experimental/numerical comparison. Also, the scope of these

models is usually restrained while in the present application we are looking for models that can include different tire treads and rolling conditions, thus our interest in numerical simulations.

1.4 The thesis scope and adopted strategy

In the present work, both a numerical and an experimental tool are used in the hydroplaning analysis. On the numerical level, a coupled SPH-FEM strategy is adopted based on a weakly-compressible SPH explicit solver developed by the LHEEA laboratory and Nextflow Software (Siemens) to solve the fluid sub-domain (the water puddle), and the Michelin in-house implicit FEM solver for the structure sub-domain (the tire). Whereas on the experimental level, the r-PIV measurements, jointly developed by the LMFA and Michelin (2014), are retained and conducted on a dedicated track at the Michelin research center of Ladoux in France. This dedicated measurement technique has a recent hydroplaning application and several comprehension opportunities are still possible.

These tools offer the possibility to analyze the velocity fields inside the tire tread pattern and in the region in front of the tire, the so-called water-bank (WB). In the present study, we are not interested in the full hydroplaning phenomenon, where no contact between the tire and the ground is achieved anymore, but rather in partial hydroplaning. In this situation, a loss in the contact patch is witnessed but the driving speed is not high enough to lose completely the contact (points A to D in Fig.1.2). Indeed, reaching very high speeds is not the goal of this thesis since we aim at studying the evolution of parameters inside the CPA, e.g., the velocity inside the grooves and the contact patch length. In addition, reaching a rolling speed close to the hydroplaning speed makes the r-PIV measurements very difficult and significantly degrades the quality of the results.

We aim to better understand the physics driving the hydroplaning phenomenon and the evolution of the flow inside the tread grooves and in the WB and its dependence on parameters like vehicle speed and water depth. The analysis is first focused on a smooth tire and therefore exclusively on the water-bank region to better understand the flow circulation inside the WB without the influence of the grooves on the flow. Note that at the best of our knowledge, only Cabut's work studied the WB for a tire with tread designs

and no work exists on slick (smooth) tires concerning the WB region. After analyzing the different phenomena that can exist in front of the tire when rolling over a water puddle, we extend the same analysis to a tire with a tread pattern with longitudinal grooves. The flow structure is obviously modified, and local velocities inside the CPA are examined. The strategy adopted to analyze the flow circulation in the case of longitudinal treads does not apply to more complex treads as the directional ones. Therefore, we propose a different method for studying a wide range of tread patterns. With it, a comparison between different treads is possible, highlighting the different behaviors regarding water drainage.

Hereafter are the three types of tire treads tested:

1. Smooth treads with no grooves (slick tire).
2. Longitudinal tire tread (e.g., the Primacy4 in Fig.5.1), a typical sculpture of summer tires. The ribs are longitudinal, and the main grooves are along the rolling axis. Some transverse grooves are present at the shoulder of the tire.
3. Directional tire tread (e.g., the Cross Climate+ in Fig.6.12), usually used in winter tires to facilitate water evacuation, the grooves make an angle with the rolling axis.

(a) (b)

Figure 1.11 – Examples of 3D sculptures currently available on the market: MICHELIN Primacy 4 (a) and MICHELIN Cross Climate+ (b)

Along with the type of tread, another parameter must be detailed which is the state of the tread:

— New state: The tire tread still has its initial and full depth, usually around $8mm$ but may vary between the different tire models.

— Worn state: The tire tread depth is reduced to $2mm$. Three points should be noted when working with worn tires, i) the process to obtain the wanted depth introduces inevitably an irregularity in the shape of the groove, ii) when reaching $2mm$ in the tread depth, the wear indicators appear and can be observed on the recorded images. These wear indicators introduce an added discrepancy between the velocity fields of the different rollings since its position may vary from one image to another and it can also not appear at all in some cases. And iii) details of the tire structure can be modified like the appearance of sipes or the disconnection of some grooves. For example in the case of the PCY4 tire, we can see in Fig.5.1 representing the new state of the tread that the transverse grooves and the longitudinal grooves in the shoulders are connected. At a worn state, this connection is no longer observable.

1.5 Conclusion

The purpose of this chapter was to put the reader into the context of the current thesis that should meet both industrial and academic expectations. The hydroplaning phenomenon has been introduced as a complex FSI problem involving a wide range of parameters that impact the tire wet grip performance. The quantification of the hydroplaning varies from one study to another putting into light the substantial work that has been provided in this matter on both experimental and numerical sides. Even though many models have been proposed to link the hydroplaning velocity to the inflation pressure and extensive analyzes have been conducted to quantify the impact of influencing parameters such as the water height or the tread depth, many interrogations remain. The numerical models have been enhanced, introducing a two-phase flow for example, or modeling more realistic and complex tires, but local phenomena such as the suction effect or the impact of vortices inside the grooves are still not well developed. Usually, it is the experimental observations that push the numerical models to be improved, but the richness of numerical data (3D flow, time-resolved data) can also lead researchers into exploring new measurement techniques in order to validate the numerical results. The current work aims to reach this experimental/numerical complementary thus advancing

the hydroplaning phenomenon comprehension for any type of tire. Indeed, the comparison between experimental and numerical results is very useful throughout this work, not only under a validation scope but also to complete missing information and have a more thorough overview of the hydroplaning problem. To our best knowledge, this is the first study where a methodology to analyze the flow around a tire to have a complementary experimental/numerical approach and to result in common analyzing tools as the segmentation method is presented.

This manuscript is divided into six chapters. The present Chapter 1 introduced the hydroplaning phenomenon and the scope of the present work. Chapters 2 and 3 are dedicated to the introduction of respectively the numerical and experimental tools that will be used throughout this study. Chapter 4 examines the case of a slick tire rolling over a water puddle. The focus is on the water flow structure inside the water-bank. Then a longitudinal tire tread is studied, more representative of the daily use, in Chapter 5. Finally, Chapter 6 focuses on a more complex tread pattern, and a dedicated method of analysis is proposed.

Chapter 2

The numerical model

To study the hydroplaning phenomenon from a numerical point of view, a coupled SPH-FE strategy has been adopted. It has initially been proposed by Hermange et al. [48] then developed by Michel [84] and it is their formulation that is retained. The following chapter is dedicated to the presentation of the fundamentals of the SPH and the FE methods along with the implementation of the coupling between the solid and the fluid solvers. If the SPH method was introduced at the end of the 70s in the astrophysics domain as a powerful numerical tool, the FE method was already occupying a prominent position in the field of numerical analysis and was being largely used in different domains but mainly in solid mechanics. Allying the flexibility of a meshless method as the SPH to model the fluid domain, and the robustness of the FE method for the tire part, the SPH-FE coupling seems a reasonable choice to model the interaction between a rolling tire with a water film. The adopted FE solver has been developed by Michelin for tire simulations for multiple years in different applications. The SPH solver has been jointly developed by the LHEEA laboratory of Ecole Centrale de Nantes and Siemens (SPH-flow software).

2.1 The Smoothed Particle Hydrodynamics (SPH) method

In this section, we will introduce the general formalism of the SPH method, and more precisely we will focus on the contribution made by the different studies conducted in the LHEEA laboratory in the FE and SPH coupling.
The SPH method was first introduced at the same time by Lucy [75] and Gingold and Monaghan [40] for astrophysical applications. It quickly appeared as a useful method to deal with the shortcomings of mesh-based methods such as violent impacts between solid objects (Schäfer et al. [110]), sloshing simulations (Delorme et al. [25]), fluid-structure

interaction (FSI) problems (Antoci et al. [3]) and free-surface flows (Oger [93]).

2.1.1 About the method

The SPH belongs to the Computational Fluid Dynamics (CFD) solving methods and is based on the resolution of the Navier-Stokes equations. The SPH works by dividing the fluid into a set of discrete moving elements referred to as particles. Each particle represents a discrete physical volume, and their Lagrangian nature allows setting their position by integrating their velocity and carrying the discrete field values. They are also seen as interpolation points and their volumes as their weight (Vila [130]). Each particle represents an interpolation point to which we associate a kernel function. The physical and kinematic variables of each particle are estimated at a specific instant given the state of the neighboring ones. In its weakly-compressible variant retained here, an explicit scheme is used to update the various variables (position, velocity, density, pressure...) to the next time step.
The main feature of the method is being mesh-free i.e, there are no pre-determined connectivities among the interpolation points. The neighborhood of each particle evolves through time, making the method particularly suitable for problems with large deformations. The absence of connectivity between particles also means that we need an original way to interpolate the different calculated fields. This introduces the basis of the SPH formalism with the definition of the kernel function and the variables' convolution.
Liquids are often modeled using the Weakly Compressible SPH (WCSPH) approach as it is thoroughly described by Monaghan [88]. This approach is adopted in the following work. It follows an explicit scheme and therefore avoids the resolution of Poisson's equation and thus a linear system. However, the explicit procedure imposes small time steps due to the sound speed constraint, and for this reason, some practitioners prefer the Incompressible SPH (ISPH) approach that implies the resolution of Poisson's equation (Cummins and Rudman [22], Shao and Lo [112]) with larger time steps. In addition, a major advantage of our WCSPH approach is the non-identification of the particles positioned at the free surface to impose the boundary conditions.

2.1.2 Past PhD developments on the SPH method at the LHEEA

The first PhD thesis under the scope of the SPH method in the LHEEA laboratory was conducted by Doring [28] in 2005. He worked on the bases of the method i.e, accuracy

of the interpolations and boundary conditions. Then, Oger [93] carried out further work on the development of the SPH method and computing code. Additional investigations were carried out regarding the generalizations of the boundary conditions, the calculation of near solid boundary local pressure, as well as the first attempts of defining a variable smoothing length in space [95]. Very quickly, the computational time problem has been raised, and research on the MPI parallelization to accelerate simulations was conducted [96]. Moreover, several studies were dedicated to the accuracy improvement of the SPH scheme like the development of a renormalization formulation [94].

Afterward, Deuff [26] initiated the first studies regarding the fluid-structure coupling using an SPH-SPH strategy applied to slamming problems. Later on, the question of scheme stability has been raised, and Guilcher [44] introduced the Riemann solver and MUSCL treatment (based on Vila [130]) to enhance the stability of the SPH scheme within the framework of wave-structure interactions. Thereafter, studies regarding the improvement of wall boundary conditions using surface methods were conducted by De Leffe [23] based on the work initiated by Marongiu [76] with a viscous flow application. Furthermore, the two-phase flow problem has been investigated with an application to viscous bubbly flows (Grenier [41], [42]).

Starting from 2012, Fourey [34] set the early basis of the current work and proposed an SPH-FE coupling strategy for FSI problems and extended it to more complex applications (Fourey et al. [35]). The need to reduce computing costs and improve the efficiency of the SPH method has been a major research focus especially when dealing with complex industrial applications, therefore new techniques were developed as the SPH refinement for which Barcarolo [7] contributed by extending the work from Reyes López et al. [107] and Feldman [31] by proposing a particle derefinement algorithm. He also worked on incompressible SPH formulation with semi-implicit resolution using Chorin scheme (ISPH). At a later stage, extensions of De Leffe's work on the boundary conditions were performed by Chiron et al. [15] with the introduction of the cut-face approach (BIM-CFA) and the application to 3D complex boundaries. Further studies were carried out concerning the refinement of the SPH domain and Chiron et al. [17] proposed the Adaptive Particle Refinement (APR) technique adopted in the current work.

Afterward, Hermange [51] adopted the SPH-FE coupling strategy in the framework of the hydroplaning application in his CIFRE thesis with Michelin. The numerical model proposed was validated via experimental works including the results of Idelsohn et al. [58]. Several optimizations were proposed to reduce computational costs. The study was ex-

tended to the rough ground as well. The hydroplaning phenomenon has been thoroughly investigated in the case of different tires (Hermange et al. [49]) with local comparisons between new and worn tire states.
In 2020, further works were dedicated to a new two-phase flow SPH scheme and its application to aircraft ditching (Hammani [46]). Recently, Michel [84] focused on the analysis and improvements in the different SPH schemes, in particular, based on Riemann scheme. He also worked on analyzing the convergence properties of various shifting techniques and proposed new shifting laws (Michel et al. [83]). In the same year, Vergnaud et al. [129] worked on a theoretical analysis of SPH schemes. He focused on increasing the order of convergence of the spatial scheme, and the surface tension problem.

2.1.3 Navier-Stokes equations

Considering a domain Ω and in a Lagrangian description, the general form of the Navier-Stokes equations for a Newtonian fluid takes this form:

$$\forall \vec{x} \in \Omega \begin{cases} \frac{d\vec{x}}{dt} = \vec{v} \\ \frac{d\rho}{dt} = -\rho \operatorname{div}(\vec{v}) \\ \frac{d\vec{v}}{dt} = \vec{g} + \frac{\vec{div}\overline{\overline{\sigma}}}{\rho} \end{cases} \tag{2.1}$$

Where $\vec{x}$ and $\vec{v}$ are respectively the position and the velocity vectors and ρ is the density. We are here considering only the gravity field $\vec{g}$ as external force.
We can express the stress tensor in (2.1) in terms of velocity using the viscous stress tensor $\overline{\overline{\tau}}$ in this form:

$$\sigma_{ij} = -P\delta_{ij} + \tau_{ij} = (-P + \lambda d_{kk})\delta_{ij} + 2\mu d_{ij} \tag{2.2}$$

where $d_{ij} = \frac{1}{2}(\frac{\partial \vec{v_i}}{\partial \vec{x_j}} + \frac{\partial \vec{v_j}}{\partial \vec{x_i}})$ is the strain rate tensor, λ is the bulk viscosity, μ is the dynamic viscosity and P the pressure. The conservation of momentum equation then becomes:

$$\frac{d\vec{v}}{dt} = \vec{g} - \frac{-\overrightarrow{grad}(P)}{\rho} + \nu(\vec{\operatorname{div}}(\overline{\overline{grad}}\,\vec{v}) + \frac{\nu}{3}\overrightarrow{grad}(\operatorname{div}\vec{v}) \tag{2.3}$$

where $\nu = \frac{\mu}{\rho}$ is the kinematic viscosity. In the hypothesis of a quasi-incompressible flow, the term $\frac{\nu}{3}\overrightarrow{grad}(\operatorname{div}\vec{v})$ expressing the volumetric expansion of the fluid can be neglected

and the system (2.1) becomes:

$$\forall \vec{x} \in \Omega \begin{cases} \frac{d\vec{x}}{dt} = \vec{v} \\ \frac{d\rho}{dt} = -\rho \operatorname{div}(\vec{v}) \\ \frac{d\vec{v}}{dt} = \vec{g} - \frac{-\overrightarrow{grad}(P)}{\rho} + \nu \vec{\Delta} \vec{v} \end{cases} \tag{2.4}$$

And to close the system, a state equation is needed to link the pressure with the density. In this work, the Cole equation is used:

$$P - P_0 = \frac{\rho_0 C_0^2}{\gamma_k} \left[\left(\frac{\rho}{\rho_0} \right)^{\gamma_k} - 1 \right] \tag{2.5}$$

Where ρ_0 and C_0 are respectively the nominal density and the nominal sound speed of the fluid, P_0 is the reference pressure, and γ_k is the polytropic constant of the fluid which is taken as 7 for water. The sound speed is then deduced using this equation and we obtain:

$$C = \sqrt{\frac{\partial P}{\partial \rho}} = C_0 \sqrt{\left(\frac{\rho}{\rho_0} \right)^{\gamma_k - 1}} \tag{2.6}$$

2.1.4 SPH formalism and operators

In the previous section, we presented the Navier-Stokes equations in a continuous form. And to present the SPH scheme in a discrete form, in particular the gradient and divergence operators leading to the construction of the scheme, we first express them in a continuous form.

In the SPH interpolation, the estimation of a function ϕ at a location $\vec{x}$ is calculated based on the neighborhood Ω of $\vec{x}$. We can express $\phi(\vec{x})$ accurately in the following way:

$$\phi(\vec{x}) = \int_\Omega \phi(\vec{y}) \delta(\vec{x} - \vec{y}) d\Omega_{\vec{y}} \tag{2.7}$$

where δ is the Dirac delta function. The above integral can be approximated through a regularizing kernel function W, therefore we can rewrite Eq. (2.7) as follows:

$$< \phi(\vec{x}) >= \int_\Omega \phi(\vec{y}) W(||\vec{x} - \vec{y}||, R) d\Omega_{\vec{y}} \tag{2.8}$$

where R is the radius of the compact support of W verifying:

$$W(\vec{x}-\vec{y},R)=0 \quad \forall \vec{y} \in \delta\Omega(\text{border of the compact support of } W) \tag{2.9}$$

Usually, the compact support shape is a disk in 2D and a sphere in 3D. Moreover, W needs to fulfill certain conditions:

1. $W(\vec{x},R) \geq 0$
2. $\int_\Omega W(\vec{x},R)\, d\vec{x} = 1$
3. $lim_{R\to 0} W(\vec{x},R) = \delta(\vec{x})$
4. $W(\vec{x},R) \in C^p(\mathbb{R}^n), p \geq 1$

In this work, the C^2 Wendland [133] kernel function is used:

$$W(q,R) = \beta \begin{cases} \frac{1}{2}(1-q^4)(1+4q) & \text{if} \quad 0 \leq q \leq 1 \\ 0 & \text{if} \quad q > 1 \end{cases} \tag{2.10}$$

and

$$\vec{\nabla} W(\vec{x},R) = \frac{\beta \vec{x}}{||\vec{x}||R} \begin{cases} -10\, q(1-q)^3 & \text{if} \quad 0 \leq q \leq 1 \\ 0 & \text{if} \quad q > 1 \end{cases} \tag{2.11}$$

where $\beta = \frac{14}{\pi R^2}$ in a 2D problem and $\beta = \frac{21}{\pi R^3}$ in a 3D problem.

The gradient interpolation of ϕ is defined as:

$$< \vec{\nabla}_{\vec{x}} \phi(\vec{x}) >= \int_\Omega \vec{\nabla}_{\vec{y}} \phi(\vec{y}) W(\vec{x}-\vec{y},R) dV_{\vec{y}} \tag{2.12}$$

The kernel gradient $\vec{\nabla} W$ has an anti-symmetric property (due to the radial symmetry of W), which means that:

$$\vec{\nabla}_{\vec{y}} W(\vec{x}-\vec{y},R) = -\vec{\nabla}_{\vec{x}} W(\vec{x}-\vec{y},R) \tag{2.13}$$

Using this property and by performing an integration by part on the gradient of ϕ we

obtain:

$$\begin{aligned} < \vec{\nabla}_{\vec{x}}\phi(\vec{x}) > &= \int_{\Omega} \vec{\nabla}_{\vec{y}}\phi(\vec{y})W(\vec{x}-\vec{y},R)dV_{\vec{y}} \\ &= \int_{\delta\Omega} \phi(\vec{y})W(\vec{x}-\vec{y},R)\vec{n}dS - \int_{\Omega} \phi(\vec{y})\vec{\nabla}_{\vec{y}}W(\vec{x}-\vec{y},R)dV_{\vec{y}} \\ &= -\int_{\Omega} \phi(\vec{y})\vec{\nabla}_{\vec{y}}W(\vec{x}-\vec{y},R)dV_{\vec{y}} \\ &= \int_{\Omega} \phi(\vec{y})\vec{\nabla}_{\vec{x}}W(\vec{x}-\vec{y},R)dV_{\vec{y}} \end{aligned} \tag{2.14}$$

where $\vec{n}$ is the local normal vector to $\delta\Omega$. Thanks to Eq. (2.9), we assume here that the kernel support is complete i.e:

$$\int_{\delta\Omega} \phi(\vec{y})W(\vec{x}-\vec{y},R)\vec{n}dS = 0 \tag{2.15}$$

Note that Eq. (2.15) is no more valid in the vicinity of wall boundaries, where specific treatments are therefore needed as described later on.

2.1.5 Discrete approximations

Given a discrete partition of the domain Ω into N particles, we denote i and j two particles in Ω, we can write this approximation by using a mid-point quadrature of (2.8):

$$\int_{\Omega} \phi(\vec{y})W(\vec{x}-\vec{y},R)d\Omega_{\vec{y}} \approx \sum_{j=1}^{N} \phi(\vec{x}_j)W(\vec{x}_i-\vec{x}_j,R)\omega_j \tag{2.16}$$

Where Ω is the compact support and ω_j is the elementary volume attributed to particle j. Similarly, the discrete gradient of ϕ can be expressed as:

$$G(\phi(\vec{x}_i)) =< \vec{\nabla}_{\vec{x}_i}\phi(\vec{x}_i) >= \sum_{j=1}^{N} \phi(\vec{x}_j)\vec{\nabla}_{\vec{x}_i}W(\vec{x}_i-\vec{x}_j,R)\omega_j \tag{2.17}$$

As usually proposed in the related literature, the discrete gradient operator is taken as:

$$G_+(\phi_i) = G(\phi_i) + \phi_i G(1) = \sum_{j=1}^{N} (\phi_j + \phi_i)\,\vec{\nabla}_i W_{ij}\omega_j \tag{2.18}$$

We used in this equation the notations $\vec{\nabla}_i W_{ij} = \vec{\nabla}_{\vec{x}_i}W(\vec{x}_i-\vec{x}_j,R)$ and $\phi_i = \phi(\vec{x}_i)$ for brevity purposes.

The discrete divergent operator D_- is proposed as:

$$D_-(\vec{f}_i) = \sum_{j=1}^{N}(\vec{f}_j - \vec{f}_i)\vec{\nabla}_i W_{ij}\omega_j \tag{2.19}$$

In the current work, we consider an inviscid fluid, therefore the viscosity is neglected and thus the absence of a Laplacian operator. We can then replace the system (2.4) with its discrete form for an Eulerian fluid:

$$\forall \vec{x}_i \in \Omega \begin{cases} \frac{d\vec{x}_i}{dt} = \vec{v}_i \\ \frac{d\rho_i}{dt} = -\rho_i \sum_{j=1}^{N}(\vec{v}_j - \vec{v}_i)\vec{\nabla}_i W_{ij}\omega_j \\ \frac{d\vec{v}_i}{dt} = \vec{g} - \frac{1}{\rho_i}\sum_{j=1}^{N}(P_j + P_i)\,\vec{\nabla}_i W_{ij}\omega_j \end{cases} \tag{2.20}$$

2.1.6 Accuracy corrections

In the SPH formalism, two consistency criteria should be satisfied:

$$\frac{R}{\Delta x_{SPH}} \rightarrow +\infty \tag{2.21}$$

and

$$R \rightarrow 0 \tag{2.22}$$

where Δx_{SPH} is the characteristic distance between two particles. But in practice, it is impossible to satisfy these criteria since the number of SPH particles is finite, and usually, the ratio $R/\Delta x_{SPH}$ is fixed between 2 and 4 which leads to (in the general case):

$$\sum_{j=1}^{N} W_{ij}\omega_j \neq 1 \tag{2.23}$$

And

$$\sum_{j=1}^{N} \vec{\nabla}_i W_{ij}\omega_j \neq \vec{0} \tag{2.24}$$

In our simulations, two values have been tested $R/\Delta x_{SPH} = 2.11$, and $R/\Delta x_{SPH} = 3$. This result is a compromise between the computational costs and convergence of the solution (Hermange [51]). Tests with these two ratio values have been conducted in Section 5.6.2.2. Equations (2.23) and (2.24) lead to the need of some corrections. We can introduce

for example the Shepard correction on the kernel function (Shepard [113]) that provides an exact estimation for constant functions:

$$< \phi(\vec{x}_i) >= \sum_{j=1}^{N} \phi(\vec{x}_j) W_{ij}^S \omega_j \tag{2.25}$$

where

$$W_{ij}^S.\omega_j = \frac{W_{ij}}{\sum_{k=1}^{N} W_{ik}\omega_k} \tag{2.26}$$

It is used in particular with surface treatment techniques as discussed in Section 2.1.8.1.

2.1.7 Weakly Compressible SPH (WCSPH)

To this point, the equations presented describe the behavior of a compressible flow and C_0 the nominal sound speed observed in the fluid. However, the flow we want to model in the present application is usually assumed as incompressible, and since the acoustic solution is of little interest to us here, the sound speed used in the computations differs from the physical one: it is chosen so as to fulfill Ma<0.1 everywhere in the flow and at all instants. The value of 0.1 is commonly adopted within the WCSPH approach (Monaghan [87]). This choice is rather legitimate due to the very small energy of the acoustic contributions and their much higher frequencies than the incompressible solution therefore not impacting the incompressible part of the flow (Hermange [51]).

2.1.7.1 Time integration and stability issues

Temporal integration In the present work, an explicit time integration is adopted. A 4^{th} order Runge-Kutta (RK4) scheme is mainly adopted.

CFL condition The time integration scheme being explicit, the following Courant-Friedrich-Levy (CFL) condition should be applied to ensure the stability of the scheme:

$$\Delta t_i \leq \Delta t_{i\,min} = k_{CFL} min_{i \in D} \frac{R_i}{C_i} \tag{2.27}$$

where Δt_i and C_i are respectively the time step and the sound speed associated to the particle i. The Courant number is taken as k_{CFL}=0.375 for the case of the RK4 scheme.

We can refer to the work of Violeau and Leroy [132] for more details about the theoretical stability criterion for the time step in the WCSPH method.

2.1.7.2 Stability of the scheme

The approximation of functions using the above mentioned kernel convolutions are rather space-centered (Vila [130]). It is well-known that using such space-centered operators conjointly with an explicit scheme leads to an unconditionally unstable scheme. The CFL condition is not a sufficient condition to ensure the stability and therefore the convergence of the scheme. In order to obtain a stable method and to assure a global convergence of the discrete system,a numerical dissipation is needed in the SPH scheme. Different techniques exist to add this dissipation. The first strategy is to directly add diffusive terms into the conservation equations, e.g., the artificial viscosity (Monaghan [87]) and the δ-SPH scheme (Antuono et al. [4]). The second approach is to adopt a Riemann-SPH scheme. It has been introduced by Vila [130] and has been adopted by some practitioners (see for instance Parshikov et al. [102] and Oger et al. [92]). The latter approach is adopted in the present work.

Riemann-SPH scheme In the Riemann-SPH formulation, the numerical diffusion is introduced indirectly when solving a Riemann problem between each pair of particles. In the Vila formalism, the interface $\vec{x}_{ij}$ between two particles i and j is supposed to be located at the mid-distance between $\vec{x}_i$ and $\vec{x}_j$. The velocity $\vec{v}_{ij}$ at the interface is assumed to be the mean value of the velocities associated with the two particles:

$$\vec{x}_{ij} = \frac{\vec{x}_i + \vec{x}_j}{2} \tag{2.28}$$

$$\vec{v}_{ij} = \vec{v}(\vec{x}_{ij}) = \frac{\vec{v}_i + \vec{v}_j}{2} \tag{2.29}$$

For an inviscid flow (the viscous stress tensor $\overline{\overline{\tau}} = 0$), the discretized form of system (2.1) can be written as:

$$\forall \vec{x} \in \Omega \begin{cases} \frac{dx_i}{dt} = \vec{v}_i \\ \frac{d\omega_i}{dt} = \omega_i \sum_{j=1}^{N} 2(\vec{v}_{ij} - \vec{v}_i).\vec{\nabla}_i W_{ij}\omega_j \\ \frac{d(m_i)}{dt} = -\omega_i \sum_{j=1}^{N} 2\rho_e \left(\vec{v}_e - \vec{v}_{ij}\right).\vec{\nabla}_i W_{ij}\omega_j \\ \frac{d(m_i\vec{v}_i)}{dt} = \omega_i \rho_i \vec{g} - \omega_i \sum_{j=1}^{N} 2\left(P_e\overline{\overline{I}} + \rho_e \vec{v}_e \otimes (\vec{v}_e - \vec{v}_{ij})\right).\vec{\nabla}_i W_{ij}\omega_j \end{cases} \tag{2.30}$$

where ρ_e, $\vec{v}_e$ and P_e are the density, velocity and pressure solutions of the Riemann problem at the interface between particles i and j, and $m_i = \omega_i \rho_i$ is the mass of particle i. We note that this scheme allows a mass transfer between particles i and j ensuring the global mass conservation of the system.

In the present work the Parshikov et al. [102] formulation is used ensuring a local mass conservation i.e. $\frac{dm_i}{dt} = 0$. This results in imposing $\vec{v}_{ij} = \vec{v}_e$. The system (2.30) is then written as follows:

$$\forall \vec{x}_i \in \Omega \begin{cases} \frac{d\vec{x}_i}{dt} = \vec{v}_i \\ \frac{d\omega_i}{dt} = \omega_i \sum_{j=1}^{N} 2(\vec{v}_e - \vec{v}_i).\vec{\nabla}_i W_{ij}\omega_j \\ \frac{dm_i}{dt} = 0 \\ \frac{d(m_i\vec{v}_i)}{dt} = m_i \vec{g} - \omega_i \sum_{j=1}^{N} 2P_e.\vec{\nabla}_i W_{ij}\omega_j \end{cases} \tag{2.31}$$

For more details about the Riemann-SPH scheme, we refer the reader to Chiron [16].

2.1.8 Boundary conditions

The treatment of boundary conditions is a challenging topic in the SPH community (Vacondio et al. [127]). Due to the mesh-free nature of the SPH method, imposing boundary conditions is far from trivial. Indeed the first difficulty lies in the imposition of boundary conditions on mobile SPH particles. And secondly, the kernel support is truncated near the limits of the SPH domain. Boundary conditions include not only wall boundaries and free-surface, but in some cases stress conditions, open boundary conditions, etc.

2.1.8.1 Wall conditions

Since viscous effects are neglected throughout this manuscript, a free-slip condition is considered at the solid boundary. Two groups of wall treatments mainly exist in the literature. The first consists of volume methods where the truncated kernel support near a boundary is completed as in the ghost-particle method (Libersky et al. [70], Oger [93], Marrone et al. [77]). The second group consists of surface methods where a discretization of the interface is considered and boundary conditions are imposed onto the walls (Marongiu [76], De Leffe [23], Mayrhofer et al. [82]). The singularities in the tire geometry and its complex shape favor the use of these surface methods. A Boundary Integral Method known as the "Cut-face approach" (BIM-CFA) proposed by Chiron et al. [15] has been retained in the present work. In this technique, boundary conditions are imposed on the discretized interface by calculating the surface terms in the SPH gradient and divergence operators. Near the boundary, equation (2.15) is not valid anymore. The BIM method consists in discretizing the surface term using the cut-face approach i.e. by cutting the $\delta\Omega$ surface into sub-elements to accurately approximate this surface term. Furthermore, to restore consistency near walls, the Shepard correction is used. Finally, by using an integration by part we obtain:

$$< \vec{\nabla}_{\vec{x}}\phi(\vec{x}) >= \frac{1}{\gamma(\vec{x})}\int_{\Omega}\phi(\vec{y})\vec{\nabla}_{\vec{x}}W(\vec{x}-\vec{y},R)dV_{\vec{y}} + \frac{1}{\gamma(\vec{x})}\int_{\delta\Omega}\phi(\vec{y})W(\vec{x}-\vec{y},R)\vec{n}dS_{\vec{y}} \quad (2.32)$$

The system (2.31) of the Riemann-SPH scheme then becomes :

$$\forall \vec{x}_i \in \Omega \begin{cases} \frac{d\vec{x}_i}{dt} = \vec{v}_i \\ \frac{d\omega_i}{dt} = \frac{2\omega_i}{\gamma_i}\sum_{j\in\mathcal{P}}\omega_j(\vec{v}_e-\vec{v}_i).\nabla_i W_{ij} + \frac{\omega_i}{\gamma_i}\sum_{s\in\mathcal{S}}S_s(\vec{v}_s-\vec{v}_i).\vec{n}_s W_{is} \\ \frac{dm_i}{dt} = 0 \\ \frac{d(m_i\vec{v}_i)}{dt} = m_i\vec{g} - \frac{\omega_i}{\gamma_i}\sum_{j\in\mathcal{P}}\omega_j 2P_e\nabla_i W_{ij} - \frac{\omega_i}{\gamma_i}\sum_{s\in\mathcal{S}}S_s(P_s+P_i)W_{is}\vec{n}_s \end{cases} \quad (2.33)$$

Where $\mathcal{P}$ and $\mathcal{S}$ are respectively the set of particles and wall surface elements within the kernel support radius of W, $\vec{v}_e$ and P_e are the velocity and pressure solutions of the Riemann problem at the interface between particles i and j. S_s, $\vec{v}_s$ and P_s are the area, the velocity and the pressure of the wall surface element s (Chiron et al. [15]). $\vec{n}_s$ is normal to the boundary (Fig.2.1) and γ_i is the discrete Shepard correction. Extensive works have been provided related to the modification of the gradient operator and the

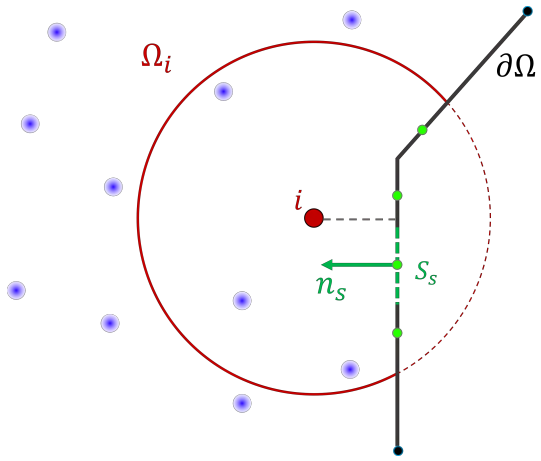

Figure 2.1 – 2D wall boundary definition with Ω_i the kernel support of the particle i partially truncated by the boundary (red dotted arc), $\partial\Omega$ is the wall composed of the segments s.

Shepard correction in particular. We refer the reader to [32], [82], [67] and [15] for more details.

2.1.8.2 Free-surface conditions

The kinematic condition implies that the fluid particles initially on the free surface will remain on it. This condition is naturally fulfilled by the Lagrangian nature of the SPH formalism (Colagrossi et al. [20]).

The dynamic condition is achieved by the continuity of the stress tensor at the free surface. In the case of Euler equations for a single-phase flow, the simple imposition of the atmospheric pressure P_0 at the surface fulfills this condition. As demonstrated by Colagrossi et al. [19], the SPH operators tend to intrinsically fulfill this dynamic condition when the convergence is reached.

2.1.9 Adaptive Particle Refinement (APR)

Local refinement in the SPH sub-domain helps to reduce computational costs. Indeed, it allows a finer spatial resolution in a specified zone of the fluid domain in order to enhance accuracy in the area we are most interested in. Initially, Nelson and Papaloizou [90] proposed a new SPH formulation taking into account a spatial variability of the smoothing length. However, this formulation did not give the possibility to implement a

dynamic refinement evolving through time and the initial disposition was preserved. Oger et al. [95] used this formulation in the case of a water wedge entry. Later on, Feldman and Bonet [30] initiated the local refinement in SPH which was improved by Reyes López et al. [107] in terms of precision and conservation properties. Then, Vacondio et al. [126] introduced for the first time a coarsening method called "coalescing" by merging particles. Afterward, Barcarolo et al. [6] worked on this coarsening procedure and proposed some improvements in particular by keeping the parent particles to preserve the flow kinematics. Last but not least, Chiron [16] suggested a generalization of these different procedures and an improvement in the time/precision compromise. The so-called APR (Adaptive Particle Refinement) has been developed as an extension of the AMR (Adaptive Mesh Refinement) already used for mesh-based methods. Each particle entering the refinement area, called parent particle, is "sub-divided" into a finite number of particles called child particles, that have smaller radius R_c and discretization Δx_c sizes. The parent particle is convected passively along the flow (without interacting with "active" particles) (Barcarolo et al. [6]). Indeed, the parent particle is maintained in the flow but is not involved in particles' field calculations. It uses the active particles' fields to update its trajectory. In a 2D problem, each parent particle present within the APR box is replaced by 4 child particles, and 8 child particles in a 3D case verifying:

$$\begin{cases} \Delta x_c = 0.5\Delta x_p \\ R_c = 0.5R_p \\ m_c = \frac{m_p}{4} \quad \text{in 2D} \qquad \text{and} \qquad m_c = \frac{m_p}{8} \quad \text{in 3D} \end{cases} \tag{2.34}$$

Where R_p, Δx_p and m_p are respectively the radius, spatial discretization and mass of a parent particle. A schematic representation of the child particles' generation process is given in Fig.2.2.

The two discretized domains do not interact with each other directly. Guard particles are introduced as a link between parent and child particles and play the role of a boundary condition. The parent particles interact with the parent guard particles and the child particles with the guard child particles as they have the same interpolation radius. A buffer zone of size R_p is created at the frontier between the coarse and refined domains (Fig.2.3). When a parent particle leaves the refinement zone, it becomes again an active particle and the child particles around it are firstly transformed into guard particles in the buffer zone, before being completely removed. The Shepard correction introduced in

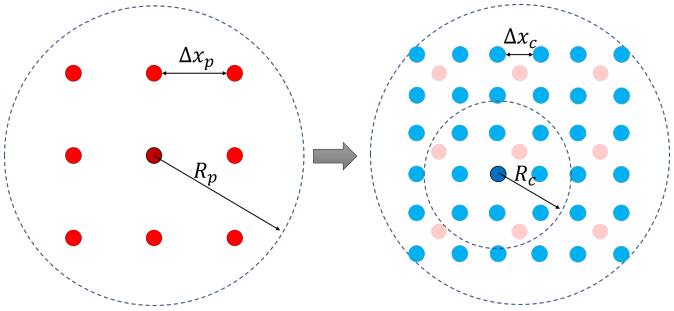

Figure 2.2 – APR principle representation, parent particles (in red) and child particles in (blue).

Section 2.1.6, is used in the APR method to assign an averaged field to the guard particles calculated over the neighboring particles. For more details about the APR formalism, we refer the reader to Chiron [16] and Chiron et al. [17].

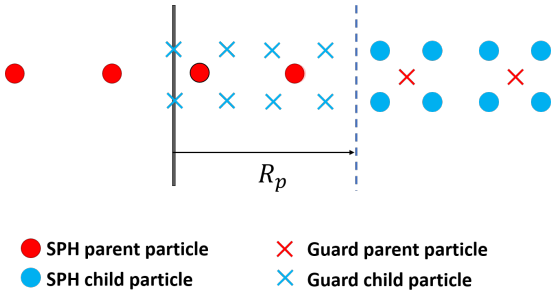

Figure 2.3 – APR process representation for one particle. The coarse region is on the left and the refined region on the right.

We give in Fig.2.4 an example of the APR application in the case of a beam impacting a free surface extracted from Chiron [16]. In this simulation, 10 APR levels are defined and we can clearly see in the figure the APR boxes delimitation represented by the colormap scales. The spatial resolution evolves from $\Delta x_{SPH} = 1.25 \times 10^{-2} m$ far from the impact region, to $\Delta x_{SPH} = 1.2207 \times 10^{-5} m$ in the area where the beam enters in contact with the free-surface. In this case, very high pressure values are reached in a very small region, and the impact happens on a microsecond scale. Therefore, in order to accurately capture these very local effects, the spatial resolution needs to be high enough but only in the impact area. Thus the need to define 10 APR levels and reduce Δx_{SPH} by a factor of 1000.

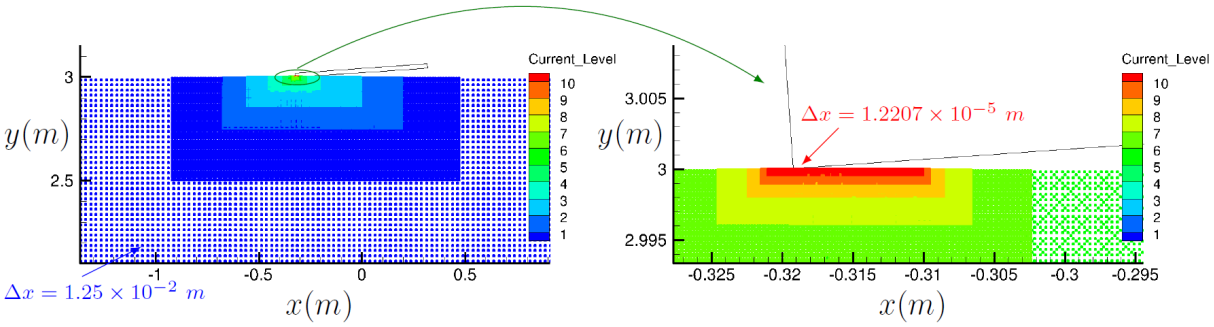

Figure 2.4 – Particles initial disposition in a beam impacting a free-surface case with 10 APR levels (global view on the left and zoomed view of the impact area on the right), image extracted from Chiron [16].

2.1.10 Particle Shifting

Due to its Lagrangian nature, the SPH method suffers from the presence of anisotropic particles disposition along flow streamlines that are detrimental to simulation accuracy (Monaghan [86], Oger et al. [92]). Paradoxically, this irregular particle distribution appears when improving the SPH scheme accuracy. Extensive studies have been dedicated to the Particle Shifting Technique (PST) as it appeared as a suitable tool to avoid this particle clustering degrading the kernel interpolation. The main idea of this technique is to add a small perturbation in the particles' positions or velocity to shift them from their Lagrangian trajectories. It was first introduced by Monaghan [86] verifying the linear and angular momentum conservation, being Galilean invariant but with no clear reason for which the shifting velocity vector could point towards zones of low concentration of particles (not derived from Fick's law). Then, Lind et al. [72] proposed a new PST within the ISPH formalism based on Fick's law shifting the particles using their gradient concentration. The particles are therefore moved from areas of high concentration to those of low concentration. Later on, Oger et al. [92] suggested a PST modifying the particles' velocity using an ALE formalism in the WCSPH framework. Sun et al. [118] also proposed a PST written in terms of velocity. Last but not least, Michel et al. [83] thoroughly addressed the PST question, exposing the conditions that should be fulfilled regarding the consistency, the Galilean and rotation invariance, and the independence from the solution. They introduced a new PST verifying the suggested properties based on Fick's law and compatible with different SPH schemes based on the WCSPH assumption as well as with the incompressible one. The latter PST is adopted in the present work.

The respect of the kinematic condition on the free surface requires the detection of the particles belonging to the free surface which is done through the algorithm proposed by Marrone et al. [78]. The particle shifting is not applied to these free-surface particles and their calculated velocities are maintained.

2.2 The Finite Element (FE) method

Since the 70s the FE method has occupied a position of predominance among the methods used in numerical analysis. This method has emerged from the need to solve partial differential equations that are mathematically difficult to handle by seeking other approaches than the pure mathematical one (Hrennikoff [57]). This new method offered a powerful tool for analysis in computational solid mechanics and its field of application expanded rapidly to aeronautical, biomechanical, and automotive frameworks. In this section, a general overview on the FE method is presented and for more details about the FE theory and its applications, we refer the reader to Dwoyer et al. [29] and Larson and Bengzon [65].
The FE method is based upon two fundamental ideas, a) the weak formulation of a boundary value problem and b) the object spatial decomposition into elements transforming a continuum area into a discrete domain. The problem is therefore reduced to the sub-domains and their connections.

2.2.1 Weak formulations in solid mechanics

We consider the domain Ω of boundary $\delta\Omega = \delta\Omega_0 \cup \delta\Omega_1$. We assume that the body is subjected to a volumic forces density $\vec{f}$. The boundary conditions on $\delta\Omega$ are given as:

— A surface density $\vec{T}$ is applied on $\delta\Omega_1$ of normal $\vec{n}$:

$$\overline{\overline{\sigma}}.\vec{n} = \vec{T} \quad \text{on} \quad \delta\Omega_1 \tag{2.35}$$

— The displacement $\vec{u}$ is given on $\delta\Omega_0$

$$\vec{u} = \vec{U} \quad \text{on} \quad \delta\Omega_0 \tag{2.36}$$

Using the Einstein notation, the equilibrium equations read:

$$\rho_s \frac{d^2 u_i}{dt^2} - \frac{\delta \sigma_{ij}}{\delta x_j} - f_i = 0 \quad \text{in } \Omega \tag{2.37}$$

$$\sigma_{ij} n_j = T_i \quad \text{on } \delta\Omega_1 \tag{2.38}$$

We note $\mathcal{C}_{ad}(U)$ the set of kinematically admissible displacement fields satisfying 2.36. We consider $\vec{u}^* \in \mathcal{C}_{ad}(U)$ and $\vec{w}^* = \vec{u}^* - \vec{u} \in \mathcal{C}_{ad}(0)$. We multiply Eq. (2.37) by the virtual displacement $\vec{w}^*$ and integrate over Ω:

$$\int_\Omega w_i^* (\rho_s \frac{d^2 u_i}{dt^2} - \frac{\delta \sigma_{ij}}{\delta x_j} - f_i) dV = 0 \tag{2.39}$$

Using Green's formula and the vectorial notations :

$$\begin{aligned} \int_\Omega \vec{w}^* . \vec{\text{div}}(\overline{\overline{\sigma}}) dV &= \int_{\delta\Omega} (\overline{\overline{\sigma}} . \vec{w}^*) . \vec{n} dS - \int_\Omega \overline{\overline{\sigma}} : \overline{\overline{\nabla}}(\vec{w}^*) dV \\ &= \int_{\delta\Omega_0} (\overline{\overline{\sigma}} . \vec{w}^*) . \vec{n} dS + \int_{\delta\Omega_1} (\overline{\overline{\sigma}} . \vec{w}^*) . \vec{n} dS - \int_\Omega \overline{\overline{\sigma}} : \overline{\overline{\nabla}}(\vec{w}^*) dV \end{aligned} \tag{2.40}$$

In addition, $\vec{w}^* \in \mathcal{C}_{ad}(0)$ then:

$$\vec{w}^* = 0 \quad \text{on } \delta\Omega_0 \tag{2.41}$$

And using the symmetry of $\overline{\overline{\sigma}}$, Eq. (2.40) becomes:

$$\begin{aligned} \int_\Omega \vec{w}^* . \vec{\text{div}}(\overline{\overline{\sigma}}) dV &= \int_{\delta\Omega_1} \vec{w}^* . (\overline{\overline{\sigma}} . \vec{n}) dS - \int_\Omega \overline{\overline{\sigma}} : \overline{\overline{\nabla}}(\vec{w}^*) dV \\ &= \int_{\delta\Omega_1} \vec{w}^* . \vec{T} dS - \int_\Omega \overline{\overline{\sigma}} : \overline{\overline{\nabla}}(\vec{w}^*) dV \end{aligned} \tag{2.42}$$

We introduce then the strain tensor associated to $\vec{w}^*$:

$$\overline{\overline{\varepsilon}}(\vec{w}^*) = \overline{\overline{\nabla}}(\vec{w}^*) \tag{2.43}$$

Finally by injecting 2.43 in 2.42, Eq. (2.39) becomes:

$$\int_\Omega \vec{w}^* . \rho_s \frac{d^2 \vec{u}}{dt^2} dV - \int_{\delta\Omega_1} \vec{w}^* . \vec{T} dS + \int_\Omega \overline{\overline{\sigma}} : \overline{\overline{\varepsilon}}(\vec{w}^*) dV - \int_\Omega \vec{w}^* . \vec{f} dV = 0 \quad \forall \vec{w}^* \in \mathcal{C}_{ad}(0) \tag{2.44}$$

Remembering that $\overline{\overline{\sigma}} = \overline{\overline{\sigma}}(\vec{u})$ because of the constitutive equation of the material, we find

that Eq. (2.44) is the weak formulation for the displacement. The existence and uniqueness of a solution $\vec{u}$ are fulfilled by the Lax-Milgram theorem (Larson and Bengzon [65]).

2.2.2 Finite Element approximation

We can express 2.44 in the form:

$$a(\vec{u}, \vec{w^*}) = l(\vec{w^*})$$

with

$$\begin{cases} a(\vec{u}, \vec{w^*}) = \int_\Omega \overline{\overline{\sigma}} : \overline{\overline{\varepsilon}}(\vec{w^*}) dV + \int_\Omega \vec{w^*}.\rho_s \frac{d^2\vec{u}}{dt^2} dV \\ l(\vec{w^*}) = \int_{\delta\Omega_1} \vec{w^*}.\vec{T} dS + \int_\Omega \vec{w^*}.\vec{f} dV \end{cases}$$

The idea here is to approximate $\vec{u}$ solution of 2.44 with finite elements. Therefore, each component of $\vec{u}$ is approximated using piecewise continuous linear functions. This leads to replacing the infinite-dimensional problem:
Find $\vec{u} \in H$ such that

$$a(\vec{u}, \vec{w^*}) = l(\vec{w^*}) \tag{2.45}$$

with a finite-dimensional version:
Find $\vec{u}_\# \in V_\#$ such that

$$a(\vec{u}_\#, \vec{w^*}) = l(\vec{w^*}) \tag{2.46}$$

Where H is a Hilbert space verifying $\vec{u}|_{\delta\Omega_0} = \vec{U}$ and $V_\#$ is a finite-dimensional subspace of H usually taken as the space of piecewise polynomial functions.

2.2.3 Spatial discretization

At this point, we need to define a grid for Ω. The domain is therefore divided into a number of elements as:

$$\Omega = \cup_{j=1}^{N_{FE}} \Omega_j \tag{2.47}$$

where Ω_j is the volume of the element j. This subdivision can be defined by a set of tetrahedral or quadrilateral elements in 3D. The space $V_\#$ would consist of functions that are linear on each element of the chosen triangulation. We must then choose a basis of $V_\#$ defined by the functions φ_k, and we note x_k the nodes of the mesh elements. Each function φ_k has a value of 1 at x_k and zero at every $x_j, j \neq k$. In the one dimensional case, the support of φ_k is the interval $[x_{k-1}, x_{k+1}]$. This has the advantage of simplifying the

integrals $\int_\Omega \varphi_j \varphi_k dV$ and $\int_\Omega \nabla\varphi_j . \nabla\varphi_k dV$ that will be zero whenever x_j and x_k do not share an edge of the mesh. The φ_k functions are known as the shape functions and the higher their order, the more precise the results. The most common elements are linear, quadratic and cubic tetrahedrons (or 3D-rectangles). More sophisticated elements can be found in the literature in order to improve the precision of the results, however they require more computing time.

2.2.4 Engineering notation

For a given material, the constitutive law can be expressed as:

$$\overline{\overline{\sigma}} = D\overline{\overline{\varepsilon}} \tag{2.48}$$

where D is the stiffness tensor. We write then the strain and stress tensors as vectors:

$$\begin{aligned} \vec{\sigma} &= [\sigma_{11}\ \sigma_{22}\ \sigma_{33}\ \sigma_{12}\ \sigma_{23}\ \sigma_{31}]^T \\ \vec{\varepsilon} &= [\varepsilon_{11}\ \varepsilon_{22}\ \varepsilon_{33}\ \varepsilon_{12}\ \varepsilon_{23}\ \varepsilon_{31}]^T \end{aligned} \tag{2.49}$$

With this notation, we can write:

$$\overline{\overline{\sigma}} : \overline{\overline{\varepsilon}} = \overline{\overline{\varepsilon}} : \overline{\overline{\sigma}} = \vec{\varepsilon}^T \vec{\sigma} = \vec{\varepsilon}^T D \vec{\varepsilon} \tag{2.50}$$

which implies

$$\int_\Omega \overline{\overline{\varepsilon}}(\vec{w}^*) : \overline{\overline{\sigma}}(\vec{u}_\#) dV = \int_\Omega \vec{\varepsilon}^T(\vec{w}^*) D \vec{\varepsilon}(\vec{u}_\#) dV \tag{2.51}$$

We can write $\vec{u}_\#$ in a matrix form:

$$\vec{u}_\# = \begin{bmatrix} u_1 \\ u_2 \\ u_3 \end{bmatrix}_\# = \begin{bmatrix} \varphi_1 & 0 & 0 & \varphi_2 & 0 & 0 & \dots & \varphi_{n_i} & 0 & 0 \\ 0 & \varphi_1 & 0 & 0 & \varphi_2 & 0 & \dots & 0 & \varphi_{n_i} & 0 \\ 0 & 0 & \varphi_1 & 0 & 0 & \varphi_2 & \dots & 0 & 0 & \varphi_{n_i} \end{bmatrix} \begin{bmatrix} q_{11} \\ q_{12} \\ q_{13} \\ q_{21} \\ q_{22} \\ q_{23} \\ \vdots \\ q_{n_i 1} \\ q_{n_i 2} \\ q_{n_i 3} \end{bmatrix} = \varphi \vec{q} \tag{2.52}$$

and in the same way:

$$\vec{w^*} = \varphi \vec{q^*} \tag{2.53}$$

where $\varphi_i, 1 \leq i \leq n_i$ are the shape functions forming a basis, n_i is the number of nodes, $\vec{q}$ is the nodal displacements vector. Each node has 3 displacements in space, therefore $\vec{q}$ is of length $3n_i$.
We introduce the strain matrix B as follows:

$$B = \begin{bmatrix} \partial/\partial x_1 & 0 & 0 \\ 0 & \partial/\partial x_2 & 0 \\ 0 & 0 & \partial/\partial x_3 \\ \partial/\partial x_2 & \partial/\partial x_1 & 0 \\ 0 & \partial/\partial x_3 & \partial/\partial x_2 \\ \partial/\partial x_3 & 0 & \partial/\partial x_1 \end{bmatrix} \begin{bmatrix} \varphi_1 & 0 & 0 & \varphi_2 & 0 & 0 & \dots & \varphi_{n_i} & 0 & 0 \\ 0 & \varphi_1 & 0 & 0 & \varphi_2 & 0 & \dots & 0 & \varphi_{n_i} & 0 \\ 0 & 0 & \varphi_1 & 0 & 0 & \varphi_2 & \dots & 0 & 0 & \varphi_{n_i} \end{bmatrix} \tag{2.54}$$

We can then express the strain and stresses in their discrete form:

$$\bar{\bar{\varepsilon}} = B\vec{q} \tag{2.55}$$

$$\bar{\bar{\sigma}} = DB\vec{q} \tag{2.56}$$

We can write 2.47 in the matrix form:

$$\vec{q^*}.\int_\Omega \left(\varphi^T \rho_s \ddot{\vec{q}} + B^T DB\vec{q}\right) dV = \vec{q^*}.\left(\int_{\partial\Omega_1} \varphi^T \vec{T} dS + \int_\Omega \varphi^T.\vec{f} dV\right) \tag{2.57}$$

The virtual work principle induces:

$$M\ddot{\vec{q}} + K\vec{q} = \vec{F}_{ext} \tag{2.58}$$

Where M and K are the $3n_i \times 3n_i$ respectively the mass and stiffness matrices, and $\vec{F}_{ext}$ is the $3n_i \times 1$ generalized load vector.

$$M = \int_\Omega \varphi^T \rho_s \ddot{\vec{q}} dV \tag{2.59}$$

$$K = \int_\Omega B^T DB\vec{q} dV \tag{2.60}$$

$$\vec{F}_{ext} = \int_{\partial\Omega_1} \varphi^T \vec{T} dS + \int_{\Omega} \varphi^T . \vec{f} dV \tag{2.61}$$

2.2.5 Time integration scheme

The time integration scheme is a key element regarding the stability and robustness of our simulations, and in particular in our case where we use an SPH-FE coupling. Two major schemes exist and are commonly used: the implicit and the explicit schemes. The implicit scheme employs a more reliable and rigorous approach in considering the equilibrium at each step of deformation, while in the explicit scheme the problem of convergence that exists in the implicit one is eliminated at the cost of solution accuracy. In practice, the explicit scheme is generally preferred when solving fast dynamic problems. In the current work, the FE solver follows an implicit Euler scheme [49] as:

$$\frac{1}{h} M \left[\frac{\vec{U}^{N+1} - \vec{U}^N}{h} - \vec{V}^N \right] + \vec{F}_{int} \left(\vec{U}^{N+1} \right) = \vec{F}_{ext} \left(\vec{U}^{N+1} \right) \tag{2.62}$$

$$\vec{V}^{N+1} = \frac{\vec{U}^{N+1} - \vec{U}^N}{h} \tag{2.63}$$

where N and $N+1$ refer to two successive instants, h is the corresponding step-size, M is the mass matrix, $\vec{U}$ and $\vec{V}$ are respectively the displacement and the velocity vectors, $\vec{F}_{int}$ represents the internal load and $\vec{F}_{ext}$ the external load, including the pressure exerted by the fluid on the structure in the SPH-FE coupling used in the present work. We note that other coupling strategies as the FVM-FEM usually consider an explicit scheme for the FE solver [39], [99]. As mentioned above, explicit schemes are usually preferred to model very fast dynamics phenomena whereas implicit schemes are usually used for less violent dynamics, where physical times are longer and larger time steps can be considered. However, Fourey [34] showed that the introduction of sufficient dissipation on the high-frequency domain maintains a stable coupling calculation despite the weakly-compressible nature of the SPH method that can affect the coupling stability, which can be achieved via an implicit FE time integration scheme.

2.3 SPH-FE coupling strategy

In FSI applications, two coupling strategies exist:

— The monolithic approach in which the solid and fluid governing equations are solved simultaneously. This approach has the advantage of intrinsically respecting interface conditions, and the continuity of variables through the coupling interface is naturally fulfilled. This strong FSI formulation is expected to maintain the accuracy and stability of the scheme. Usually, a single software is used in this case. This approach is rather difficult to adopt for complex problems since fluid and solid sub-domains have their own physics and time scales, leading to a different more suitable numerical method for each of the fluid and the solid.

— The partitioned approach in which the solid and fluid equations are solved separately or alternately in time. This coupling results in a more adapted solver for each sub-domain and optimizations can be performed independently on each solver. The critical point in such an approach is the information transfer at the interface between the fluid and the solid which can alter the stability of the coupling. Energy conservation is therefore a major issue and has been thoroughly addressed in Hermange [51]). The partitioned approach is retained in the present study.

For more details about the monolithic and partitioned approaches, we refer the reader to Michler et al. [85] where a comparison between the computational efficiency of the two approaches was carried out.

The SPH-FE weak coupling adopted in this work has been discussed and validated in Fourey et al. [35] and in Hermange et al. [52]. The structure part is modeled with the FE method described in the previous section, while the fluid domain uses the SPH method. The FE solver provides the updated location and velocity of the solid nodes in response to the fluid local pressure loads provided by the SPH solver. Moreover, the maximum fluid time step allowed is expected to be smaller than the solid one, due to the weakly compressible assumption and the sound speed value, therefore the SPH solver imposes its time step on the FE solver. A CPS (Conventional Parallel Staggered) algorithm is adopted with an optimization proposed by Hermange et al. [48] and further analyzed by Michel [84]. It is based on the introduction of a ratio p between fluid and solid time steps as :

$$\Delta t_{FE} = 0.8 p \Delta t_{SPH} \tag{2.64}$$

here a safety coefficient of 0.8 is taken. The CPS algorithm makes the assumptions that the fluid loading on the structure $F_{f/s}$ does not vary significantly between two consecutive

instants t_n and t_{n+1}, i.e. $F_{f/s}^{n+1} \approx F_{f/s}^{n}$. To respect this assumption with the introduction of the ratio p, we need to ensure that $F_{f/s}^{n+p} \approx F_{f/s}^{n}$. The regulation of the ratio p is performed at the end of each loop according to variations of the fluid loads according to the following algorithm:

$$\begin{cases} \text{if} \quad 0.075 < \dfrac{\left|\sum\limits_k ||\vec{F}_{f/s}^{k,n+p}|| - \sum\limits_k ||\vec{F}_{f/s}^{k,n}||\right|}{\sum\limits_k ||\vec{F}_{f/s}^{k,n}||} \leqslant 0.15 \quad \text{then} \quad p = p-1 \\ \text{if} \quad \dfrac{\left|\sum\limits_k ||\vec{F}_{f/s}^{k,n+p}|| - \sum\limits_k ||\vec{F}_{f/s}^{k,n}||\right|}{\sum\limits_k ||\vec{F}_{f/s}^{k,n}||} \leqslant 0.075 \quad \text{then} \quad p = p+1 \\ \text{otherwise} \quad p = 1 \end{cases} \tag{2.65}$$

where $\vec{F}_{f/s}^{k,n}$ is the fluid loads on the wet structure face k at the instant t_n. A linear extrapolation of the nodes' positions is carried out for each fluid step according to:

$$\vec{x}_i^{n+l} = \vec{x}_i^{n} + l\Delta t \vec{v}_i^{n}, \qquad 1 \leqslant l \leqslant p \tag{2.66}$$

where $\vec{x}_i$ and $\vec{v}_i$ are respectively the position and the velocity of node i. We note that considering the very small time steps, a linear extrapolation seems rather reasonable. Furthermore, each loop should ensure Eq. (2.64), but in practice it is impossible to define the SPH time step $\Delta t_{n+i} (1 \leqslant i \leqslant p)$ at the beginning of the loop due to variations of the sound speed and the respect of the CFL condition (Eq. (2.27)). Therefore Δt_{n+i} is estimated in the following way:

$$\Delta t_{n+i} = 0.8\Delta t_n, \qquad 1 \leqslant i \leqslant p \tag{2.67}$$

where Δt_n has been determined according to the CFL condition. This leads to:

$$\Delta t_{FE} = 0.8p\Delta t_n \tag{2.68}$$

This p-CPS scheme is presented in Fig.2.5. Moreover, to limit computational costs, a distributed memory parallelization of the SPH solver is used via the MPI library Oger et al. [96]. Structured in a multi-node framework, the code is scalable on several thousands of CPU cores to perform multi-threaded computations. The FE solver is also parallelized

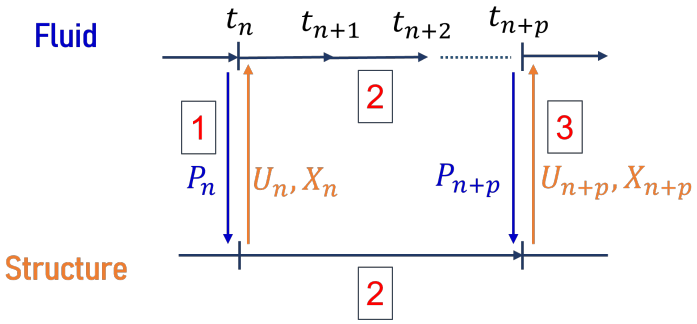

Figure 2.5 – p-CPS coupling algorithm scheme

over multiple CPU cores. The SPH-FE coupling program is responsible for managing the data exchange through non-blocking MPI communications (Fig.2.6). More details can be found in Fourey et al. [35], Hermange et al. [48] and Michel [84]

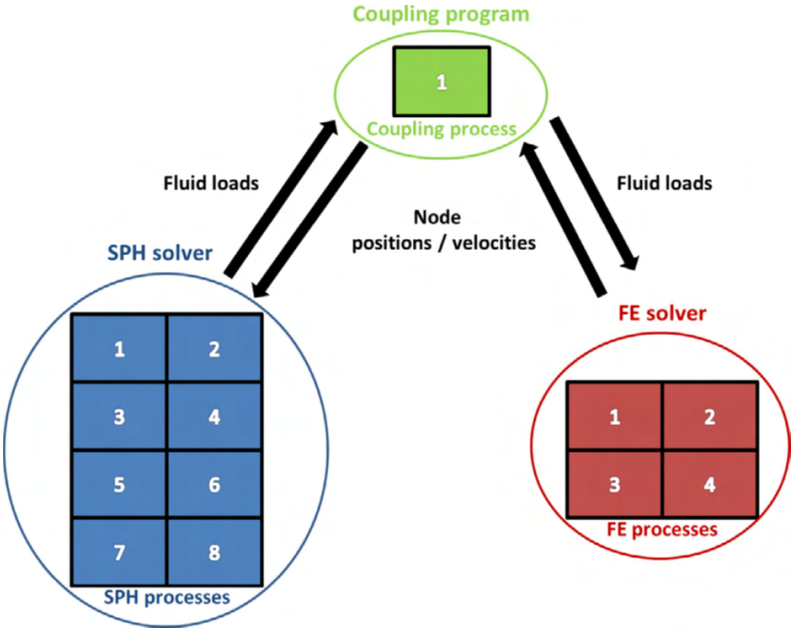

Figure 2.6 – Example of an SPH-FE coupling strategy where 8 cores and 4 cores respectively for SPH and FE solvers are used, and a single core is dedicated to the coupling program (Hermange et al. [48]).

2.4 FSI model of a tire rolling over a puddle of water

2.4.1 The tire model

A tire is a very complex object and is the result of an efficient arrangement of several components made up of different materials including synthetic and natural rubbers, textile and metal reinforcing materials, and a wide range of additives. We represent in Fig.2.7 the internal structure of a classical commercial tire with the main components:

— Sidewall: It is composed of a blend of rubbers and it protects the side of the tire from impact with curbs and the road. Important details about the tire are written on the sidewall, such as the tire size.

— Tread: It is the tire part in direct contact with the ground, it is often composed of a thick layer of rubber, for which the composition and the design will change depending on the type of surfaces (snow, wet, dry...) and the purpose of the tire (grip, durability, energy saving). It provides traction and turning grip, and is designed to resist wear, abrasion, and heat.

— Belts: They are made up of very fine, resistant steel or nylon cords bonded into the rubber. They guarantee resistance to turning strains and help maintain the shape of the tire while driving fast.

— Radial plies or carcass plie: Structural layer of the tire, the carcass plie also consists of rubber reinforced with textile or steel cords. These cords largely determine the strength of the tire and help it hold its shape due to pressure. Standard tires contain about 1400 cords, each one can resist a load of 15kg.

— Inner liner: It is a rubber layer responsible for air impermeability.

— Bead: It consists of a steel wire that clamps firmly against the rim to ensure the positioning of the tire and an airtight fit.

Two main groups of tires exist on the market, “summer” and “winter” tires. Among the differences between these two groups, we find the rubber stiffness and the tread design. Both categories are of interest in this work. Moreover, the behavior of the tire changes over time due to its wear. Concerning the hydroplaning, we only take into consideration the reduction of the tread depth to study worn tires. The operation of tread depth reduction is done internally starting from a brand-new tire.
Throughout this work, three types of tires are studied:

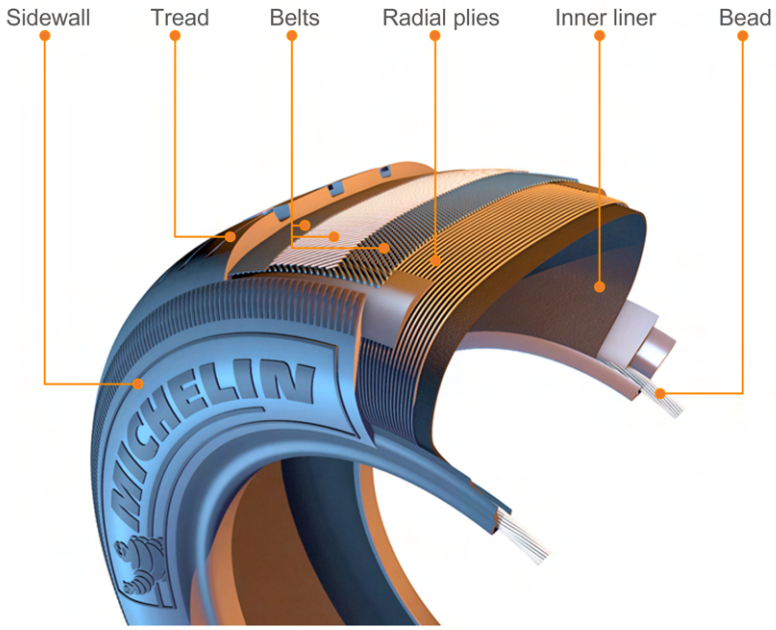

Figure 2.7 – Scheme of a tire composition

- Slick tires with a smooth tread. This case is not studied as it has previously been done by Kumar et al. [63] for example. Indeed, it is not a simplification of our numerical model, but it is rather an analytical case to focus exclusively on the water-bank region.
- Summer tires with a longitudinal tread design.
- Winter tires with a directional tread.

The strategy of analyzing the water flow circulation inside the CPA (Contact Patch Area) and in the WB (Water-Bank) is different between these three tire categories. An experimental investigation has been carried out by Cabut et al. [11] in the case of the Michelin Primacy 4 (PCY4), a summer tire with longitudinal grooves that is also studied in the present work both experimentally and numerically. Other works can be found in the literature focusing on the case of longitudinal tread, on a numerical level we can cite the work of Grogger and Weiss [43] and more recently Hermange [51], Gillard [39] and Tang et al. [120]. Other tread geometries have been investigated by Cho et al. [18], Donatellis et al. [27] and Michel [84], and a V-grooved tread by Koishi et al. [62] and Jenq, Chiu, et al. [60].
In our case, the retained numerical tire model is as close to the real tire as possible in

order to reduce as much as we can errors that can be generated by the tire model inaccuracy. The different composite layers presented in Fig.2.7 are taken into consideration with their different constitutive laws. The development of the tire model starts with the 2D FE mesh of the tire cross-section represented in Fig.2.8. Then, the 3D tire model is generated by revolving the 2D tire mesh around the wheel axis (Fig.2.9(a)). However, the tread is not axisymmetric and is generated separately, from the circular repetition of a 3D pattern. The FE mesh is usually refined in the area where the tire is in contact with the water film.

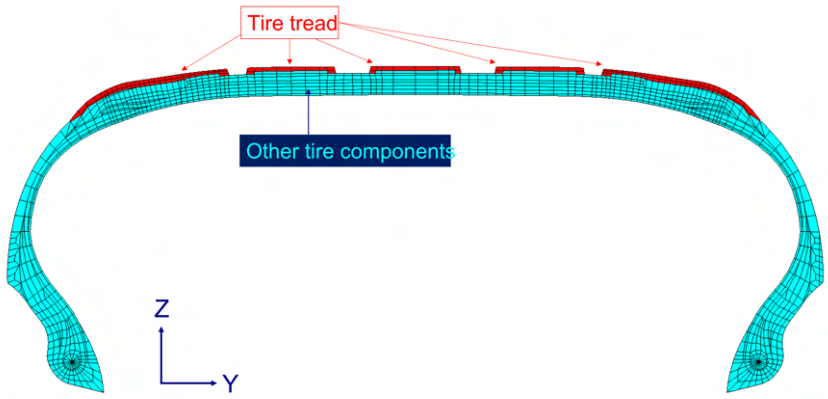

Figure 2.8 – 2D cross-section in the plane YZ of the PCY4 worn FE mesh, we highlight the tire tread in red.

2.4.2 The fluid domain

We define the fluid domain first by giving its length L (along X), width l (along Y), and height H_w (along Z). The center of the tire and the puddle belongs to the Y=0 axis, and Z=0 corresponds to the ground level. The width of the fluid domain should exceed the width of the tire to avoid border effects and keep the tire surrounded by water as in the r-PIV tests. The length of the puddle should be high enough to reach a stable regime and keep some water in the front wave to not perturb the analysis. Second, we choose the fluid resolution Δx_{SPH} and the SPH interpolation radius R by giving the ratio $R/\Delta x_{SPH}$. These values are chosen according to the compromise between robustness, accuracy, and computation speed. Usually a value of $\Delta x_{SPH} = 0.25mm$ is taken in the refined region of the fluid domain, and $R/\Delta x_{SPH} = 2.11$ (as stated in section 2.1.6). As so, for a worn tire with a $2mm$ of remaining tread depth, 8 particles can be represented inside the grooves in

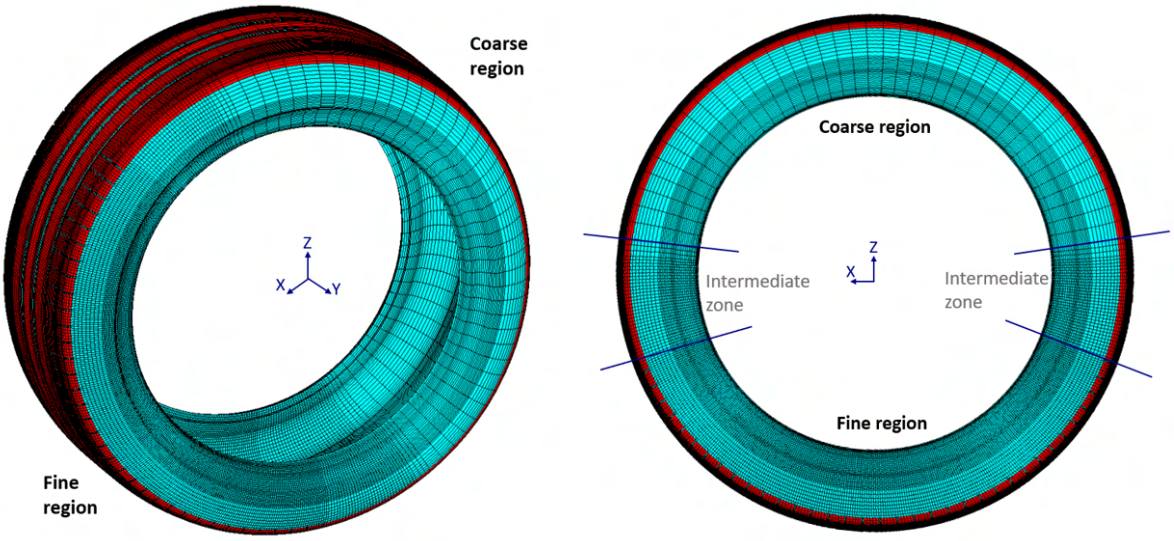

(a) (b)

Figure 2.9 – 3D view of the PCY4 worn FE model, the fine and coarse regions of the mesh are highlighted in (b). The tire tread is represented in red.

the refined region of the fluid. We usually define one or two APR boxes centered in the CPA to obtain the resolution of $\Delta x_{SPH} = 0.25mm$ without increasing dramatically the number of particles in the whole fluid domain. Outside the APR boxes, $\Delta x_{SPH} = 1mm$. Moreover, since the SPH method employed in this work follows a weakly-compressible approach, it imposes very small time steps linked to the CFL condition. The water sound speed is therefore artificially reduced to limit the computational time and is set to $C_0 = 250m.s^{-1}$. These values have been proposed by Hermange [51] and are discussed in Section 5.6.2. The SPH parameters will be specified again each time numerical results are presented throughout this work. A representation of the fluid domain is given in Fig.2.10. We zoom in on the region where the fluid domain is refined.

2.4.3 The ground

In the current study, an ideal smooth ground is considered. It is modeled as a rigid wall. A slip-free rolling is considered with no friction between the tire and the ground. Therefore, there is no limit on the transverse effort F_y on the tire. This is a reasonable assumption since this force component is usually very low in our simulations. From the SPH point of view, since viscous effects are neglected, a free-slip wall condition is considered with the

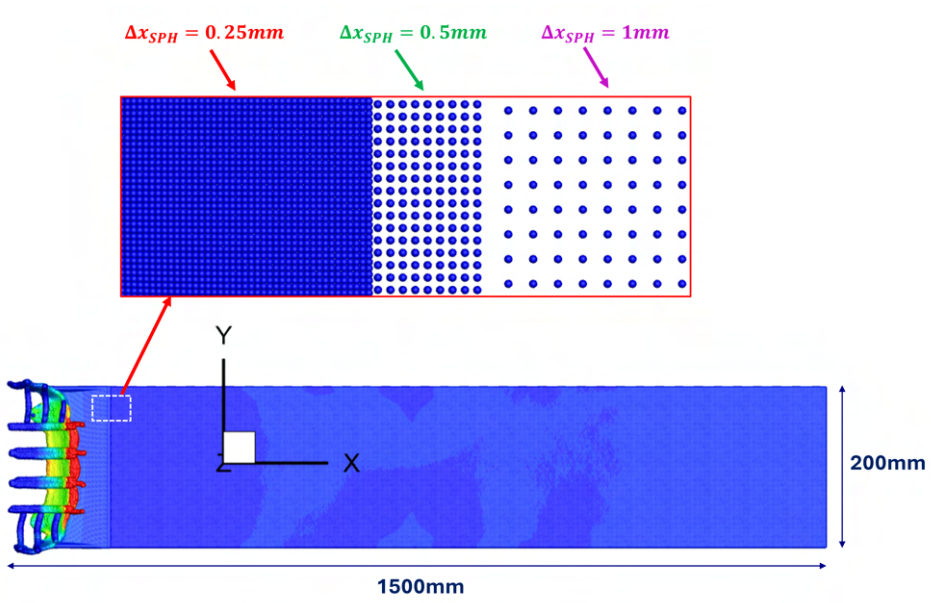

Figure 2.10 – View XY of the SPH fluid domain (a), for clarity reasons, the tire is not represented. We highlight the region where the fluid domain is refined (2 APR boxes in this case).

boundary:

$$\vec{v}_{\text{fluid}}.\vec{n} = \vec{v}_{\text{wall}}.\vec{n} \tag{2.69}$$

where $\vec{n}$ is the normal vector to the wall.

In the literature, 3D hydroplaning simulations usually consider a smooth ground in their models (Cho et al. [18], Oh et al. [97], Vincent et al. [131], Hermange et al. [49]). However, some studies extended hydroplaning simulations to a realistic rough road (Li et al. [69], Zhu et al. [139]). Indeed, it is possible to digitize the topography of a soil thanks to imaging techniques. For instance, Hermange et al. [48] studied the case of a ground geometry obtained from real road measurements at Michelin's facilities. The ground is then described in the (XY) plane with a specific spatial resolution. Such configurations with a complex rough road are very challenging from the numerical point of view, although using a mesh-free method for the fluid solution is considered an efficient alternative. Due to the roughness of the ground, water may stay confined between the rubber and the road, and mesh-based methods would not be able to model this phenomenon. Nevertheless, in the present work, only a smooth ground is considered. The main target of the current work is related to the efficiency of the tire tread, and the complexity of both the numerical and

experimental tools is such that considering a rough ground can only be done subsequently.

2.4.4 Preparation of the rolling over the water puddle

Before the phase of rolling on a wet ground, we realize a stationary rolling simulation on a dry ground on the axisymmetric model. Indeed, Michelin's internal FE software Deli only offers the possibility to simulate stationary rollings on an axisymmetric geometry. Then, after this primary calculation, we extrapolate all the fields (deformation, contact, velocity, etc.) on the full 3D model. The initialization of the solid part is decomposed through the following steps:

1. Initial state: The specifications of the tire model are verified (inflation pressure, type of rim...). The convergence parameters are entered.
2. Creation of the 3D axisymmetric model: This model has an axisymmetric tread that will be changed later to the full 3D tread. The mesh is decomposed into fine and coarse regions as presented in Fig.2.9(b). The fine zone corresponds to the section on which the tire will roll.
3. Mesh rotation and inflation at the specified inflation pressure: A rotation is applied to place the mesh refined region upstream of the CPA. At this stage, the tire is mounted on the rim and inflated.
4. Crushing at the specific load: The tire is loaded by increment until the ground resulting force reaches the targeted load. The tire deforms on the rigid ground as given in Fig.2.11.
5. Stationary rolling at the given velocity V_0: A stationary rolling is computed to obtain the steady-state needed to initialize the fluid-structure calculations.
6. Construction of the full 3D model with the right tread: In this step, the procedure restarts from the inflated 2D model. A contact condition is created on the tire tread to create the interface between solid and fluid sub-domains. The correct tread is then applied.
7. Field interpolations on the full 3D model: All the computed fields from the stationary rolling are interpolated on the full 3D model.
8. Preparation of the 3D dynamic rolling: The input files are prepared with the imposed translation and rotation extracted from the stationary rolling. We apply a symmetric load on two nodes from the tire rotation axis. It corresponds to a quarter of the tested vehicle load in the r-PIV.

9. Extraction of the tire skin for the SPH-FE coupling: This last step is required to extract the tire skin mesh corresponding to the interface between the fluid and solid sub-domains. The skin mesh is extracted using the contact conditions defined in step 6. The coupling between Deli and SPH-flow is activated and the full 3D model is ready to numerically roll over the water film.

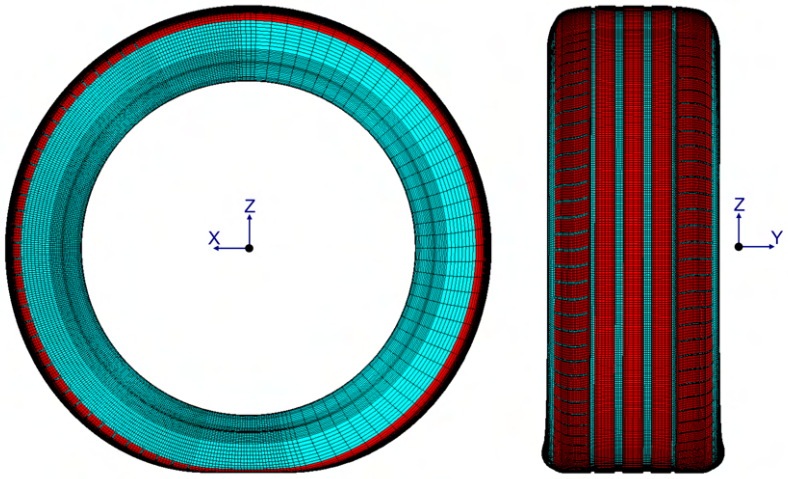

Figure 2.11 – 2D view in the XZ plane (left) and in the YZ plane (right) of the tire deformed after crushing on the ground under the given load. The tire tread is colored in red.

We give in Fig. 2.12 a 3D representation of the tire rolling over the water puddle. We usually define two APR boxes, one embedded inside the other focused on the CPA and the WB regions. This is a good compromise between the accuracy of the results and the computational costs. In the refined area, $\Delta x_{SPH} = 2.5 \times 10^{-4} m$ while in the coarse area $\Delta x_{SPH} = 1 \times 10^{-3} m$. In the rest of this study, we give more details about the spatial refinement of each simulation when presenting its results.

2.5 Conclusion

The aim of this chapter was to give the reader an overview of the numerical strategy adopted in this work. First, we presented the SPH method from its basis to the different advanced techniques developed by the LHEEA laboratory. A section was also dedicated to the FE method and its fundamentals. However, our aim is not hard coding within the SPH nor the FE solvers, thus the brief presentation of these numerical methods. This

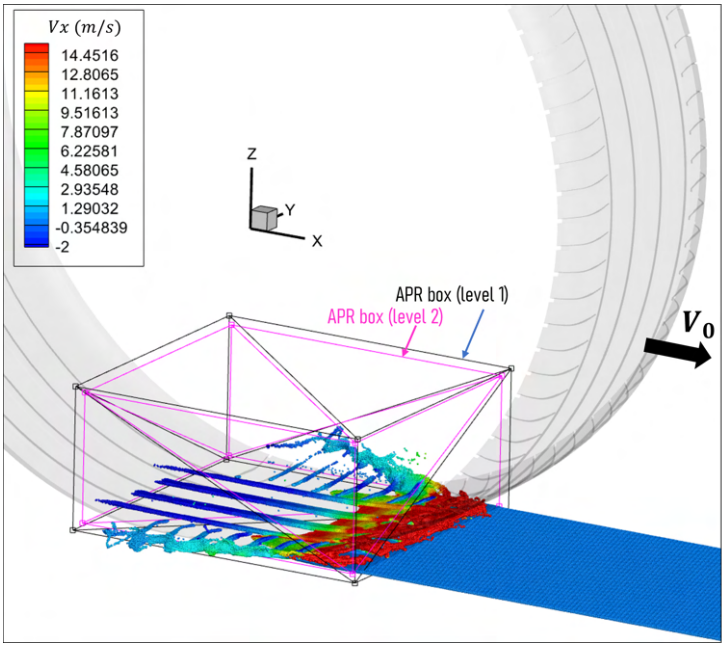

Figure 2.12 – 3D representation of the PCY4 tire (only the tire tread is shown) rolling over a water puddle. Two APR boxes are defined here, their edges are respectively depicted in black and pink.

chapter also provided details about the SPH-FE coupling strategy adopted in the case of modeling the FSI problem of a tire rolling over a puddle of water. We highlighted the complexity of such a model thus the different optimization techniques incorporated in our simulations to reduce computational costs while maintaining stability and accuracy. The next chapter focuses on the dedicated experimental tool used to measure local velocity fields around the tire and inside the tread grooves during the rolling phase.

Chapter 3

The refracted Particle Image Velocimetry (r-PIV)

Particle Image Velocimetry (PIV) is an optical measurement technique by which the velocity field of a region within the flow is measured in a plane. A pair of images of the seeded fluid flow is recorded with a double frame camera at two successive instants, and through a 2D correlation algorithm, the displacement of illuminated particles' set is estimated. A double pulsed laser light sheet is used for plane illumination. The PIV technique is a non-intrusive method and was initially developed to measure the two planar velocity components of the flow (2D-2C). The PIV method has never been used for hydroplaning measurements until the collaboration between Michelin and the LMFA laboratory which started in 2014 studying the feasibility of PIV application to a tire rolling through a puddle application. PIV was adapted particularly regarding the illumination that is only possible via refraction due to accessibility constraints. For this reason, later on, Cabut et al. [13] enforced the use of such extension of PIV, especially concerning the particularity of the illumination and the consequences on particle images and measurement location. This led to the refracted PIV (r-PIV). For this, he used a laboratory bank and did in-situ experiments.

After an overview of the state of the art concerning measurements in tire-related flows using r-PIV, the test facility is described for non-time resolved measurements. Then we will introduce the displacement field calculation in typical r-PIV processing, and we will end with the application of this strategy to our case of study. Post-processing tools specific to the tire application are also discussed. Finally, the equipment used for a feasibility study for Time-Resolved r-PIV (TR-PIV) measurements is described in the last subsection.

3.1 The refracted Particle Image Velocimetry (r-PIV)

The refracted Particle Image Velocimetry (r-PIV) is used for velocity measurements in liquid films developing along a flat surface in specific cases where different constraints preclude the classical illumination technique using a planar light sheet parallel to the wall. In such a case as the one depicted in Fig.3.1 the illumination inside the liquid film is obtained thanks to the refraction of the incident inclined light sheet at the solid/liquid interface. Due to spurious ambient light usually generated by the illumination process inside the liquid film, fluorescent particles are used to filter the wavelength of the emitting laser.

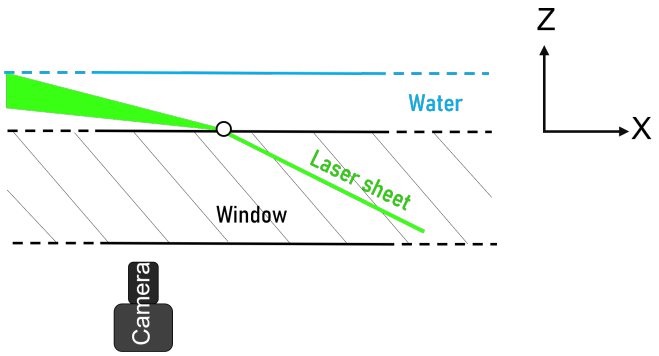

Figure 3.1 – Scheme of the illumination method for velocity measurements inside a liquid film using refraction.

3.1.1 Measurement error modeling for r-PIV

The main source of error in r-PIV measurements is due to the thickness of the light sheet propagating after refraction. Cabut developed first for a single phase flow a simplified model which predicts the ideal form of the cross-correlation function between two images for a given ensemble of individual fluorescent particles located at different random heights inside the liquid film. The input of the models for an elementary interrogation area are i) the intensity distribution I(z) inside the light sheet, ii) the actual diameter of the seeding particles, iii) different parameters of the receiving optic (working distance, aperture, focal length, object plane position, distance object plane/lens position, distance particles/object plane), iv) the time delay between images, and finally v) an ideal velocity profile $V_x(z)$. The output of the model is the actual velocity measured in the interrogation area resulting from the individual contributions of the seeding particles. The model has been validated

in a simplified academic channel flow (Cabut et al. [12]). In addition, the model has been modified for the case of a two-phase flow with bubble columns by introducing a transmission factor in the individual contribution to the cross-correlation of each seeding particle; this factor takes into account an attenuation coefficient induced by the bubbly medium.

3.1.2 Application of r-PIV to a tire-related flow

The r-PIV technique has been used in-situ in a dedicated track by Cabut et al. [11] in the case of a summer tire (MICHELIN Primacy 4) with longitudinal and transverse grooves, in a new or worn state. Due to the low repetition rate of the double cavity Yag laser, measurements were not time-resolved; to perform ensemble-averaging of the individual velocity fields, measurements were repeated over a set of independent runs for the same control parameters (car speed and water film height). For increasing car speeds, the velocity field developing in front of the contact area, in the so-called water-bank, shows a self-similar structure except for large velocities, provided that streamwise coordinate X and velocity component V_x are normalized by the water-bank length and the maximum V_x velocity inside the water-bank. The variability of the flow from one run to the other is mainly observed near the shoulders due to local hydrodynamic perturbations induced by the periodic occurrence of transverse grooves.

The flow in the four longitudinal grooves is highly dependent on the state of the tire, new or worn. For a new tire, the velocity profile $V_x(x)$ undergoes some small-scale spatial fluctuations from one run to the other, due to the interconnection between longitudinal and transverse grooves, nevertheless, the shape of the velocity profile at the scale of the longitudinal groove length is nearly the same for different runs. It has been shown that velocity profiles $V_x(x)$ measured for increasing car speeds, before the appearance of hydroplaning, have a self-similar shape provided that the longitudinal coordinate X is normalized by the contact patch length. For worn tires, the small-scale variability between runs is strongly reduced due to the lack of interaction between longitudinal and transverse grooves. However, the velocity profile $V_x(x)$ undergoes a strong variability due to the random position of the worn indicator in the contact area: the flow in the longitudinal grooves is periodically perturbed by the worn indicator whose height is very close to the groove's height.

The flow inside longitudinal grooves shows some bubble columns either for new or worn tires; these column bubbles are trapped inside elongated vortex structures whose existence

was hypothesized by Yeager [136] since the mid-70s. Measurements have shown that the number of vortices in a groove is a function of its geometrical aspect ratio in a cross-section. Despite the bias effect due to the volume illumination in the grooves, the deduction of these secondary flows was made possible thanks to the masking effect of the bubble column for seeding particles located in the upper part of the groove, as predicted by the two-phase optical model.
Finally, it was demonstrated that the characteristic fluid velocity inside a transverse groove is correlated with its longitudinal location X inside the contact area; the correlation is nearly linear for both new and worn tires. For new tires, water is expelled from transverse grooves located near the leading part of the contact area, while a suction effect is measured for grooves near its trailing part. For worn tires, in the absence of a geometrical connection between transverse and longitudinal grooves, water is always expelled outside the groove.

3.2 Test facility

As stated before, measurements are performed on an in-situ track at Ladoux. The dedicated area is a dry straight road with a transparent portion made of a thick PMMA block that is embedded in the ground and was used for previous studies [50] [13]. The studied tire rolls on this transparent window, on which a water film is initially at rest, delimited by a seal, and is height controlled. For safety issues, all emitting and receiving optics are located under the ground level in a dedicated room. Therefore, it is not possible to generate a planar light sheet parallel to the ground as should be done with a standard Planar-PIV (P-PIV) measurement system, and a specific optical arrangement is needed for the targeted application. The overall scheme of the installation is presented in Fig.3.2.

3.2.1 Emitting optics

The experimental setup has previously been detailed by Cabut et al. [13], [11]. The source of light is a dual cavity pulsed laser emitting at a wavelength of 532nm and with a repetition rate of $60Hz$. The energy of each pulse is around $100mJ$ and their length is around 5 ns. The light sheet generated at the exit of the emitting device is directed toward the inlet inclined face of the transparent window. The angle $\theta_p = 64°$ (Fig.3.3) is equal to the theoretical angle predicted by Snell-Descartes laws as a critical angle for full

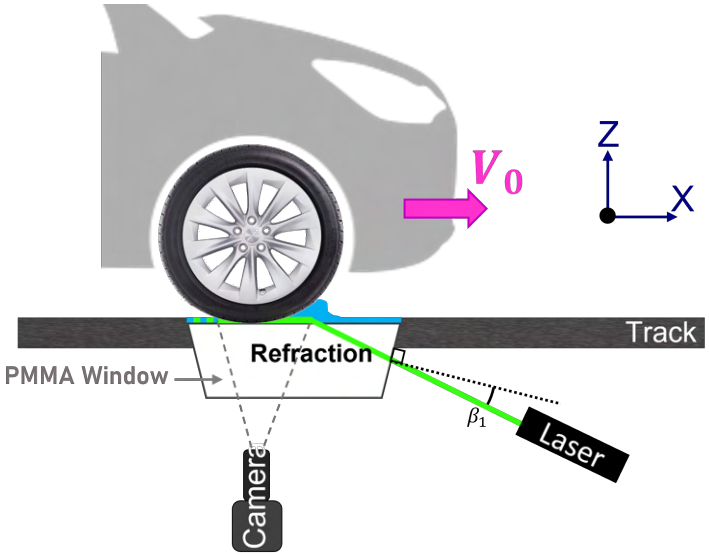

Figure 3.2 – Scheme of the in-situ r-PIV installation

reflection at the PMMA/water interface for an incoming light sheet normal to the inlet inclined face. We represent in the same figure the propagation of the incident laser beam, its trajectory crossing the first interface, the air-PMMA interface, is calculated following Snell-Descartes law:

$$\theta_t = arcsin(\frac{n_1}{n_2} sin(\theta_i)) \tag{3.1}$$

where θ_i and θ_t are respectively the incident and transmitted angles, and $n_1 = n_{air}$ and $n_2 = n_{\text{PMMA}}$. The ray crosses a second interface afterwards, a PMMA-water interface, and its trajectory is calculated following the same law taking $n_1 = n_{\text{PMMA}}$ and $n_2 = n_{\text{water}}$. The theoretical values of the refractive indexes of the PMMA and water at $532nm$ and 20°C are respectively $n_{\text{PMMA}} = 1.49$ and $n_{\text{water}} = 1.33$. A small angle of the light sheet with the normal allows, after refraction, the propagation of the light sheet inside the liquid film, with a high spreading rate. Therefore, for a small thickness of the water film, the vertical intensity profile I(z) of illumination is nearly uniform in the area of interest, and the liquid film is considered as illuminated in the volume, introducing some bias in velocity measurements for inhomogeneous actual velocity profiles in the vertical direction. Such bias due to both emitting and receiving optics has been analyzed by Cabut et al. [12].

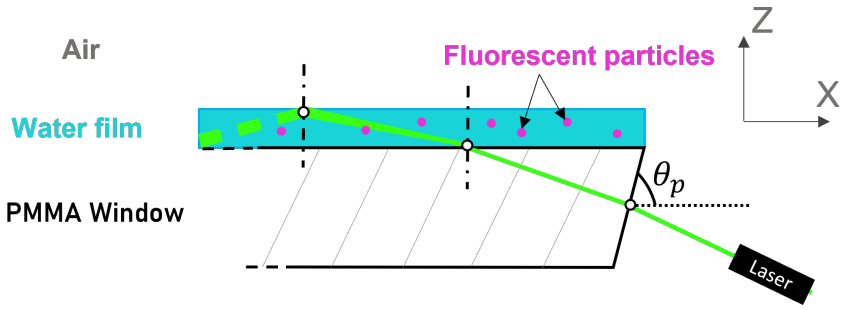

Figure 3.3 – Detail of the refraction processes of the laser sheet at the air/PMMA and PMMA/water interfaces.

3.2.2 Receiving optics

We are currently using an sCMOS (scientific Complementary Metal Oxide Semiconductors) camera equipped with a double shutter with a minimum inter-framing time of $120ns$. The camera's sensor is 2560 pixels in the X-direction and 2160 pixels in the Y-direction. The sensor has a spectral range of 370-1100nm, and maximum quantum efficiency of 60% around $600nm$. The camera is equipped with a lens of $100mm$ of focal length and an aperture number of 5.6. Depending on the distance between the camera and the water film ($2m$ approximately), the field of view is around 220x190mm.

3.2.3 Seeding

The tracers used in this application are fluorescent particles doped with Rhodamine B allowing a high signal-to-noise ratio, as soon as a narrow-band filter, centered around $584nm$ with a bandwidth of $\pm$ $10nm$ is mounted on the camera lens. The particles are rather spherical with a nearly Gaussian diameter distribution with a mean value of d_p= $35\mu m$ and a standard deviation of about $5\mu m$. To quantify inertia effects of particles, we have evaluated their Stokes number $St = \frac{\tau_p}{\tau_f}$ where τ_p is the particle response time and $\tau_f = \frac{L_0}{U_0}$ is the characteristic time scale of the flow. Inside the CPA, L_0 can be taken as the CPA length L_x and U_0 as the streamwise velocity V_x inside the grooves. The relaxation time is calculated as $\tau_p = \frac{\rho_p d_p^2}{18\mu}$ where $\rho_p = 1.19kg/m^3$ is the particles density and $\mu \approx 1.10^{-3} Pa.s$ (20 °C) the water dynamic viscosity. We can thus estimate that $St < 10^{-5}$ which is small enough and we can then consider that the particles perfectly follow the fluid inside the tread grooves (see, e.g., Taniere et al. [121]). However, in the leading edge of the WB, the particles are subject to high accelerations and this reasoning is not valid

anymore. Cabut [10] concluded that for particles of d_p= 35μm the maximum difference between the particle velocity and the fluid velocity is around $0.04V_0$. Nevertheless, once the velocity front is reached by the particle, this differential tends to zero and the particle's velocity in the WB corresponds to the fluid velocity.

3.2.4 Synchronization of the acquisition

To ensure the synchronization of the laser and the camera with the rolling of the tire on the window, a programmable timing unit (PTU) is used in combination with the commercial software DaVis 8. Optical sensors located some meters before the water puddle calculate the actual car's speed V_0 and generate a trigger signal with a time delay. This delay is computed with a real-time processor and adjusted to trigger the r-PIV system when the tire is at a pre-defined location inside the camera's field of view, whatever the value of V_0. The time-delay δt between the two-pulses of the laser is adjusted to the vehicle speed, e.g., for $V_0 = 11.11 m.s^{-1}$ we fix $\delta t = 225 \mu s$. Before each run, the driver sets the car in position at the beginning of the track and waits for the water film to reach its targeted value H_w. When the test starts, a process of seeding, rolling, illuminating, and image recording is achieved. For the analysis of the flow repeatability, since r-PIV measurements are not time-resolved with the system, the overall procedure is repeated over a set of N independent runs for a fixed couple of operating parameters V_0 and H_w.

3.3 Major shortcomings and challenges of the r-PIV

The hereby presented measurement facility is very specific to the hydroplaning application and is far from being a straightforward 2D measurement of the velocity field inside the tread grooves and the WB. Indeed, a long and demanding installation is required apart from all the weather hazards and the iterative post-processing phase. Note also that the r-PIV trials are one of the numerous tests done on the Michelin track. In so, the time dedicated to the present tests is very difficult to obtain and has to be planned well in advance. Any kind of weather perturbation (wind, ice, rain, ...) are reasons to cancel the programmed trials. Furthermore, the present measurements have to be done during the night to limit the ambiant light, thus the period for trials is scarce during a year (mainly during winter because the sun sets earlier than in other periods). This section is dedicated to the main challenges and difficulties specific to the r-PIV measurement strategy. It is

divided into the difficulties encountered before the acquisition and the ones linked to the post-processing phase.

3.3.1 Before the acquisition

3.3.1.1 Thickness of the laser sheet

One of the main shortcomings of using the r-PIV technique is the unknown propagation characteristics of the laser sheet inside the water puddle. In [12], Cabut et al. performed measurements of the light sheet profile for both the PIV and the r-PIV configurations. While the intensity profile along the Z-axis appeared sharp and nearly symmetric in the case of the P-PIV, the measurements for the r-PIV showed a wider and strongly asymmetric profile. The large thickness of the laser sheet can therefore introduce an added bias in the r-PIV measurements. As propagating inside the water, due to multiple reflections (inside PMMA block and water), the intensity profile can be taken as a flat intensity profile in the main part of the measurement regions as in the work of Cabut et al. [13] for in-situ configuration.

3.3.1.2 Depth of focus

The depth of focus defines the sharpness of the particles in the recorded image. This parameter is of interest to determine which particles contribute the most in the cross-correlation operation, i.e. particles that are located on the camera object plane in the water puddle. Cabut et al.[12] developed a measurement technique to determine the object plane position in the fluid at rest. An inclined dotted plate was placed inside the water puddle so that its lower edge touches the ground and its higher edge crosses the free surface, and images of this target were taken to determine the positions of the best-focused dots along the Z-axis. For an aperture number of 5.6, the object plane position was established at $z_{OP} = 0.45H_w$. The same aperture number is kept in this work to ensure a good focus with a maximum signal-to-noise ratio.

3.3.1.3 Weather conditions

The test facility of the r-PIV as presented in Section 3.2, is not sheltered and the measurement campaigns are therefore dependent on the weather conditions, in particular the wind, the the rain, and the temperature. In some cases, the measurements should be

suspended if there is a lot of wind for example which disturbs the free surface at rest, or in case of low temperatures (below 0° C) which can compromise the safety of the pilot due to lack of grip in the regions where the water projections freeze and become a slippery iced surface. Finally, heavy rain introduces air bubbles in the water puddle and makes the recorded images of very low quality. The tests are conducted during the night when the ambient light is the lowest to increase the signal-to-noise ratio.

3.3.1.4 Number of repetitions

For a given set of parameters (V_0,H_w) and a given tire, multiple rollings are conducted. This allows us to do some statistical operations and average over the N recorded images. But the determination of the number N is very difficult to establish since it needs to be high enough to erase the systematic measurement errors and obtain a representative 2D field, but it also needs to fit in the dedicated time allowed for the tests. Usually, we fix $N = 8$, however, for specific applications, it can either be increased or decreased.

3.3.2 After the acquisition

3.3.2.1 Images post-processing

The difficulty of the post-processing phase is about choosing the right parameters for the cross-correlation operation. Usually, an iterative process is required where different parameters are tested. The main parameters are:

— The interrogation window size

— The number of iterations

— The windows overlapping

— The weighting function

However in theory, if the processed image is well seeded, with a good intensity level, and with the right δt between the two frames, these parameters should not dramatically change the cross-correlation results. But in our case, it is frequent to have images with low intensity levels in some regions and inhomogeneous seeding. Moreover, a large gap in the velocity levels inside the grooves and inside the WB is observed, which necessitates a compromise in the interrogation window size. Last but not least, the application of a geometric mask on the recorded image is usually required before the cross-correlation phase and the generation of these masks is very dependent on the image quality, which

introduces an added difficulty for any targeted automation. In some cases, the definition of the mask border is difficult, particularly in the case of smooth tires where the frontier CPA/WB is usually not sharp.

3.3.2.2 Disrepencies between runs and image overlaying

As stated in Section 3.3.1.4, several rollings are performed for each set of parameters (V_0,H_w) and a given tire. But at each rolling, the position of the tire on the PMMA window changes, and a shift is created in the tire footprint from one image to the other (up to $20mm$ in the streamwise direction and $40mm$ in the spanwise direction). So an overlaying strategy should be proposed to put all images in the same referential before comparing or ensemble averaging them (details in Section 3.5). Moreover, as it has been stated before, tires in a worn state are also tested, and these tires present some geometry mismatches (presence of the wear indicator in different positions clogging a groove and difference in the grooves' widths). Therefore, the analysis becomes even more difficult. It also adds the necessity to choose suitable images for further comparison with the numerical results.

3.4 Image acquisition and processing

The velocity field is generated using the commercial software DaVis. The cross-correlation between a pair of images is performed with an iterative process using interrogation areas of decreasing size. Before generating the velocity field of each run, a geometric virtual mask is applied to the raw images. It is a sensitive task since from one image to another not only the tire deformation is not the same due to the dynamics of the fluid, but also the image illumination changes. The purpose of the mask is primary to remove regions without seeding particles (out of fluid flow regions), but also to enhance the cross-correlation quality near the groove's borders. The mask is generated using our image processing algorithm. This mask determination method is different from Cabut's work [10] in which a manual process is adopted. The present procedure accelerates the post-treatment phase which can be very time-consuming when the number of images to process is important. In addition, despite the driver's skills, the location of the CPA inside the field of view can undergo some disparity from one run to the other. The variability appears to be mainly in the spanwise direction Y; a small jitter in the X location of the CPA can be explained by i) small departures of the actual water film depth from the targeted one, and ii) a slight disparity in the vehicle velocity between the different repetitions. At this stage, the origin

O is the one resulting from the calibration of the camera, and its location inside the field of view is arbitrary.

3.5 Common referential definition and ensemble averaging strategies

We intend to analyze the flow in the water-bank and inside the grooves for a set of independent runs. Therefore, the location of the CPA, or at least its leading edge, needs to be collapsed to define a common coordinate system for all the velocity fields, with a common origin O with some physical relevance to the flow structure around the tire and inside the CPA. For a reference run, the image Img_0 is first chosen, then the (X,Y) offsets of the other images (runs), relatively to Img_0, need to be computed against Img_0. To generate the offsets and put the images in the same referential, two different strategies can be adopted:

— Intensity-based strategies: the Mask correlation method and the Intensities correlation method. The results of these methods are directly linked to the illumination quality of the raw images.

— Velocity-based strategy: the Velocities correlation method. To generate the offsets using this method, the cross-correlation should be performed first and therefore the velocity field associated to each image is created. The offsets generated may vary by changing the correlation parameters (interrogation window size, post-processing operations...).

These three methods are more or less efficient depending on the tire tread, the quality of the illumination, and the quality of the cross-correlation.

3.5.1 Mask correlation: X and Y offsets

The main idea of this method is based on the generation of a binary image called a « Mask » from each raw r-PIV image. The Masks are created using Python, following these operations:

1. Gaussian blur (Fig.3.4(b)): In image processing, a Gaussian blur is the result of smoothing an image by a convolution with a Gaussian function. It is used to reduce image noise and detail.

2. Standard deviation filter (Fig.3.4(c))
3. Local threshold (Fig.3.4(d))
4. Binary threshold (Fig.3.4(e)): It converts an image from color or grayscale into a binary image.
5. Closing (Fig.3.4(f)): Morphological closing is a dilation followed by an erosion. The effect of the closing operation is to remove background pixels that fit the structuring element, i.e. closing tends to close gaps in the image.
6. Opening (Fig.3.4(g)): The opening operation erodes an image and then dilates the eroded image, it is the reverse of closing. The morphological opening is useful for removing small objects and thin lines from an image while preserving the shape and size of larger objects in the image.

These generated Masks tend to hide the rubber/road contact area and let only the grooves and the WB visible. A final manual operation is included where the user can modify the Mask created with the algorithm to whiten/blacken certain regions to either correct some errors or to intentionally hide some grooves for example or other areas for a specific study (Fig.3.4(h)). This part is completely subjective and dedicated to a precise treatment of the image.

Each Img_j has its associated Mask_j $(0 \leq j \leq N-1)$. Afterward, an operation of correlation between Mask_j and Mask_0 is performed to generate X_j and Y_j offsets. This method tends to overlay the images according to the position of the grooves and not the water-bank, especially in the case of directional treads, but it gives very satisfactory results concerning the Y-offsets. Two main advantages of this method are pointed out:

— It requires less intervention from the user.

— The masks generated can be imported in DaVis as geometric masks to generate velocity vectors only in the areas of interest allowing to remove wall and surface patch area effects where noising signal biases the results.

3.5.2 Velocities correlation: X offset

This method is based on a quite different idea. The different tires present the common property to push the liquid to the front, with the appearance of the so-called water-bank with a peak value on the V_x velocity profile, bounded by relatively sharp falling and raising edges. Most of the existing tire models also generate locally a plateau in the V_x profile

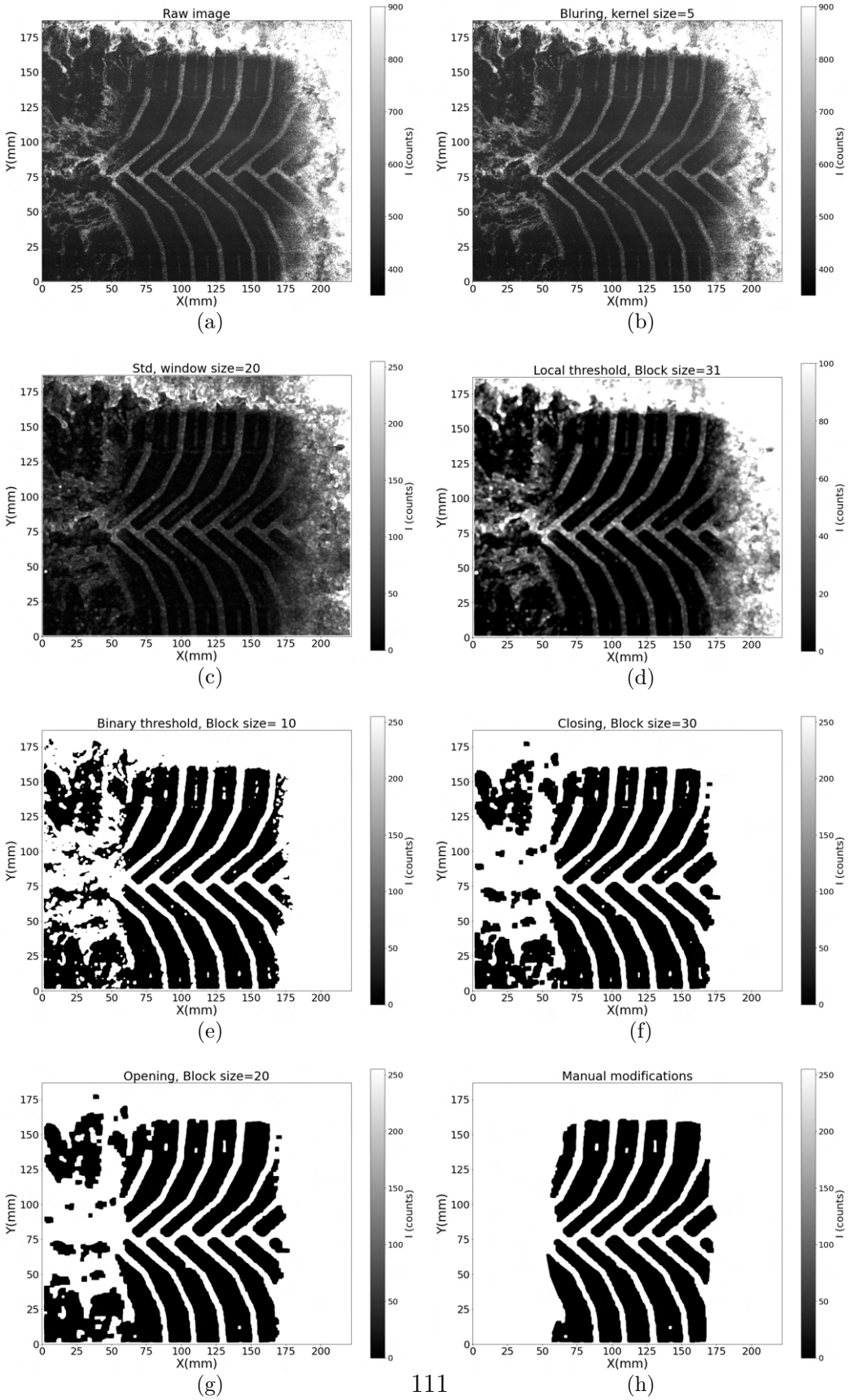

Figure 3.4 – Images of the different steps of mask generation from the raw image (a) to the manual modifications (h): Michelin Cross Climate+ worn, $V_0 = 8.33m.s^{-1}$ and $H_w = 1.5mm$.

behind the tire, with a zone of sharp gradient near the CPA trailing edge, as depicted in Fig.3.7 for the case of the MICHELIN Alpin 6 tire (A6) detailed in Section 6.2. The X-offset is then deduced from the displacement corresponding to the peak value of the cross-correlation between V_x velocity profiles. The main assumption for this method is first the existence of such characteristic peak whatever the kind of tire studied, then that the global shape of the velocity profile in the WB remains nearly similar from one run to the other for a given tire model.

The first step is to determine the instantaneous Y-offsets over the N runs. Two possibilities exist, either to use the Y-offset generated by the Mask correlation method if it is satisfactory or to create it manually. In the latter case, an easily identifiable point on each image is selected using the tread pattern of the tire, e.g., the top of the central zigzag groove depicted with red dots in Fig.3.5 in the case of the MICHELIN Alpin 6. The Y-offsets are calculated via the rule: Y-offset$_j$=Ycoordinate$_{\text{Img}_0}$ - Ycoordinate$_j$ for $0 \leq j \leq N-1$. At this point, we can collapse at the best the N images along the Y-axis. The X-offsets are then determined as follows. We note V_{jI} the Y-shifted velocity field of the run j that is computed for masked images (the mask applied are the ones detailed in section 3.5.1). In order to remove some potential small-scale noise, the velocity field is then spatially averaged along Y in a band centered around $Y = 0$, as shown in green in Img$_0$ (Fig.3.7(a)). The resulting spatially Y-averaged velocity $V_{jII}(x)$ is related to $V_{jI}(x, y)$ by the relation:

$$V_{jII}(x) = \frac{1}{y_2 - y_1} \sum_{y_i=y_1}^{y_2} V_{jI}(x, y_i) \tag{3.2}$$

Then comes the actual correlation step between the $V_{jII}(x)$ profiles and the $V_{0II}(x)$ one. The cross-correlation of two discrete functions f and g in $\mathbb{R}^N$ is defined as:

$$h[k] = (f * g)[k - N + 1] = \sum_{m=0}^{N-1} f[m]g[m - k + N - 1] \tag{3.3}$$

for $k = 0, 1, 2..., 2(N-1)$ and $g[n] = 0$ if $n \notin [0, N-1]$. Then we extract r as $h[r] = max(h)$, the position of maximum correlation between f and g. Finally, the offset of g to best match f is:

$$\text{X-offset} = r - N + 1 \tag{3.4}$$

The curves of $V_{jII}(x)$ are plotted together on Fig.3.7(c), this for each j $(0 \leq j \leq N-1)$. X-offset$_j$ are determined to correspond to the maximum correlation for each case. Each offset corresponds to the translation for the best curve shape matching. Therefore, this

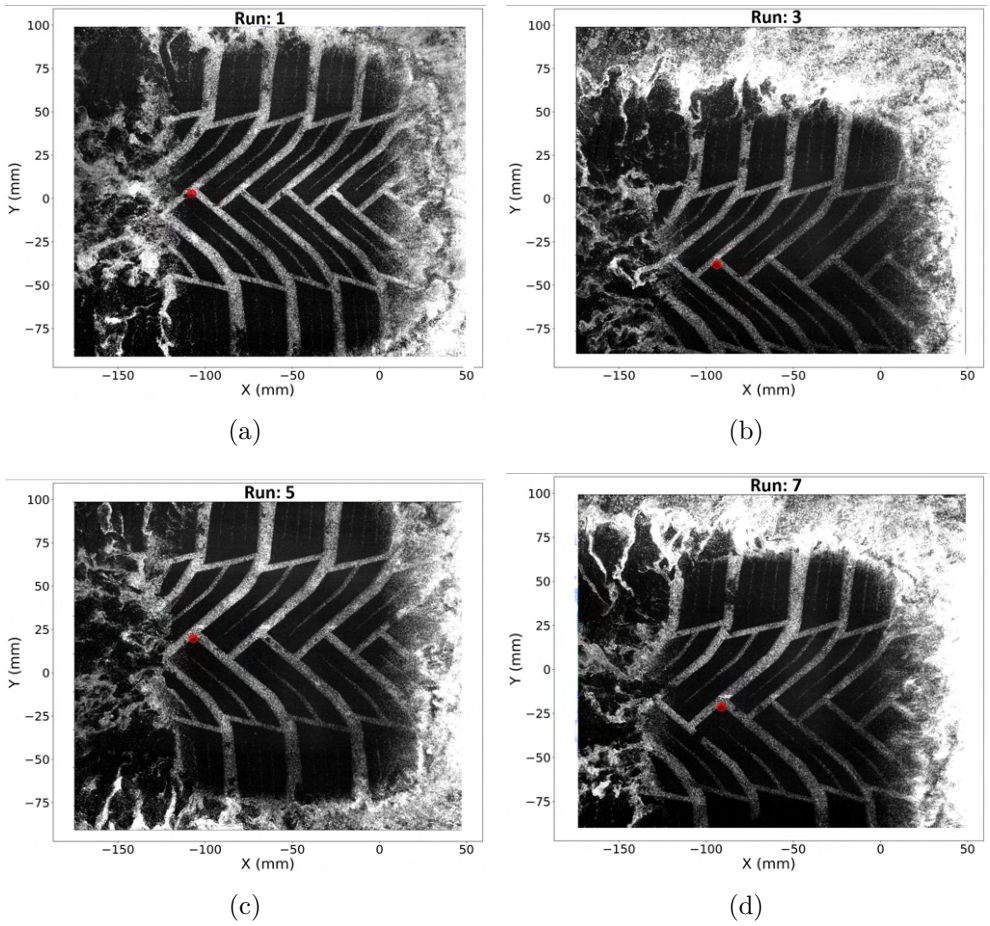

Figure 3.5 – Raw intensity images (Frame 0) for four independent runs. The red dot on the images shows the relative position of a given arbitrary point located on the edge of the central zigzag groove: MICHELIN Alpin 6 worn, $V_0 = 11.11m.s^{-1}$ and $H_w = 1.5mm$.

method tends to overlay the images according to the position of their WB. In the case of the A6 for example, the Fig.3.7(d) indicates the final shifting; even if the peak value of the profiles undergoes some variations from one run to the other, the collapse of the positions of the rising and falling edges of velocity profiles is very satisfactory. We define the following criterion to evaluate the quality of the overlapping:

$$Error_{overlap} = \sigma(X_{slope\,WB_j}) \tag{3.5}$$

where

$$X_{slope\,WB_j} = min\{\text{abscissa}(diff(V_{jII}) > 0.04)\} \tag{3.6}$$

and $diff(.)$ is the differential. This criterion calculates the standard deviation between the abscissa $X_{slope\,WB_j}$, location of the sudden change in the slope between the CPA and the WB in the V_{jII} profiles around $X = -10mm$ in Fig.3.7(d). The value of 0.04 is chosen to be higher than the fluctuations of $diff(V_{jII})$ around 0, but low enough to capture the beginning of change in the slope of V_{jII} profile. We give in Fig.3.8 the $diff(V_{jII})$ profiles in the case of the A6 worn at V_0=11.11$m.s^{-1}$ and $H_w = 1.5mm$ zoomed between $X = -40mm$ and $X = 20mm$. In this case $Error_{overlap} = 2.38mm$ a low value indicating that the profiles are well overlapped.
The location $X = 0$ is common for all runs but remains at this stage somewhat arbitrary. In Fig.3.7(b) the CPA region is bounded by the dashed vertical lines in the grey-level image intensity profile along X-axis. It corresponds to the area where the illumination is the lowest since the tire is in contact with the ground. We decide to define $X = 0$ as the location of the right dashed line where the grey-level gradient increases suddenly. The abscissa of this point noted X_{origin}, is determined using the following criteria:

$$X_{origin} = min\{\text{abscissa}(diff(I) > 0.3)\} \tag{3.7}$$

The value of 0.3 is also chosen to be higher than the fluctuations of $diff(I)$ around 0, but low enough to capture the beginning of the change in the slope of the intensity profile. We give in Fig.3.6 the $diff(I)$ profile for Img_0 in the case of the A6 worn at V_0=11.11$m.s^{-1}$ and $H_w = 1.5mm$ zoomed between $X = -40mm$ and $X = 20mm$ Concerning the position

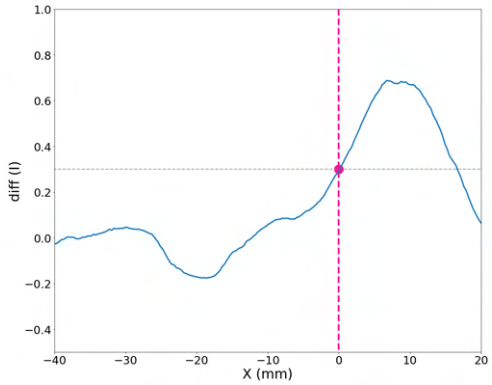

Figure 3.6 – $diff(I)$ profile for the A6 worn at V_0=11.11$m.s^{-1}$ and $H_w = 1.5mm$ for Img_0. The position of $X_{origin}$is highlighted with the vertical dashed line.

of $Y = 0$, it has been chosen so that it corresponds to the center of the middle zigzag groove.

With this choice, we introduce a natural separation between the flow inside the grooves of the CPA ($X \leqslant 0$), and in the WB in front of the tire ($X \geqslant 0$) which is the region where the water velocity and the pressure are the highest. This last region is responsible for the main part of the fluid lift and therefore the reduction of the CPA when the car velocity increases.

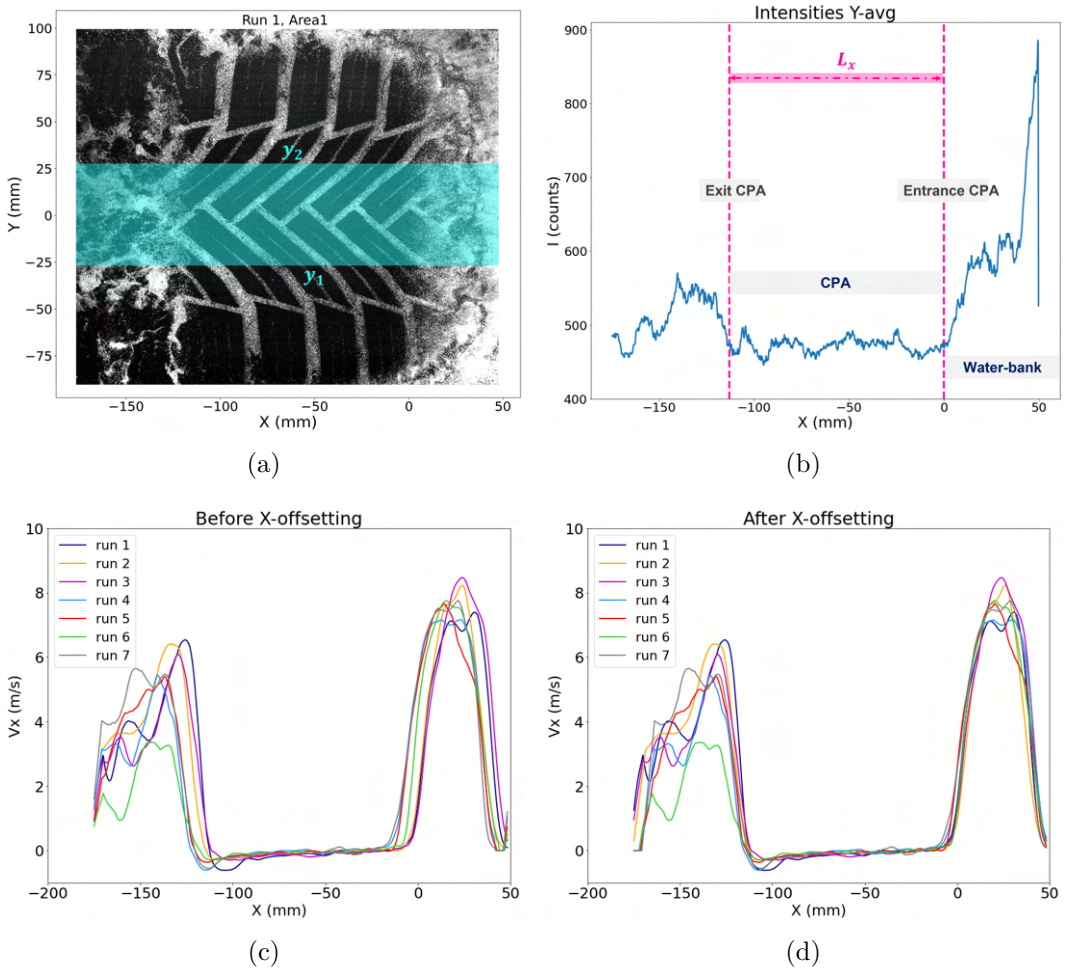

Figure 3.7 – Area 1 highlighted in blue on a raw image of the A6 worn at V_0=11.11$m.s^{-1}$ and $H_w = 1.5mm$ (a), image intensities space averaged along Y-axis in Area 1 and highlight of the different region of interest (b) and V_x space averaged along Y-axis in Area 1 before (c) and after(d) X-offsetting using the Velocities correlation. The run 1 is chosen as the reference image here (Img_0).

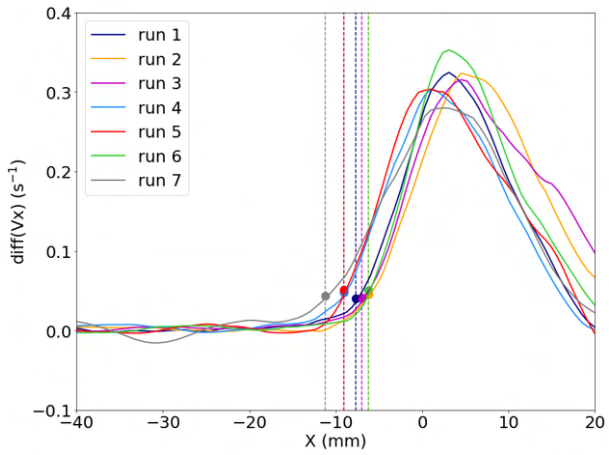

Figure 3.8 – $diff(V_{jII})$ profiles for the A6 worn at V_0=11.11$m.s^{-1}$ and $H_w = 1.5mm$ corresponding to the velocity profiles in Fig.3.7(d). The positions of $X_{slope\,WB_j}$ are highlighted with the vertical dashed lines.

3.5.3 Intensities correlation: X offset

The main idea is to use the grey-level intensity distribution inside raw images. This method has previously been used by Cabut et al [11] for a tire model with four central longitudinal grooves. In that case, the X-offset for different runs was deduced from the grey-level profile along a narrow band including the central rib with straight edges; such a profile is nearly uniform with a very low noise level for the region located inside the CPA and presents a strong gradient near the front edge of the CPA due to the contribution of seeding particles present in the liquid phase, just in front of the central rib. In this method, the Y-offset is generated just like in the Velocities correlation method, either using the Mask correlation method, or the manual one.
The advantage of this method compared to the velocities-correlation is that it is not dependent on the quality of the cross-correlation and the values of the velocity fields. However, it is directly dependent on the quality of the illumination. We give in Fig. 3.9 an example of the intensity levels space averaged in the central area of the contact patch before and after the offsetting for the Slick225 smooth tire. In this case, $Error_{overlap} = 2.11mm$ which corresponds to a good quality of offsetting.

3.5.4 Comparison between the offsetting strategies

In the following section, we give an example of the results obtained using the three different offsetting strategies in the cases of a longitudinal tread and a directional tread.

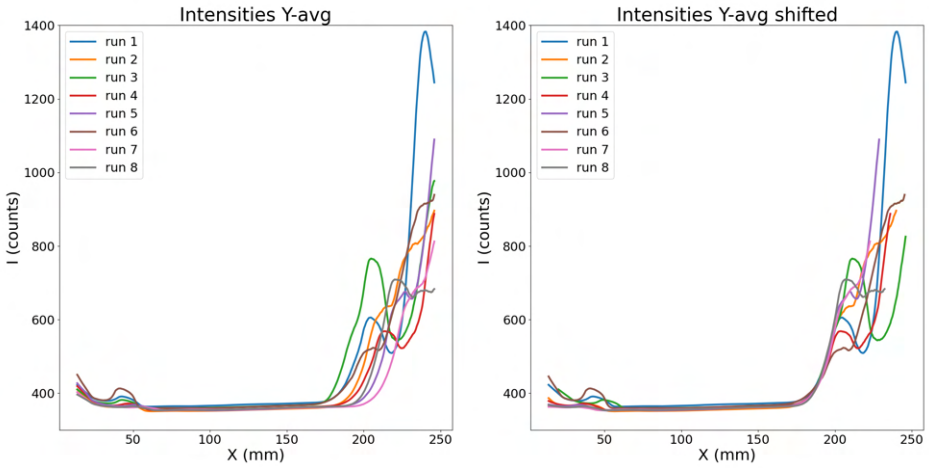

(a) Intensity levels before (left) and after (right) the overlapping

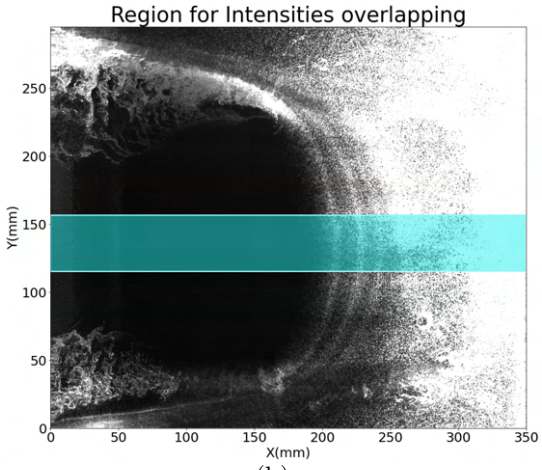

(b)

Figure 3.9 – Intensity levels before (upper left) and after (upper right) intensities overlapping for the Slick225 at $V_0 = 8.33m.s^{-1}$, $H_w = 8mm$ and N=10 runs. Run 2 is chosen as the reference image in this case (Img_0). The space average of the intensities is calculated in the highlighted area in blue on the raw image (bottom).

This will allow us to choose the most suitable strategy for each tire tread case. In practice, there is no generalization when working with a specific tire tread, the results are dependent on the quality of the acquisition and the cross-correlation parameters. Therefore, in practice, this operation of comparison between the offsetting strategies is usually adopted each time we change of tire tread.

3.5.4.1 Case of a longitudinal tread

We consider here the case of the Michelin Primacy 4 (PCY4) tire in a worn state at $V_0 = 8.33m.s^{-1}$ and $H_w = 1.5mm$. The cross-correlation parameters are:

— Initial passes: 3 passes with a 96x96 pixel window with an overlap of 50% and a circular weighting.

— Final passes: 4 passes with a 32x32 pixel window with an overlap of 75% and a circular weighting.

— Geometric mask applied on the raw images before the correlation.

The X-offsets obtained with the Velocities correlation, the Intensities correlation, and the Mask correlation are presented in Fig.3.10(a). The Y-offsets obtained with the Mask correlation and the manual selection are presented in Fig.3.10(b). Moreover, to better render the difference between the results obtained with each offsetting strategy, we plot the V_x offsetted profiles of all the N runs Y-averaged in the longitudinal groove highlighted in Fig.3.11(a): Velocities correlation in Fig.3.11(b), Intensities correlation in Fig.3.11(c) and Mask correlation in Fig.3.11(d). We can see that the results concerning the Y-offsets are

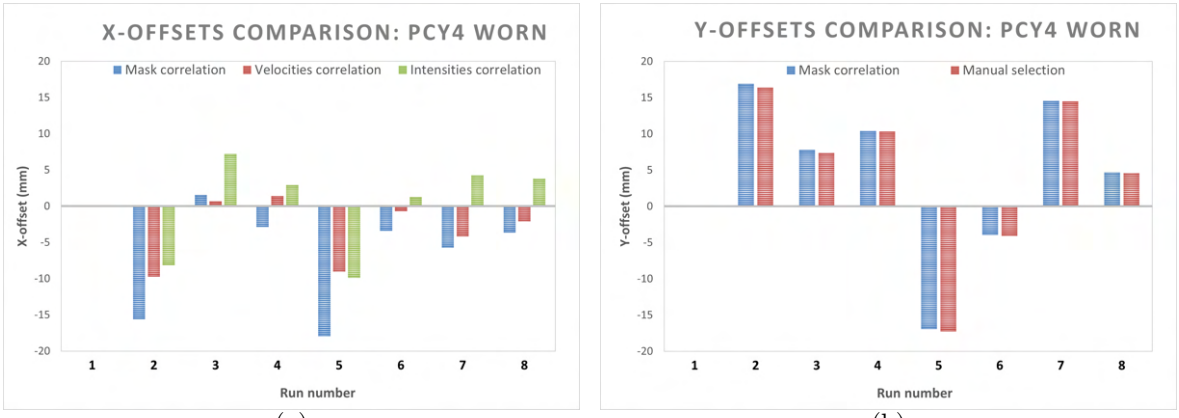

(a) (b)

Figure 3.10 – X-offsets (a) and Y-offsets (b) generated using the different offsetting strategies in the case of the PCY4 worn at $V_0 = 8.33m.s^{-1}$, $H_w = 1.5mm$ and $N = 8$ runs.

rather close between both methods in the case of the PCY4 tire. When using the manual method, we choose a point in the lower edge of the upper longitudinal groove to generate the Y-offsets. The Mask correlation method shows good results and overlays properly the masks along Y-axis. The presence of a simple geometry as the four longitudinal grooves facilitates the correlation operation. Concerning the X-offset, the Mask correlation tends

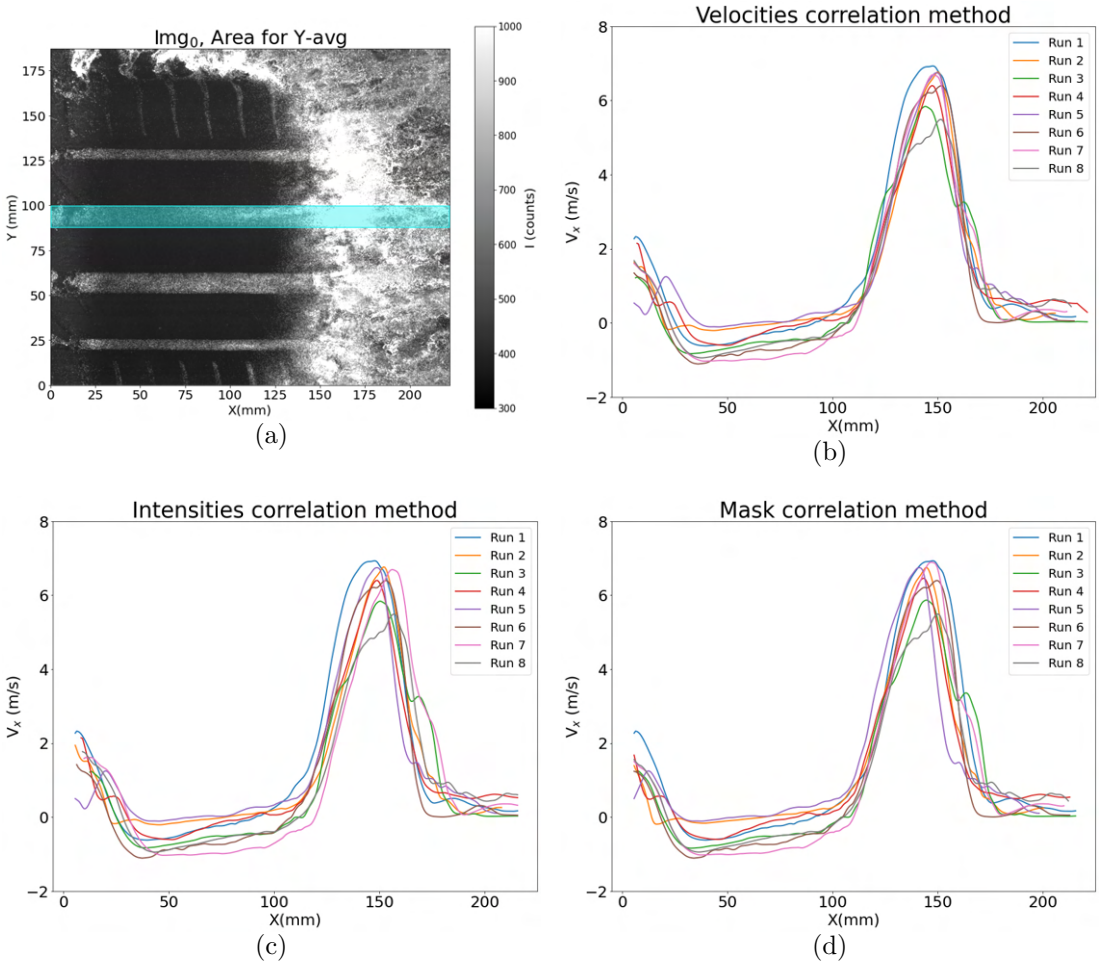

Figure 3.11 – Comparison between the three overlapping methods in the case of the PCY4 worn at $V_0 = 8.33m.s^{-1}$, $H_w = 1.5mm$ and $N = 8$ runs. The V_x profiles of all runs are plotted Y-averaged in the area highlighted in blue in (a). Profiles obtained after using the velocities correlation method are plotted in (b), the intensities correlation in (c), and the mask correlation in (d).

to overlay the maximum of white regions (grooves), while the velocities correlation tends to overlay the peaks of velocity profiles along the selected region of correlation (upper longitudinal groove in this case), and finally, the intensities correlation overlays the grey-level image intensity profiles along the central rib based on the sudden change in their slope that corresponds to the CPA/WB border. The final choice about the overlaying strategy to keep is based on the velocity profiles plotted in Fig.3.11 by calculating $Error_{overlap}$. The results obtained are presented in Table 3.1. The Mask correlation seems to give the best results.

Strategy adopted	Intensities correlation	Mask correlation	Velocity correlation
$\mathbf{Error_{overlap}}(mm)$	4.14	2.33	3.28

Table 3.1 – Comparison between the overlapping strategies for the PCY4 worn at $V_0 = 8.33m.s^{-1}$ and $H_w = 1.5mm$

3.5.4.2 Case of a directional tread

We consider here the case of the MICHELIN Alpin 6 (A6) tire in a worn state at $V_0 = 8.33m.s^{-1}$ and $H_w = 1.5mm$. The cross-correlation parameters are:

— Initial passes: 3 passes with a 96x96 pixel window with an overlap of 50% and a circular weighting.

— Final passes: 4 passes with a 32x32 pixel window with an overlap of 75% and a circular weighting.

— Geometric mask applied on the raw images before the correlation.

As in the previous paragraph, the X-offsets are given in Fig.3.12(a) and the Y-offsets in Fig.3.12(b). The V_x offsetted profiles Y-averaged in the central area highlighted in Fig.3.13(a) are given in Figures 3.13(b), 3.13(c) and 3.13(d). In the case of a directional

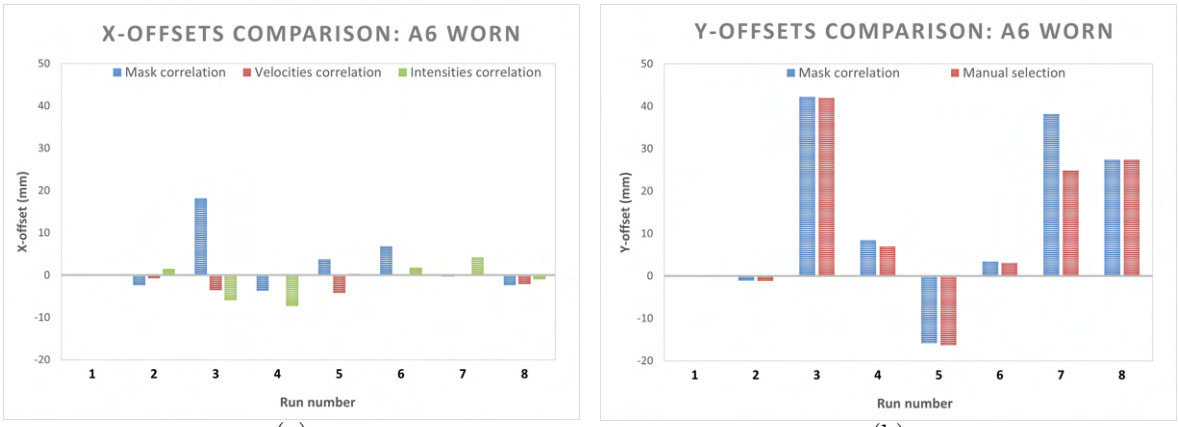

(a) (b)

Figure 3.12 – X-offsets (a) and Y-offsets (b) generated using the different offsetting strategies in the case of the A6 worn at $V_0 = 8.33m.s^{-1}$, $H_w = 1.5mm$ and $N = 8$ runs.

tread as well, the Mask correlation method gives very satisfactory results concerning the Y-offsets. This method overlays the central zigzag grooves and therefore the CPA in the spanwise direction. But concerning the X-offsets, it gives very mixed results as we can see in Fig3.13(d). Moreover, for the tire considered, its complex groove shapes (zigzag

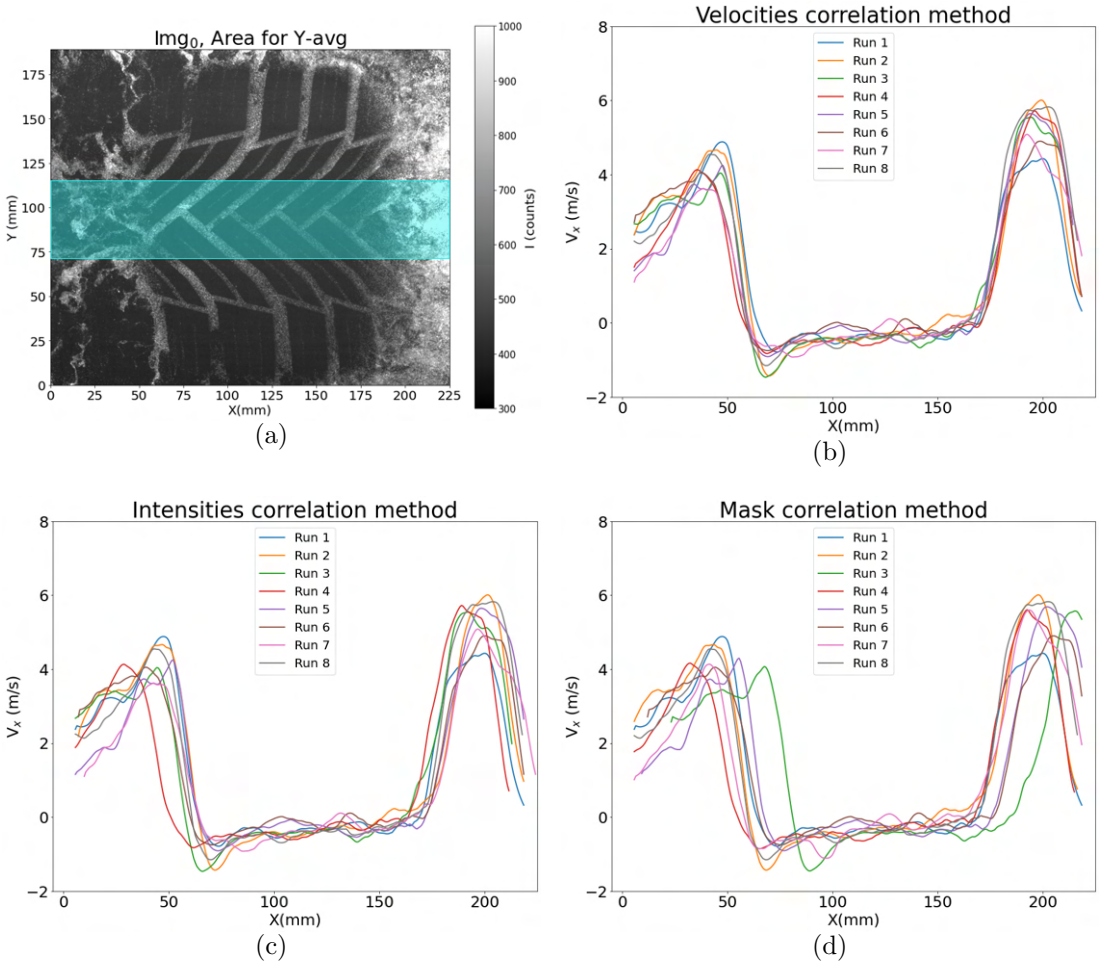

Figure 3.13 – Comparison between the three overlapping methods in the case of the A6 worn at $V_0 = 8.33m.s^{-1}$, $H_w = 1.5mm$ and $N = 8$ runs. The V_x profiles of all runs are plotted Y-averaged in the area highlighted in blue in (a). Profiles obtained after using the correlation method are plotted in (b), after the intensities correlation in (c) and after the mask correlation in (d).

and directional grooves) lead to much noisier grey-level profiles inside raw images in the X-direction near the tire mid-plane than for a tire with longitudinal grooves. Therefore, the peak detection of the cross-correlation between grey-level profiles is somewhat difficult to obtain (Fig.3.13(c)). The results obtained for the calculation of $Error_{overlap}$ are given in Table 3.2. The Velocities correlation minimizes $Error_{overlap}$ and is therefore preferred in this case to generate the X-offsets.

Strategy adopted	Intensities correlation	Mask correlation	Velocity correlation
$\mathbf{Error_{overlap}}(mm)$	5.43	11.17	2.86

Table 3.2 – Comparison between the overlapping strategies for the A6 worn at $V_0 = 8.33m.s^{-1}$ and $H_w = 1.5mm$

3.6 Time-Resolved r-PIV (TR-PIV)

In this section, we present an overview of the application of the Time-Resolved r-PIV (TR-PIV) for the hydroplaning analysis. These measurements have been carried out to assess the possibility and the difficulties of using this technique. This is done following the implementation of the r-PIV in the measurement strategy of Michelin for all types of tires. The TR-PIV should allow to obtain time-resolved measurements and thus make it possible to approach numerical calculations made in parallel as a complementary tool. This first phase should lay the groundwork for the potential of this technique and its interest in future development in tire performance evaluation. Finally, this could consolidate the elements of comparisons or completion compared to numerical calculations providing additional elements of reliability. Note that preparatory work has been carried out within the LMFA laboratory in Centrale Lyon to ensure rapid implementation and avoid last-minute problems due to a lack of a component or its nonconformity with the installation. This was essential to limit the use of the track and to ensure that the reservation time would be sufficient. On the other hand, one week has been booked for the use of the test track to make these first tests. The climatic weather unfortunately greatly disrupted the tests (wind and rain). However, as we will see the preliminary results obtained under very poor conditions are very encouraging (Section 4.8).

3.6.1 TR-PIV equipment

We first compare the TR-PIV system with the classic r-PIV set-up on the Ladoux track. In addition to its higher repetition rate (from 1 to several kHz), the TR-PIV system differs on the following points:

- The dynamic range of the fast camera (12 bits), is lower than that of a conventional camera (16 bits).
- The lowest spatial resolution of the sensor for a fast camera (1000x1000 pixels), against 2560x2160 pixels for the usual camera.

- The energy of the pulses of the fast laser (on the order of $20mJ$), is lower than that of a low-rate laser (on the order of $200mJ$). The loss of energy inherent in the fast laser is nevertheless partially outweighed by the larger dimension of the pixels of the fast camera (20x20μm), compared to those of the slow camera (6.5x6.5μm).
- Light pulses of longer duration (of the order of $120ns$ for the fast system, against $10ns$ for the conventional system).

It is therefore mainly on the brightness and dynamic aspects of the sensor that the TR-PIV is less efficient than the classic r-PIV.

3.6.1.1 Emitting optics characteristics

The light sheet is generated by a dual cavity pulsed laser that belongs to the LMFA (Continuum MesaPIV) emitting at a wavelength of $532nm$ (Fig. 3.14(a)). An articulated arm is fixed at the laser output allowing the laser beam to be routed to the optics that generate the light plan (Fig. 3.14(c)). The focal length of the cylindrical lens at the optical output is -50mm.

3.6.1.2 TR-PIV seeding

The same fluorescent particles used for r-PIV measurements are used for the TR-PIV (mean diameter of 35μm), with re-emission at λ= 584nm for excitation at λ= 532nm (details in Section 3.2.3).

3.6.1.3 Receiving optics characteristics

The pair of images are recorded using a fast camera belonging to the LMFA: Photron FastCam 64 Go (Fig. 3.14(b)). The objective is a Lensbaby Velvet of 85mm of focal length, and an aperture number of 1.8.

3.6.1.4 Synchronization of the acquisition

A synchronization unit of the LMFA allows synchronizing the passage of the vehicle on the PMMA window with the triggering of the laser and the fast camera, using the Davis10.1 software marketed by the LaVision company. A dedicated computer has also been used, interfaced with the camera by Ethernet cable. As the camera is only interfaced with version 10 of the commercial software DaVis from LaVision, and versions 10 and 8

(a) Fast laser

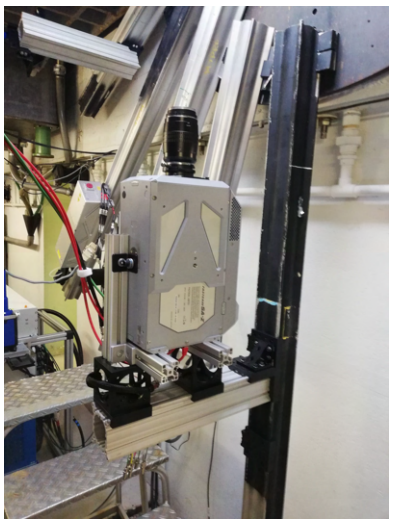

(b) Fast camera

(c) Articulated arm output

Figure 3.14 – Photos of the fast laser (upper left), the fast camera (upper right), and the optics in the output of the articulated arm (bottom)

(the one used by Michelin) not being backward compatible, the LMFA provided during the analysis with a dongle that allowed using version 10.1. When the on-track sensor detects the vehicle, the PTU generates a trigger signal that initiates the recording when the arrives at the PMMA window. A pre-determined number of images is given to record the full passage of the tire on the window. In the end, only a limited number of images are processed for which the illumination is high enough for the cross-correlation operation.

3.6.2 Experimental installation

The same dedicated track and the installation principle of the r-PIV are used when working with the TR-PIV (Fig. 3.2). The tests are conducted in the same way as the r-PIV; namely the car rolling over the window on a fixed water height at a specific speed, triggering the laser and the camera and the recording of the images. The main challenge of the new installation was to find the best solutions to adapt the light path with the new laser and the camera positioning. As stated before, the installation has greatly benefited from the rapid settlement of the equipment. Let us recall that the preliminary tests at the LMFA allowed to:

— Establish in the laboratory, on a static assembly using a MICHELIN Primacy 4 tire, the possibility of illuminating at a rate of about 1 kHz by refraction with a fast laser the water-bank in front of the contact area, and even potentially inside the longitudinal grooves. The tests were carried out in September 2020 with the same fluorescent particles as those used in Ladoux, and the set-up that was implemented in Cabut's work [12].

— Identify the future location of the rapid laser and its power supply (much larger than the low-rate laser currently used at Ladoux on the test track).

— Design in the LMFA, for on-site implementation, a mechanical interface for positioning and fastening the fast camera, compatible with the fastening systems available at Ladoux.

— Carry out preliminary tests at the LMFA to simulate the trigger generation device for the synchronization of the rapid laser/camera assembly with the simulated passage of the vehicle and to prepare various synchronization solutions that can be used for the track tests.

3.7 Conclusion

In this chapter, we have presented the r-PIV, a dedicated measurement technique for the hydroplaning application. The test facilities and the measurement installation have been detailed along with the specific difficulties of this method in particular the thickness of the laser sheet and the laser propagation inside the water film that is very different from the P-PIV. Moreover, the nature of the measurement procedure imposes a definition of a common referential between the images recorded, therefore different overlaying strategies

have been proposed and compared for different tire treads. This allowed us to choose the most suitable strategy and obtain the best overlaying depending on not only the tread geometry but also the image intensity levels. Finally, the TR-PIV has been introduced as a new measurement method, to our best knowledge never used before in the hydroplaning framework, and a powerful tool to obtain a time-resolved water circulation. In the following chapter, we start the analyses of what may seem like the simplest tread geometry, the slick tires with a smooth tread. Both the numerical and experimental tools presented in the two previous chapters are used to locally investigate the water-bank region.

Chapter 4

Slick tires

This chapter is dedicated to the study of what can be considered the simplest model of tires in terms of geometry, tires with a smooth tread (i.e., having no tread pattern). They are known as slick tires and are generally used for racing only since they are quite dangerous if the road surface is wet (Fig.4.1). To our knowledge, this is the first time that the r-PIV is used to study such tires. The same installation is used as detailed in Chapter 3. For the slick tires, we focus on the flow circulation mainly in front of the tire and also in the shoulder region since there is no water flow in the CPA. However, we keep in mind that the CPA region is an important parameter when studying the hydroplaning phenomenon, but the r-PIV as we are using it determines the flow behavior and not the footprint area. Other experimental methods are used within Michelin to determine the surface of the CPA and its evolution with the vehicle velocity for example or the water depth [50]. In the slick tire case, the flow can only be pushed to the front or to the shoulders and the focus will therefore be only on the water-bank (WB) region.

Figure 4.1 – Example of a racing Slick tire: MICHELIN 31/71-18 Pilot Sport GT S9M RFID.

It is legitimate to wonder about the relevance of studying this type of tire tread since the present work aims to propose conception rules for the tread design to reduce the occurrence of the hydroplaning phenomenon. Actually, the slick tire offers the possibility of an in-depth analysis of the WB and this region is extremely involved during the hydroplaning since the pressure in the WB is at its highest and therefore the main part of the fluid lift is concentrated there [39]. Moreover, parametric studies can be conducted like the effect of the tire dimension or the water height, without introducing the tread design factor. Throughout this chapter, we present some details about the post-processing phase and the main optical challenges concerning this specific tire. Then we study the flow structure of the WB for a single run before looking at multiple runs highlighting the flow variability that exists. Furthermore, we seek more information about the WB structure by writing mass budgets in front of the tire and varying some parameters such as the water depth and the tire width. Moreover, comparisons with numerical results from SPH-FE simulations are discussed. Finally, we introduce the Time-Resolved r-PIV (TR-PIV introduced in Chapter 3) as a new promising experimental tool to study the structure of the water flow in the hydroplaning application.

4.1 Context

In this chapter we will focus on the case of four slick tires: Slick205, Slick225, Slick275 and Slick315 with respective widths $205mm$, $225mm$, $275mm$ and $315mm$. The first two dimensions are standard for tourism cars, the two largest ones are more attributed to sports cars (e.g., Porsche Cayenne 27). The purpose of studying the effect of the tire's width is to analyze the different behavior of the flow when the tire is enlarged i.e., if there is a privileged direction to the flow drainage and if this flow deviation stays the same when the tire is wider. This can lead us to have more efficient tread conception rules when translating to a larger tire. The treaded tires studied in the following chapters have one of the two first dimensions. We give in Fig.4.2 the YZ view for the Slick225 and the Slick315 meshes that are used for the numerical computation. A parametric study by progressively reducing the water depth from $8mm$ to $1.5mm$ is conducted. By doing so, we want to better understand the effect of such a parameter in the hydroplaning situation and the appearance of different regimes depending on the value of H_w. We give a summary of the measurements' configuration for the Slick tires in Appendix A.

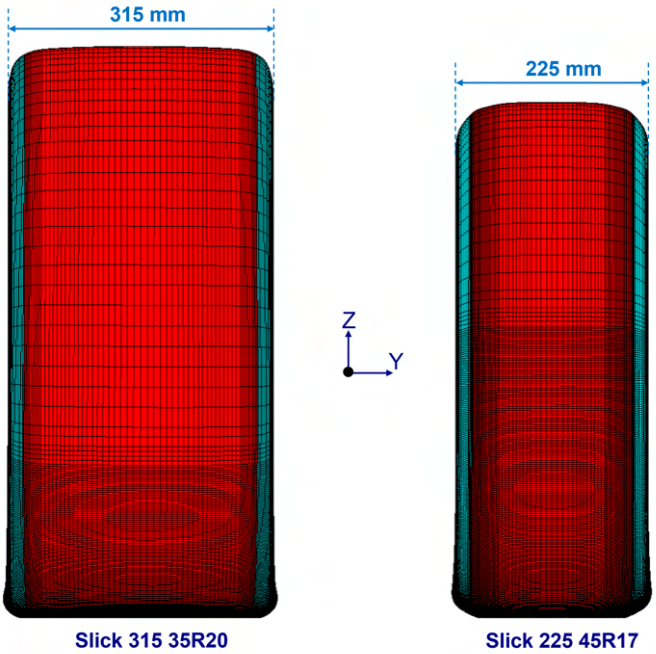

Figure 4.2 – 2D view in the YZ plane of the Slick315 (left) and the Slick225 (right) meshes after crashing on the ground. The smooth tread is represented in red. We highlight the tire section width.

4.2 Post-processing phase

The post-processing phase is very crucial since it directly influences the final velocity field on which our analysis and conclusions are based. The parameters we focus on are 1) the geometric masks applied to the recorded images before the correlation phase, and 2) the parameters of the PIV cross-correlation itself. We undertake this study because first, the slick tire has never been studied in the r-PIV framework, and second due to the difficulty in measuring inside the CPA/WB frontier. Indeed this region represents a singularity because of the low illumination. Therefore, varying the cross-parameters helps us determine if the results in this region very close to the tire are affected or not.

4.2.1 Influence of masks

We recall that a mask is a binary image used to hide some regions of the raw recorded image in order to avoid them when calculating the velocity field through the PIV cross-correlation algorithm (Chapter 3). This procedure increases the accuracy of the results near the mask border since we locally improve the signal-to-noise ratio allowing a better

spatial resolution as the interrogation windows are necessarily shifted with overlapping with the masked zone (noisy zone for PIV process). In the case of smooth tires, we apply a mask on the whole CPA region. However, the detection of the CPA borders is not a simple matter, since the frontier between the CPA and the WB is poorly contrasted and an iterative trial/error process between mask modification and velocity calculation is needed. Therefore, automatic detection of this CPA/WB is difficult to apply and the algorithm presented in Section 3.5.1 to automatically generate the masks based on image processing is not used in the case of Slick tires.

We give in Fig.4.3 an example for the Slick225 where three manually created masks were tested with different CPA/WB frontiers. The masks are designated by Mask01, Mask02, and Mask03. The purpose is to demonstrate a case where the mask is too close to the CPA (Mask01), a case where the mask erases a part of the WB (Mask03), and a rather satisfying mask (Mask02) that hides fully and only the CPA. We give in Fig.4.4 the velocity magnitude $|\vec{V}|$ obtained with the three masks along with the case where no mask is applied. We can see how the CPA is very noisy in Fig.4.4(a) as it is supposed to be a dry area and the velocity is exactly zero there. It is the region we want to hide when applying the geometric masks. To compare the velocity field obtained with the different Masks, we choose to look at the velocity profile Y-averaged in a horizontal band. This facilitates the comparison and the quantification of the difference between the profiles generated with the three masks. To avoid any asymmetry that may exist between the upper and lower shoulder of the tire, we focus on the center region where the component V_x is the highest. Therefore, we compare the velocity profiles focusing on the frontier region highlighted with the blue rectangle in Fig.4.3(a).

We give in Fig. 4.5 the results obtained, in (a) we represent the velocity profiles along X axis and Y-averaged between $Y = 140mm$ and $Y = 195mm$ (horizontal blue lines in Fig.4.3(a)), and in (b) we zoom between $X = 165mm$ and $X = 215mm$ (vertical blue lines in Fig.4.3(a)) at the CPA/WB frontier where the comparison is the most pertinent. We want to highlight in this example the difficulty of accurately defining the region to mask. Therefore, for the present case, we plot the grey-level image intensity profile in red along with the velocity profiles Y-averaged in the same area. The frontier CPA/WB corresponds to the detachment between the tire and the ground and thus an increase in the grey-level image intensity corresponding to the transition zone from the CPA to the WB. The grey levels around 370 counts correspond to the background and are inherent to the CPA zone. According to Fig.4.5(b), we can see that it is around $X = 180mm$ that

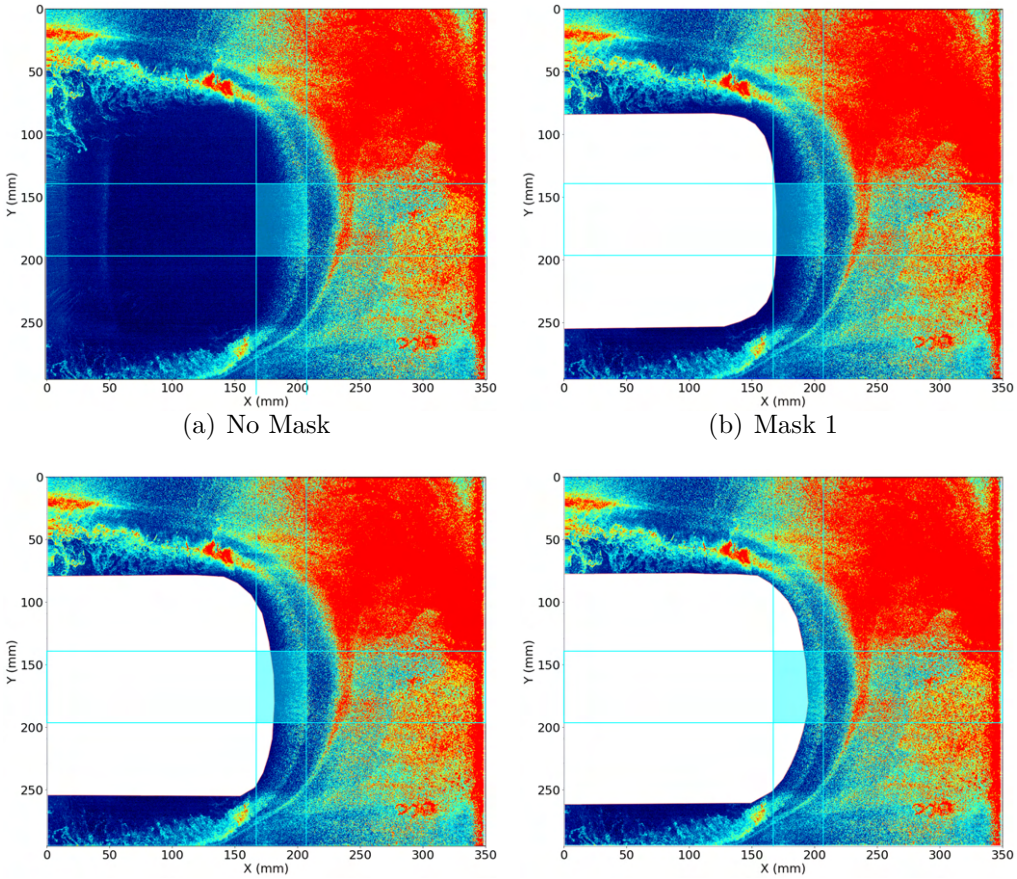

(a) No Mask (b) Mask 1

(c) Mask 2 (d) Mask 3

Figure 4.3 – Raw intensity images (Frame 0) for the Slick225 at $V_0 = 8.33m.s^{-1}$ and $H_w = 8mm$, (a) without applying a mask, (b) after applying Mask01, (c) after applying Mask02 and (d) after applying Mask03.

we see that increase and where the mask should end. However, let's not forget that this reasoning is made in a section between $Y = 140mm$ and $Y = 195mm$, and to be perfectly rigorous and to generate a strict CPA/WB border, the same operation should be done all over the Y axis in even smaller sections. In the example presented in Fig.4.5, Mask02 is chosen since its border corresponds roughly to $X = 180mm$ (increase in the intensity levels profile). Indeed, Mask03 cuts some of the WB region and Mask01 is inside the CPA leading to a velocity profile with some errors near the CPA/WB frontier.

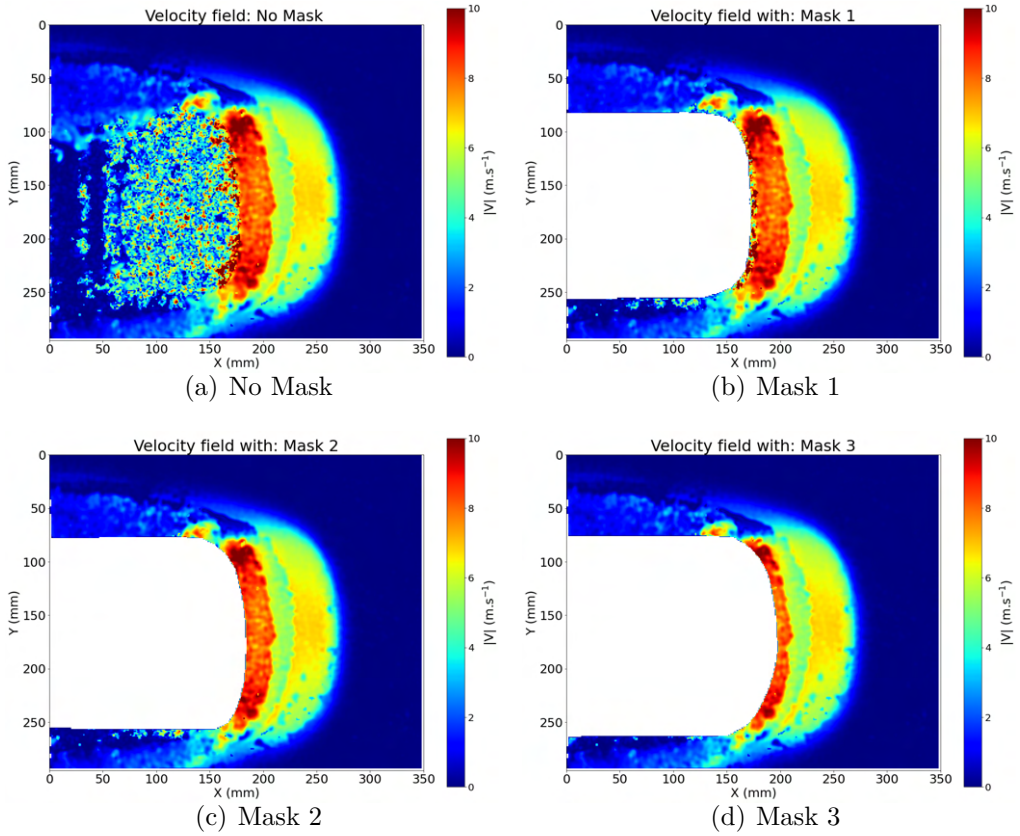

(a) No Mask (b) Mask 1

(c) Mask 2 (d) Mask 3

Figure 4.4 – Velocity field $|\vec{V}|$ for the Slick225 at $V_0 = 8.33m.s^{-1}$ and $H_w = 8mm$, (a) without applying a mask, and respectively after applying Mask01 (b), Mask02 (c) and Mask03 (d). The cross-correlation parameters used are of the REF case in Table 4.1.

4.2.2 Influence of cross-correlation parameters

The cross-correlation between a pair of images is performed with an iterative process using interrogation areas of decreasing size. Among the cross-correlation parameters we find:

— Interrogation window (IW) size: We give in Fig4.6 a representation of some interrogation windows against the size of the image. The initial size chosen is dictated by the maximum displacement of seeding particles. The final size with its overlapping factor results in a compromise between signal-to-noise ratio and spatial resolution.

— Overlap value between adjacent interrogation windows.

— Weighting functions: The window weight function is an additional weighting in the convolution of the data to avoid boundary effects at the beginning/end of the data.

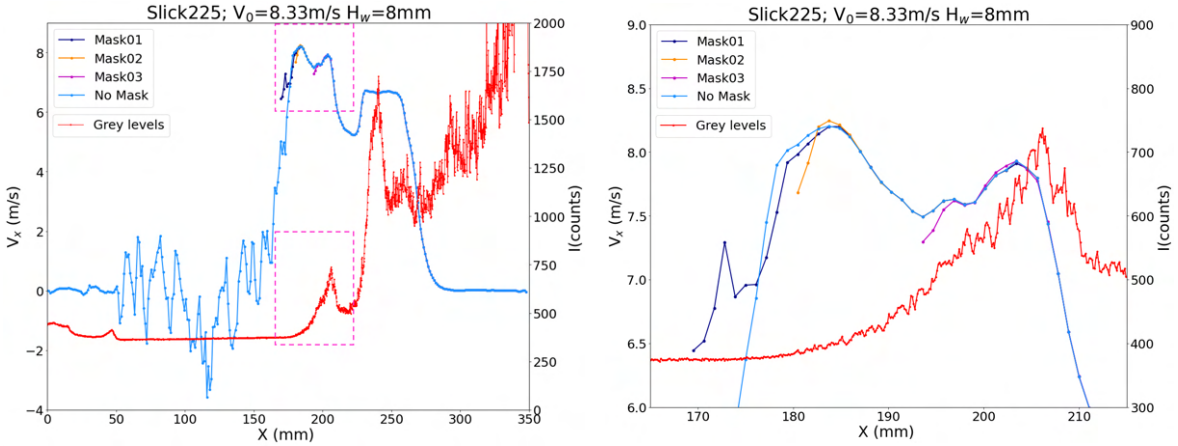

Figure 4.5 – Grey-level image intensity and velocity profiles Y-averaged in the area of interest (delimited by the two blue horizontal lines in Fig.4.3 (a)) of the configurations with masks and the one without a mask. The same profiles are represented in (b) but zoomed in the area outlined with the pink dotted rectangles in (a) (corresponding to the Y-averaged velocity inside the blue rectangle in Fig.4.3 (a)).

We give in Fig.4.7(b) the velocity profile Y-averaged between $Y = 140mm$ and $Y = 195mm$ (pink horizontal lines in Fig4.7(a)) for different configurations of cross-correlation. The reference case is done with an initial IW size of 96x96 pixels with 50% of overlapping and for the final passes 32x32 pixels with 75% of overlapping. A circular weighting is applied in both passes. The cases studied are summarized in Table 4.1. The cells corresponding to the changed parameters from the reference case are highlighted.

Table 4.1 – Sum up of the different configurations to test cross-correlation parameters

Case name	**IW initial passes**	**IW final passes**	**Overlapping**	**Weight function**
REF	96x96 pixels	32x32 pixels	50% - 75%	circular
64x64, 32x32	64x64 pixels	32x32 pixels	50% - 75%	circular
96x96, 24x24	96x96 pixels	24x24 pixels	50% - 75%	circular
96x96, 48x48	96x96 pixels	48x48 pixels	50% - 75%	circular
128x128, 32x32	128x128 pixels	32x32 pixels	50% - 75%	circular
Overlap 25-50	96x96 pixels	32x32 pixels	25% - 50%	circular
SquareWeight	96x96 pixels	32x32 pixels	50% - 75%	square

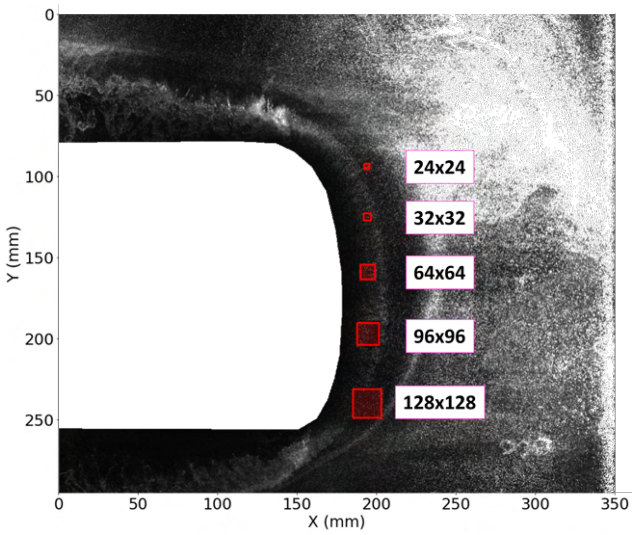

Figure 4.6 – Schematic representation of interrogation window sizes (in pixels) on the Slick225 at $V_0 = 8.33m.s^{-1}$ and $H_w = 8mm$

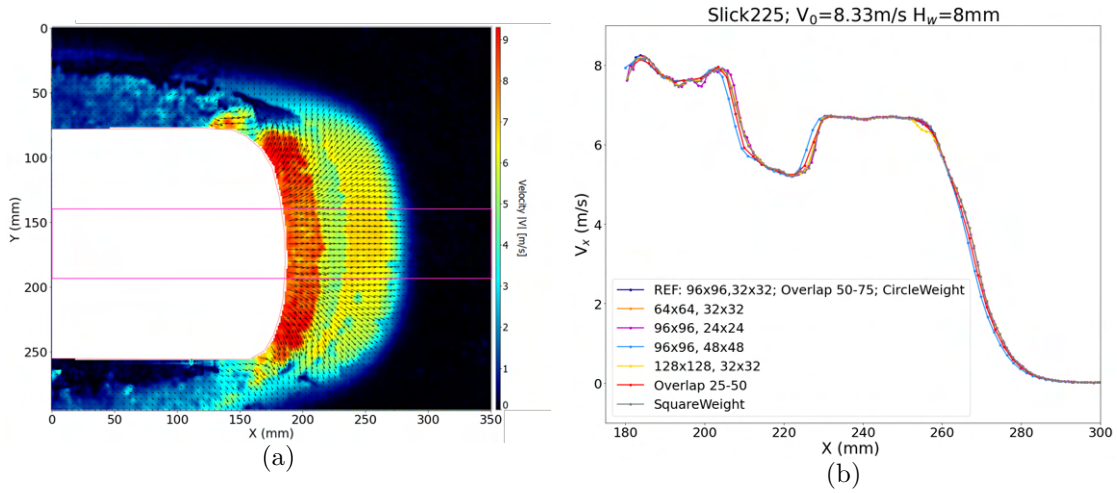

(a) (b)

Figure 4.7 – $|\vec{V}|$ field of the Slick225 $V_0 = 8.33m.s^{-1}$ and $H_w = 8mm$ (a) and the Y-averaged velocity profile V_x for the different configurations studied

We can see in Fig.4.7(b) that the velocity profiles are rather similar to the reference case which gives us more confidence in the choice we made according to the cross-correlation parameters and the quality of both the image acquisition and the cross-correlation operation. However, there is a region of singularity near the tire where measurements are difficult there because of the very low particle seeding concentration and illumination. Moreover, the results presented are focused on the center region of the WB, the same

analysis near the shoulders should be conducted which should be done in future investigations.

Beyond the influence of both mask position and interrogation area size, the effect of i) pre-processing of raw images ii) measurement uncertainties due to the peak detection in the inter-correlation function iii) and the size distribution of particle's image should be investigated, and quantified in the future. This has not been done in the present thesis due to a lack of time.

4.3 Flow structure and variability in the experimental results

In this section, we focus on the study of the flow structure in the WB region. We analyze, as an example of the process done for every rolling, a single run at a fixed vehicle velocity V_0 and water height H_w. Then we study the variability observed in the velocity profiles when processing N runs. Finally, a parametric study to analyze the effect of H_w is conducted. This analysis is driven by the very different velocity profiles observed for respectively a low (around $2mm$) and a high value of H_w (around $8mm$). The aim is to know if different flow regimes exist depending on the value of the water depth, and if so, how is the flow 3D macro-structure affected in the WB region.

4.3.1 Analysis of a single run at a given (H_w, V_0)

In this section, we analyze the velocity field of a single run for the Slick225 (Run33). The objective here is to have a qualitative overview of the WB structure in the case of a smooth tread. We choose the case with $H_w = 8mm$ and $V_0 = 8.33m.s^{-1}$.

4.3.1.1 Principal flow circulation in the (XY) plane

We give in Fig.4.8 a cartography of the velocity magnitude $|\vec{V}|$ in both a fixed referential (4.8(a)), and in a referential linked to the vehicle moving at V_0 (4.8(b)). First, we can observe that the flow just at the exit of the CPA ($180mm < X < 210mm$) has a higher velocity than the vehicle. We also observe in Fig.4.8(b) a rather high velocity in the shoulders area ($50mm < Y < 100mm$ and $230mm < Y < 280mm$) that is attributed

to a spanwise evacuation as we can see in Fig.4.9 where the V_y component of the velocity is high in this region (around V_0).
Moreover, if we look at Fig4.8(b) starting from the right where the flow is moving at V_0 and the tire is at rest, we first notice a region where the flow is decelerated ($230mm < X < 270mm$), then a second region where the flow is accelerated ($210mm < X < 230mm$) and finally a third region where it is slowed down again until reaching zero at the CPA border. In the reference frame moving with the car, the 2D map of the velocity magnitude shows that the flow is globally significantly decelerated in front of the central part of the tire, while it is accelerated around the shoulders. These results are qualitatively in accordance with the known fact that the main pressure increases in the middle part of the WB, and low pressures appear around the shoulders, a general feature of flows around bluff bodies like, e.g., an ellipse ([125]).

Moreover, we can look at the evolution of the different components of the velocity Y-averaged in the WB in 5 subregions designated by DY1 to DY5 as depicted in Fig.4.10(a). The subregions have an equal width of $35mm$ (arbitrarily chosen to limit the number of such regions) and have been chosen uneven to have a central zone, in this case, DY3. This subregion decomposition of the WB allows us not only to study synthetically the repartition of the V_x and V_y from the center to the shoulders, but also to have an idea about the symmetry of the profiles against the Y-axis (DY1 against DY5 and DY2 against DY4). We note that we choose to plot the absolute transverse velocity component $|V_y|$ to facilitate the comparison between the subregions, but we emphasize that in DY4 and DY5, $V_y < 0$. Before commenting on the symmetry of the profiles, we draw the reader's attention to the fact that in reality there is always a camber angle between the vertical axis of the wheel and the vertical axis of the vehicle (Z-axis). For regular modern cars, a small camber angle is usually desired (0.5–1°) to ensure a good balance and cornering grip, braking grip, and delay tire wear. The Slick225 is mounted on this type of vehicle. Due to the camber angle, the CPA is not perfectly symmetric against the Y-axis and this can partly lead to the slight asymmetries that we can observe between DY1 and DY5, and between DY2 and DY4 in V_x and V_y profiles (Figures 4.10(c) and 4.10(d)). Moreover, if we look at Fig.4.10(c), we can see that it is in the center region DY3 that the streamwise flow is the highest and we can also observe that the decrease in the V_x profile between $X = 210mm$ and $X = 230mm$ is also observed closer to the shoulders in (DY2, DY4) and also in (DY1, DY5). It should be noted that the decrease in V_x is not homogeneous along the Y-axis and is more significant from DY2 to DY1 (or DY4 to DY5) than from DY3

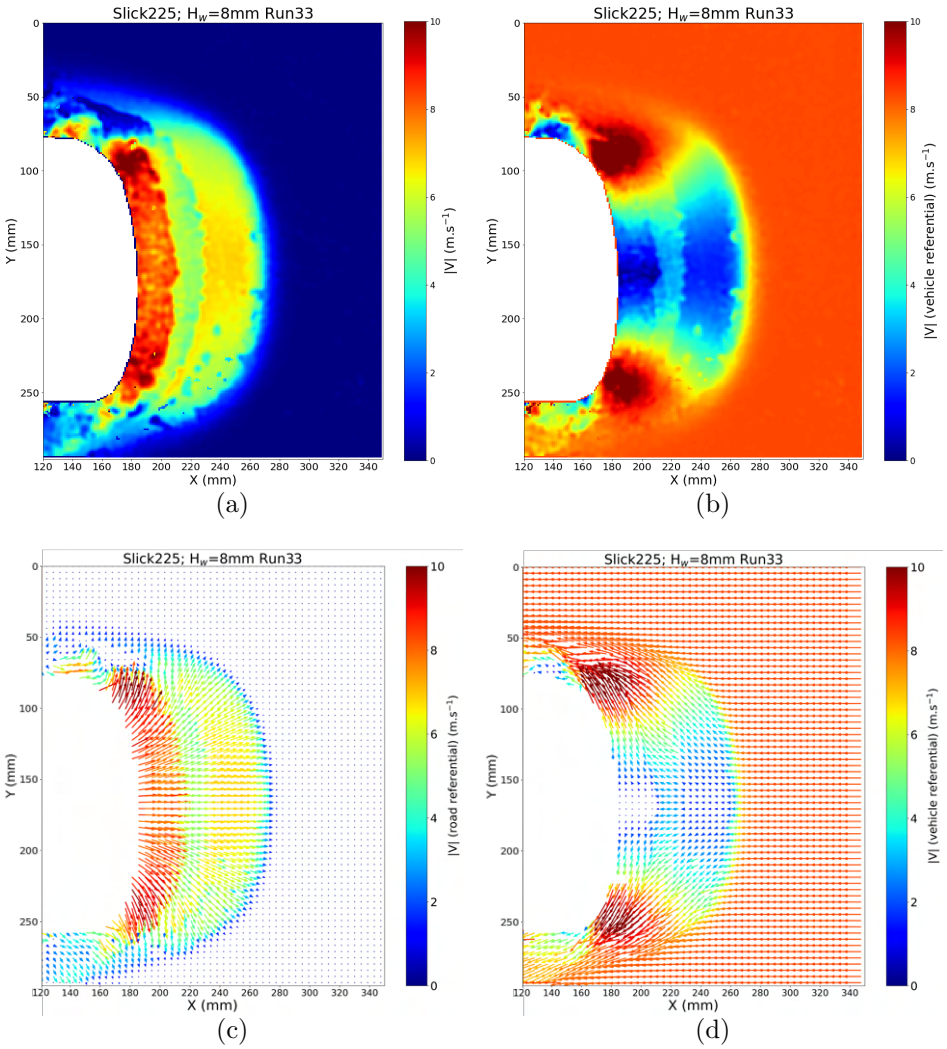

Figure 4.8 – Colormaps of the velocity field $|\vec{V}|$ for the Slick225 case in the road referential (a) and the vehicle referential (b). The same fields are represented with arrows illustrating the velocity direction (c and d). For clarity reasons, only one arrow over 4 is represented.

to DY2 (or DY3 to DY4). We can also see that unlike in DY2 and DY3, in DY1 the V_x profile reaches its maximum near $X = 240mm$ and not in the area just in contact with the tire.

As for the evolution of the flow in the transverse direction (Fig.4.10(d)), it is clear that its highest value is reached in the shoulders area (DY1, DY5) and we can also notice a rather linear decrease. However, we do not observe a region where $|V_y|$ rapidly drops as seen in the V_x profile near $X = 210mm$. Although we see a very slight change in the slope of V_y in (DY2, DY4) and also in (DY1, DY5) near $X = 210mm$, it is not as significant as

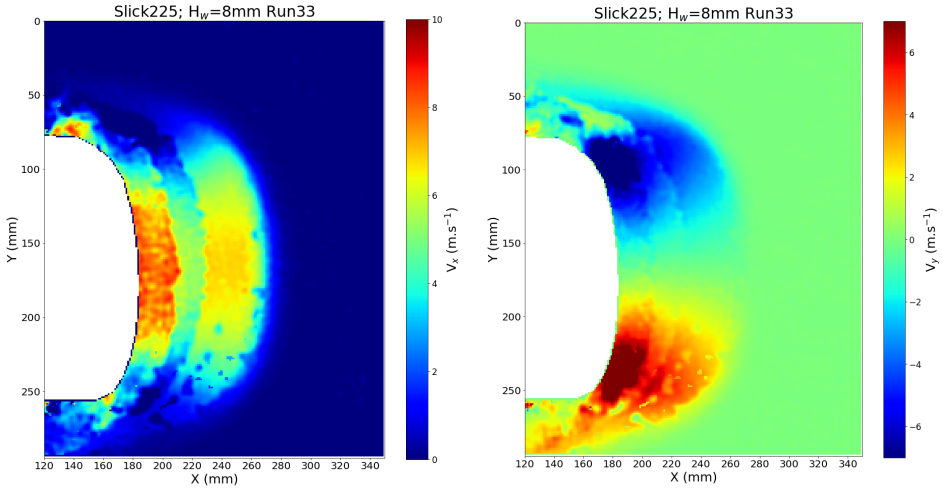

Figure 4.9 – Cartographies of V_x (a) and V_y (b) for the Slick225: Run33

for the V_x component.
Furthermore, we give in Fig.4.11 the V_y profiles X-averaged in the subregions designated respectively from Dx1 to Dx8 from the closest area of the WB to the furthest (Fig.4.11(a)). We can see that the $V_y(y)$ profiles are linear and this linearity is preserved when the subregion gets further from the tire.

Last but not least, the streamlines corresponding to this flow circulation in the moving referential of the vehicle are generated (Fig.4.12). If we assume that in this referential the flow is steady, then these streamlines coincide with the trajectory of the fluid particles. Therefore, the analysis of the streamlines' pattern provides a qualitative global overview of the evolution of the incoming fluid approaching the tire. The origins of the streamlines are chosen at $X = 345mm$ where the puddle has a velocity of $-V_0$, and are taken evenly-spaced along the Y-axis with a $2mm$ step for clarity reasons. We can notice how the streamlines are converged near the shoulders meaning that the flow is accelerated, whereas they are expanded in the center where the flow is therefore decelerated. This joins what we have already said about the increasing pressure in the center of the WB against a decreasing pressure in the shoulders. We can also see that there is a region where the streamlines do not cross near the frontier between the CPA and the WB. However, $|\vec{V}|$ (in the vehicle referential) is not equal to zero in this region, questioning the hypothesis that the flow is homogeneous along the vertical axis. The following section intends to clarify this observation.

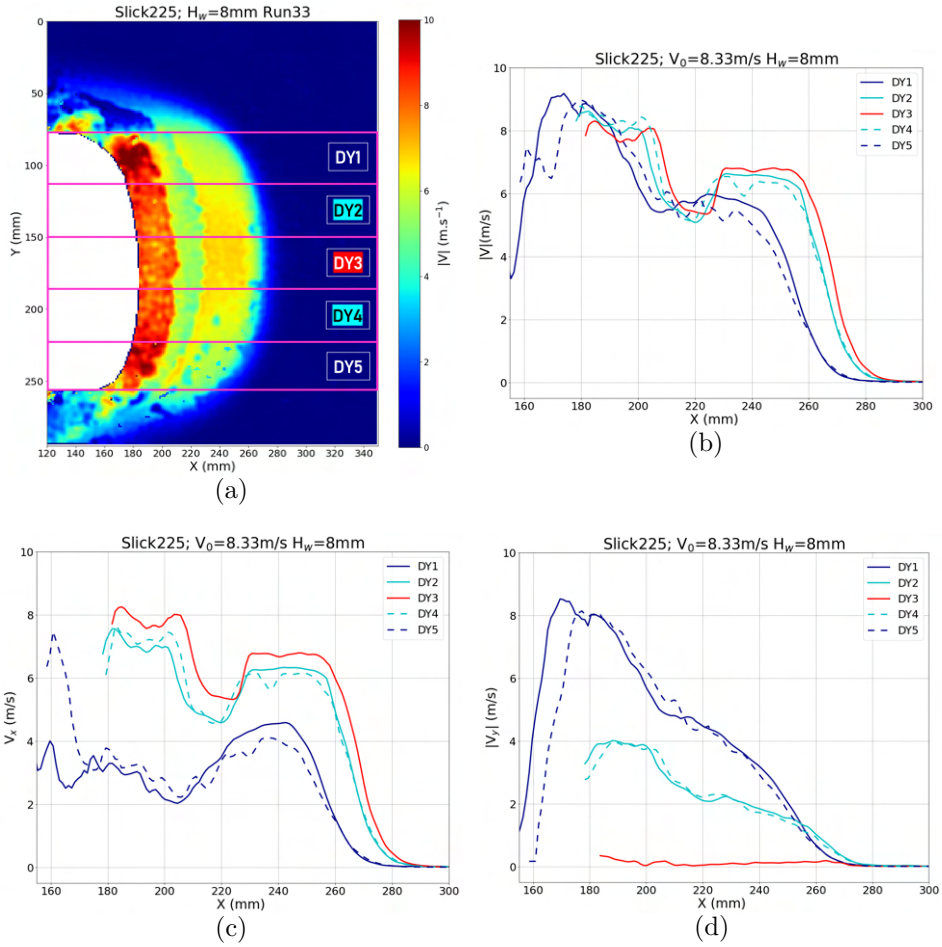

Figure 4.10 – WB division in the spanwise direction (top left) and velocity profiles evolution Y-averaged in these 5 subregions: $|\vec{V}|$ (top right), V_x (bottom left) and $|V_y|$ (bottom right)

4.3.1.2 Secondary flow circulation

To further investigate the flow circulation in the WB and have more information about the 3D effects that can exist, we look at the 2D velocity divergence. Indeed, since the flow is considered incompressible, we have:

$$div_{3D}(\vec{V}) = 0 \tag{4.1}$$

$$\underbrace{\frac{\partial V_x}{\partial x} + \frac{\partial V_y}{\partial y}} + \frac{\partial V_z}{\partial z} = 0 \tag{4.2}$$

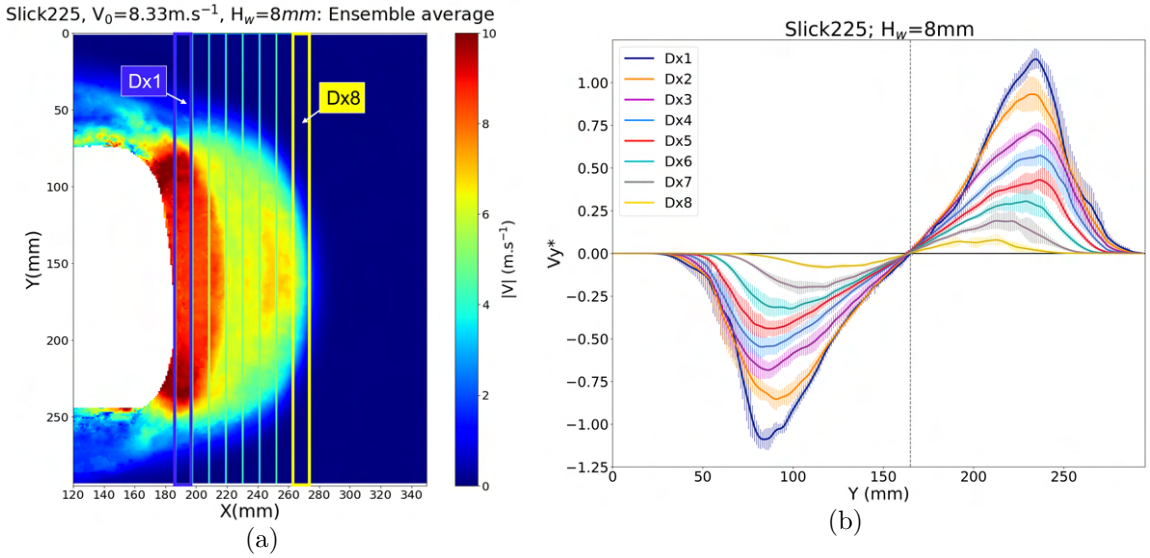

Figure 4.11 – WB division in the longitudinal direction (a) and velocity component V_y profiles evolution X-averaged in these 8 subregions. The envelopes represent the standard deviation between the N=8 runs.

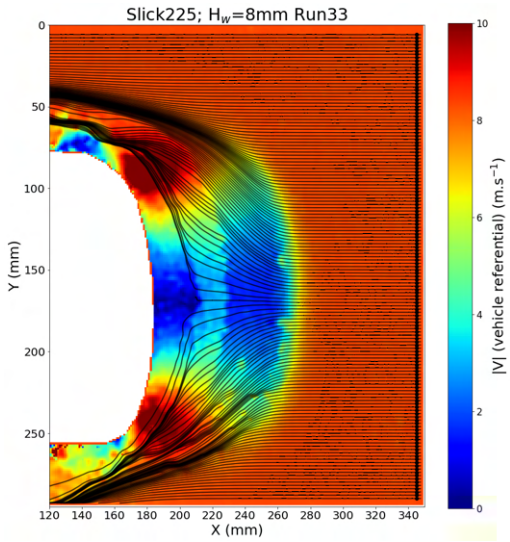

Figure 4.12 – Streamlines generation for the Slick225 along with the $|\vec{V}|$ field.

$$div_{2D}(\vec{V}) = -\frac{\partial V_z}{\partial z} \tag{4.3}$$

Therefore, by looking at $div_{2D}(\vec{V})$ we can have an idea of the flow circulating outside the (XY) plane in the Z direction. We give in Fig.4.13(a) the $div_{2D}(\vec{V})$ cartography.

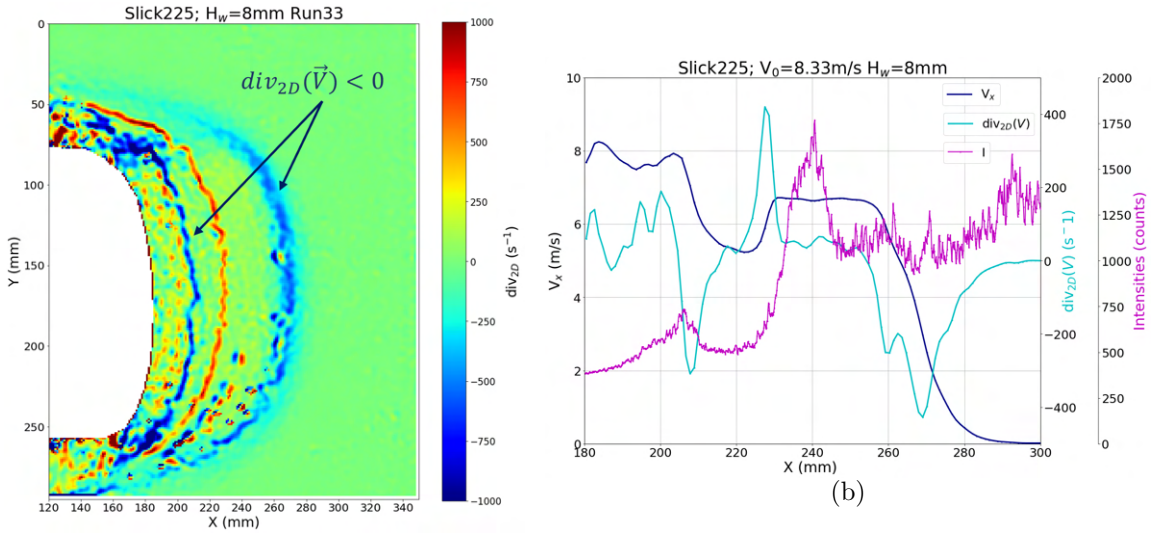

Figure 4.13 – Cartography of the 2D divergence of the velocity ($div_{2D}(\vec{V})$) (left) and the V_x, $div_{2D}(\vec{V})$ and intensity profiles Y-averaged between $Y = 140mm$ and $Y = 195mm$ (right): Run33

We can observe that the three regions we have highlighted above when studying $|\vec{V}|$ in the tire referential (Fig.4.8(b)) are delimited by the 2 minimum of the $div_{2D}(\vec{V})$ map (designated by the two arrows in Fig.4.13(a)). We notice two negative peaks at $X = 270mm$ and $X = 210mm$ then a positive peak at $X = 235mm$. Considering that $\frac{\partial V_z}{\partial z} = -div_{2D}(\vec{V})$, then if $div_{2D}(\vec{V}) < 0$ then $\frac{\partial V_z}{\partial z} > 0$ and inversely. We expect that the negative peak around $X = 270mm$ corresponds to an elevation of the free surface since the flow at $X > 270mm$ is coming at $-V_0$ (tire referential) and is meeting the tire at rest. Then we enter the region where the flow is accelerated ($210mm < X < 230mm$) and the borders of this region correspond to the positive and negative peaks in $div_{2D}(\vec{V})$ (Fig.4.14). This suggests that some 3D effects could exist in this area.

The 2D nature of the r-PIV measurements does not give us the possibility to have direct measurement of the vertical flow, however, we are capable to capture the ascendant/descendant movements when we look at the $div_{2D}(\vec{V})$ cartography. One possible hypothesis could be the presence of a secondary flow induced by the strong adverse pressure gradient imposed on water approaching the contact patch area (in the moving frame). Such a secondary structure exists for flow developing over fixed walls and approaching a semi-immersed body (Launay [66]). Due to viscosity, a flow separation appears in front of the obstacle and is responsible for the existence of the so-called "horseshoe" vortex.

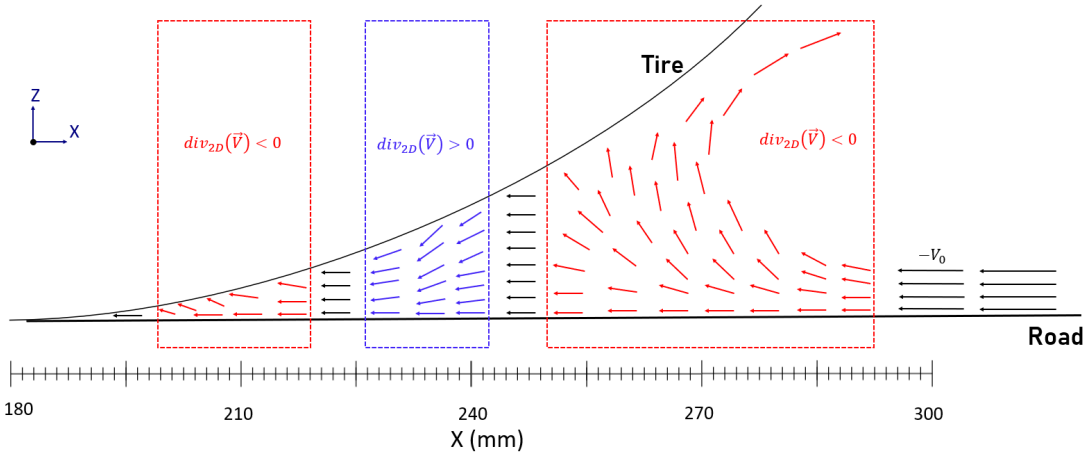

Figure 4.14 – Scheme in the XZ plane for the WB region near the median plane of the tire along the Y axis. We highlight the flow vertical circulation in the three regions corresponding to the change of sign in $div_{2D}(\vec{V})$. In red the regions where $div_{2D}(\vec{V}) < 0$ i.e. $\frac{dV_z}{dz} > 0$, and in blue the area where $\frac{dV_z}{dz} < 0$. The arrows are represented in the tire referential. This scheme represents an artistic rendering of the possible 3D flow extrapolated from the $div_{2D}(\vec{V})$. Positions of ascending and descending flows are approximate.

The main cause of the horseshoe vortex is the rotation in the incoming flow at the junction of a flat surface and a vertically placed bluff body (Fig.4.15). The presence of the body results in streamwise adverse pressure gradients causing a 3D separated flow region in front of the bluff body and multiple horseshoe vortices are formed. In addition, the spanwise pressure gradients cause the near-wall flow to move around the obstacle. The primary horseshoe vortex and the smaller secondary vortices are of opposite rotation to preserve the streamline topology (Simpson [114]). The geometry of the obstacle (ratio height to width, the bluntness of the nose) as well as the Reynolds number play a major role in the structure of juncture flows. We can see in Fig.4.16 an oil-flow visualization where multiple horseshoe vortices have been observed around a cylinder. Separation lines have been highlighted (at S and S_1) inducing a nodal point of attachment between them. This alternation between saddle points and nodal points indicates the presence of a series of vortices around the obstacle (Fig.4.16(b)). We can observe that on the image on the right in Fig.4.16(a), there is a clear similarity between the streamlines depicted and the streamlines that we have generated in Fig.4.12 with the presence of a saddle point S where the streamlines are deviated. Unfortunately, the region very close to the tire has a low illumination and the velocity field is rather noisy which makes it very difficult to generate streamlines to compare with the results of Baker [5] between S and A_e in Fig.4.16(a).

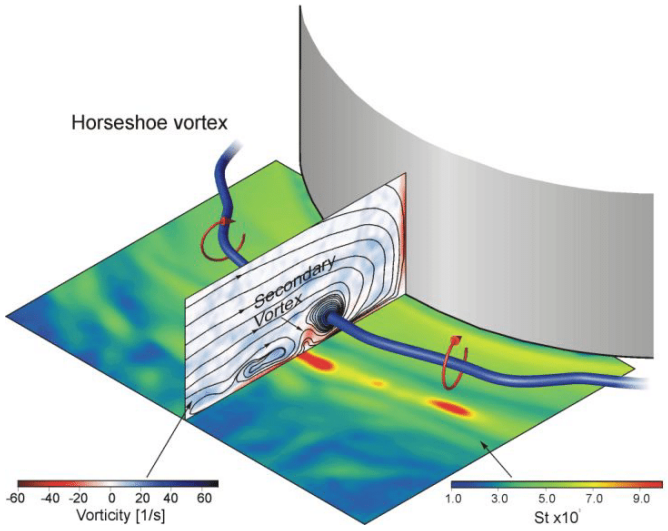

Figure 4.15 – Horseshoe vortex mechanism in front of a circular cylinder from Praisner et al. [105].

To proceed with the analysis, we give in Fig.4.13(b) the profiles of V_x, $div_{2D}(\vec{V})$ and the grey-level image intensity I of the raw image, Y-averaged between $Y = 140mm$ and $Y = 195mm$ (as in the previous section). We can observe that the grey-level image intensity profile is not homogeneous, with regions where the intensity is rather high (around $X = 240mm$) and other regions where the intensity is low (near the tire). The particles' distribution seems to be heterogeneous with a clustering near $X = 240mm$ and a region with lower particles' density near $X = 220mm$. This arrangement is likely to be induced by the 3D effects that exist in the WB.

Finally, we plot the streamlines along with the $div_{2D}(\vec{V})$ field in Fig.4.17. We can observe that close to the CPA/WB frontier, the streamlines deviate to the shoulders as they circumvent the CPA following the region when $div_{2D}(\vec{V}) < 0$. They are strongly deflected near the peak in $div_{2D}(\vec{V})$ close to $X = 210mm$.

However, the analogy between the horseshoe vortex described in the literature and the flow in front of the slick tire in the moving frame is not evident. In the first situation, the velocity V_x at the wall is zero due to viscosity, while in the present case the velocity at the wall is equal to $-V_0$ in the moving frame. The common features between both configurations are a flow evolving along a flat wall, the sign of the pressure gradient $\partial P/\partial x$, and the positive value of $\partial V_x/\partial z$.

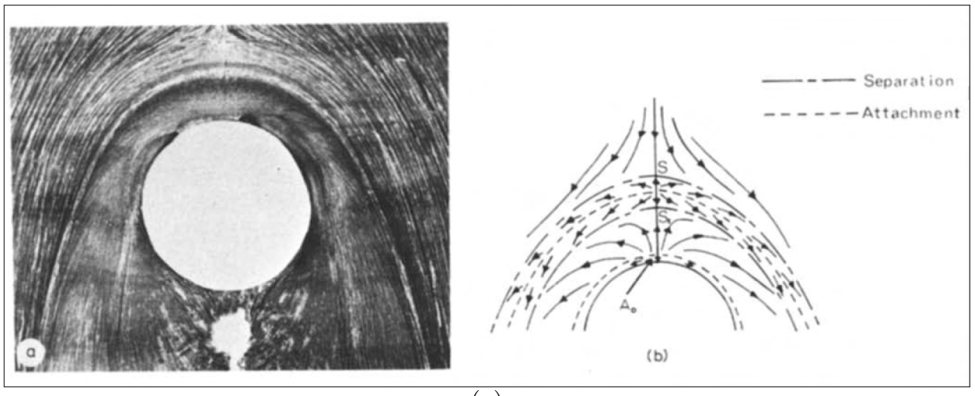

(a)

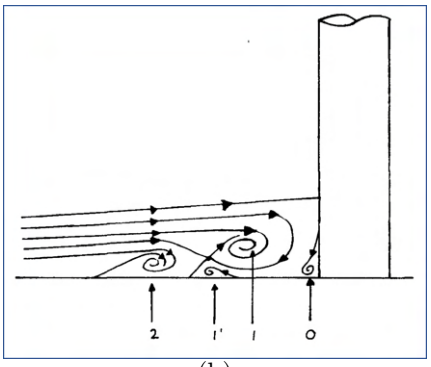

(b)

Figure 4.16 – Photograph of the flow pattern around a cylinder on a wind tunnel floor (a). The corresponding surface streamlines are sketched in (b). S and S_1 are respectively the saddle points of the primary and secondary separation. In (c) the flow pattern induced from (a) and (b) is given. Four vortices are highlighted (0,1,1' and 2). Images extracted from Baker [5]

4.3.2 Flow variability at a given (H_w, V_0)

In this section, we highlight the intrinsic variability that exists in the WB of a smooth tire for a given set (H_w, V_0) when considering N runs. We give in Fig.4.18 the standard deviation associated with the ensemble averaging over the $N = 8$ runs. We can observe that both STD(V_x) and STD(V_y) increase near the shoulders. This has also been observed in the case of a longitudinal tire (PCY4) by Cabut [10] and has been explained by the change in position of the C-type grooves from one run to another. In the case of a slick tire, one can hypothesize that the horseshoe vortices generate such variations between the different runs in particular when looking at STD(V_x) in front of the tire. We find it also increasing in the region where $div_{2D}(\vec{V}) < 0$.

We plot the velocity profiles Y-averaged in the center area as we did to generate

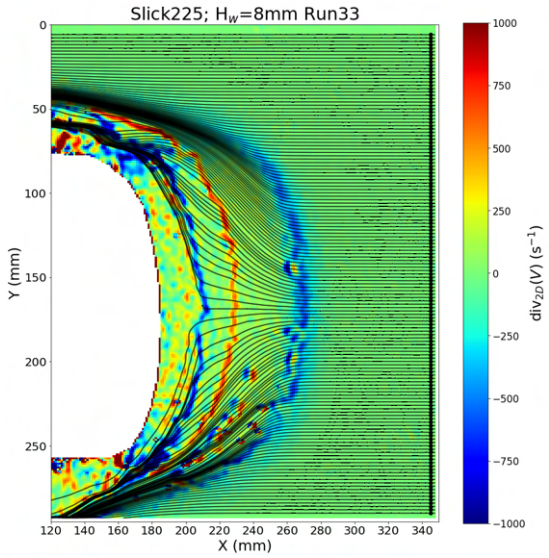

Figure 4.17 – Streamlines generation for the Slick225 along with the $div_{2D}(\vec{V})$ field.

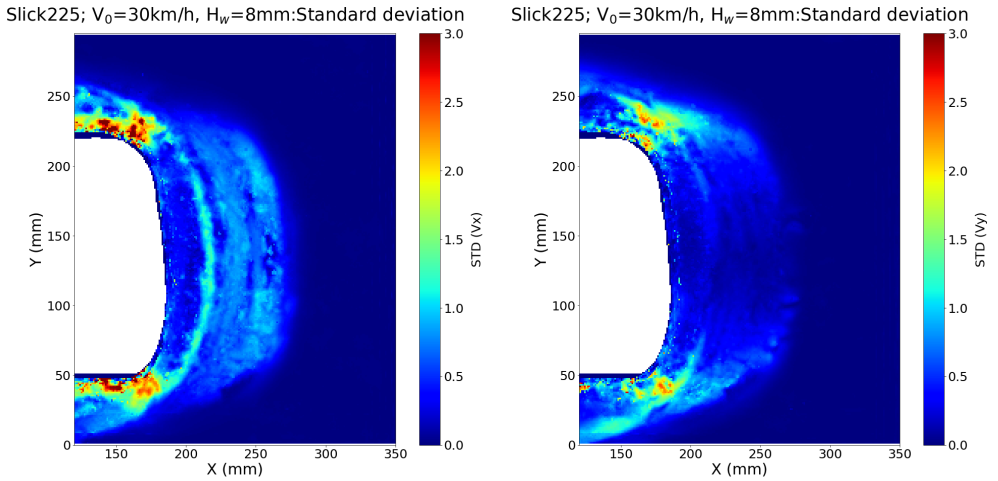

Figure 4.18 – Colormap of the standard variation STD(V_x) regarding the V_x component (a) and STD(V_y) regarding the V_y component (b). Colormaps are in ($m.s^{-1}$).

Fig.4.13(b). We present in Fig. 4.19 the results obtained for $N = 8$ runs in the case of the Slick225 at $V_0 = 8.33m.s^{-1}$ and $H_w = 8mm$.

We choose to plot the velocity profiles of all the 8 runs on purpose to highlight the discrepancies that exist in the WB between the different runs. We specify that for all images, a mask has been applied and the cross-correlation parameters are those from the reference (REF) case ones as depicted in Table 4.1. Moreover, based on the profile of

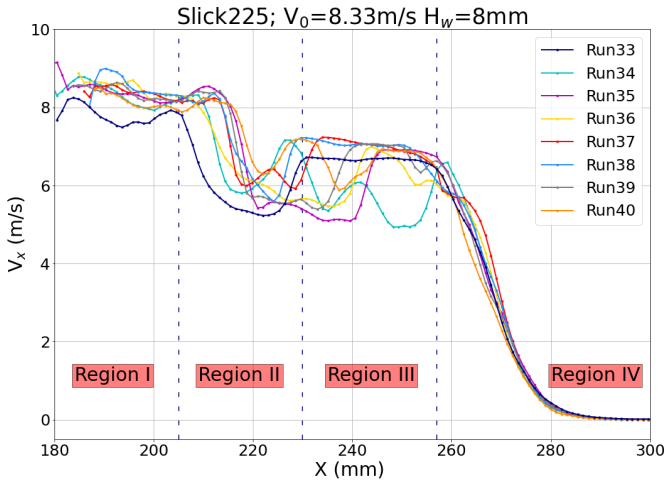

Figure 4.19 – Y-averaged velocity profiles V_x for $N = 8$ runs.

Run33, we can identify four regions a) Region I for which V_x is a rather constant value close to V_0, b) Region II for which V_x drops rapidly to near $0.6V_0$ then after a small plateau increases again, c) Region IV for which V_x is nearly uniform again at a value around $0.85V_0$, and finally d) Region IV where the V_x decreases until reaching zero. For clarity purposes, we only represent the four regions in the case of Run33, separated by dashed vertical lines in Fig.4.19. This four-region scheme is more or less the same for all the other runs, however, Regions II and III, in particular, present in some cases different behaviors, e.g., Run34 and Run40. We can also notice in Run35 a rather big plateau in its Region II but a small one in its Region III, which is quite the opposite with Run33. We give in Fig.4.20 the colormaps of $|\vec{V}|$ (in the vehicle referential) and $div_{2D}(\vec{V})$ for Run34 and Run35. We can see that Run35 and Run33 have rather similar colormaps, but for Run34 we can see a different behavior with more perturbations in both $|\vec{V}|$ and $div_{2D}(\vec{V})$.

4.4 Local analysis of the velocity field

Considering the disparities in the results between one run and the other, we want to analyze an ensemble averaged velocity field over $N = 8$ runs (among which Run33). The Velocities correlation detailed in section 3.5.2 is used here to overlay the images along the X-axis. Regarding the Y-axis, the Mask correlation is preferred (even if the masks themselves generated with this method are not used afterward).

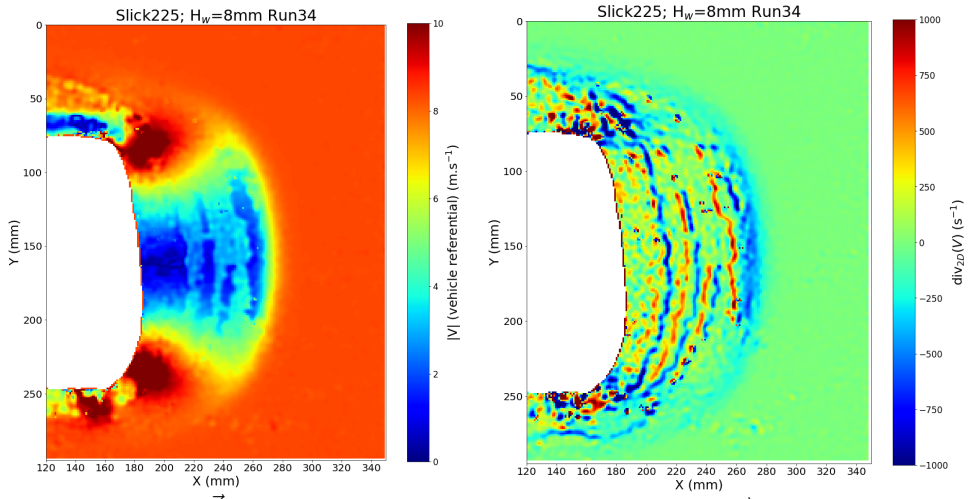

(a) $|\vec{V}|$; Run34

(b) $div_{2D}(\vec{V})$; Run34

(c) $|\vec{V}|$; Run35

(d) $div_{2D}(\vec{V})$; Run35

Figure 4.20 – Colormaps of $|\vec{V}|$ and $div_{2D}(\vec{V})$ in the vehicle referential for Run34 (respectively upper left and right) and Run35 (respectively bottom left and right).

4.4.1 Ensemble averaged velocity field

We give in Fig.4.21 the results of the ensemble averaging in the vehicle referential (moving referential at V_0). To study the evolution from the shoulder to the center as we have done in the case on a single run, we divide the WB into 5 regions of equal width as depicted in Fig.4.22(a). Results are given in Fig.4.22. By looking at the standard deviation envelopes, we can see that the fluctuations are not very important between all studied runs, however, it is the highest in region II.

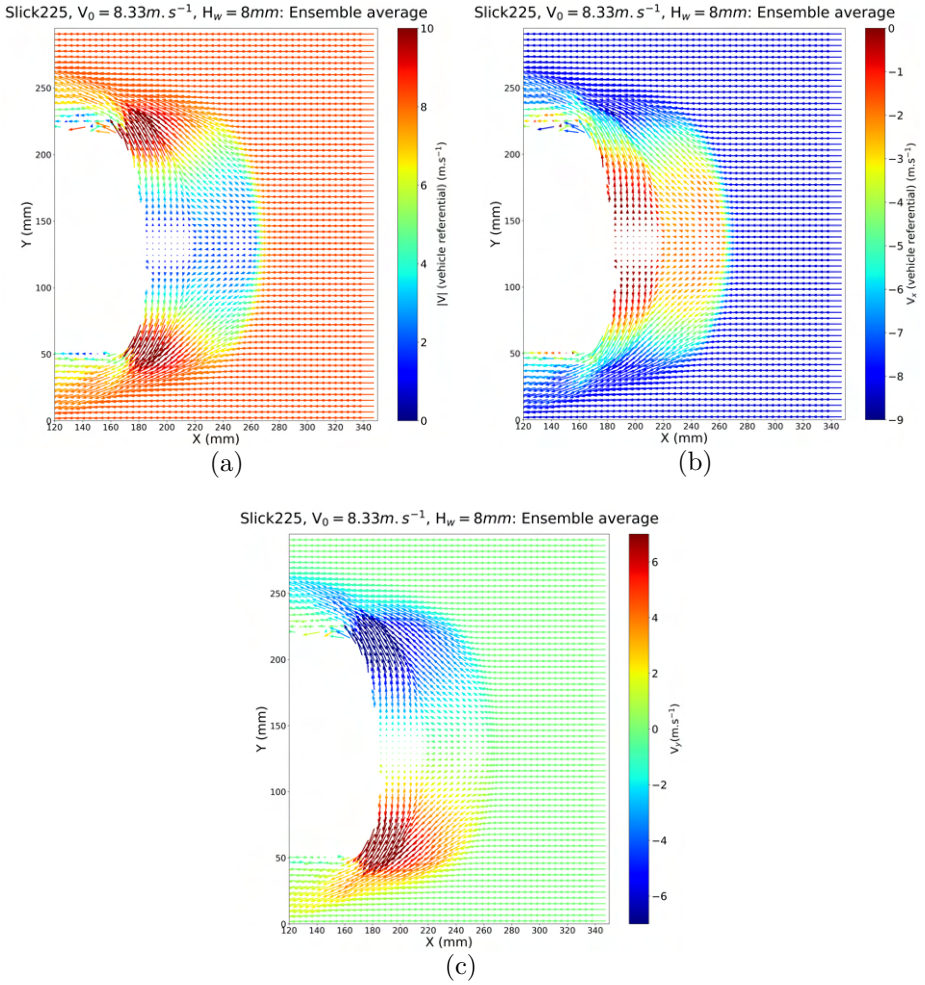

Figure 4.21 – Ensemble averaged velocity fields for the Slick225 at $V_0 = 8.33m.s^{-1}$, $H_w = 8mm$ and $N = 8$ runs. The Velocities correlation strategy is kept here for the overlapping operation along X-axis and the Mask correlation regarding the Y-offset. The fields are represented in the vehicle referential: (a) norm of $\vec{V}$, (b) V_x component and (c) V_y component.

4.4.2 Effect of the vehicle velocity V_0

We compare here the velocity profiles for different values of V_0. We focus on both the center region of the WB and the shoulder region. Results are presented in Fig.4.23. The definitions of DY3 and DY5 are the same as in Fig.4.22(a). First, we observe in Fig.4.23(a) that the three profiles are rather superimposed, highlighting self-similarity in the central region regarding the flow drainage when V_0 is increased. Second, we can see that the three curves present i) a region where V_x is constant, ii) a region where V_x decreases suddenly,

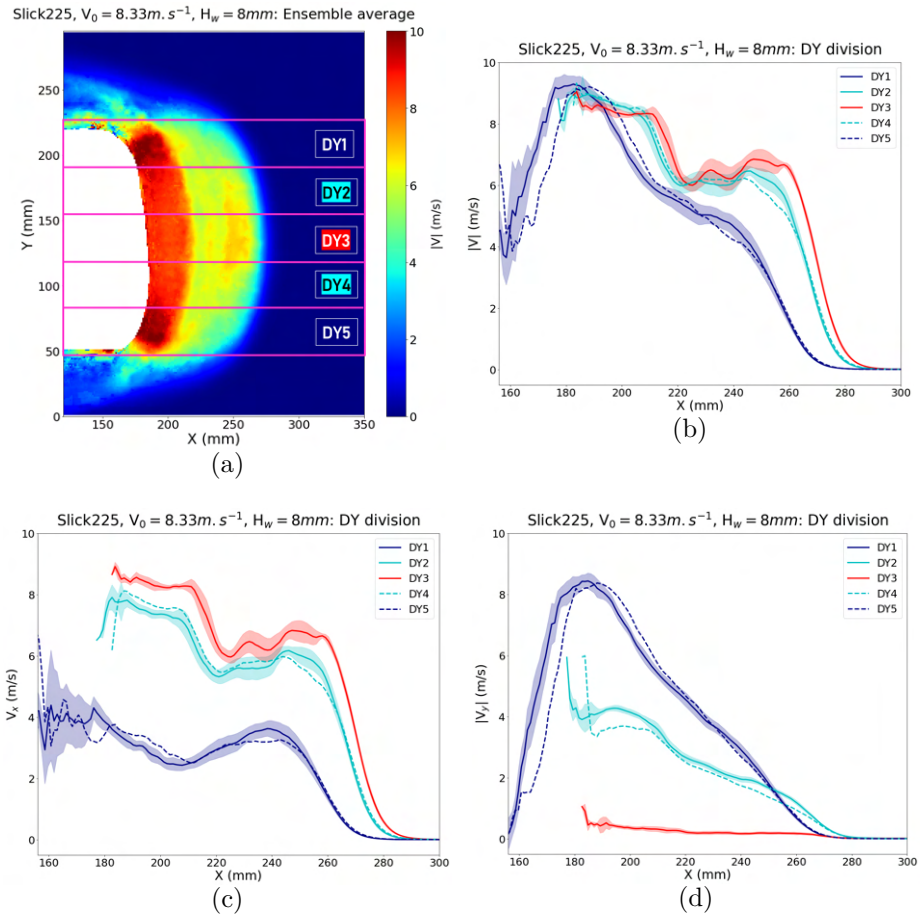

Figure 4.22 – WB division in the transverse direction (top left) and velocity profiles evolution Y-averaged in these 5 subregions: $|\vec{V}|$ (top right), V_x (bottom left) and $|V_y|$ (bottom right). The envelopes represent the standard deviation between the different runs. For clarity reasons and symmetry considerations, only envelopes of DY1, DY2, and DY3 are represented. The results are given in a fixed referential.

then iii) a region where V_x stays rather constant again, and finally, iv) a region where V_x decreases to reach zero. We note that in region i), V_x is close to V_0 for all cases, however, the length of this region increases with the vehicle velocity V_0. It means that the water is pushed further away from the tire when V_0 is higher in the longitudinal direction not linearly with V_0.

If we look at V_y in the shoulder area in Fig.4.23(b) we can notice that the three profiles have also the same shape: a linear increase with a high slope, and a linear decrease with a lower slope. The maximum value of V_y is close to V_0. The profiles present a clear similarity. Nevertheless for the highest car speed ($V_0 = 11.11m.s^{-1}$) the ensemble averaged velocity

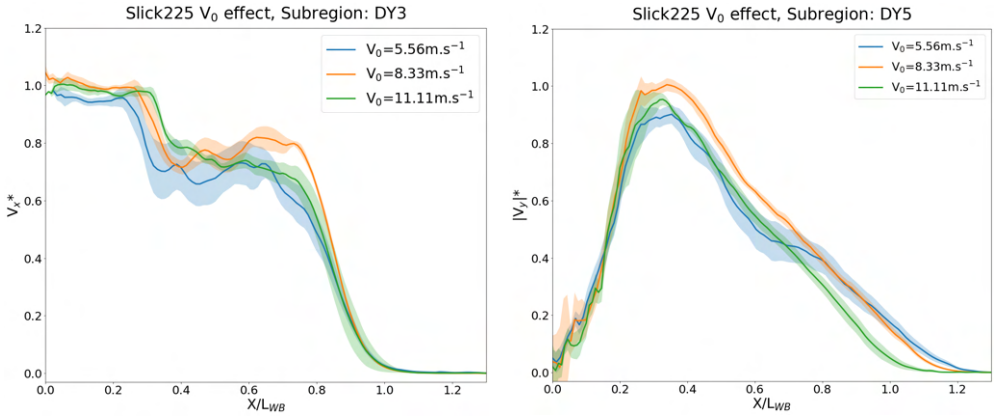

(a) (b)

Figure 4.23 – Velocity profiles V_x^* (a) and V_y^* (b) for three vehicle velocity values V_0. In (a) the Y-averaging is done in the central region DY3, while in (b) the profiles are generated in the shoulder region DY5. Each profile is normalized by its respective V_0. The X-axis is normalized by the respective WB lengths: $L_{WB}(V_0 = 5.56m.s^{-1}) = 96mm$, $L_{WB}(V_0 = 8.33m.s^{-1}) = 100mm$, $L_{WB}(V_0 = 11.11m.s^{-1}) = 110mm$.

profile seems to evolve towards a structure with only two flat zones without the equivalent of region II in Fig4.19 as it has been measured for lower V_0 values.

4.5 Mass budgets

In this section, we aim to write a mass budget inside a closed fluid domain from r-PIV measurements to have a global analysis and also some additional information to go deeper into the flow mechanisms. The major challenge subsists in the 2D nature of r-PIV results regarding a three-dimensional flow. This requires an additional term into the mass budget indicating the presence of out-of-plane circulation compared to a classical mass budget regarding a 2D flow with $div_{2D}(\vec{V}) = 0$. Moreover, in a fixed referential the flow is actually unsteady. Therefore, the mass budget is written in a moving referential (vehicle referential) with a stationary hypothesis to put to zero the term on the right side of the mass budget equation. Finally, this mass budget analysis will help us to characterize and quantify the flow drained into the shoulders and also highlight the importance of the 3D local mechanism in the establishment of these budgets.

Let us consider a volume of the fluid defined by the positions of its sections S_1 and S_4 perpendicularly to X-axis at respectively $X = x_1$ and $X = x_4$, S_2 and S_3 perpendicularly to Y-axis at respectively $Y = y_2$ and $Y = y_3$, and S_5 and S_6 perpendicularly to the Z-axis

at respectively $z = z_0 - \frac{\varepsilon}{2}$ and $z = z_0 + \frac{\varepsilon}{2}$ as depicted in Fig.4.24. We consider:

— z_0 the altitude of a point inside the WB

— $\varepsilon << 1$ and therefore the two sections along Z are very close

— x_1 is always selected in the region where the flow is at rest (in the road referential)

— y_2 and y_3 are symmetric against the middle axis of the WB along the spanwise direction

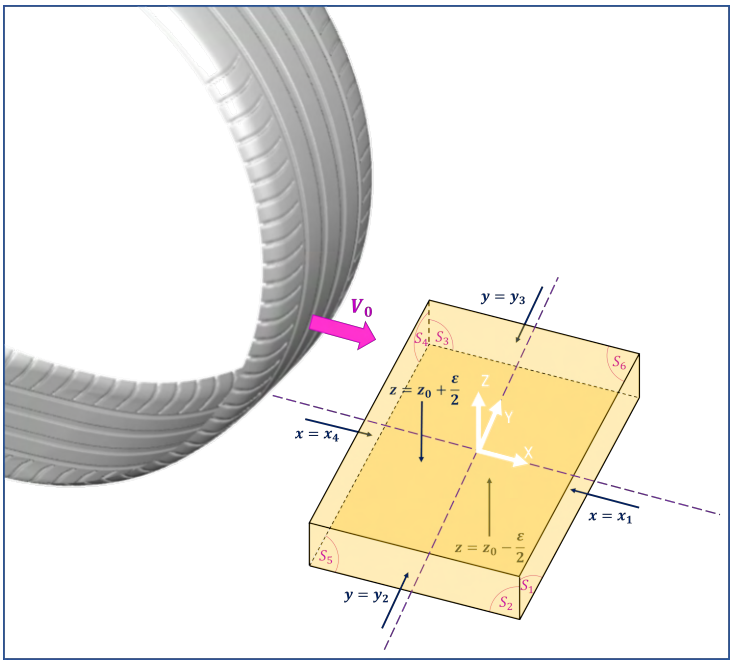

Figure 4.24 – Scheme of a fluid control volume in front of the tire

We want to express the mass budget in the vehicle referential as we consider the flow stationary in this referential and in the limit $\varepsilon \to 0$. We designate the mass fluxes across the 6 sections of the volume by d_1 to d_6 as:

- $d_1 = \int\int_{S_1} \rho[V_x(X = x_1, Y, Z) - V_0]dydz$
- $d_2 = -\int\int_{S_2} \rho[V_y(X, Y = y_2, Z)]dxdz$
- $d_3 = \int\int_{S_3} \rho[V_y(X, Y = y_3, Z)]dxdz$
- $d_4 = -\int\int_{S_4} \rho[V_x(X = x_4, Y, Z) - V_0]dydz$
- $d_5 = -\int\int_{S_5} \rho[V_z(X, Y, Z = z_0 - \frac{\varepsilon}{2})]dxdy$
- $d_6 = \int\int_{S_6} \rho[V_z(X, Y, Z = z_0 + \frac{\varepsilon}{2})]dxdy$

The normal to each section is taken directed to the outwards of the volume. Since the flow is considered stationary and incompressible, then the mass conservation reads:

$$d_{3D} = d_1 + d_2 + d_3 + d_4 + d_5 + d_6 = 0 \tag{4.4}$$

Considering the studied flow in the vehicle referential, we expect that $d_1 < 0$, $d_2 > 0$ and $d_3 > 0$.
We now focus our attention on the mass budget when ε is very small and tends towards zero.

4.5.1 Taylor expansion of the velocity field

Details of the calculations are given in Appendix B. We find that the mass budget can be written in the form:

$$\rho\varepsilon(\int_{y_2}^{y_3}(V_x - V_0)d_y - \int_{y_2}^{y_3}(V_x - V_0)dy + \int_{x_1}^{x_4} V_y dx - \int_{x_1}^{x_4} V_y dx + \int_{x_1}^{x_4}\int_{y_2}^{y_3} \frac{\partial V_z}{\partial z} dxdy) = 0 \tag{4.5}$$

and, due to the Taylor expansion, it is independent of ε. The last term including $\frac{\partial V_z}{\partial z}$ is specific to the mass budget equation including a vertical velocity gradient.

4.5.2 Results obtained

4.5.2.1 Results at fixed (V_0,H_w) and effect of Dy_{23}

We consider here the volume of interest inside the WB of the flow around a Slick tire. We fix y_2 and y_3 symmetrically against the axis of symmetry of the WB. We want here to study the evolution of mass budget as a function of the position of x_4. We present the results obtained for the Slick225 at $V_0 = 8.33m.s^{-1}$ and $H_w = 8mm$ in Fig.4.25. To better visualize each contribution compared to d_1, all quantities are normalized by $(-d_1)$. The mass budget is designated by MB.
First, we can see in Fig.4.25(a) that the 3D mass budget $(d_1 + d_2 + d_3 + d_4 + d_5 + d_6)$ is nearly zero for all x_4 positions inside the WB which asserts the previous approximations established and confirm that measurements are valid. However, the 2D mass budget $(d_1 + d_2 + d_3 + d_4)$ is only equal to zero in the area where the flow is at rest $(x > 290mm)$ in the fixed frame attached to the ground. We observe that when x_4 gets closer to the CPA, the 2D mass budget decreases considerably and its profile presents some strong variations.

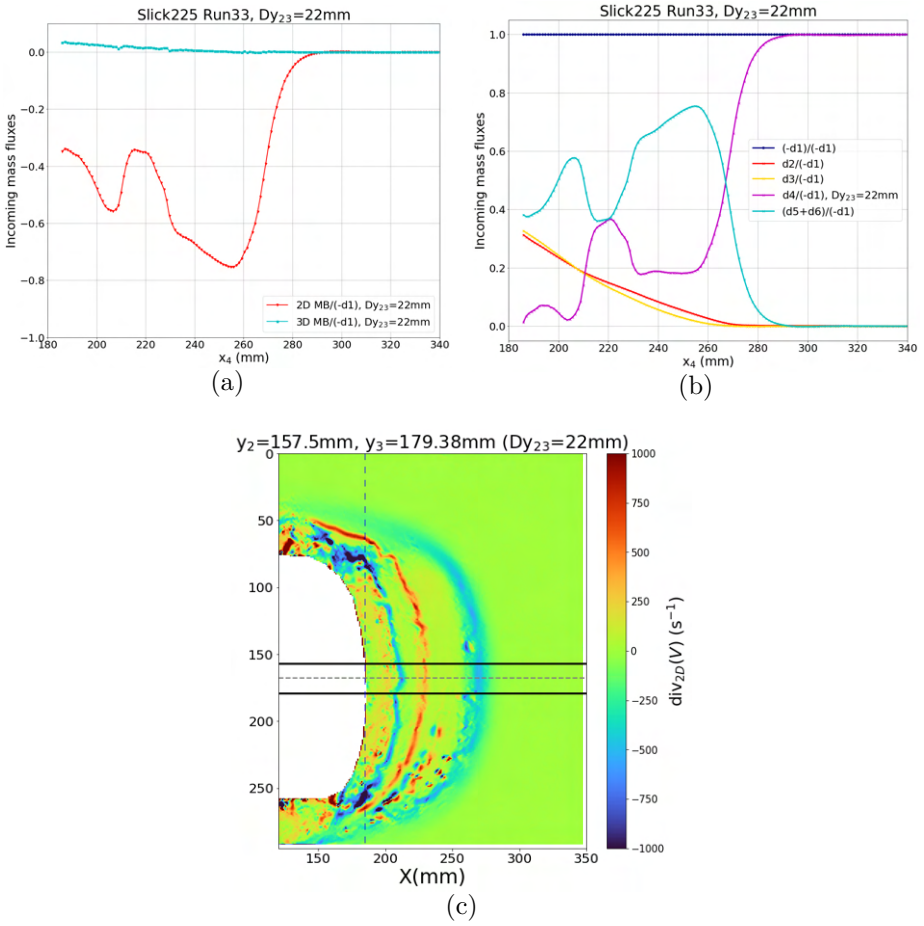

Figure 4.25 – Evolution of the 2D and 3D mass budgets with X_4 position (a) and decomposition of the mass budget contributions on the sections S_1 to S_6 (b). All quantities are normalized by $-d_1$. In (c) the colormap corresponds to $div_{2D}(\vec{V})$. The positions of y_2 and y_3 are represented with horizontal bold lines. The vertical dashed line is positioned at $X = 185mm$.

The minimum is reached near $X = 255mm$. To understand this variation in the 2D mass budget, we refer at Fig.4.25(b). One can notice when $x_4 > 290mm$, that d_4 and d_1 cancel each other as all the flow entering the volume from S_1 is evacuated through S_4. Starting from $x_4 > 290mm$ and moving closer to the CPA, d_4 decreases while $d_5 + d_6$ increases. This means that less fluid is evacuated through the S_4 section and at the same time, a vertical movement appears creating a 3D circulation, in accordance with the negative divergence inside the wide blue band at the leading edge of the CPA. Actually, a part of the flow is also evacuated in the spanwise direction through S_2 and S_3 but it is rather low compared to the other sections, however, it becomes high very close to the tire since d_4 is

near zero in that region.

At this instant, this analysis has been conducted for an arbitrary position of the lateral sections S_2 and S_3, and it should be completed by a parametric study to highlight the evolution of the mass budget for different positions of Y_2 and Y_3 or more precisely, for a different width $Dy_{23} = (Y_3 - Y_2)$ to determine some change in the flow behavior due to mainly the shoulder ejections. The results are given in Fig.4.26. For clarity reasons only d_2 is plotted since we can consider its symmetry with d_3 (Fig.4.26(b)). The analysis is conducted for seven values of Dy_{23}, the lowest value ($Dy_{23} = 22mm$) corresponds to the results presented in Fig.4.25 and for the largest value ($Dy_{23} = 153mm$) we represent the positions of y_2 and y_3 in Fig.4.26(c) with the bold horizontal lines. We give the results obtained for only $x_4 = 185mm$ corresponding to the closest position from the CPA/WB frontier. We give the full evolution of the profiles with x_4 in Appendix C. First, we can see in Fig.4.26(a) that the 3D mass budget stays null whatever the value of Dy_{23} which is reassuring. Second, in Fig.4.26(b) the $d_2/(-d_1)$ is nearly constant indicating a linear evolution of d_2 with Dy_{23}. This means that V_y has a linear evolution not only along X-axis (Fig.4.10(d) and Fig.4.28(b)) but also along Y-axis which has been observed in Fig.4.11. Moreover, we can observe that the higher is Dy_{23}, the higher is $d_4/(-d_1)$ and the lower $(d_5 + d_6)/(-d_1)$. This means that the 3D circulation does not evolve linearly with Y. This can be caused by the curved shape of the tire and therefore the velocity field in the (XY) plane while the S_4 section is a straight section of the YZ plane.

This first analysis using the mass budget was done at a fixed water depth $H_w = 8mm$. We have seen the evolution of the different flow contributions over the sections S_1 to S_6 highlighting the important out-of-plane effects. We quantified the spanwise ejection in front of the tire in comparison with the vertical flow. It would be therefore interesting to study the evolution of this decomposition when the water film thickness is decreased. This will be the subject of the following section.

4.5.2.2 Effect of H_w

In this section, we analyze the evolution of the flow structure for decreasing water heights, from $H_w = 8mm$ down to $H_w = 1.5mm$. We give in Fig.4.27 the streamlines corresponding to $H_w = 6mm$, $H_w = 4mm$ and $H_w = 2mm$ plotted in the vehicle referential. The background colormap corresponds to $|\vec{V} - \vec{V_0}|$. First, we can see that the WB length

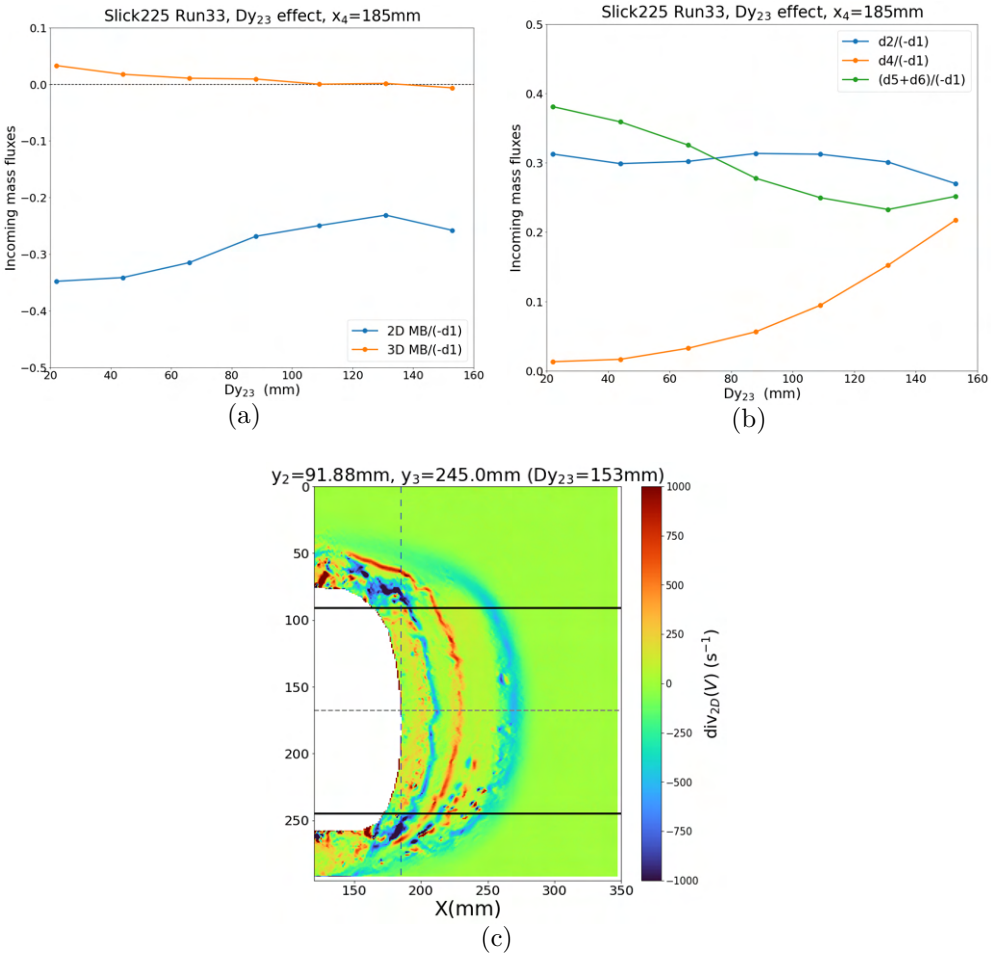

Figure 4.26 – Evolution of the 2D and 3D mass budgets profiles (a), d_2, $(d_5 + d_6)$ and d_4 (b) for different values Dy_{23} for $X_4 = 185mm$. All quantities are normalized by $(-d_1)$. We plot the limits Y_2 and Y_3 in the case of the largest value considered of $Dy_{23} = 153mm$ with the horizontal black lines (c).

is clearly reduced when the water depth is decreasing. Then, we observe that the region close to the tire that the streamlines do not cross, is still present and its length does not seem to change. Moreover, the region where $|\vec{V} - \vec{V_0}|$ is the lowest in front of the tire (in blue) is getting wider when H_w decreases, while in the shoulders $|\vec{V} - \vec{V_0}|$ seems to gets lower with H_w.

We focus now on the center region of the WB (DY3 in Fig.4.10(a)) for the streamwise flow and in the upper shoulder region (DY1 in Fig.4.10(a)) for the spanwise flow. We give the results obtained in Fig.4.28 where V_x and V_y are normalized by $V_0 = 8.33m.s^{-1}$. We add the standard deviation between the runs as the envelopes of the curves. First,

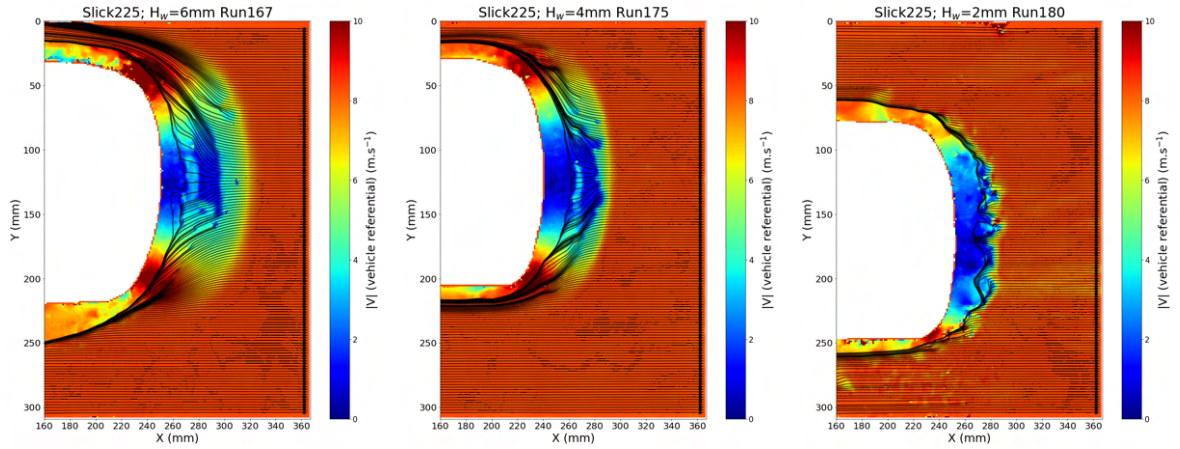

(a) (b) (c)

Figure 4.27 – Streamlines generation for the Slick225 along with the $|\vec{V}|$ field in the vehicle referential. In (a) it corresponds to $H_w = 6mm$, in (b) to $H_w = 4mm$ and in (c) to $H_w = 2mm$.

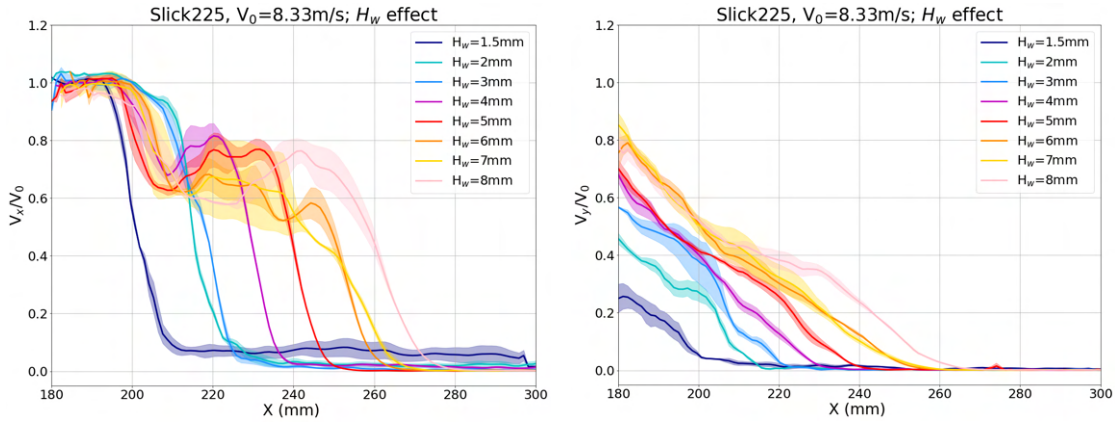

(a) V_x/V_0 in DY3 (b) V_y/V_0 in DY1

Figure 4.28 – Y-averaged velocity profiles V_x/V_0 (left) and V_y/V_0 (right) for $N = 3$ runs respectively in the center region (DY3 in Fig.4.10(a)) and in the upper shoulder DY1. The envelope of the profiles is calculated based on the standard deviation between the runs.

we note that for $H_w = 1.5mm$, the velocity profile is not perfectly null in front of the WB, this is due to the presence of some optical noise in this region. Then, if we consider Fig.4.28(a), we can see that there is a change in the profiles starting from $H_w = 4mm$. Indeed for $H_w < 4mm$, the $V_x^* = V_x/V_0$ profiles present a single plateau close to 1 then they decrease to zero, whereas for $H_w \geq 4mm$ they present a more complex evolution with a non-monotonic decrease and usually with a second plateau after an increase as

we have seen in the previous section. This change in the profiles is the sign of a specific regime establishment as soon as the water depth is higher than $4mm$ ($H_w \geq 4mm$) for $V_0 = 8.33m.s^{-1}$. A new phenomenon seems to appear when H_w increases. We give in Fig.4.29(a) the WB length evolution as a function of H_w. It is calculated based on the V_x^* profiles (Fig.4.28(a)) and is taken as the abscissa X_w corresponding to $V_x^*(X_w) = 0$. We note that in the case of $H_w = 1.5mm$, the V_x^* profile does not reach zero after its decrease, but rather a value around 0.07. This is possibly caused by the water jet projections that we are able to capture with the r-PIV at this low value of water height. For this case, we take X_w the abscissa that corresponds to $V_x^*(X_w) = 0.07$. We can see in Fig.4.29(a) that the evolution of the WB length is rather linear with H_w. We plot then the same V_x^* profiles but we normalize the abscissa axis with the WB length (L_{WB}), the results are presented in Fig.4.29(b).

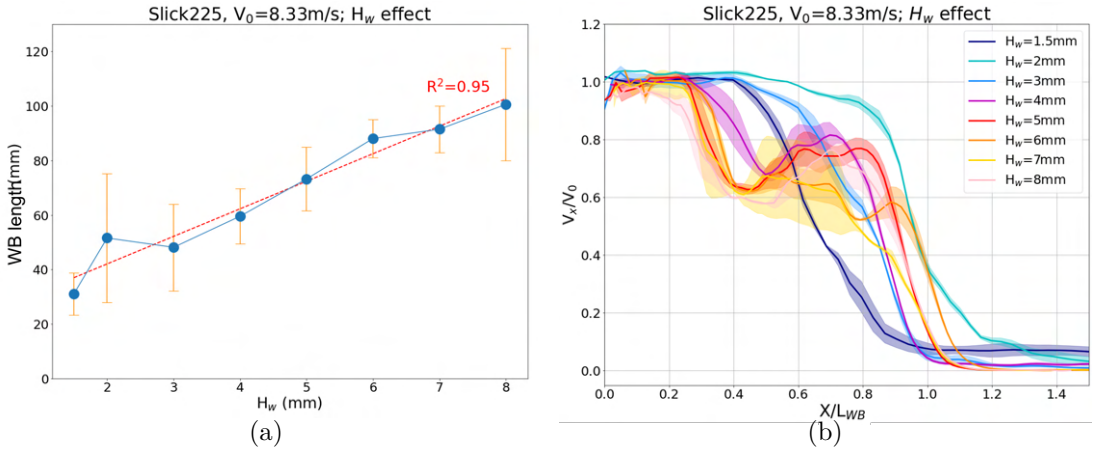

(a) (b)

Figure 4.29 – Evolution of the WB length with the water height for the Slick225 at $V_0 = 8.33m.s^{-1}$ (left), and the V_x/V_0 profiles Y-averaged in the central region along the X-axis normalized by the WB length at each H_w (right)

Furthermore, concerning the mass budget, we want to study the evolution of the different contributions d_1 to d_6 for a lower value of H_w than the $8mm$ already investigated. We present the results obtained in Fig.4.30 for $H_w = 3mm$ along with $H_w = 8mm$ for the Slick225 at $V_0 = 8.33m.s^{-1}$. The value of x_4 is fixed at $185mm$ corresponding to the CPA/WB frontier. The full profiles are given in Appendix D. First, we can observe in Fig.4.30(a) that for both cases the 3D mass fluxes budget is null again. Concerning the 2D mass budget, we can see that for $H_w = 3mm$ it is nearly twice the value for $H_w = 8mm$. To better understand this difference in behavior near the tire, we can look at Fig4.30(b)

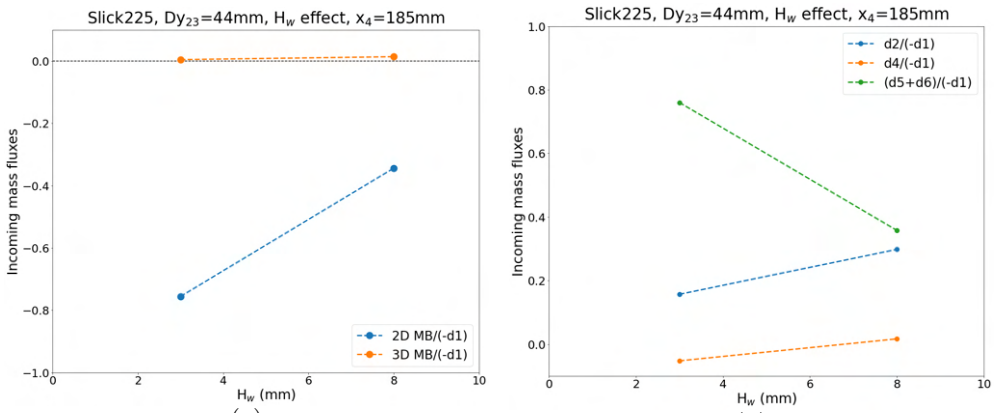

Figure 4.30 – Evolution of the 2D and 3D mass budgets profiles (a) and decomposition of the mass budget contributions on the sections S_1 to S_6 (b) for $H_w = 3mm$ and $H_w = 8mm$ normalized by $(-d_1)$, for $x_4 = 185mm$. The results for $H_w = 8mm$ correspond to the Run33 and are previously presented in Fig.4.25. The results for $H_w = 3mm$ belong to Run178.

where we can see the different contributions over S_1 to $S6$ sections. The d_i $(1 \leqslant i \leqslant 6)$ quantities are normalized by $(-d_1)$ of the corresponding water depth. We can see that $d_2/(-d_1)$ is nearly twice higher for $H_w = 8mm$ than for $H_w = 3mm$, while it is quite the opposite for $(d_5 + d_6)/(-d_1)$. This indicates that in the region very close to the tire when the water height is increased, the flow tends to be evacuated in the spanwise direction towards the shoulders rather than in the vertical direction which is the case for lower H_w values.

We present in Fig.4.31 a scheme of the flow circulation in a fluid volume where x_4 is very close to the tire and x_1 is in the region where the flow is at rest. The arrows indicate the direction of the in-plane and out-of-plane net mass fluxes. The r-PIV has offered the possibility to quantify the increase in the lateral ejection when the water film thickness is increased.

4.6 Effect of the tire width

At the beginning of the current chapter in 4.1, we have risen the issue of the tire width effect and we have addressed it as one of the objectives of the slick tire analysis. We may recall the four tire dimensions selected:

— Slick205: section width of $205mm$ and rim diameter of $16''$

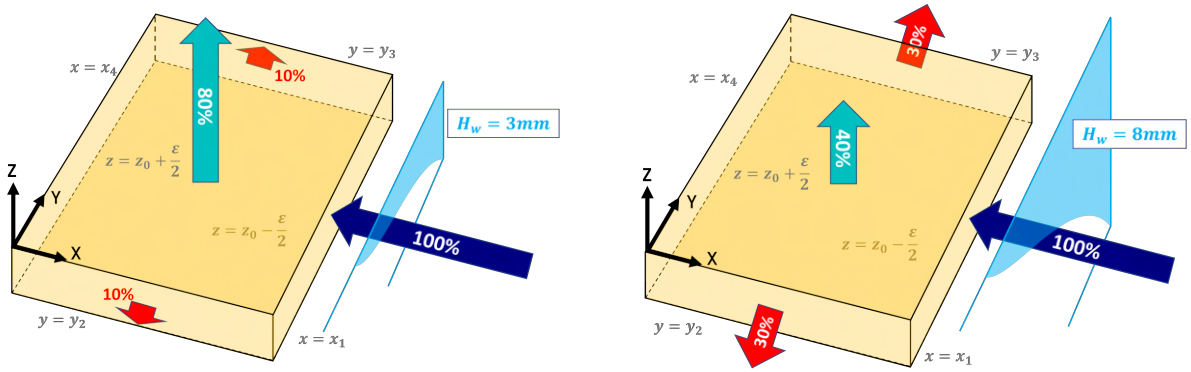

(a) (b)

Figure 4.31 – Schematic representation of the mass fluxes in the WB when x_4 is close to the tire for $H_w = 3mm$ (left) and $H_w = 8mm$ (right)

— Slick225: section width of $225mm$ and rim diameter of $17''$ (all previous results were obtained for this tire)

— Slick275: section width of $275mm$ and rim diameter of $20''$

— Slick315: section width of $315mm$ and rim diameter of $20''$

4.6.1 Analysis of the velocity field

We give in Fig.4.32 the ensemble average velocity fields $|\vec{V}|$ obtained for the different dimensions of the slick tire studied. First, we note that in the case of the Slick315 (Fig.4.32(d)), the velocity field is not complete in the transverse direction. Indeed, the tire is very large and was never tested before in the r-PIV. A larger field of view could have been taken, but it would have been to the detriment of the resolution of the image velocity field. We preferred preserving the same field of view as the Slick275 and focusing on the upper part of the velocity field. However, the hypothesis of a symmetric field against the Y-axis is not strictly respected especially for the largest tire mainly due to the important camber angle of the vehicle. We note that a specific vehicle is needed for both the Slick275 and the Slick315 because of their large dimensions.

When we look at Fig.4.32, we observe that the global structure of the velocity field in the WB is rather similar between the four tires. Close to the CPA, the velocity is high and it decreases suddenly after around $20mm$ from the frontier CPA/WB. Close to the shoulders, the water is pushed along the transverse direction, while in the center it is

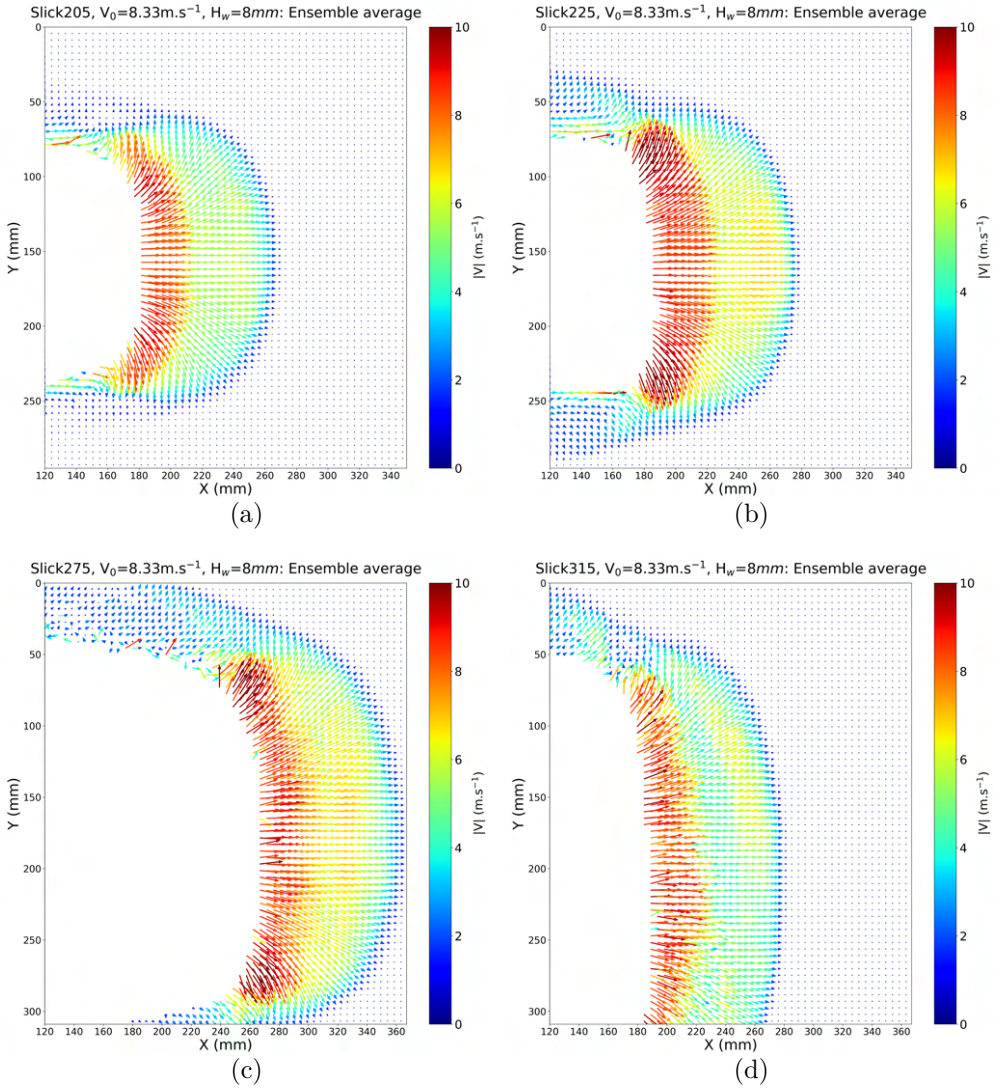

Figure 4.32 – Ensemble average velocity fields $|\vec{V}|$ $(N = 8)$ for respectively the Sick205 (a), Slick225 (b), Slick275 (c) and Slick315 (d) at $V_0 = 8.33m.s^{-1}$ and $H_w = 8mm$. For clarity reasons, only one arrow over 4 is represented.

pushed along the longitudinal direction. However, we can see that the shape of the WB is rather round for the narrow tires, and it gets more elliptic for the larger ones. This is probably caused by a larger deformation of the tire due to the increasing hydrodynamic pressure in the center of the WB.

Furthermore, since our objective is to assess the efficiency of the water drainage depending on the tire's width, in the following we quantify the water expulsion from the center to the shoulder area and analyze its evolution with the tire dimension. Therefore, we define

the following quantity:

$$B_y(W) = \frac{1}{(X_{sup} - X_{inf})} \int_{X_{inf}}^{X_{sup}} V_y(x, W)dx \tag{4.6}$$

where

$$W(\%) = 100 * \frac{(Y_{middle} - Y)}{\text{Tire Width}} \tag{4.7}$$

We designate by Y_{middle} the median plane of the tire. If $W = 0$, it means that $Y = Y_{\text{middle}}$, and if $W = 50\%$ then $Y =$ Tire Width. This definition of W is useful to compare equivalent Y positions for different tire widths. We note that the parameters B_y and d_2 (previously defined in the mass budget analysis) are rather close in terms of definition and should give nearly the same results regarding the rating of the tire widths. However, B_y not only follows the shape of the CPA/WB frontier but also gives information along the WB width, it is therefore computationally more expensive.
First, we give in Fig.4.33 the results for the Slick225 case to clarify the quantities mentioned above. In this example, 10 values of Y are considered, with a constant distance ΔY between two consecutive positions. The Y_{middle} position is designated with the red dotted line. To each position Y (i.e W value), corresponds $B_y(W)$ plotted in Fig.4.33(b). The X_{inf} position follows the shape of the mask and is defined for each value of Y, whereas the X_{sup} is unique and is taken at the border of the image ($\approx 350mm$).

We give in Fig.4.34 the results obtained regarding the evolution of B_y for the four tires considered. In the case of the Slick225, 10 values of the variable Y are considered constraining the distance ΔY. For the other tires, we fix the number of Y positions so that ΔY is proportional to the tire's width. Therefore, consecutively 9, 12, and 14 positions are considered for the Slick205, Sick275, and Slick315.

First, we observe a similar behavior between the Slick205 and the Slick225 until $W = 25\%$. The B_y profiles of the Slick275 and the Slick315 are also rather close. We can also see that there is a rather linear evolution of the B_y profiles, especially in the increasing phase, and the difference in the slopes between the two narrowest tires and the two largest ones is very clear. Furthermore, all the profiles reach their maximum between $W = 30\%$ and $W = 40\%$. It is the region where the water expulsion to the shoulder is at its highest. Moreover, the Slick315 has the lowest values of B_y everywhere in the WB whereas the Slick225 has the highest values nearly for all W values. The B_y representation quantifies the increase in lateral expulsion at a given Y position, e.g., for $W = 20\%$ we observe that narrower tires eject water nearly 60% more than the larger tires.

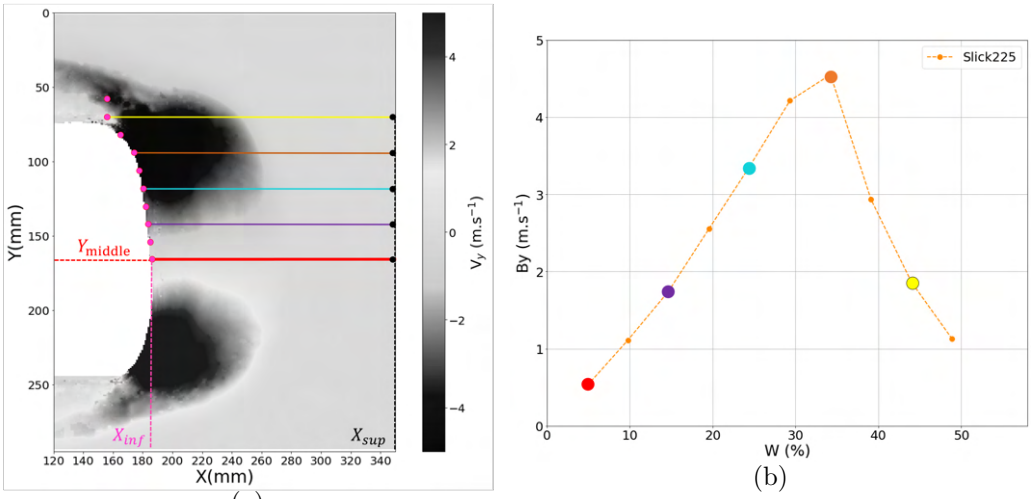

(a) (b)

Figure 4.33 – In (a) we represent the positions of Y by the horizontal lines (only 1 position over 2 is represented for clarity reasons). To each of these positions correspond a value of $B_y(W)$ plotted in (b). The same colors are used to designate the Y position and the corresponding B_y value. The X_{inf} and X_{sup} are highlighted successively with pink and black dots.

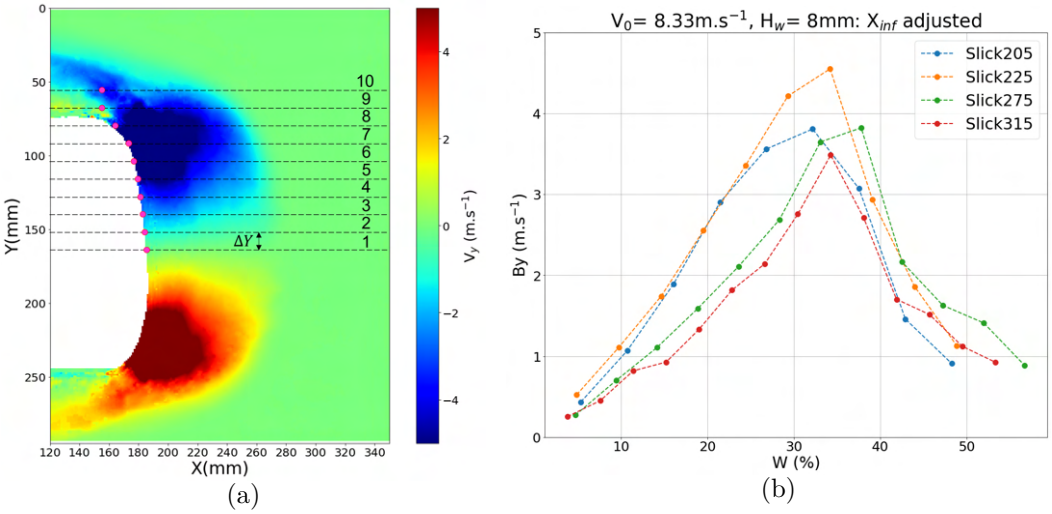

(a) (b)

Figure 4.34 – In (a), the Y positions are depicted with the horizontal dotted lines (10 positions in this example). The result regarding the evolution of B_y for each tire width is given in (b) for $V_0 = 8.33m.s^{-1}$ and $H_w = 8mm$.

We can also look at the water expulsion in the longitudinal direction, and since it is in the center of the WB that it is the highest, it is in this region that we plot the V_x profiles Y-averaged in a horizontal band centered on Y_{middle}. The width of the band is

taken proportional to the tire width and is equal to $50mm$ in the case of the Slick225 (Fig.4.35(a)). The results are given in Fig.4.35(b). The profiles are shifted in a way that their decreasing regions match (end of the WB near $X = 285mm$). First, we observe that

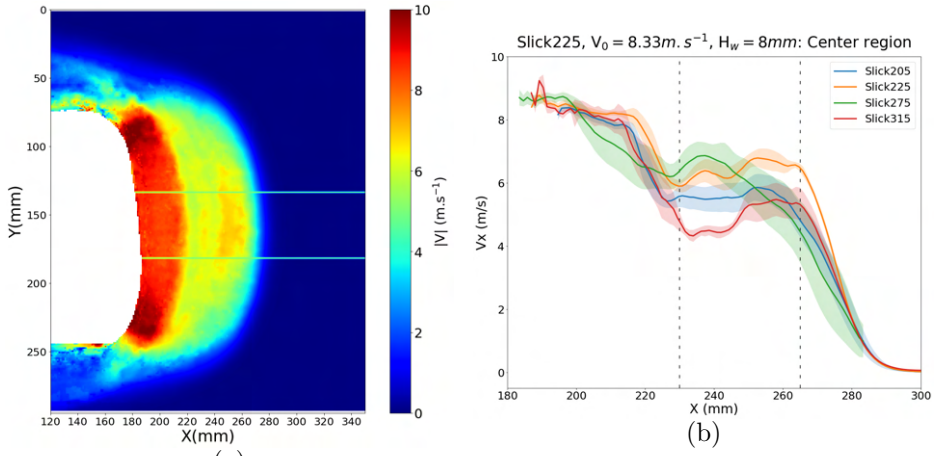

Figure 4.35 – Highlight of the center region for the Slick225 with the green horizontal lines (a), and V_x profiles Y-averaged in the center zone for the different tire widths studied (b).

the WB length is rather independent of the tire width and is close to $100mm$. The velocity near the CPA/WB frontier is also independent of the tire width and is equal to V_0. The four V_x profiles present i) a region close to the CPA where V_x is rather constant, ii) then a sudden decrease, iii) a second region where V_x is rather constant, iv) and finally a sudden decrease to zero (decomposition in Fig.4.19). The main difference between the profiles can be observed in region III ($230mm < X < 265mm$ highlighted with the vertical dashed lines in Fig.4.35(b)). The Slick315 case presents the lowest values of V_x in this region, while for the other tire widths the difference is not very important between the profiles.

4.6.2 Effect on the mass budget

Since the analysis of the mass budget has shown itself a rather good tool to grasp the flow circulation in the WB, this section aims to follow the evolution of the flow ejection in front of the tire when increasing the tire width. We present the results obtained in Fig.4.36. The section Dy_{23} is fixed to $22mm$ for the Slick225 and is modified proportionally to the tire's width for the other dimensions to keep the same relative section width. The vehicle speed is still fixed at $V_0 = 8.33m.s^{-1}$ and the water height at $H_w = 8mm$. The x_4 position corresponds to the closest one to the tire in each case, and the full profiles are provided

in Appendix E. On one hand, we can observe in Fig.4.36(a) that the 3D mass budget is

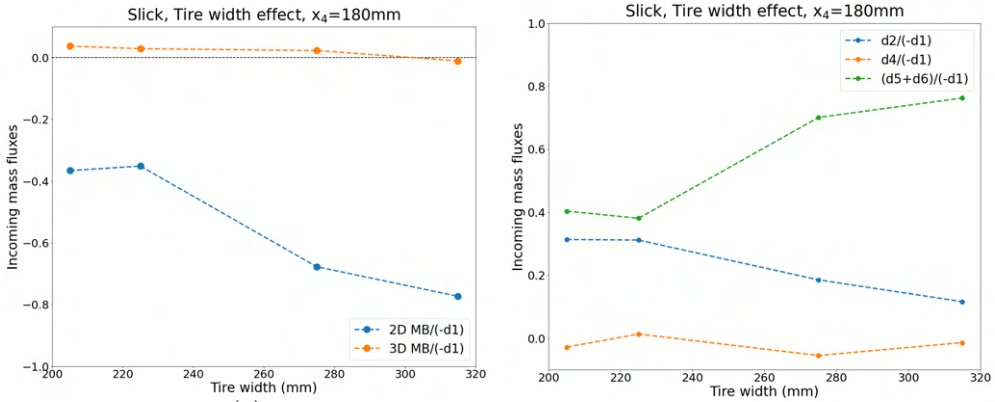

(a) (b)

Figure 4.36 – Evolution of the 2D and 3D mass budgets profiles (a) and decomposition of the mass budget contributions (b) and (c) for $H_w = 8mm$, $V_0 = 8.33m.s^{-1}$ and four tire widths. The x_4 position is fixed at the corresponding closest position to the tire. All contributions are normalized by $(-d_1)$. The results for the Slick205 correspond to the Run25, the Slick225 Run33, the Slick275 Run119, and the Slick315 Run63.

still null for all the tire widths. On the other hand, we can see that the wider the tire, the higher the 2D mass budget (in absolute value). However, the gap between the Slick225 and the Slick275 is much higher than the one between the Slick205 and the Slick225, the same observation goes for the gap between the Slick275 and the Slick315. We note for a given couple of tire models $T1$ and $T2$ the relative gap:

$$E_{T1/T2} = 100 \times \frac{\text{2D MB}(T1) - \text{2D MB}(T2)}{\text{2D MB}(T1)} \tag{4.8}$$

For example for $x_4 = 180mm$, $E_{Slick205/Slick225} \approx 14\%$, $E_{Slick225/Slick275} \approx 37\%$ and $E_{Slick275/Slick315} \approx 40\%$. In addition, we look at the different contributions over the sections S_1 to S_6 in Fig.4.36(b). We can see that d_2 and $(d_5 + d_6)$ have a quite opposite evolution with the tire width. Indeed, d_2 gets lower while $(d_5 + d_6)$ gets higher when the tire width is increased. The increase in the tire width and the decrease in the water height seem to have the same effect on the evolution of the mass budget. Nevertheless, the difference between the Slick205/Slick225 is not as noticeable as between the Slick225/Slick275 or the Slick275/Slick315.

As already stated in Section 1.2.3, a more rounded footprint increases the hydroplaning speed. The r-PIV measurements showed that the larger the tire, the less rounded its CPA

and the less efficient its lateral ejection compared to a narrower tire which is in good agreement with what is already known in the literature. But with the r-PIV, we were able to quantify for each Y position this difference by calculating the lateral flow rate. In addition, the study of B_y and the position of its peak along the tire width W can lead to some valuable information concerning the design of the tread pattern i.e. the position of the grooves and their orientation.

4.7 Comparison with numerical results

With the r-PIV measurement method, local velocities of the water flow are accessible, opening the possibility of a local comparison between numerical and experimental results. In this section, we present the numerical results obtained with the coupled SPH-FE simulations and the comparison with the previously presented r-PIV results. We aim to not only continue our validation of the numerical tool, but also go deeper into the understanding of the physical phenomena intervening during the rolling of a slick tire in the WB region. Another aspect is to see if the different post-processing parameters defined and used for r-PIV results analysis could be done with the numerical tool. We remind the reader that the numerical simulations are conducted in a 3D framework, opening the possibility to complete the previously constructed view of the flow circulation in front of the tire.

4.7.1 Slick225 at fixed (H_w,V_0)

We run the simulation for the Slick225 at $H_w = 8mm$ and $V_0 = 8.33m.s^{-1}$. The numerical and physical parameters are given in Table 4.2. We note that the $R/\Delta x_{SPH}$ has been chosen after the parametric study on the Test-Bench given in Section 5.6.2.2. The total number of particles is around 18M. The FE tire mesh has 321 552 solid elements. The computation time is around 620h on 48 CPUs for the SPH solver, 20 CPUs for the FE solver, and 1 CPU for the coupling algorithm. We note that no camber angle is considered in the numerical model. All details on the numerical tool are given in Chapter 2. We only give here the specific elements necessary for the present applied tire case.

Given the 2D nature of r-PIV measurements, we start by giving an XY view of the velocity magnitude $|\vec{V}|$ at two different altitudes of the water puddle ($Z < 1mm$ and $Z < 8mm$) in Fig.4.37. We can refer to Fig.4.35(a) for the experimental result in the

Physical parameter	Value
Puddle dimensions (XY) plane	L_x=1250mm L_y =280mm
H_w	8mm
V_0	8.33$m.s^{-1}$
ρ_{water}	1000$kg.m^{-3}$
g	9.81 $m.s^{-2}$
P_{tire}	2.2 $bars$
$Load$	380daN

Numerical parameter	Value
$\Delta x_{SPH_{min}}$	0.33mm
$R/\Delta x_{SPH}$	3
C_0	250$m.s^{-1}$
k_{CFL}	0.375

Table 4.2 – Physical and numerical parameters

same conditions. First, we observe that the overall shape of the WB in the XY plane is

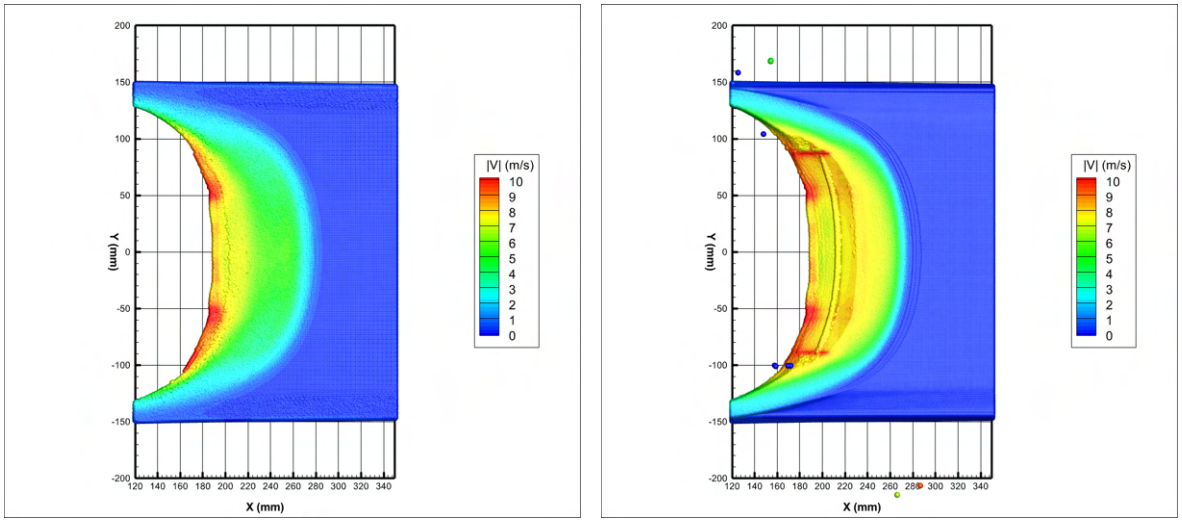

(a) (b)

Figure 4.37 – (XY) view of the Slick225 ($H_w = 8mm$) at $Z < 1mm$ (a) and $Z < 8mm$ (b) from the numerical calculation. The colormap corresponds to the $|\vec{V}|$ field. For clarity issues, only the fluid is represented (not the tire, nor the road), and also we limit the view between $X = 120mm$ and $X = 350mm$.

qualitatively very close to the one obtained with the r-PIV. Both WB length and width are very close numerically and experimentally (Table 4.3). The symmetry of the velocity field against the median plane $Y = 0$ is preserved.

However, we note that in the region very close to the tire, the fluid velocity is underestimated numerically. We do not distinguish a clear separation between the region where $|\vec{V}| \approx V_0$ and $|\vec{V}| \approx 6m.s^{-1}$ as it exists experimentally (Fig.4.35(a)). Furthermore, we can

Table 4.3 – WB length and width numerical vs experimental: Slick225 $H_w = 8mm$

	Length WB (mm)	Width WB (mm)	Tire load (daN)
Numerical	280	110	380
Experimental	250	120	380

see that $|\vec{V}|$ increases in the shoulder region compared to the center region ($|Y| > 50mm$). Second, if we look more closely in the center region between $Y = -2.75mm$ and $Y = 2.75mm$, we can observe the evolution of V_x in Fig4.38(a). The colormap corresponds to the altitude of the particles Z. In blue the particles close to the ground and in red the ones near the tire or at the free surface. The corresponding r-PIV profile is also represented with the black solid line ($DY3$ profile in Fig.4.22(c)).

We observe that the higher the particle, the higher its streamwise velocity until $X = 270mm$ which corresponds to the particles in the jet falling back. Furthermore, the V_x profile corresponding to the particles close to the ground presents a three-region shape with i) a region where V_x is constant around $7m.s^{-1}$ until $X = 215mm$, ii) a region where the velocity decreases and stay around $5m.s^{-1}$, and finally iii) a region where the V_x goes to zero. It certainly reminds us of the four regions defined in Fig.4.19 for the experimental profile of V_x in the center of the WB. Nevertheless, in regions II and III, the velocity measured is never higher than $7m.s^{-1}$ which corresponds to the particles at $Z < 8mm$. But the r-PIV profile stays inside the envelope that the particles with different Z values starting from $X = 215mm$.

Furthermore, we look at the evolution of $V_y(x)$(Fig.4.38(b)) that we can compare to DY1 (Fig.4.22(d)) and represented also with the black solid line. The colormap is still designating to particles' altitudes Z. We note that in the region very close to the tire (that we remind the reader is very challenging to measure experimentally mainly due to the low seeding particle concentration and illumination) we do not capture numerically the increasing phase of $V_y(x)$ between $X = 160mm$ and $X = 190mm$. This may be the limit of our spatial resolution. It may also be caused by the removal of the SPH particles in this region by the algorithm due to their very high pressure as they are stuck between the tire and the ground. However, the decreasing phase in $V_y(x)$ fits rather well the experimental results even if the velocity is still underestimated especially close to the tire. Also, the length of the WB is nearly similar between the r-PIV results and the numerical results.

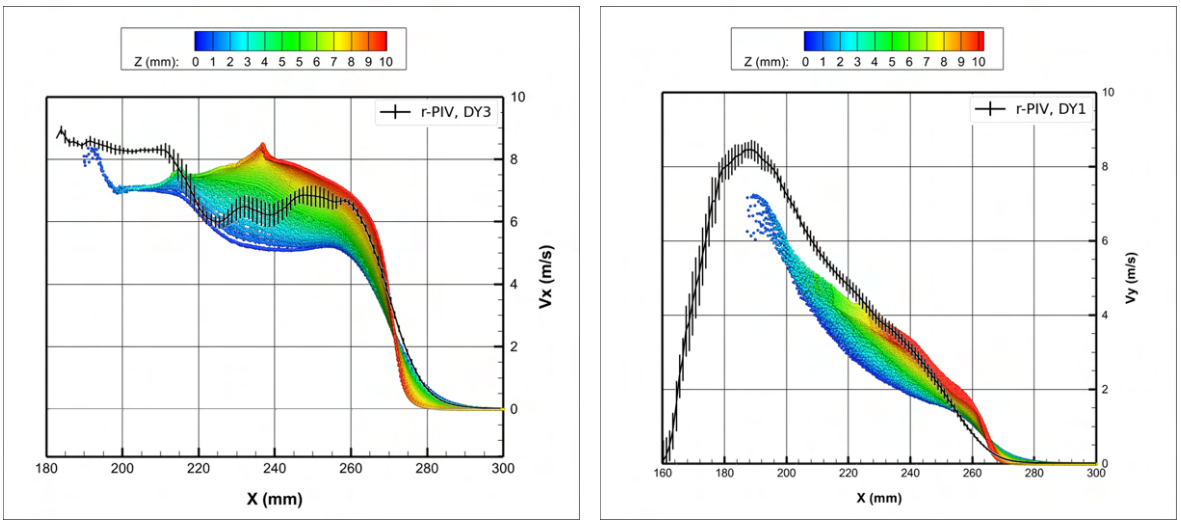

(a) (b)

Figure 4.38 – Evolution of V_x with X between $Y = -2.75mm$ and $Y = 2.75mm$ (a), and V_y with X between $Y = 47.5mm$ and $Y = 52.5mm$ (b). The colors represent the altitude Z of the particle, and each point represents an SPH particle. We overlay the corresponding r-PIV results with the error bars representing the standard deviation between the N runs. Case Slick225 $H_w = 8mm$.

In addition, we look at the evolution of $V_y^*(y)$ (Fig4.39) to compare with the r-PIV results given in Fig.4.11(b). The same WB subdivision depicted in Fig.4.11(a) is applied. Only one Dx over 2 is represented. The colormap represents the particles' altitude Z. The r-PIV profiles are overlayed with the numerical results. First, we note that the evolution of $V_y^*(y)$ is linear between one shoulder to the other as observed experimentally for each Dx. Moreover, the velocity is higher for the upper particles but this phenomenon tends to get homogenized when Dx is further from the tire. The experimental results fit more the numerical results corresponding to the upper particles.
Also, we give in Fig.4.40 an XZ cut view in the middle of the WB. We aim here to see if we can capture the secondary flow that we hypothesized in section 4.3.1.2. If we look at Fig.4.40(b), there is only one important ascendant flow corresponding to the elevation of the free surface and the water jet ejection in front of the tire. No horseshoe vortex is clearly observed as the flow is mainly in the (XY) plane between $X = 180mm$ and $X = 260mm$. Further simulations should be carried out to better explain this phenomenon. We remind the reader that the simulation uses an inviscid fluid hypothesis, and it is very likely that this simplifying assumption inhibits any vortex formation. Moreover, a higher spatial res-

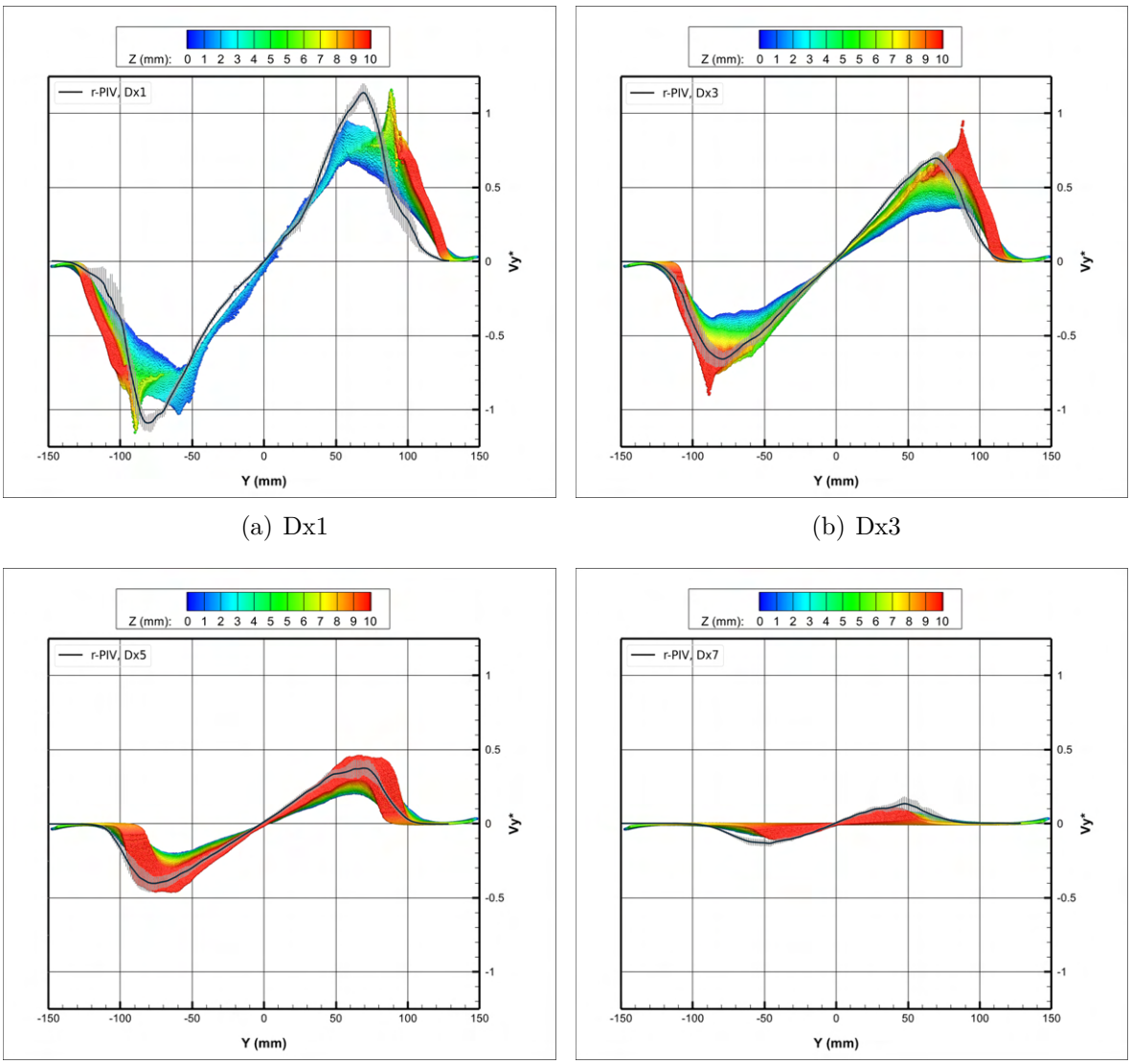

(a) Dx1 (b) Dx3

(c) Dx5 (d) Dx7

Figure 4.39 – Evolution of V_y^* with Y in respectively Dx1 (a), Dx3 (b), Dx5 (c) and Dx7 (d). The WB vertical decomposition into 8 subregions is identical to the one done with the r-PIV results and given in Fig.4.11(a). The colors represent the altitude Z of the particle, and each point represents an SPH particle. We overlay the corresponding r-PIV results with the error bars representing the standard deviation between the N runs. Case Slick225 $H_w = 8mm$.

olution is certainly required to capture such vortex as well as the viscous effects in the boundary layers.

Last but not least, we note that the particles' size changes at $Z = 5mm$ (as visible more

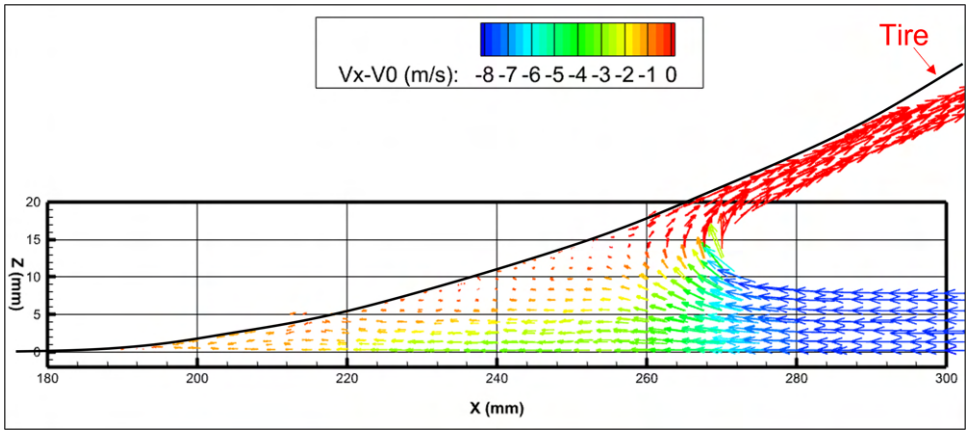

(a)

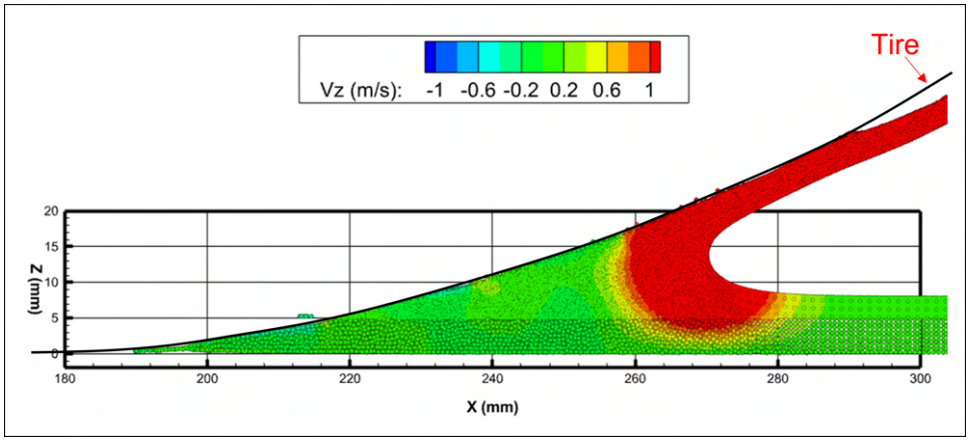

(b)

Figure 4.40 – XZ view in the middle of the WB between $Y = -2.75mm$ and $Y = 2.75mm$. In (a) we represent the flow circulation with arrows in the vehicle referential, and in (b) we depict V_z. Case Slick225 $H_w = 8mm$.

clearly in Fig.4.40(b)). This is due to the presence of an APR box whose lower edge is positioned in this location. It was not meant to be like that, the APR box should incorporate all particles along Z-axis, but we benefit from this mistake to appreciate the continuity of the velocity field at $Z = 5mm$ despite the change in the spatial resolution.

4.7.2 Slick225 for lower water depth

We run the simulation for the Slick225 at a lower water depth, here we choose $H_w = 3mm$ since it was observed experimentally that it is the limit before the change in regime in V_x. The numerical and physical parameters are given in Table 4.4. The total number

of particles is around 20M. We note that the width of the water puddle $L_y = 200mm$ is slightly lower than the tire's total width ($225mm$). This shouldn't be the case and it was unintentional. Luckily, the shoulder region does not seem to have dried as it will be seen thereafter, and we still can benefit from the results of this simulation.

Physical parameter	**Value**
Puddle dimensions (XY) plane	L_x=1500mm L_y =200mm
H_w	$3mm$
V_0	$8.33m.s^{-1}$
ρ_{water}	$1000kg.m^{-3}$
g	$9.81\ m.s^{-2}$
P_{tire}	$2.2\ bars$
$Load$	$380daN$

Numerical parameter	**Value**
$\Delta x_{SPH_{min}}$	$0.25mm$
$R/\Delta x_{SPH}$	3
C_0	$250m.s^{-1}$
k_{CFL}	0.375

Table 4.4 – Physical and numerical parameters

We give in Fig.4.41 a view in the plane (XY) of the $|\vec{V}|$ field. We can see that compared to Fig.4.37(b), the velocity near the tire seems higher in the central region for $H_w = 3mm$. However in the shoulders, it is quite the opposite and we note that $|\vec{V}|$ is higher for $H_w = 8mm$. We also observe that the WB length increased when the water depth increased (around $100mm$ for $H_w = 8mm$ and around $60mm$ for $H_w = 3mm$).

Moreover, if we subdivide the WB into DY1 to DY5 as we did in Fig.4.22(a) and we look at $V_x(x)$ in DY3 (center of the WB) and at $V_y(x)$ in DY1 (shoulder) we obtain results in Fig. 4.42. The experimental results are also plotted along with the numerical results for $H_w = 3mm$ and $N = 3$.

We observe in Fig.4.42(a) that the value of V_x near the tire is very close to the one obtained experimentally which was not the case for $H_w = 8mm$. The higher spatial resolution can partly explain this improvement in the results. However, we can see that the length of the WB is overestimated numerically. Indeed, the length of the region close to the tire where V_x is nearly constant is found higher in the simulations. And in opposition to $H_w = 8mm$ case, particles seem to have nearly the same velocity regardless of their altitude Z. This result is very interesting since if the velocity field is weakly inhomogeneous in the vertical direction Z in the major part of the WB, we can assume the same result to be also valid for the pressure field. Such a simplification could lead to a first determination of the hydrodynamic pressure through r-PIV measurements with the hardware used in this work, using time-resolved r-PIV, and even non-time resolved r-PIV measurements.

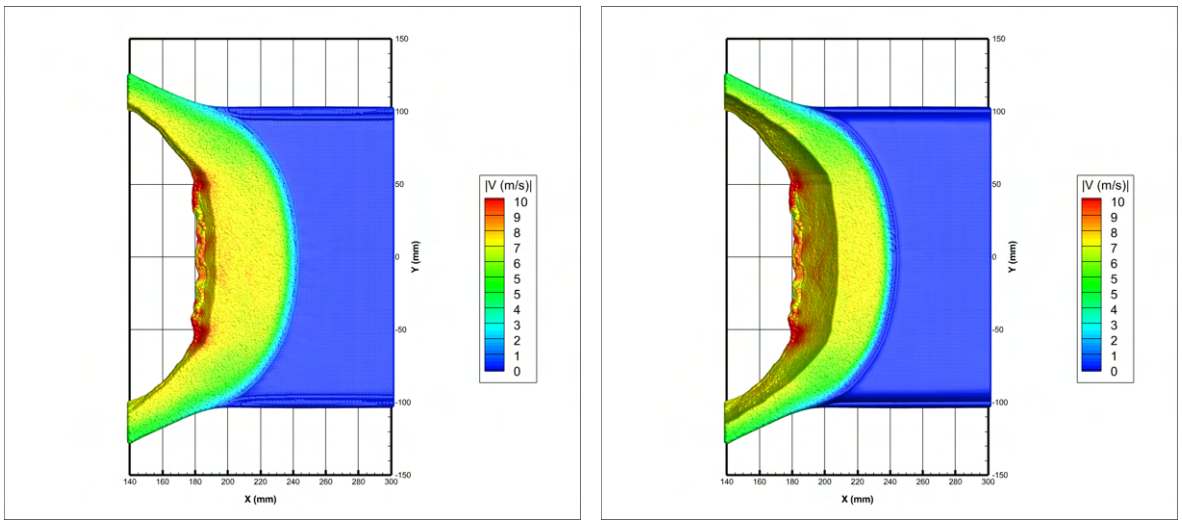

(a) (b)

Figure 4.41 – (XY) view of the Slick225 ($H_w = 3mm$) at $Z < 1mm$ (a) and $Z < 3mm$ (b) from the numerical calculation. The colormap corresponds to the $|\vec{V}|$ field. For clarity issues, only the fluid is represented (not the tire, nor the road), and also we limit the view between $X = 140mm$ and $X = 300mm$.

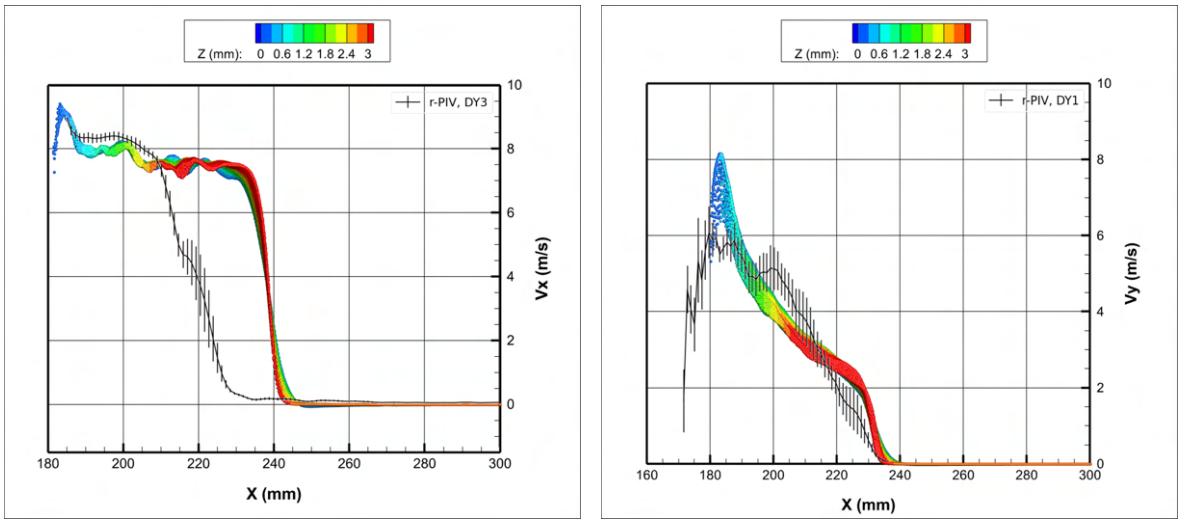

(a) (b)

Figure 4.42 – Evolution of V_x with X between $Y = -2.75mm$ and $Y = 2.75mm$ (a), and V_y with X between $Y = 47.5mm$ and $Y = 52.5mm$ (b). The colors represent the altitude Z of the particle, and each point represents an SPH particle. We overlay the corresponding r-PIV results with the error bars representing the standard deviation between the N runs. Case Slick225 $H_w = 3mm$.

Pressure is until now the key missing property for more exhaustive simulation/experiment comparisons.
Now if we look in the shoulder region (Fig.4.42(b)) we note that the numerical and experimental results are rather close with a linear decrease from the CPA frontier to the end of the WB especially with the r-PIV results. It is close to the tire that the gap between the results increase and we find that V_y is overestimated numerically which is the opposite from the $Hw = 8mm$ case. Nevertheless, we note that the number of repetitions is low ($N = 3$) and the standard deviation is high, especially in the CPA/WB frontier, which is a very challenging region for the r-PIV measurements as already mentioned before.
Also, we give in Fig.4.43 an XZ cut view in the middle of the WB. as it have been done in the case $H_w = 8mm$ (Fig.4.40). It is not clear if there is a change in the regime between $H_w = 8mm$ and $H_{=}3mm$ as the velocity field V_z is very similar between the two configurations.

To conclude this section, we have seen that the global behavior of the flow is well captured numerically, especially for $H_w = 8mm$. The WB characteristics are very close between numeric and experimental results with the right dimensions and velocity values in the central region and the shoulders as well. However, due to not only the relatively coarse spatial resolution but also the absence of a viscous model, secondary flow circulation was not well captured and we couldn't have more information about the hypothetical horseshoe vortex or any unsteady phenomenon. To help us answer some of the questions that remain concerning the slick tire, the following section is dedicated to the Time-Resolved r-PIV and its application to this smooth tread case.

4.8 Time-Resolved r-PIV: a feasibility

As introduced in Section 3.6.1, we did in the present work the first trials with the Time-Resolved r-PIV system (TR-PIV). The objective was not only to test a new measurement tool but to obtain some information about the stationary character of the flow. The images recorded with the TR-PIV are consisted of 2 frames generated successively, but at a recording rate ($1kHz$ at least) sufficient to be able to carry out the correlation with frame 0 of two successive images. This is not possible in classic r-PIV where the correlation is applied to the 2 frames of the same image. Note that this is an opportunity to study the difference between the velocity fields obtained by using a correlation between

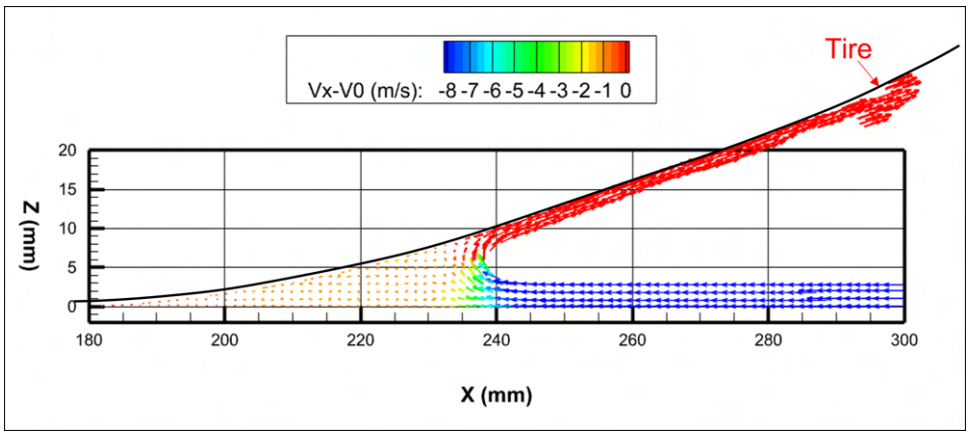

(a)

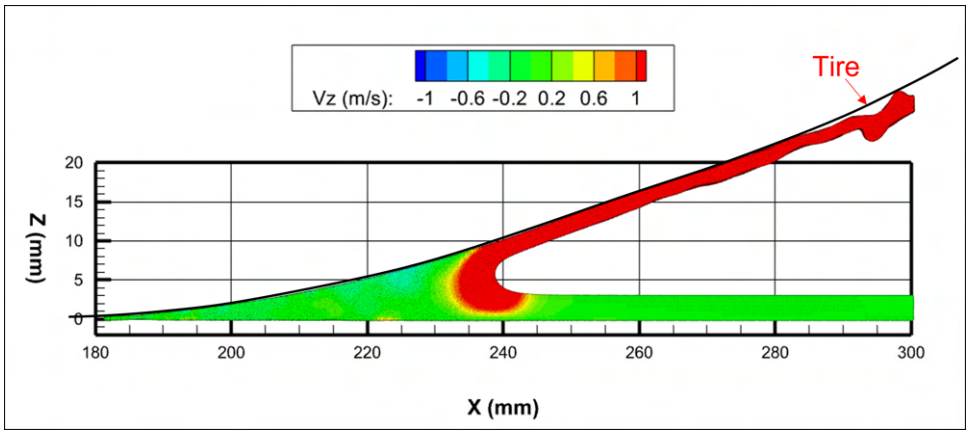

(b)

Figure 4.43 – XZ view in the middle of the WB between $Y = -2.75mm$ and $Y = 2.75mm$. In (a) we represent the flow circulation with arrows in the vehicle referential, and in (b) we depict V_z. Case Slick225 $H_w = 3mm$.

frames or between successive images. This possibility is specific to the TR-PIV, and it allows us to compensate for the low quality of one of the two laser illuminations. This was the case during our feasibility tests. Furthermore, due to very bad weather conditions during the TR-PIV test campaign, few images were fit to be post-processed and analyzed. Indeed, the wind and rain downgraded the images' quality and added difficulty to what was the first attempt to use the TR-PIV in a hydroplaning application.

We will focus on the results obtained with the smooth tire Slick225 at H_w=7mm. A comparison between results obtained with the correlation between frames and the correlation between successive images is conducted. Moreover, we present a comparison between results obtained with the TR-PIV and the r-PIV. The recording rate is fixed to $1kHz$ for

all the results presented below.

4.8.1 Raw images

We present here a brief comparison between a raw image obtained with the TR-PIV and one obtained with the r-PIV for the Slick225 at $V_0 = 8.33m.s^{-1}$ and $H_w = 7mm$. As mentioned in section 3.6, the dynamic range and the spatial resolution of the fast camera are lower than that of the classic one. We give in Fig. 4.44(a) an example of an intensity image (Frame 0) from r-PIV measurements. We define the rectangular region in red in which we plot the evolution of the grey-level intensity along the X-axis averaged in the Y-direction. We can see that in the WB the grey-level intensity reaches nearly 1000 counts (green area), and in the CPA where it is the lowest, it is around 400 counts (Fig. 4.44(b)). On the other hand, when we look at an image from the TR-PIV measurement (Fig. 4.45(a)), we can see that in the CPA, the grey-level intensity is lower than 20 counts, and in the WB it reaches 200 counts (Fig. 4.44(b)).

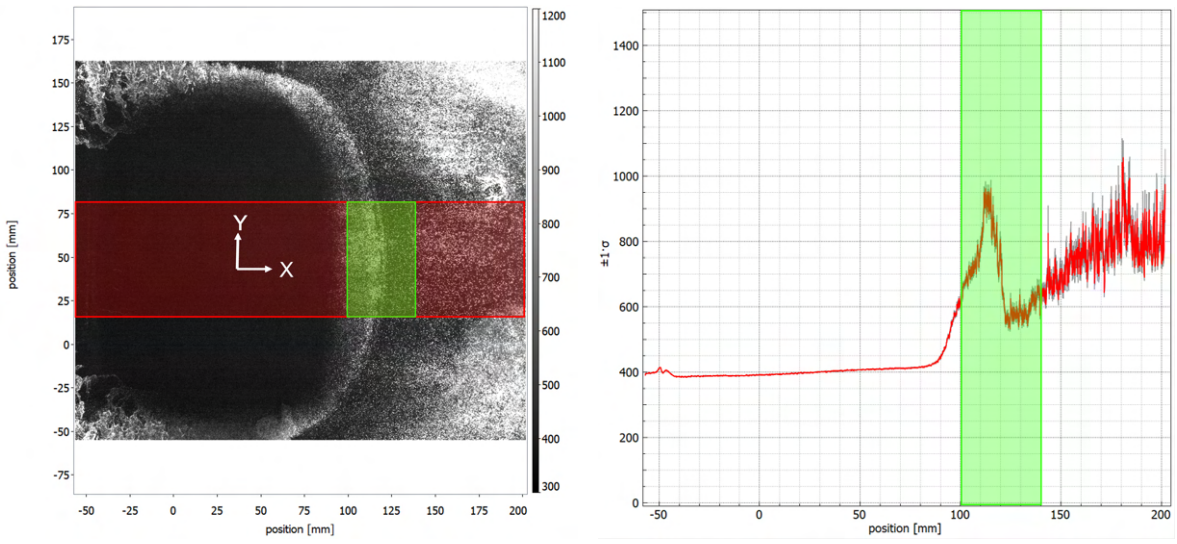

(a) (b)

Figure 4.44 – Raw intensity image (Frame 0) from r-PIV of the Slick 225 at V_0=30km/h and H_w=7mm (a), and intensity levels in the selected region (b)

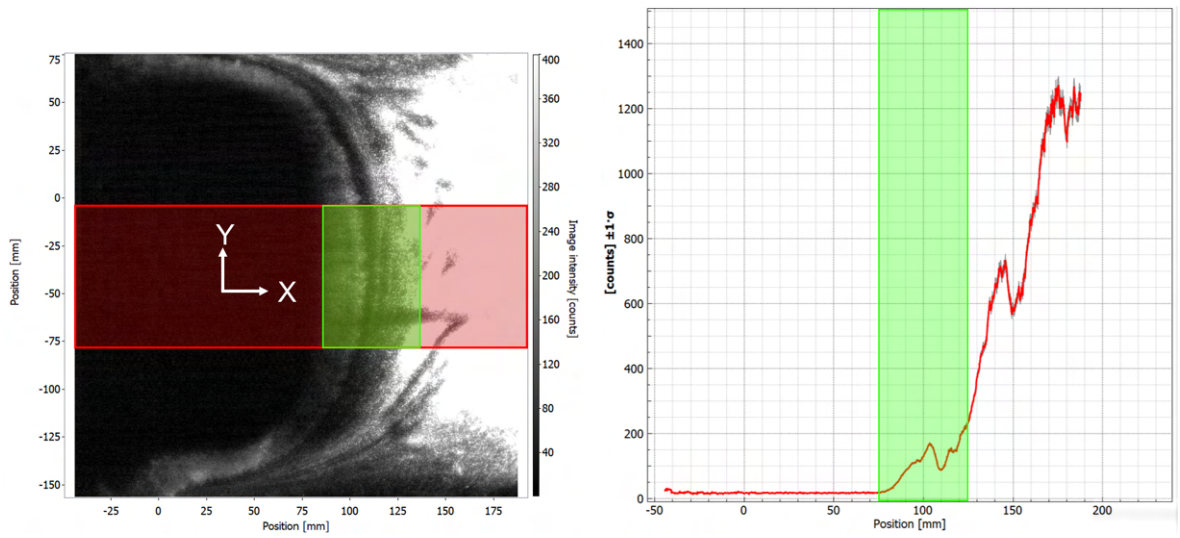

(a) (b)

Figure 4.45 – Raw intensity image (Frame 0) at t_{25} from TR-PIV of the Slick 225 at V_0=30km/h and H_w=7mm (a), and intensity levels in the selected region (b)

4.8.2 Masking strategy

In the case of the TR-PIV, the masks are generated semi-automatically. The idea is to use the same mask for all images of the same series since we suppose that the CPA is only translated constantly longitudinally during one rolling. The first mask is created manually on the software DaVis (geometric mask) upon one of the images of our series. The chosen image should present a complete CPA. This operation is identical to the one for the r-PIV in the case of the Slick tires used in the previous sections. The mask is then imported on python and translated along the X-axis to produce successive masks for a complete temporal set. Knowing the recording rate f=1kHz and the car speed V_0=8.33$m.s^{-1}$, we obtain the offset δx between two consecutive masks:

$$\delta x = \frac{V_0}{f} = 8.33mm \tag{4.9}$$

Finally, these masks are imported on DaVis and then applied to the images of the series (Fig. 4.46).

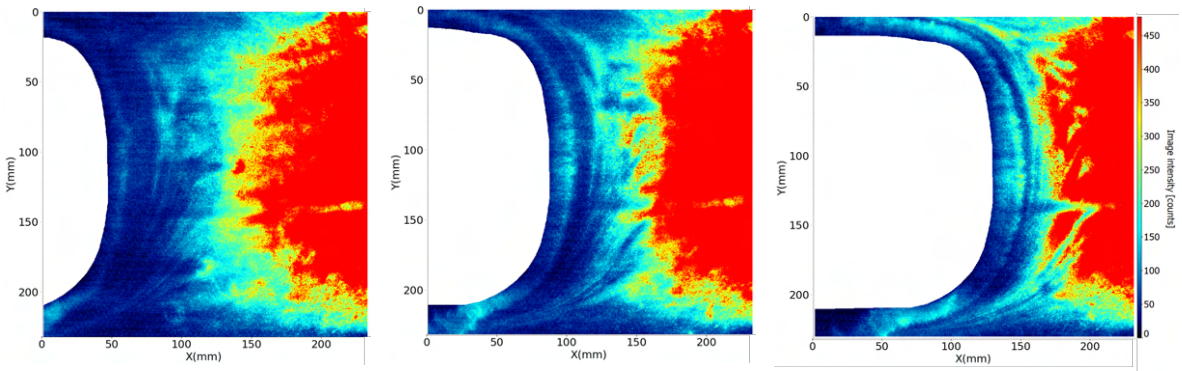

(a) (b) (c)

Figure 4.46 – Masks applied on raw images from the TR-PIV (Frame 0): image t_{15} (a), image t_{20} (b) and t_{25} (c).

4.8.3 Effect of the correlation method

In this section, we will study the difference between the two correlation methods that the TR-PIV can offer in comparison with the r-PIV as stated just above. The first method is to generate the velocity field by correlating two successive images, in this case, we only consider frame 0 of each image and do not work with the second frame. This can be interesting, e.g., in a case in which the two successive frames have an important illumination difference. We will call this method F0. We give in Fig. 4.47 a capture of the two frames in the same intensity scale. The second method is to correlate for each image its two frames, just like in r-PIV, and generate the associated velocity field. The advantage of this method is that since the δt between the two illuminations is smaller than $N{=}\frac{1}{f}{=}1ms$, the quality of the correlation should be enhanced (smaller displacement of the fluorescent particles). The time interval δt is fixed according to the vehicle speed such as for $V_0 = 8.33m.s^{-1}$ it is equal to $300\mu s$. We call this method F0-F1.

For the comparison between the two methods, we choose the cross-correlation parameters of the REF case in Table 4.1. First, we give respectively in Figures 4.48(b) and 4.48(c) the velocity fields $|\vec{V}|$ corresponding to the instant t_{22} for the F0 and the F0-F1 method. We choose the instant t_{22} arbitrarily between all images where the WB is complete. We give as well the $|\vec{V}|$ field obtained with the r-PIV in Fig.4.48(a). First, when comparing the TR-PIV and the r-PIV fields, we observe that i) in the region close to the CPA/WB frontier, the velocity field in the TR-PIV case is not as homogeneous as it is in the r-PIV case. Moreover, ii) the velocity level further from the CPA/WB frontier is higher in the TR-PIV case ($7.5m.s^{-1}$ against $6m.s^{-1}$ for the r-PIV). And iii) in the shoulder region

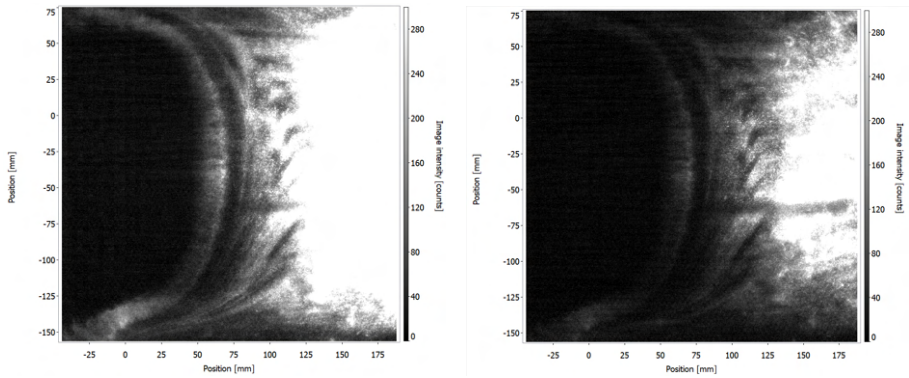

(a) t_{21} Frame 0 (b) t_{21} Frame 1

Figure 4.47 – Raw image at t_{21} of the Slick225 at V_0=30km/h and H_w=7mm: Frame 0 (left) and Frame 1 (right), δt = 300μs

close to the CPA/WB frontier, the velocity field is higher than in the center region in the case of the r-PIV measurements. This is not very clear in the TR-PIV measurements.

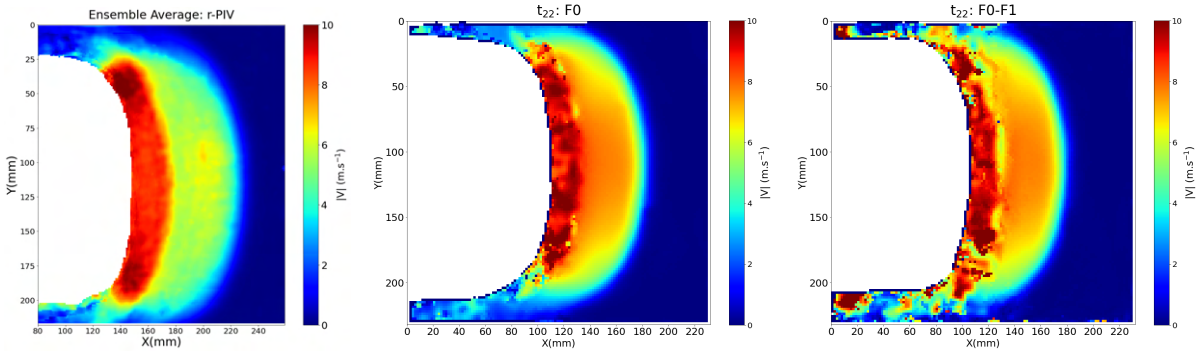

(a) (b) (c)

Figure 4.48 – Velocity fields $|\vec{V}|$ from respectively the r-PIV measurements (a), the TR-PIV with the F0 method (b) and the F0-F1 method (c) at the instant t_{22}. The result obtained with the r-PIV is for $N = 10$, $V_0 = 8.33m.s^{-1}$ and $H_w = 7mm$.

Concerning the comparison between the F0 and the F0-F1 methods, we observe that far from the CPA/WB frontier, the velocity fields obtained in both cases are rather similar. However, close to this frontier, we can see that when using the F0-F1 method, the velocity field is even less regular and present more disruptions. To see if this phenomenon is inherent to the correlation method and is present for all images of the series, we plot the V_x profiles Y-averaged in the central region. The horizontal bands for the space averaging

are highlighted in red rectangles in Figures 4.49(a) and 4.49(b). We give in Fig. 4.49(c) the translated curves of V_x Y-averaged in the central region for F0 and in Fig. 4.49(d) for F0-F1. The curve corresponding to the image p of the series is shifted by $-p.\delta x$ in order to overlay all the V_x profiles in each series. We give as well the V_x profile corresponding to the r-PIV measurements.

First, if we focus only on one of the two methods and compare the V_x profiles of different

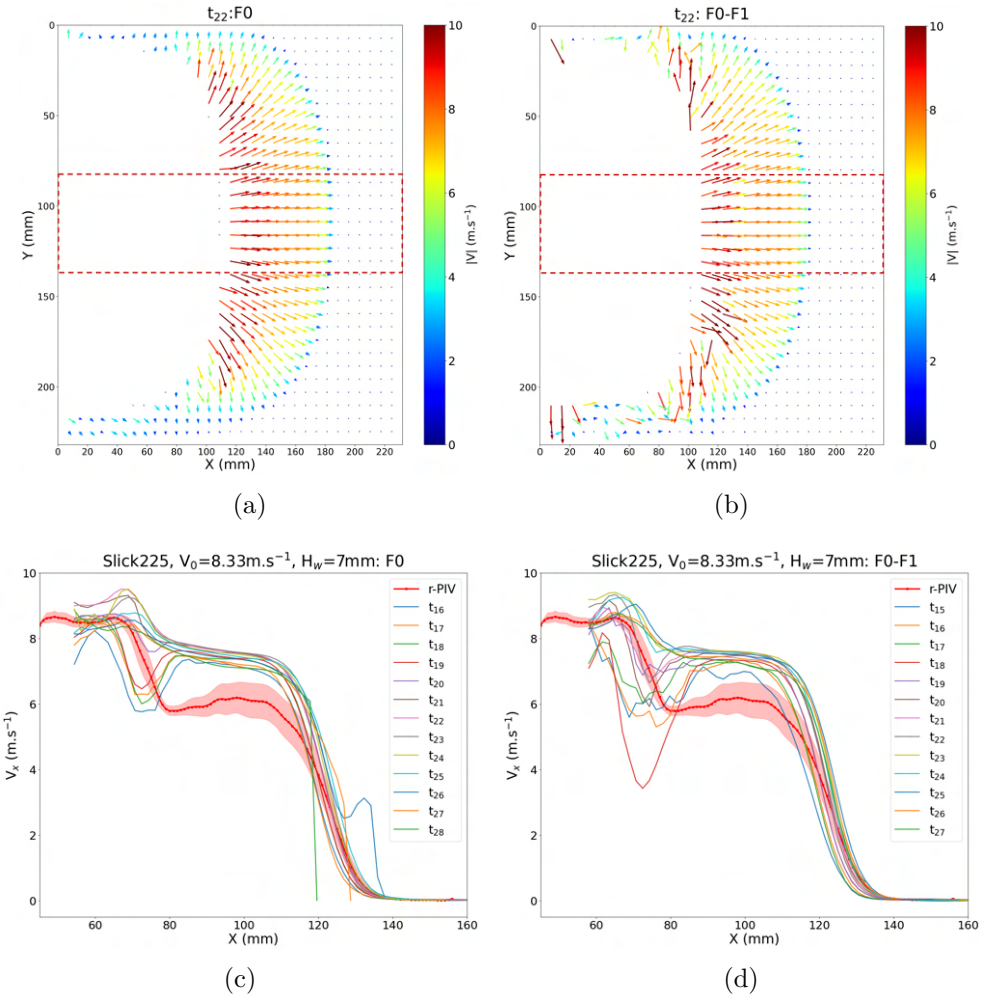

Figure 4.49 – In (a) and (b) the velocity fields $|\vec{V}|$ for respectively the F0 and the F0-F1 method at the instant t_{22}. For clarity purposes, only one arrow over 4 is plotted. We highlight with the red dotted lines the region where we calculate the space averaging along the Y-axis. And in (b) and (c) we give the results obtained from the space averaging regarding the V_x profiles for respectively the F0 and the F0-F1 method. The equivalent results obtained with the r-PIV are also given.

instants, we can see that there is a phenomenon that appears around $X = 70mm$. Indeed, in the F0 case, the profiles corresponding to the first instants (t_{16} to t_{20}) show a sudden drop in V_x that disappears progressively over time. Whereas in the F0-F1 case, this drop in V_x is even more important and stays longer in time. However, a rather steady state is reached and the V_x profiles become similar. It is less the case of the F0-F1 correlation. It is difficult to say if there is indeed a transitional unsteady regime in the WB during the rolling of the tire, or if it is due to some measurements bias in relation to the adverse wind conditions for these measurements. The uniformity of the water depth and the value of the water depth itself were poorly controlled during these experiments. In addition, we note that for the first instants, the tire is at the left limit of the frame where the illumination is at its lowest, and therefore this can decrease the cross-correlation quality. Furthermore, when the TR-PIV results are compared to the r-PIV we can see that the velocity levels are higher not only close to the tire but also far from it especially from t_{20}.

4.8.4 Analysis of the time-resolved large-scale flow structure using the streamlines

One of the objectives of the TR-PIV measurements is to study the evolution of the flow with time since for one rolling we are able to capture multiple images at different instants. After looking at V_x in the middle of the WB, we look at the streamlines generated in the vehicle referential (Fig.4.50). We can see that the streamlines' structure in the moving frame is rather similar from t_{22} to t_{27}. This suggests for such a tire tread that the main source of variability of the flow in the reference frame attached to the ground is mainly due to its convection at speed V_0 imposed by the car motion, at least in a wide central part of the WB. Such a result should be checked with further measurements done under more satisfying weather conditions, and for more representative tire models for which a part of the incoming flow is directed inside grooves. Measurements at higher frequency f should also be conducted to be able to capture possibly existing phenomena at a smaller time scale. It is believed that under good weather conditions such measurements could be done at a repetition rate up to $5kHz$, without loss of the laser power.

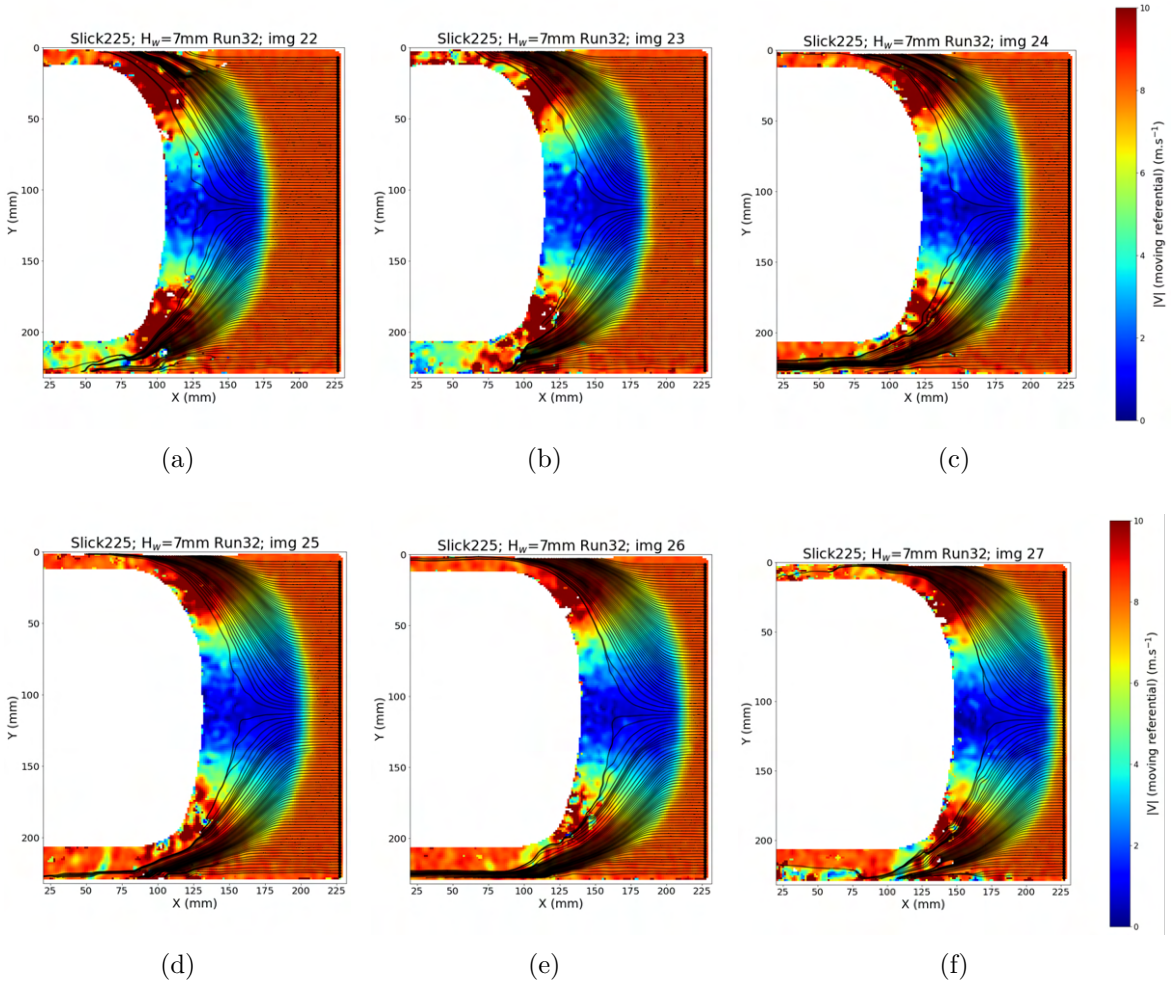

(a) (b) (c)

(d) (e) (f)

Figure 4.50 – Streamlines generation in the vehicle referential for the Slick225 at $V_0 = 8.33m.s^{-1}$ and $H_w = 7mm$. The colormap corresponds to $|V - V_0|$. The instants t_{22} to t_{27} are depicted. The F0-F1 method is used.

4.9 Conclusion

In this chapter, an analysis of the flow structure inside the WB of slick tires has been exposed. It has been shown that the region near the CPA/WB frontier is very challenging due to the lack of illumination and required special attention in the post-processing phase. The experimental analysis exhibited a rather complex circulation of the flow that we separated into a planar primary flow and a secondary out-of-plane flow. In regard to the three-dimensional behavior of the water flow, a hypothesis about the existence of a horseshoe vortex just in front of the tire was emitted from the experimental results and

mass budget analysis. We have tried to corroborate this assumption via numerical results, but it seemed that the numerical model still needs to be improved (e.g., introducing the viscosity) with a more refined spatial discretization to better capture the very local phenomena experimentally observed. Nevertheless, the numerical results seemed qualitatively rather satisfying concerning the overall shape of the WB and the fluid velocity field. From a pure parametric point of view with experimental results, we have pointed out the impact of the water depth on the WB structure, highlighting a limit value that beyond it, the streamwise velocity profile changes.

Another important point was dedicated to the width effect, emphasizing the change in the spanwise flow drainage as a function of the tire width. The different questioning about the three-dimensional flow circulation led to the introduction of the mass budget analysis as an interesting tool to quantify the different water ejections in and out of plane from our 2D r-PIV measurements. We were able to express inside the WB the mass budget performed and include out-of-plane terms. This resulted in the quantification of the spanwise ejection in comparison with the out-of-plane circulation. Such analysis was conducted for the different cases of slick tires. This allowed quantifying such budget as a function of the tire width and the water film height. We have observed that when the water height increases, the drainage to the shoulders increases too, while the contribution of ascendant flow rate decreases. The same evolution has been observed when decreasing the tire width. Maximum regions of water lateral expulsion have been shown for the increased tire width using the B_y quantification, which can lead to some tread design rules about the groove's optimal position and direction.

Finally, the TR-PIV has been tested for the first time in the hydroplaning framework, despite adverse weather conditions, and more particularly for the slick tire study. The technical feasibility of this method has been first proven and images of the flow around the slick tire have been recorded with a repetition rate of $1kHz$. The time-resolved images constitute very powerful outputs to answer questions concerning the flow variability between independent runs or for a single run. And the first results showed that apart from the CPA/WB frontier that presents some singularities, no significant unsteady phenomenon has been observed in a frame convicted at the car speed. Nevertheless, it is clear that such measurements have to be improved and optimized before confirming such results. These preliminary tests certainly showed the high potential of the TR-PIV to enrich experimental results and be able to compare more quantities with the numerical simulations. For example, the low time-variability of the velocity field structure during

one run can provide some useful guidelines for the direct evaluation of the pressure field inside the WB using r-PIV measurements.
After analyzing the flow structure of a WB in the case where the tire tread is smooth and does not contribute to the water drainage, we extend our study in the next chapter to the case of a summer tire with a longitudinal tread.

Chapter 5

Case of a longitudinal tread

In the previous chapter, we studied the case of a smooth tire and focused our analysis on the water-bank region. Starting with slick tires is a good strategy to have an in-depth look into the physics involved when rolling over a water puddle, however, they are mostly used for high-performance driving and are not very representative of the daily usage in passenger cars. Tires with sculptures are the most widespread, and a large variety of tread patterns exist on the market in order to respond to different requirements and driving conditions. For example, directional tread patterns (designed to roll forward in one direction only) have very good handling on snow, while symmetrical tread patterns are more efficient regarding the rolling resistance and wear (Horne [54]). Therefore, some design elements like the groove ratio and the shape of the tread (symmetrical, directional...) have an important impact on wet grip performance (Maycock [80],Fwa et al. [36]). However, these same parameters may degrade other tire performances like the dry grip highlighting the difficult balance designers have to find between the multiple performances to satisfy (dry grip, wet grip, noise, comfort, wear...) and certifications to pass (Wies et al. [134]). In the present chapter, we study the case of a tire with longitudinal tread, MICHELIN Primacy 4 (PCY4), a commercial summer tire. In Cabut et al. [11] [10], a thorough investigation of this tire in both new ($h = 8mm$, $H_w = 8mm$) and worn states ($h = 2mm$, $H_w = 1.5mm$) is proposed based on experimental results obtained with the r-PIV. The velocity fields inside the grooves are analyzed using ensemble averaging performed over a set of independent snapshots, recorded with the same operating parameters. In the present study, we focus on the worn state of the tire ($h = 2mm$) rolling over a puddle of $H_w = 1.5mm$, representative conditions encountered by the customers. A comparison with numerical results is provided based on the coupled SPH-FE simulations resulting in an investigation of the physics driving this phenomenon and also an insight into our tools' limits. Some numerical parameters were investigated in a testing case and a new physical phenomenon was taken into account to better fit experimental results.

5.1 Tire model

The PCY4 225/45 R17 is a summer tire with a symmetrical tread (Fig.5.1) with four longitudinal grooves (oriented in the direction of rolling) of two types and symmetrically disposed that we note: type B the largest ones (around $12mm$ of width) close to the tire center, and type A narrower ($6mm$ of width) and close to the shoulders. On the shoulder area, transversal grooves exist and connect with A-type grooves noted type C (around $3-4mm$ of width). Finally, very thin transversal grooves exist linking two B-type grooves or an A-type with a B-type groove: the sipes. The width of these sipes is too small to contain a sufficient number of fluorescent particles and to allow velocity measurements. As stated before, we are interested in worn tires. The worn state is obtained from buffing new tires in order to control the tread depth and reach the target of $h = 2mm$. This value is very close to the WI height and is, therefore, representative of the usage. It is also frequently considered when studying worn tires ([122]). Among the modifications that appear on the tread pattern when obtaining this worn state, there is the disconnection of grooves A and C, and the near disappearance of sipes (Fig.5.1).

5.2 Numerical setup and post-processing phase

5.2.1 Numerical setup of the PCY4

We give in Fig.5.2 a 3D view extracted from coupled SPH-FE simulation in the case of the PCY4 tire. The input parameters for the numerical model are given in Table 5.1. The total number of particles is around 5.5M particles. The total computation time is about 400h on 48 CPUs for the SPH solver, 20 CPUs for the FEM solver, and 1 CPU for the coupling algorithm. The high calculation cost is in part due to the FE solver limitations imposed by its implicit nature. An explicit scheme would certainly reduce calculation time, but it would also alter the stability of the simulations. The tire mesh has 478 620 solid elements. Regarding the tread geometry, some simplifications have been considered compared to a real tread design:

— The wear indicators are not modeled for simplification purposes. Indeed, the worn state is obtained by numerically buffing a new tire which does not include these WI.

— The spacing between C-type grooves is constant. In real tires, the spacing varies to satisfy some noise requirements and other technical criteria.

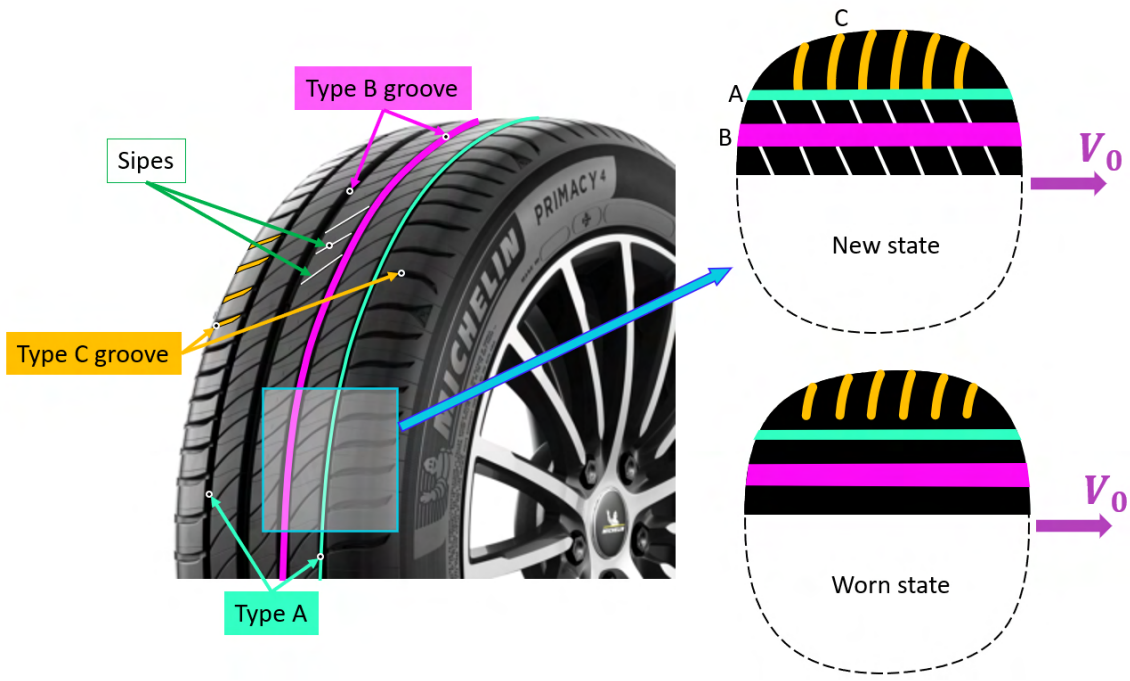

Figure 5.1 – Details of the PCY4 tread design with highlights of the different groove types: A (green), B (pink), C (orange), and sipes (white). On the right is a simplified sketch of the CPA for both new (upper part) and worn (lower part) states. Since the tread is symmetric, only the upper half of the CPA is sketched for simplification issues.

— The sipes are ignored in the tire mesh.

Physical parameter	**Value**
Puddle dimensions (XY) plane	L_x=1500mm L_y =200mm
H_w	1.5mm
V_0	13.89$m.s^{-1}$
ρ_{water}	1000$kg.m^{-3}$
g	9.81$m.s^{-2}$
P_{tire}	2.4$bars$
Load	480daN

Numerical parameter	**Value**
$\Delta x_{SPH_{min}}$	0.25mm
$R/\Delta x_{SPH}$	2.11
C_0	250$m.s^{-1}$
k_{CFL}	0.375

Table 5.1 – Physical and numerical parameters

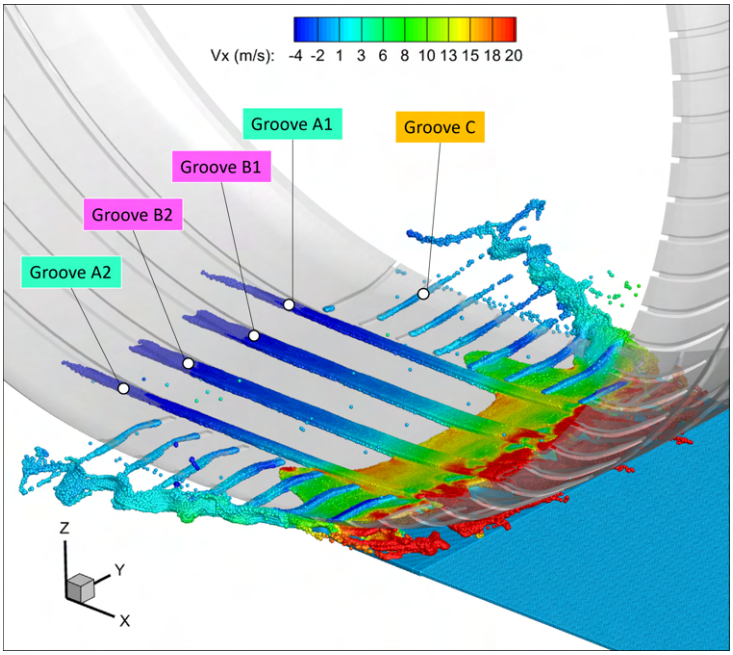

Figure 5.2 – Snapshot from simulation result: velocity field V_x for the PCY4 at $V_0 = 13.89m.s^{-1}$ and $H_w = 1.5mm$.

5.2.2 Post-processing phase and velocity extraction

In order to compare experimental and numerical data of dynamic flows, it is important that we make sure we are comparing identical values. This is our issue concerning velocity fields. On one hand, every experimental run trial results in N velocity fields for one tire, at a given H_w and V_0, but the camera shot does not happen strictly at the same time for every rolling. This results in the X-offset between the PIV frames that we addressed in Chapter 3. On the other hand, our numerical simulations last around $0.01s$ with a graphic output every $10^{-4}s$. By completing the transitional phase, we are at about $15ms$ of the total simulation time for the PCY4 at $V_0 = 13.89m.s^{-1}$ for example. Indeed, we give in Fig.5.3 the time history of different numerical outputs to evaluate if the steady state has been reached or not. At first, the tire gradually rises on the puddle, the grooves start to fill and the water is ejected towards the front and the shoulders. The duration of the transition phase mainly depends on the water film thickness H_w for a set of numerical parameters. We can see in Fig.5.3(a) that the fluid lift has reached a rather constant value from $T = 16ms$ around $80daN$. The road lift (Tire loading - Fluid lift) has nearly reached a constant value of $400daN$. We can also follow the evolution of the contact patch loss S/S_0 in Fig.5.3(b). These global values help us determine if a steady state is attained or not,

however, we cannot be sure that kinematically a steady state is reached. A time history of the velocity inside the longitudinal groove for example should be done to determine if the transitory phase is over. In the present study, we determine the establishment of the regime by looking at the global outputs as in Hermange et al. [49].

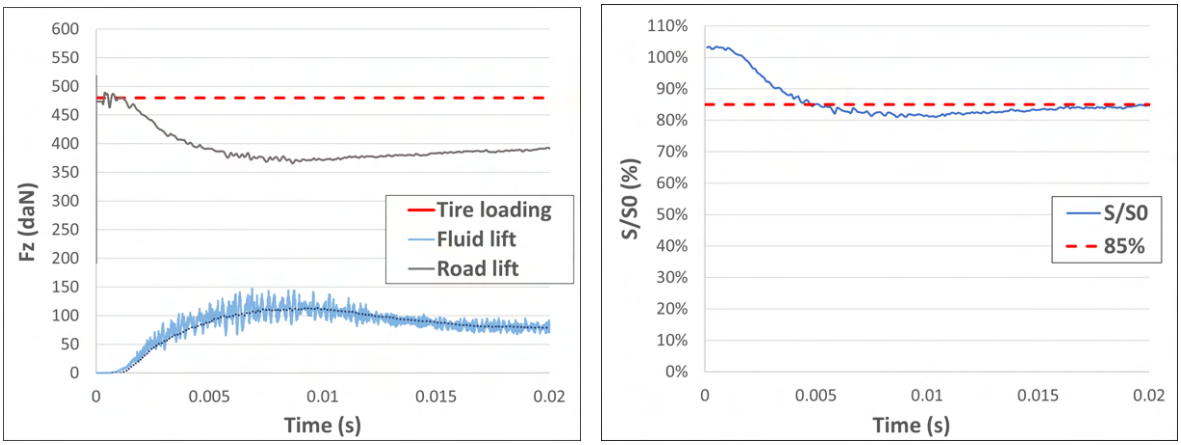

(a) (b)

Figure 5.3 – Time history of the fluid and road lift (a) and for the contact patch area for the PCY4 at $V_0 = 13.89m.s^{-1}$, $H_w = 1.5mm$: numerical results

When we reach the regime establishment, we have a given number of outputs that we can exploit for comparison with experimental results, either by time-averaging them or by choosing a single one to work with. Moreover, the r-PIV measurements result in a 2D velocity field and our simulations are in the 3D space. This means that we have access to different Z-locations inside the puddle. We should then determine if we need to make an average of the velocity field along the water film thickness aside from the time averaging operation as well.

To build a comparison strategy between a 2D velocity field obtained experimentally and a 3D time-resolved velocity field obtained numerically, we choose to construct a 2D velocity field from the numerical calculations using so-called "slices". A slice is a plane that we define in space over which a Shepard interpolation (2.25) is calculated on the neighboring SPH particles. We give in Fig.5.4 a configuration where three slices were defined inside the water puddle, with a normal following the Z-axis, at different altitudes, and centered in the CPA. By doing so, at each Z-location we obtain a 2D velocity field that we can compare with r-PIV results. In Fig.5.5 we give an example of a velocity field obtained with two slices, respectively positioned at locations $Z = 0.25mm$ and $Z = 1.5mm$ and

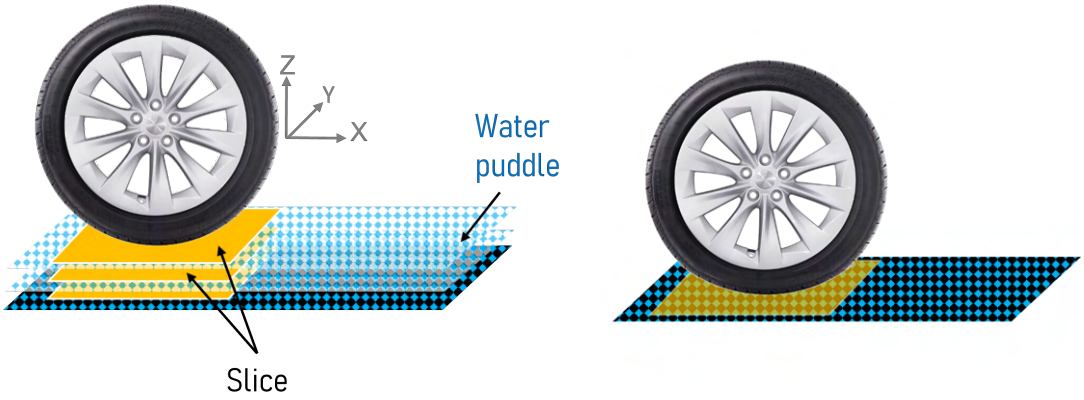

(a) Exploded view (b) Real view

Figure 5.4 – Scheme of a slices configuration in exploded (a) and real (b) views.

centered around the CPA. Both slices are $300mm \times 300mm$ in the X and Y directions. As mentioned above, it is possible to create slice post-treatments over multiple time steps

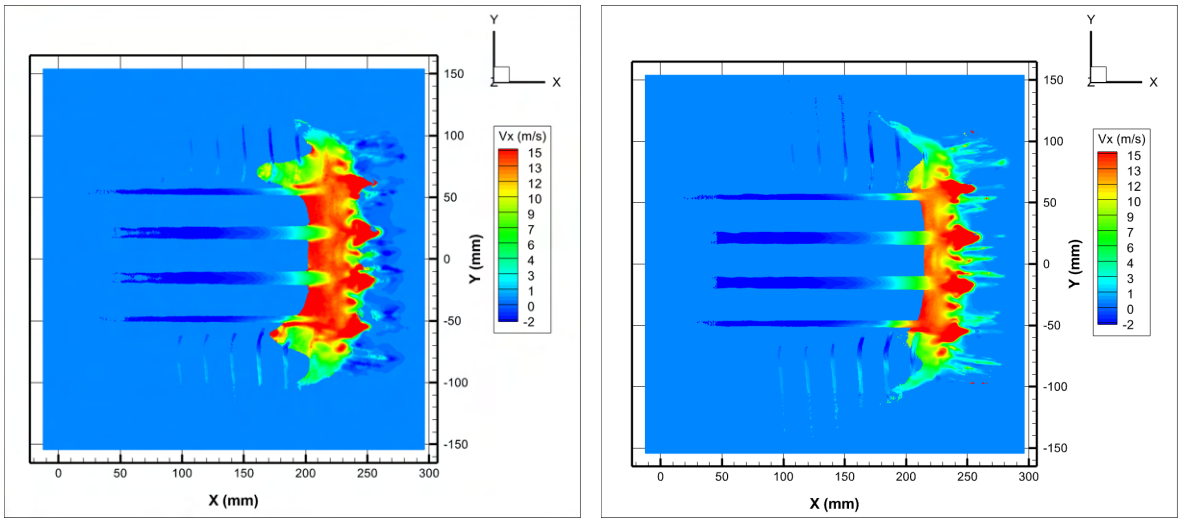

(a) $Z = 0.25mm$ (b) $Z = 1.5mm$

Figure 5.5 – V_x field interpolated on a slice for the PCY4 case at $V_0 = 13.89m.s^{-1}$ and $H_w = 1.5mm$. On the left the slice is positioned at $Z = 0.25mm$ and on the right at $Z = 1.5mm$.

and over different Z altitudes for each time step. Therefore, it is possible to generate an averaged velocity field over space and time from numerical results. The slice is usually translated at velocity V_0 to always have the same relative position to the tire. However, if we are interested in one of the longitudinal grooves, and if we suppose that we reached

a steady state, only one time step is enough in this case.

5.3 Comparison between numerical and experimental results at a fixed (V_0,H_w)

5.3.1 Contact patch area

First, we compare the contact patch evolution between the wet and dry configurations both numerically and experimentally (Fig.5.6). The experimental results are obtained following the rest protocol detailed in [50].

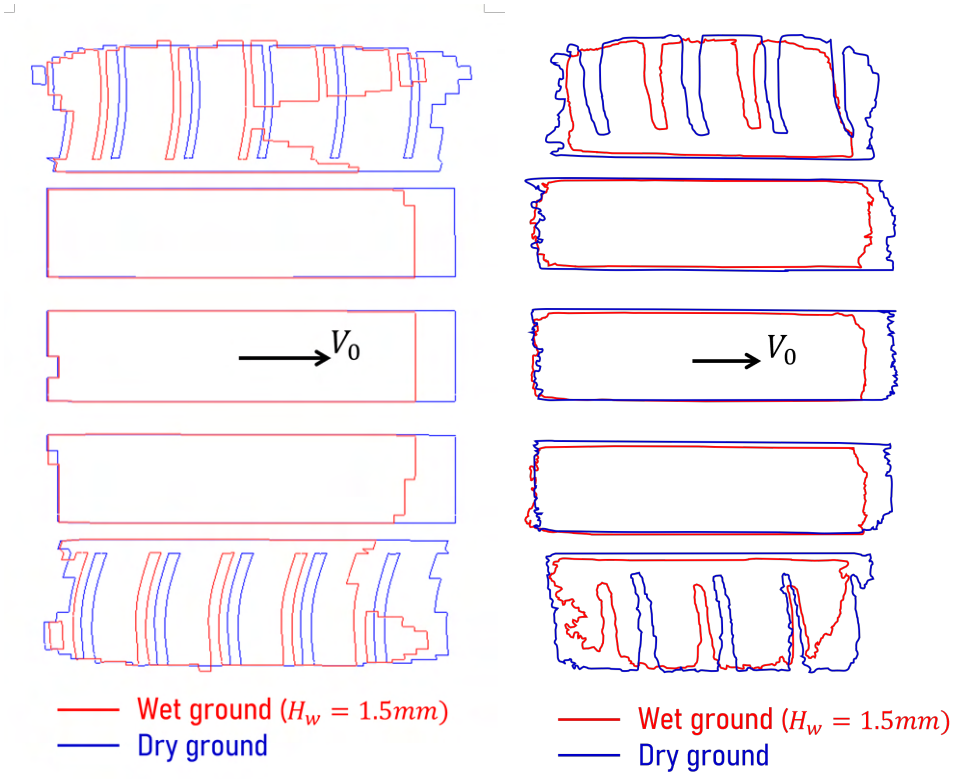

(a) Numerical (b) Experimental

Figure 5.6 – PCY4 at $V_0 = 13.89m.s^{-1}$, $H_w = 1.5mm$.

Moreover, the loss of contact patch is a global parameter often used to evaluate the wet performance of a tread pattern against another one. It is the ratio of the actual contact patch area S and a reference contact patch area S_0 calculated for a dry rolling at the same vehicle speed. We give in Table 5.2 the results obtained numerically versus

Table 5.2 – Comparison of the numerical and experimental contact patch area and length for the PCY4 at $V_0 = 13.89 m.s^{-1}$.

	$S/S_0(\%)$	$L_x(mm)$	Tire load (daN)
Numerical	85%	103	480
Experimental	89%	85	380

in-site measurements (protocol detailed in [50]). We also give L_x the length of the CPA to compare. We can see that for S/S_0, the numerical results are very close to the experimental ones, however, the contact loss seems to be a little underestimated numerically, especially in the X direction i.e. L_x. We note that in the case of the PCY4, not the exact same load has been applied on the tire experimentally and numerically (25% higher in r-PIV measurements). This certainly impacts the results as it can explain the difference in L_x. This difference in the tire load was not intentional.

5.3.2 Overall velocity field

We give in Fig.5.7 the velocity fields obtained experimentally (on the left) and numerically (on the right) for the PCY at $V_0 = 13.89 m.s^{-1}$, $H_w = 1.5mm$. Regarding the r-PIV results, the velocity correlation is preferred here to generate an ensemble averaging over the $N = 4$ runs. An automatically generated mask on each image has been applied as detailed in Section 3.5.1. Regarding the numerical velocity field, different slices have been included in the post-processing to assess the evolution of V_x^* at different altitudes Z_i $(1 \leqslant i \leqslant 9)$ from the ground with regular spacing. We note that the interpolated velocity fields given in Fig.5.5 correspond to the present rolling conditions. We draw the reader's attention to the difference between this space averaged result and the two local slice results depicted in Fig.5.5 (obtained with identical rolling conditions).

We can observe that the general water circulation is respected in the WB where the ejection is towards the front of the tire in the center and then towards the shoulders when we get further from the center. In the B grooves, we see that close to the WB the velocity increases, and then it decreases when moving to the rear of the tire. The present resolution chosen for the r-PIV processing does not give satisfying results in C grooves, whereas numerically we have a clear water drainage from the CPA towards the shoulders and we see it increasing as the groove is closer to the WB. However, we will not be interested in these

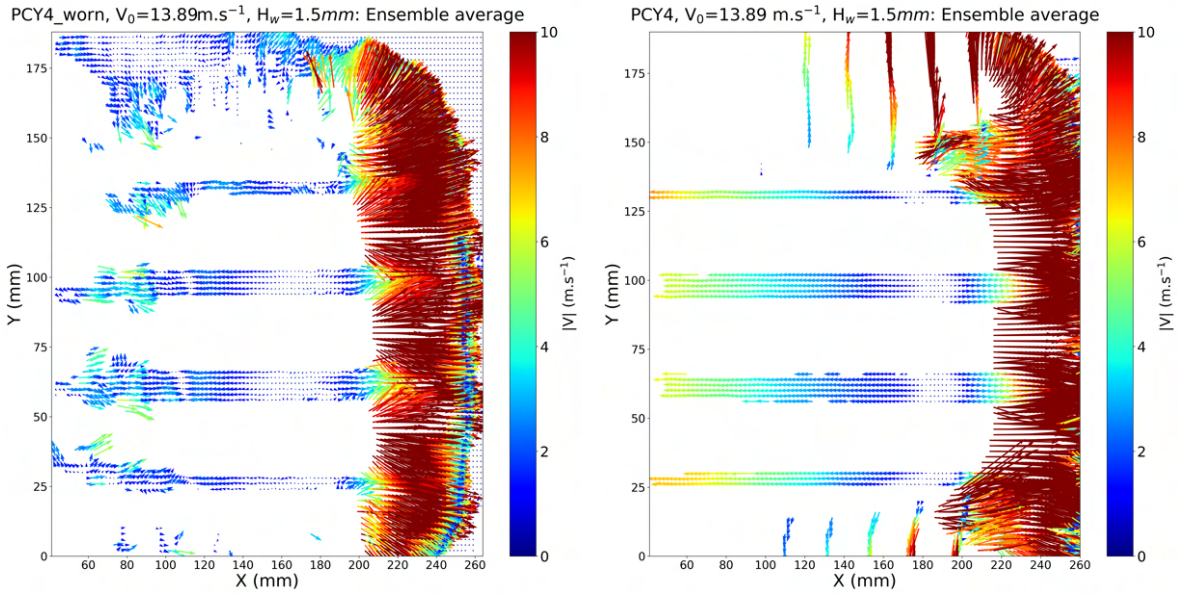

(a) Experimental (b) Numerical

Figure 5.7 – On the left, the ensemble averaged velocity field obtained experimentally, and on the right, the interpolated velocity field space averaged over the slices obtained numerically. For clarity issues, one vector over 4 is plotted in (a) and one over 8 in (b): PCY4 at $V_0 = 13.89m.s^{-1}$, $H_w = 1.5mm$.

grooves for the present. We can also see on the numerical field that between $Y = 135mm$ and $Y = 155mm$ (and between $Y = 10mm$ and $Y = 20mm$), a water film enters between the tire and the ground which is not observed experimentally. This may be caused by an overestimated contact pressure in the shoulders (between $Y = 155mm$ and $Y = 175mm$ in the upper half) and thus a tire tread deformation that is not representative of the reality letting the fluid enter this region. In addition, we observe that experimentally the fluid is entering the CPA at the rear of the tire inside the longitudinal grooves whereas numerically the fluid is still pushed outside the CPA. Last but not least, another difference is observed in the region in front of the ribs. We can see that experimentally, the flow is significantly drained laterally whereas numerically it is mainly directed streamwise. This may affect the fluid velocity at the grooves' entrance.

We give some XZ views from simulation results in order to help visualize the out-of-plane structure of the flow inside a longitudinal groove (Fig.5.8) and in front of the central rib (Fig.5.9) and a shoulder rib (Fig.5.10). We note that the particles' density change in the region in front of the tire where the water puddle is still at rest corresponds to the limit of the APR boxes. Moreover, we can clearly see that the fluid has a negative velocity in

the rear of the CPA which is quite the opposite of experimental results. This difference will be further discussed in Section 5.6.3.

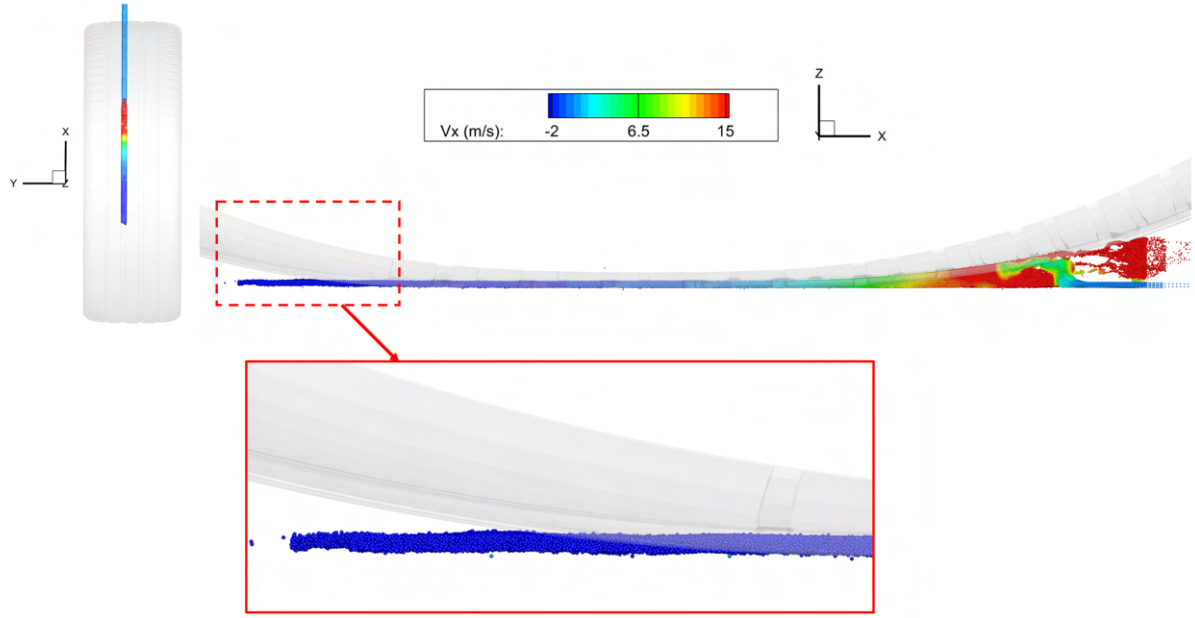

Figure 5.8 – Snapshot from simulation result: XZ cut view inside Groove B1 (right). The tire tread is shown in transparency. On the left, an XY view is given where only groove B1 is filled. We zoom on the rear region of the groove.

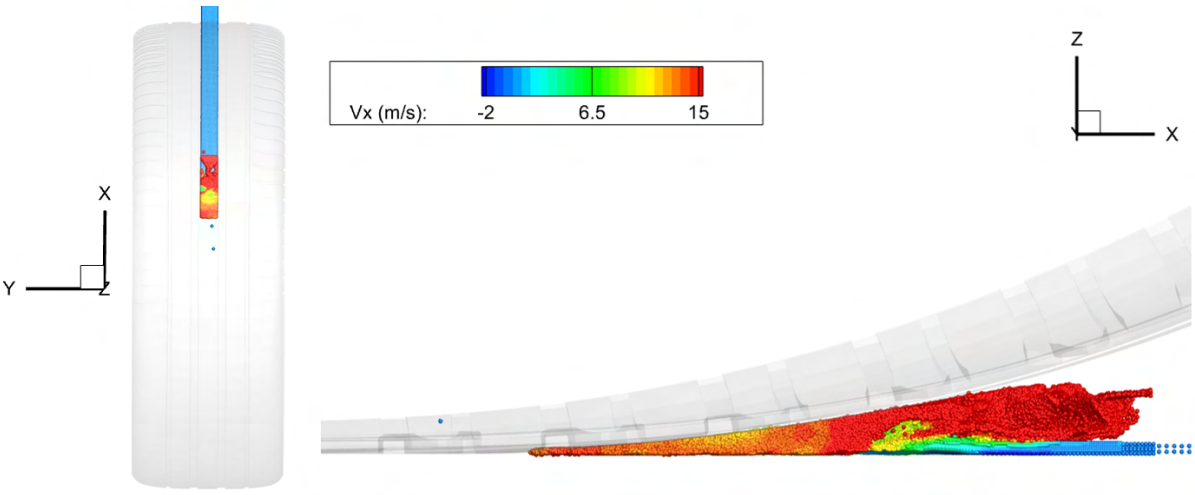

Figure 5.9 – Snapshot from simulation result limited to the central rib. The tire tread is shown in transparency. On the left, the XY view is given and on the right the XZ view.

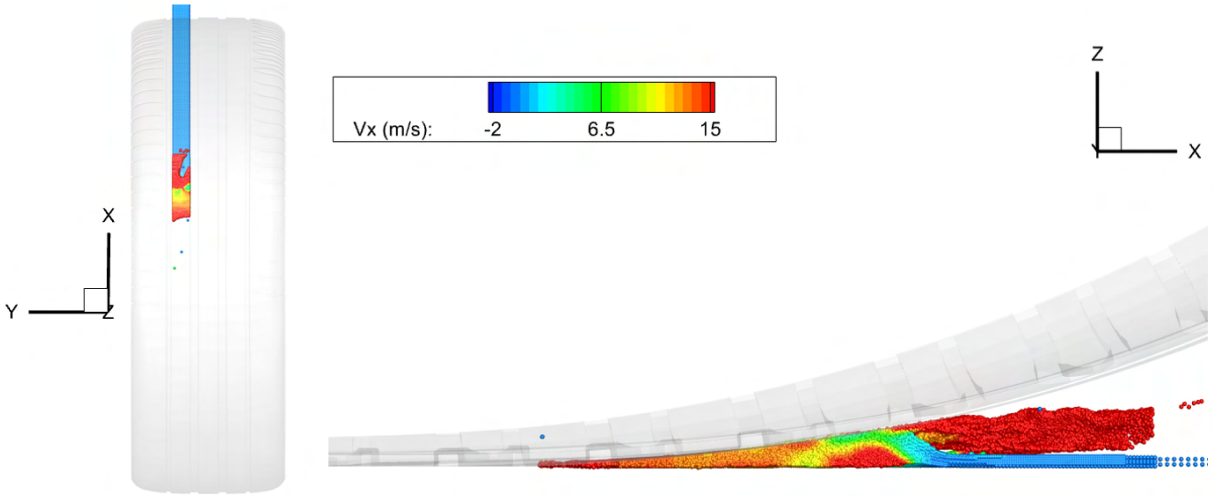

Figure 5.10 – Snapshot from simulation result limited to the shoulder rib. The tire tread is shown in transparency. On the left, the XY view is given and on the right the XZ view.

5.3.3 Inside the longitudinal groove type B

We focus now our study on groove B1 (Fig.5.2) because i) the experimental results are less scattered in this groove, ii) in the hydroplaning process, the wider the longitudinal groove, the lower the hydroplaning velocity meaning that a wider longitudinal groove is playing a more important role in the drainage process than a narrower one as the groove A1 and A2, iii) the hydrodynamic pressure is higher in the center of the tire resulting in a more important flow inside B1 and B2 than in A1 and A2, and iv) for symmetry considerations, groove B1 and groove B2 are expected to be similar (at least numerically since no camber angle is imposed).

The results of the comparison between numerical and experimental data in groove B1 are presented in Fig.5.11. Different slices have been included in the numerical post-processing to assess the evolution of V_x^* at different altitudes Z_i ($1 \leqslant i \leqslant 9$) from the ground with regular spacing. We also outline the entrance and exit of the CPA corresponding to r-PIV profile with the vertical dotted red lines. The region where V_x^* has been calculated is shown in Fig.5.12. We draw the reader's attention to the relative positioning of the numerical and the experimental profiles. Indeed many possibilities exit but we choose to overlay the curves based on the position of the WB increasing phase. First, we can see that while the interpolation plane is far enough from the ground (Z_1) and from the groove's bottom (Z_9), the velocity V_x^* does not evolve inside the groove except eventually at the rear of the CPA.

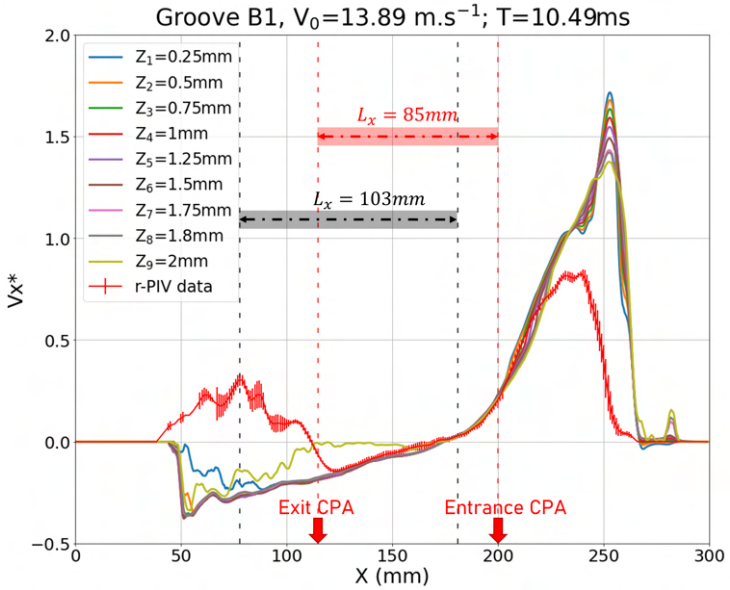

Figure 5.11 – Comparison between V_x^* profiles from experimental data (red curve) and over different interpolation planes' altitudes from numerical data at $T = 10.49ms$. $H_w = 1.5mm$, $V_0 = 13.89m.s^{-1}$. The experimental results are obtained for $N = 4$, the error bars represent the standard deviation between the runs. The exit and entrance arrows, as well as the L_x colored in red correspond to the r-PIV profile. The L_x in gray corresponds to the numerical profiles.

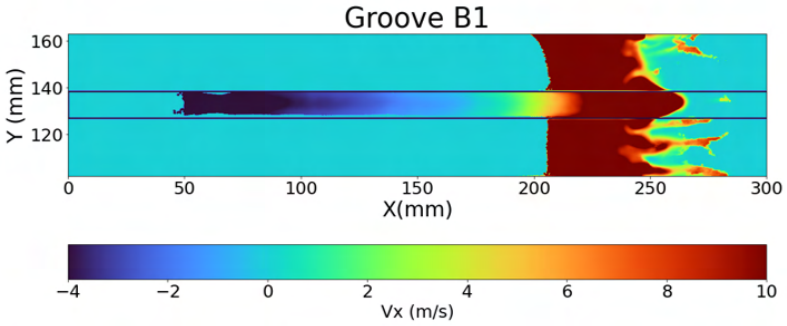

Figure 5.12 – Highlight of Groove B1 from numerical results. The two horizontal blue lines define the averaging area along Y-axis which corresponds to the groove's width. The velocity field is obtained by averaging V_x over the interpolation planes.

However, inside the WB region V_x^* gets higher by 20% for the planes closer to the ground for $X \approx 250mm$. Furthermore, inside the WB, the V_x^* values are much higher numerically (around $20m.s^{-1}$) than experimentally (around $11m.s^{-1}$). Also, still regarding the WB, we can observe that its length is also higher numerically by around 30%. Moreover, we

observe that experimentally $V_x^* > 0$ in the rear of the CPA ($50mm \leqslant X \leqslant 100mm$). We see that numerically we are unable to grasp this phenomenon correctly. One can assume the presence of a suction effect that is absolutely not captured numerically. Cabut [10] observed experimentally a rather similar phenomenon in the case of the transverse groove in the shoulder region of a PCY4 at a new state and linked it to the deformation of the rubber blocks. Improving the numerical results in this region should affect the velocity inside the whole longitudinal groove, as this suction effect strongly affects the kinematics inside the groove by water trailing. This will be further discussed in section 5.6.3.

5.3.4 Pressure field

The pressure field obtained numerically is given in Fig.5.13(a). As expected, it is inside the WB that the hydrodynamic pressure is the highest and therefore the major part of the fluid lift. We can also see in Fig.5.13(b) the acoustic effects on the pressure field caused by particles squashed between the tire and the ground. However, these acoustic effects should not have an impact on the incompressible solution as already explained in Section 2.1.7. On the experimental side, getting access to the pressure field can be considered as a future perspective for further comparisons with the numerical results.

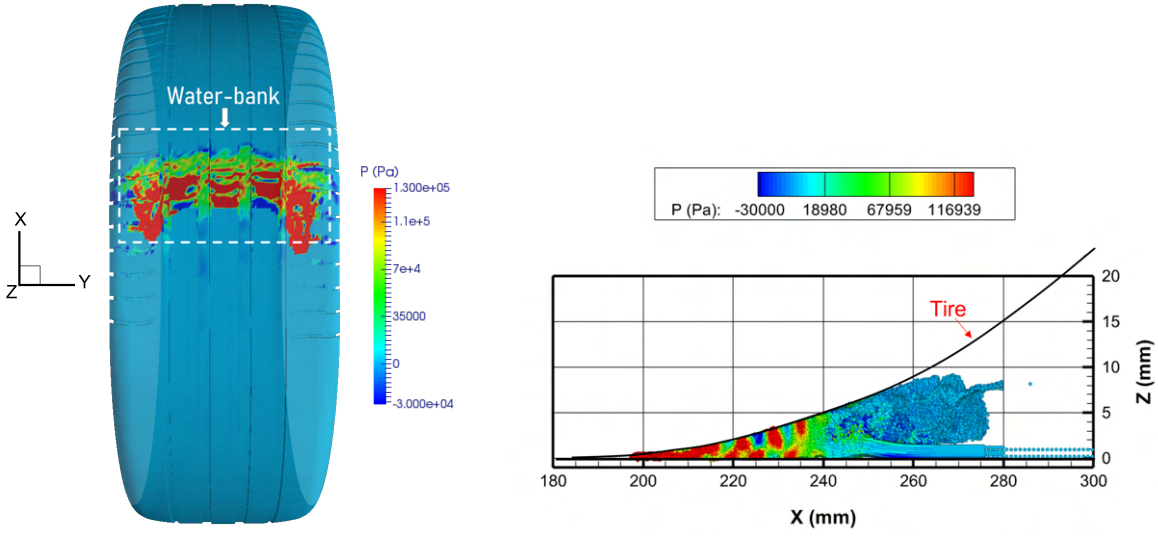

(a) (b)

Figure 5.13 – Pressure field on the tire tread of the PCY4 from numerical simulation (a). And on the right an XZ view in front of the central rib of the pressure field.

5.4 Comparison with experimental results: effect of the vehicle speed V_0

The results for the PCY4 at a worn state for four vehicle speeds are presented in this section: V_0=8.33$m.s^{-1}$, V_0=11.11$m.s^{-1}$, V_0=13.89$m.s^{-1}$ and V_0=16.67$m.s^{-1}$. No higher velocity was tested, because, as demonstrated in Hermange et al. [50] from $V_0 = 19.44m.s^{-1}$, the remaining contact patch surface starts to drastically decrease (for a tread depth $h = 2mm$). The same numerical and physical parameters given in Table 5.1 are used except for the water film thickness $H_w = 1mm$. We should note that this difference in the water depth is certainly altering the quality of our comparisons, but we should still be able to build an acceptable analysis. Indeed, in the experimental work of Hermange et al. [50] we can see that when comparing S/S_0 at $H_w = 1.5mm$ and $H_w = 1mm$ for $V_0 \leqslant 16.67m.s^{-1}$ there is no significant difference in the case of $h = 2mm$. This means that global parameters seem to not be affected by this change in H_w for this V_0 range. However, on a more local level, it is true that a difference may appear between results at $H_w = 1.5mm$ and $H_w = 1mm$, but the overall evolution of the velocity inside the tread pattern when V_0 increases is expected to be qualitatively the same otherwise we would see an impact of global parameters. Therefore, we tolerate this comparison between numerical results at $H_w = 1mm$ and experimental results at $H_w = 1.5mm$.

In the present section, we focus on groove B2 because the standard deviation in the experimental velocity measurements is lower in B-type than in A-type grooves. Grooves C will be discussed in section 6.3. Figures 5.14(a) and 5.14(b) show the averaged dimensionless velocity field V_x^* along X-axis in groove B2 and in the WB from r-PIV tests and numerical simulations respectively. The r-PIV results are for $H_w = 1.5mm$ because experimentally reaching $1mm$ of water film thickness is very complicated, it would take a very long time for film stabilization to allow a run. Otherwise, any light wind would break the water film, drying certain regions. The numerical results are generated as a spatial average over four slices: $Z_1 = 0.5mm$, $Z_2 = 1mm$, $Z_3 = 1.5mm$ and $Z_4 = 1.9mm$. Only one time step is considered for each V_0. The X-axis is normalized by the CPA length L_x (values are given in Fig.5.15(a)).

It is important to note that in Fig.5.14 the overall shape of the curves is rather similar between the numerical and experimental results. We can see that the velocity increases

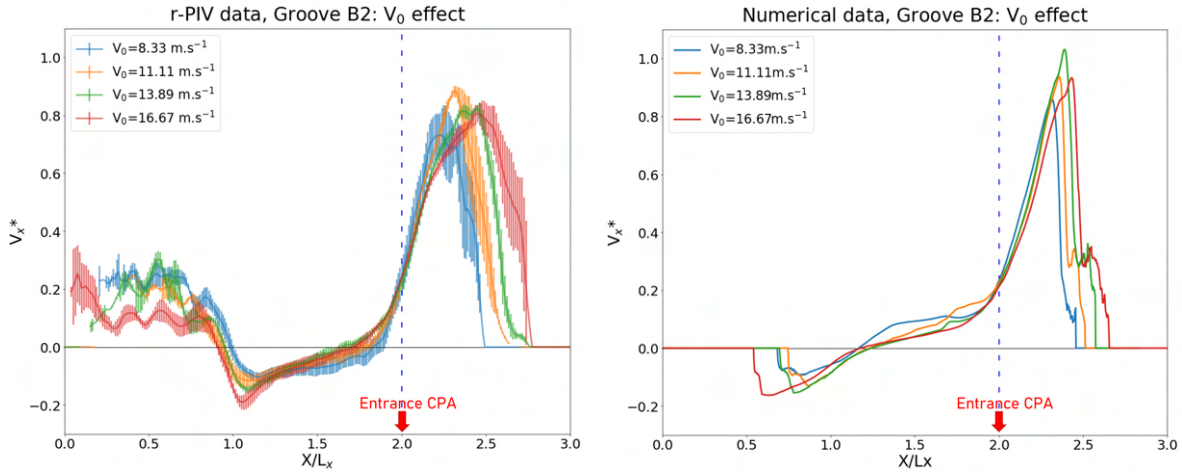

(a) Experimental (b) Numerical

Figure 5.14 – V_x^* profiles inside and in front of groove B2 for different vehicle speeds. The Y axis is normalized by V_0 and the X-axis by L_x. The entrance of the CPA highlighted by the vertical dashed line. On the left, we present the experimental results and on the right the numerical ones.

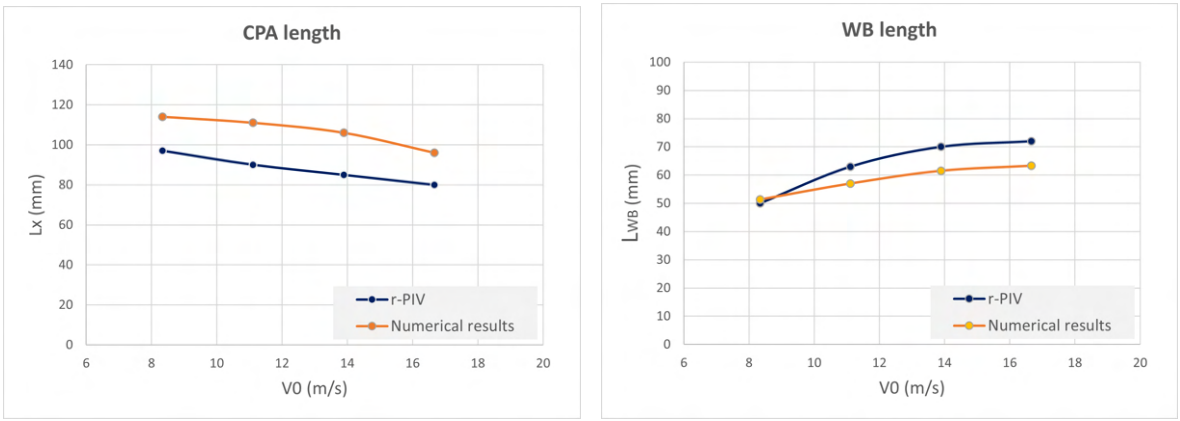

(a) (b)

Figure 5.15 – Contact patch length (a) and water-bank length (b) evolution for different V_0 values obtained both experimentally and numerically.

inside the WB and strongly decreases inside the tread groove. The tendency in the experimental/numerical difference in the results is rather the same as the one previously observed for a single V_0 even for $H_w = 1mm$. In Fig.5.15, we observe that the CPA length is still overestimated numerically but we capture the same tendency as the r-PIV results. Regarding the WB length, we see that r-PIV results are higher than L_{WB} numerically ex-

tracted. This is in opposition with the $H_w = 1.5mm$ case ($V_0 = 13.89m.s^{-1}$). In addition, the gap between the two curves seem to be rather constant except for $V_0 = 8.33m.s^{-1}$. Last but not least, in the rear of the CPA ($X/L_x < 1$), we still obtain a negative velocity from the simulations. We will further focus on this region in Section 5.6.3. Despite these differences between the numerical and experimental results we still capture rather close tendencies when V_0 is increased which is very encouraging.

5.4.1 Inside the longitudinal groove

We can observe that there is a similarity between the velocity profiles inside the longitudinal groove when V_0 is increased. The values of V_x^* are between $-0.2V_0$ and $0.2V_0$ for both experimental and numerical profiles, increasing from the CPA exit to its entrance. However, we observe that near $X/L_x = 1$, the water flow is ejected more rapidly towards the rear of the tire where the vehicle speed is increased in both cases. This evolution is not linear since $|V_x^*|$ gets higher in this region. The values reached in the rear of the CPA are very close between numerical and experimental results (between $-0.1V_0$ and $-0.2V_0$). Nevertheless, we note that the water ejection to the rear of the tire in the r-PIV results dominates meanly the full groove's length, whereas numerically the water is nearly evenly ejected to both the front and the rear of the CPA. An important part of the water is ejected to the front too in this case. This difference in the water drainage can partly explain the difference in L_x observed in Fig.5.15(a).

5.4.2 Inside the water-bank

Concerning the WB region, the peak of V_x^* is very close for the different vehicle speeds in both numerical and experimental results and is around $0.8V_0$ to $0.9V_0$. However, the WB length L_{WB} increases more rapidly in the r-PIV measurements than in the numerical results as we can see in Fig.5.15(b). A longer WB induces a larger volume of water in front of the tire increasing the hydrodynamic pressure and deforming the structure. This is in accordance with the higher CPA lengths obtained numerically than the values measured experimentally. In addition, the shape of the WB is more peak-shaped regarding numerical results which is not the case experimentally. Indeed, the velocity drops very suddenly in the simulations at the end of the WB. It was already the case for $H_w = 1.5mm$ (Fig.5.11), it is therefore not linked with the difference in the water depth.

It has to be remembered that the conditions are not exactly the same inducing some differences between the numerical and experimental results in particular concerning the water film depth H_w. This can explain the lower CPA length for the r-PIV measurements and the narrower WB. The difference in the data post-treatment that is imposed by the different natures of numerical and experimental results can also introduce some discrepancies. But other phenomena are not at all captured numerically like the positive velocity behind the tire observed experimentally. This has been observed systematically for all PCY4 cases and is possibly responsible for the shape of V_x inside the longitudinal groove. This phenomenon is further investigated in Section 5.6. Moreover, in order to assess the impact of the numerical parameters on the obtained results and try to improve the computed velocity field, a tool called the Test-Bench is used and is the subject of that section.

5.5 Streamlines generation: Comparison with Slick225

In this section, we aim to generate streamlines inside the WB of the PCY4 to compare with the results obtained with the slick tire in the previous chapter. We consider r-PIV measurements at $V_0 = 8.33m.s^{-1}$ and $H_w = 8mm$ for the PCY4 new ($h = 8mm$) and the Slick225. The streamlines corresponding to these flow circulations in the moving referential of the vehicle are given in Fig.5.16. Concerning the PCY4, their origins are chosen at $X = 219mm$ where the puddle has a velocity of $-V_0$. The same figure already presented in the previous chapter is considered here for the Slick225 (Fig.4.12), we just zoom in on the WB. For clarity purposes, the streamlines are taken evenly-spaced along the Y-axis with a $2mm$ step.

We can clearly see in Fig.5.16(a) how the streamlines enter the longitudinal grooves in particular B grooves. Fewer streamlines enter A grooves as the flow is nosier in these narrower grooves. We can also see that in front of the ribs, the streamlines are deviated a little which reminds us of the region in front of the slick tire where no streamline enters. Indeed, if we assume that the region in front of the ribs has a similar behavior as the WB of a slick tire, we can hypothesize the existence of smaller horseshoe vortices in front of these ribs forcing the streamlines to deviate.

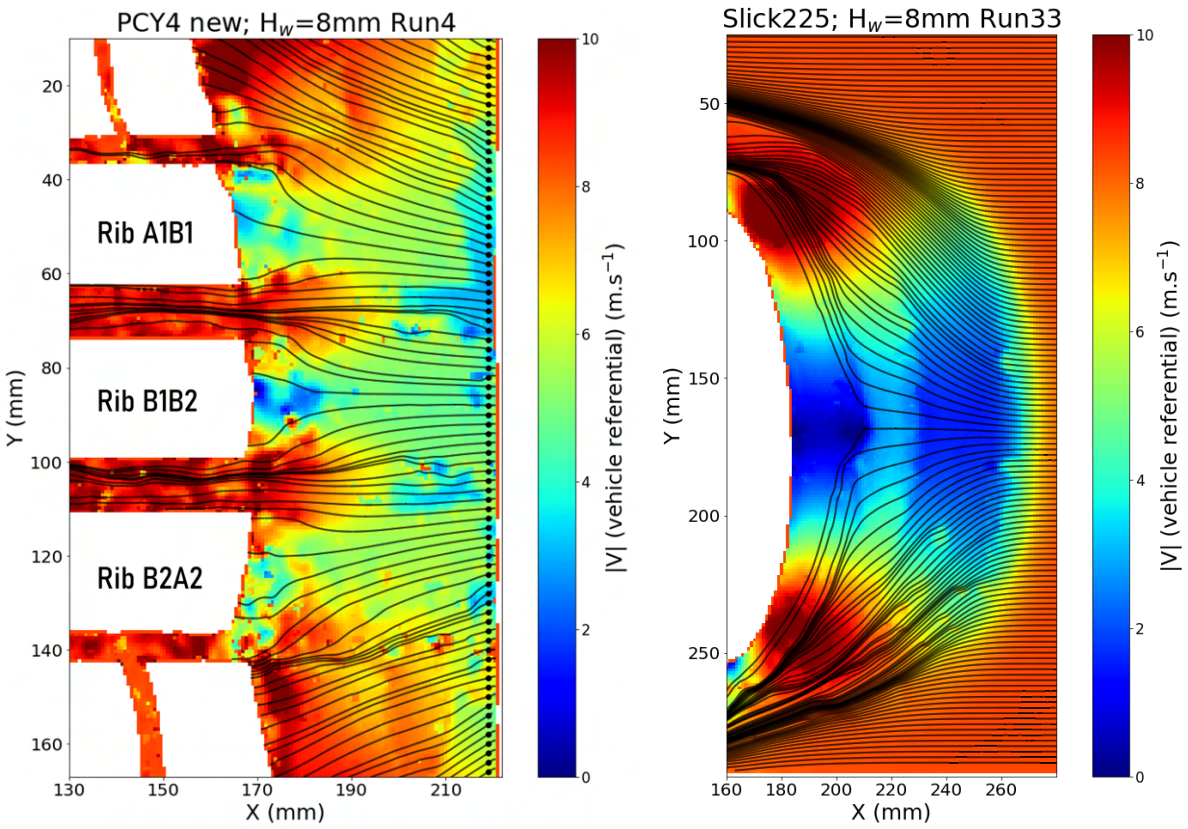

(a) (b)

Figure 5.16 – Streamlines generation for the PCY4 new (a) and Slick225 (b) along with the $|\vec{V}|$ field: r-PIV measurements at $V_0 = 8.33 m.s^{-1}$ and $H_w = 8mm$.

5.6 Towards improving the numerical results: a parametric study on a simplified model

5.6.1 About the Test-Bench

The Test-Bench is a pure SPH model where the structure part is not resolved anymore. It has been developed in order to run hydroplaning simulations rather quickly compared to the fully coupled SPH-FE simulations. This allows us to test different numerical parameters. The fully coupled simulations can take around 3 weeks while on the Test-Bench it takes between one hour and 2 days to reach a steady state. Inputs of this simplified hydroplaning model are given hereafter:

- The pre-deformed mesh of the tire previously calculated with the coupled SPH-FEM

tool. We extract it for a certain number of time steps that will correspond to the number of time steps we will solve with the Test-Bench.

- The fluid velocity field corresponding to the initial state from which the calculations on the Test-Bench will run. It has to be extracted from the fully coupled simulation.

Computing time is also reduced by reducing the SPH domain. Indeed, in our case, we are interested in the central B1 groove of the PCY4 tire, and therefore the puddle width is reduced to fill only that groove as presented in Fig.5.17. For a simplification purpose, and since no SPH-FE coupling is considered, no APR boxes are included and the whole puddle has the same spatial resolution. However, it is important to note that this simplified model

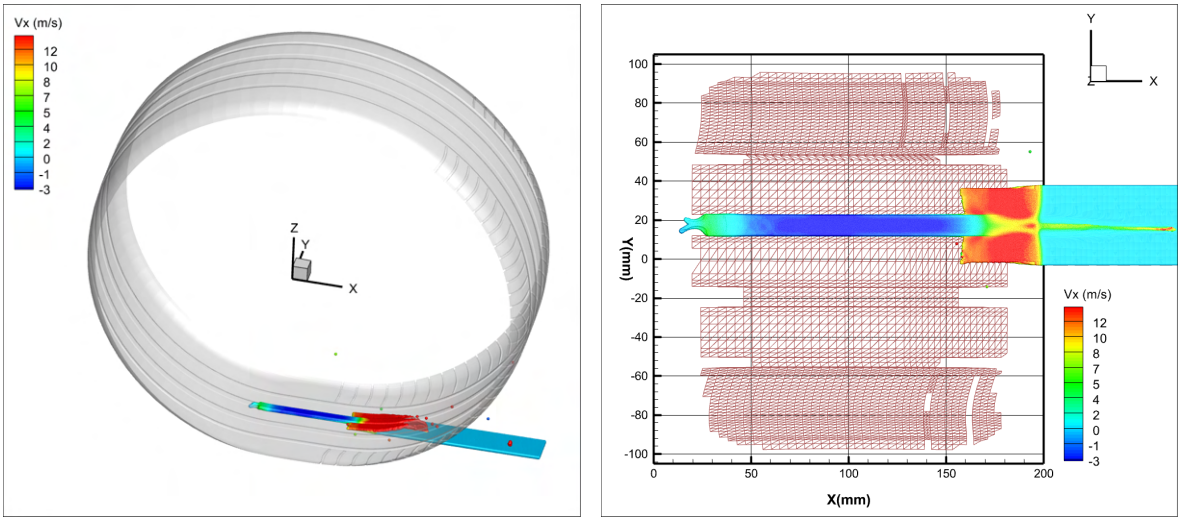

(a) (b)

Figure 5.17 – On the left, a 3D view of the Test-Bench configuration where only groove B1 is filled and the tire is shown in transparency. On the right, an XY view for the same configuration with the tread mesh. For clarity purposes, the view is for $Z \leqslant 2mm$.

is not actually treating physical hydroplaning since no FSI is present anymore. Indeed, the variations that may occur to the flow due to the change in the parameters (numerical/physical), do not impact the tire deformations. Therefore, the Test-bench solution will be different from the fully coupled solution.

5.6.2 Numerical parameters effect

5.6.2.1 Effect of the nominal sound speed C_0

A reference simulation on the Test-Bench has been conducted with the same parameters as the fully coupled simulation given in Table. 5.3. There are nearly 386 000 particles in this reference simulation compared to the fully coupled one where there was 1 084 000 particles at t_1=1.5ms. We note that concerning Δx_{SPH}, we choose the minimum value that we had in our SPH-FE simulation.

Physical parameter	**Value**
Puddle dimensions (XY) plane	L_x=100mm L_y =27mm
H_w	1mm
V_0	13.89$m.s^{-1}$
ρ_{water}	1000$kg.m^{-3}$
g	9.81$m.s^{-2}$
P_{tire}	2.4$bars$
Load	480daN

Numerical parameter	**Value**
$\Delta x_{SPH_{min}}$	0.25mm
$R/\Delta x_{SPH}$	2.11
C_0	250$m.s^{-1}$
k_{CFL}	0.375

Table 5.3 – Physical and numerical parameters of the reference simulation on the Test-Bench

Results are compared using three interpolation planes defined inside groove B1 (Fig. 5.18(a)). We compare the history of the velocity field V_x in those three cross-section planes between the reference simulation and the study case. Therefore, we calculate a space averaged velocity at each time step in the area designated by the dashed line in Fig. 5.18(b). This area is defined in the reference simulation. The interpolation planes are chosen in such a way that P1 is near the end of the contact patch, P2 is near the front and P3 is at the beginning of the water-bank. These planes are translated at the same velocity V_0 as the tire. We recall that in our fully coupled simulations, we used a value of $C_0 = 250m.s^{-1}$. This is a good compromise between ensuring small density variations and limiting CPU costs by maximizing the time step size. The aim of this study is to quantify the error in our calculations due to a rather low nominal sound speed value. We give in Figures 5.19, 5.20 and 5.21 the time history of the V_x over respectively P1, P2 and P3 for 5 values of C_0: $250m.s^{-1}$ (reference simulation), $400m.s^{-1}$, $500m.s^{-1}$, $800m.s^{-1}$ and $1000m.s^{-1}$. First, we observe that for P1 the velocity is null until t≈5ms and for P2 until t≈3ms, this is because the water did not reach those planes yet. Second, we can see that over the three planes, the norm of the velocity is lower for higher values of C_0. But between $C_0 = 800m.s^{-1}$ and $C_0 = 1000m.s^{-1}$ there is not a significant difference. It seems

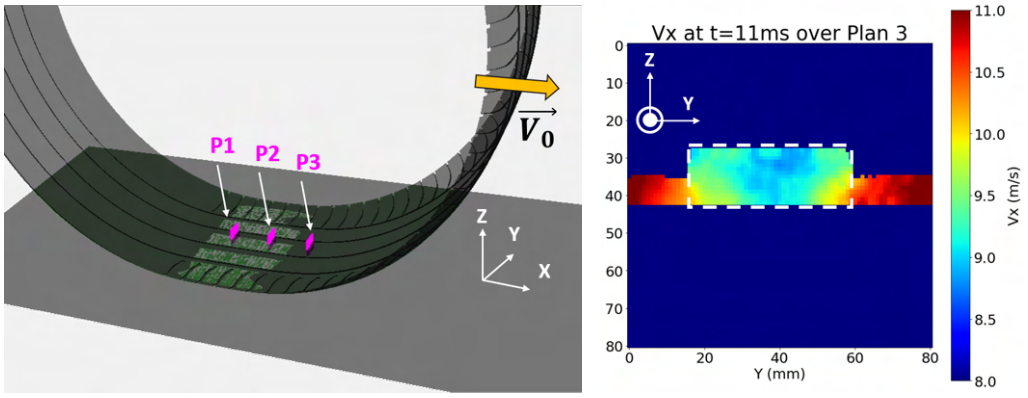

(a) Position of the interpolation planes (b) V_x field on P3 at t=11ms

Figure 5.18 – Scheme of the interpolation planes (left) and V_x field from the reference simulation in Test-Bench at t=11ms over the plan P3.

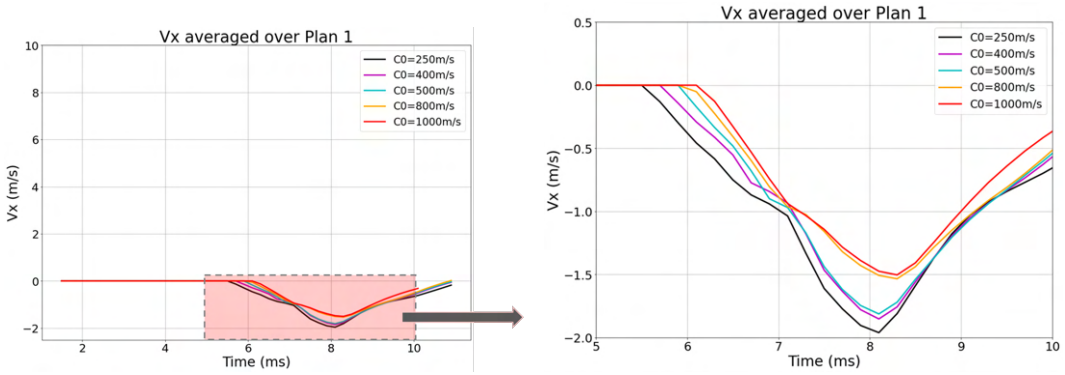

(a) V_x time history over P1 (b) Zoom between t=5ms and t=10ms

Figure 5.19 – V_x time history over P1 : C_0 effect

that we have reached the limit value of C_0 beyond which no notable improvements are noticed. Over P1, e.g., V_x is 25% lower for $C_0 = 1000m.s^{-1}$ than for $C_0 = 250m.s^{-1}$ at its maximum. We note that the reference case took 4h on 48 CPUs while the $C_0 = 1000m.s^{-1}$ case took 16h over 48 CPUs as well.

We can also study the evolution of the fluid lift with the sound speed. Therefore, we define a horizontal plane (normal Z) very close to the tread wall at Z=1.8mm, covering the contact patch length (Fig. 5.22). We remind the reader that since we are working with a worn tire, the remaining tread depth is about 2mm, but inside the contact patch, the tire is deformed when loaded and the tread depth in this area is around 1.8mm. This plane is a BIM-CFA (Boundary Integral Method Cut-Face Approach) plane and is

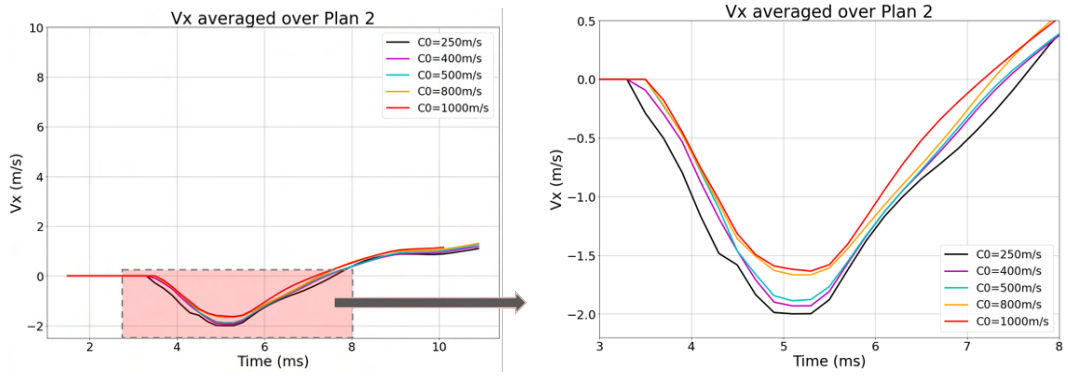

(a) V_x time history over P2 (b) Zoom between t=3ms and t=8ms

Figure 5.20 – V_x time history over P2 : C_0 effect

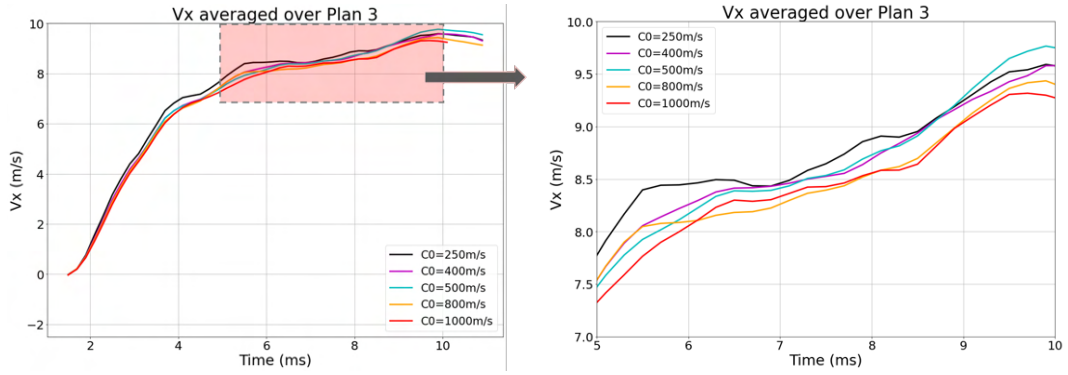

(a) V_x time history over P3 (b) Zoom between t=5ms and t=10ms

Figure 5.21 – V_x time history over P3 : C_0 effect

considered as a temporal conservative force sensor. The force output is calculated following the last term of the third equation in the system (2.33). Therefore, we can have access to the history of the fluid load on this plane and study its evolution with the sound speed (Fig. 5.23). The BIM-CFA plane follows the tire as it is translated at a horizontal velocity V_0. We can see that the fluid lift increases with the sound speed inside the central groove and the difference between C_0=250$m.s^{-1}$ and C_0=1000$m.s^{-1}$ can reach 200%. This dependency has been also observed by Michel [84] in the case of a V-shaped tread pattern. He highlighted the concentration of these effects in the contact patch area. However, the effect of C_0 on a global parameter like the contact patch area is seen as minor.

In summary, we conclude that using $C_0 = 250m.s^{-1}$ introduces a 25% error in the velocity in the rear of the CPA and nearly 10% in the entrance of the CPA. The fluid lift is also reduced by 65% inside the CPA. The value of C_0 chosen in our fully coupled

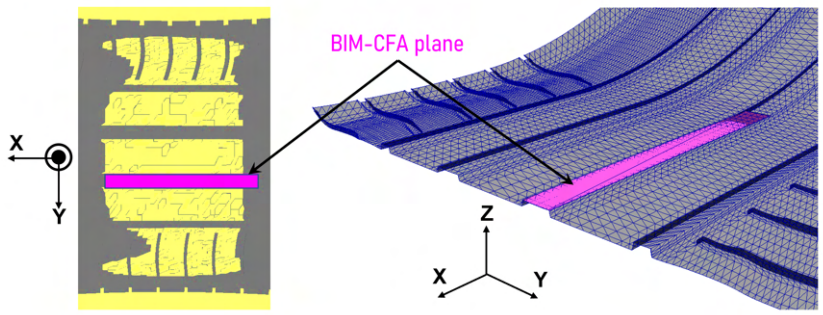

Figure 5.22 – BIM-CFA plane position in the contact patch (left) and cut view of the plane inside B1 (right).

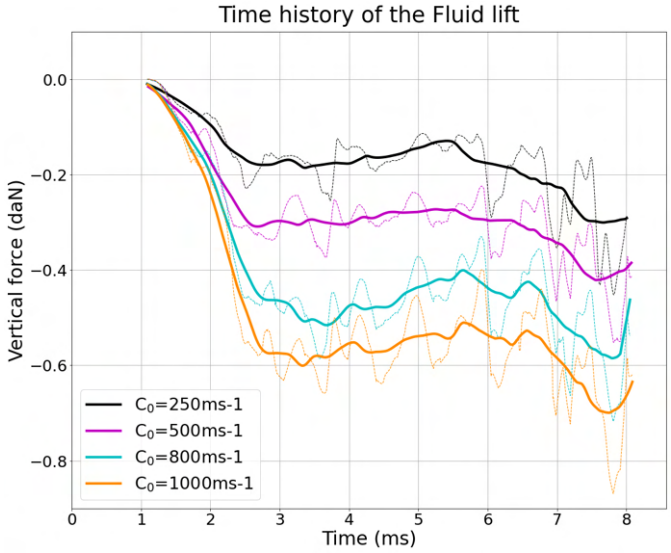

Figure 5.23 – Time history of the fluid lift on the BIM-CFA plane for different C_0 values. The dashed lines are the rough values and the solid lines represent the smoothed tendencies.

simulation gives us the possibility to limit the computational costs (which are still very high), it is a compromise between the calculation duration and the precision of the results. The present section helped us to quantify the errors induced by such a low value of C_0.

5.6.2.2 Ratio $R/\Delta x_{SPH}$ effect

In this section, we aim to study the effects of the ratio $R/\Delta x_{SPH}$ on the water flow inside the central groove. Using low values of the ratio tends to increase quadrature errors

and decrease the numerical viscosity leading to less regular fields. Therefore, we want to quantify the effect of this ratio with the Test-Bench. We choose three values of $R/\Delta x_{SPH}$: 2.11 (reference simulation), 2.4 and 3. The reference simulation parameters are the same as given in Table 5.3 with $C_0 = 250m.s^{-1}$. In the first approach, we change the k_{CFL} to maintain a constant value of the fluid time step for all ratios:

$$k_{CFL} = 0.375\frac{2.11}{R/\Delta x_{SPH}} \tag{5.1}$$

We see in Fig. 5.24 that the velocity inside the central groove is slightly higher when $R/\Delta x_{SPH}$is increased. This is seen in particular when we compare $R/\Delta x_{SPH}$=2.11 and $R/\Delta x_{SPH}$=3 (around 9% in P2 and 15% in P1).
Moreover, we define the total flow rate as:

$$\text{Total flow rate} = \int_t V_x.S_{plan}\, dt \tag{5.2}$$

And the dimensionless total flow rate:

$$\text{Dimensionless Total flow rate} = \frac{\text{Total flow rate}}{\text{Total flow rate REF}} \tag{5.3}$$

where S_{plan} is the surface of the area defined in Fig. 5.18(b) and Total flow rate REF is the total flow rate of the reference simulation.
If we compare the dimensionless total flow rate over P3, we cannot conclude a clear trend and the ratio does not seem to have a significant effect (Fig. 5.25(c)). Therefore, we choose to look into the planes P2 (Fig. 5.25(b)) and P1 (Fig. 5.25(a)) while keeping in mind that the analysis in these regions does not take into consideration the first time steps of the simulation (the water flow reaches P2 at around $3ms$ and P1 at $5ms$). In P2, there is a clear evolution of the flow rate with the ratio as for $R/\Delta x_{SPH}$=3 it is increased by 40%. Concerning P1 there is no clear tendency concerning the evolution of the total flow.

We present in Fig. 5.26 the time history of the fluid lift for the three $R/\Delta x_{SPH}$ ratios. The same BIM-CFA plane is considered here as described in Fig. 5.22. We can see that the fluid lift increases for a higher value of the ratio inside the central groove, this difference can reach 27% around t=8ms between $R/\Delta x_{SPH}$=2.11 and $R/\Delta x_{SPH}$=3. This has also been observed by Michel [84] and has been identified as a hypothetical "clog" effect. For a fixed Δx_{SPH}, the increase of the ratio leads to an increase in the solid surfaces the particles are in contact with (the tire and the road). This may lead to locally

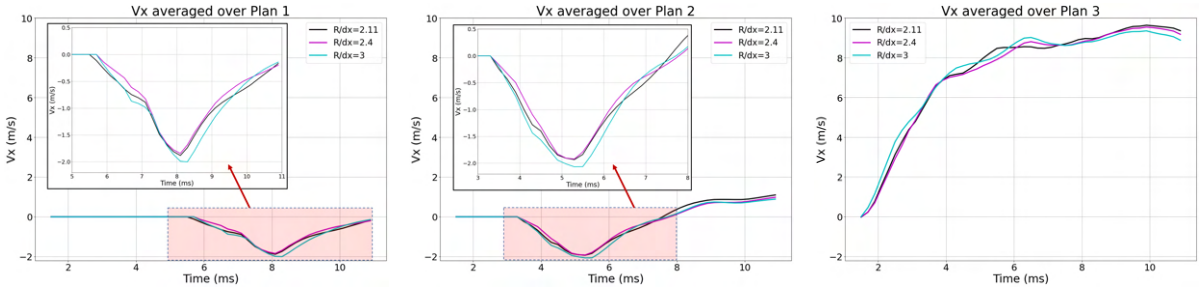

(a) (b) (c)

Figure 5.24 – Time history of V_x over P1 (left), P2 (middle) and P3 (right) for different $R/\Delta x_{SPH}$ ratios, with a fixed SPH time step

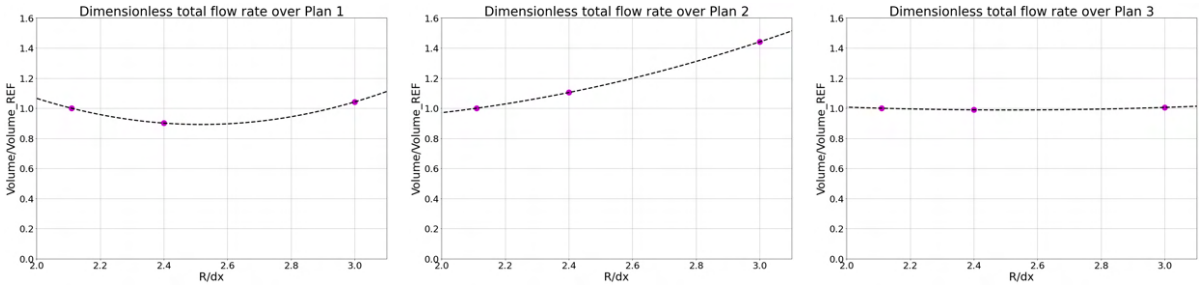

(a) (b) (c)

Figure 5.25 – Variation of the flow rate over P1 (left), P2 (middle) and P3 (right) for different $R/\Delta x_{SPH}$ ratios, with a fixed SPH time step

reaching higher pressures and slowing down the particles. This phenomenon is particularly present when the orifice's characteristic length is close to Δx_{SPH} (in our case it is around $8\Delta x_{SPH}$=2mm).

We add that in the case where k_{CFL} is fixed at 0.375 (reference simulation), the results obtained do not vary significantly from those presented above (Fig. 5.27). We can also look at the evolution of the dimensionless total flow rate between $R/\Delta x_{SPH}$=2.11 and $R/\Delta x_{SPH}$=3 for different Δx_{SPH} values over P3 (Fig. 5.28). In this case, we also keep the reference value of k_{CFL}= 0.375. We observe that the effect of Δx_{SPH} is superior to that of $R/\Delta x_{SPH}$.

To summarize, the effect of the ratio $R/\Delta x_{SPH}$ is less straightforward regarding the velocity inside the longitudinal groove than the effect of C_0, but when looking at the lift force, the tendency was clear. The greater the ratio, the greater the lift force, but also the higher computational costs. Nevertheless, an increase in $R/\Delta x_{SPH}$ has a lower impact on

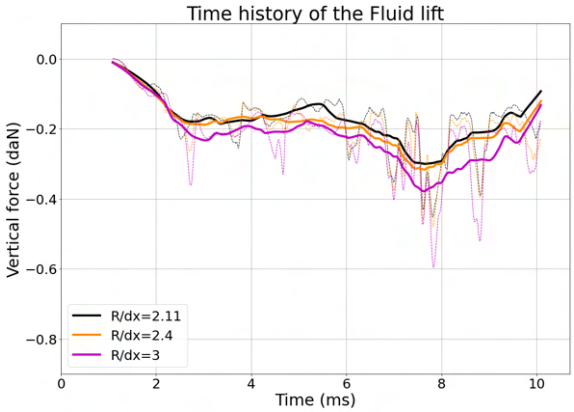

Figure 5.26 – Time history of the fluid lift on the BIM-CFA plane for different $R/\Delta x_{SPH}$ ratios. The dashed lines are the rough values and the solid lines represent the smoothed tendencies.

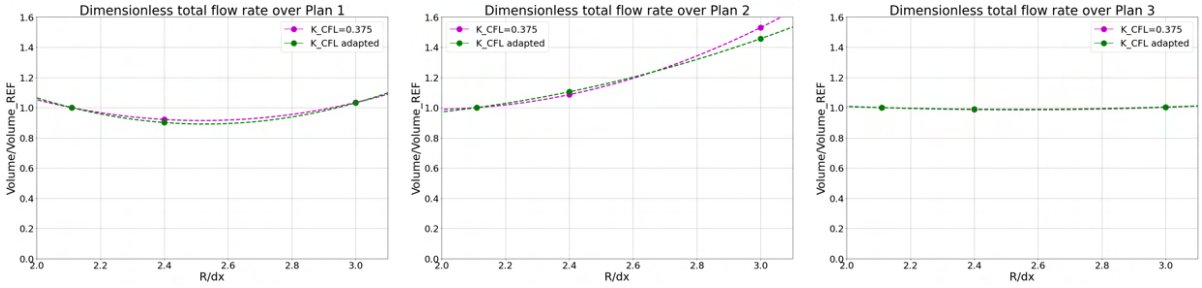

(a) (b) (c)

Figure 5.27 – Variation of the flow rate over P1 (left), P2 (middle) and P3 (right) for different $R/\Delta x_{SPH}$ ratios, with a fixed k_{CFL}=0.375.

the computing time than an increase in C_0 and an accurate estimation of the fluid forces sent by the SPH solver to the FE solver is crucial during an FSI coupling. Therefore, increasing $R/\Delta x_{SPH}$ seem to be a good compromise between the accuracy of the results and the computational costs.

5.6.3 Physical model improvement: Flow separation technique

In this section, we propose some attempts to improve the numerical model in order to capture the phenomenon of suction of the flow inside the CPA in the rear region that we have experimentally observed in the case of the PCY4 tire. We refer the reader to Fig.5.8 to recall the result previously obtained with the fully coupled model where we can see the tire detaching from the puddle with no particles attached to it. The water height is

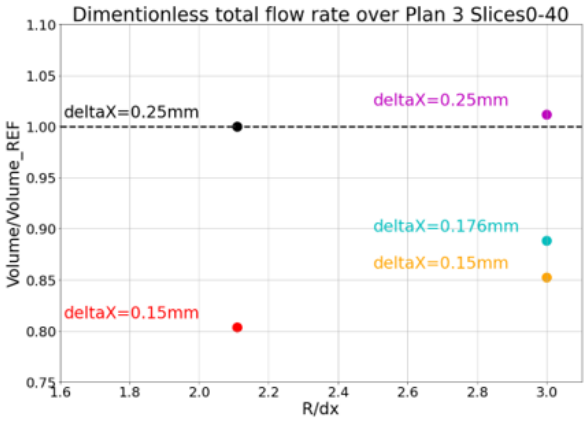

Figure 5.28 – Variation of the flow rate over P3 for $R/\Delta x_{SPH} = 2.11$ and $R/\Delta x_{SPH} = 3$, with a fixed k_{CFL}=0.375 and for different Δx_{SPH} values

increased to $H_w = 1.5mm$ to fit at best the experimental configuration. The physical and numerical parameters are given in Table 5.4. We note that a ratio $R/\Delta x_{SPH} = 3$ has been chosen after the parametric study conducted in the previous section.

Physical parameter	**Value**
Puddle dimensions (XY) plane	L_x=100mm L_y =27mm
H_w	1.5mm
V_0	13.89$m.s^{-1}$
ρ_{water}	1000$kg.m^{-3}$
g	9.81$m.s^{-2}$

Numerical parameter	**Value**
$\Delta x_{SPH_{min}}$	0.25mm
$R/\Delta x_{SPH}$	3
C_0	250$m.s^{-1}$
k_{CFL}	0.375

Table 5.4 – Physical and numerical parameters for the Test-Bench configuration

The improvements proposed here are based on the work of Michel [84] (Chapter 4). These improvements were inspired from the work of Sun et al. [117]. Michel introduced a model of jet detachment compatible with the suction effects. We note that a treatment for jet detachment is already present in our numerical model. It consists of stopping the interactions between the particle and the wall if the pressure is negative which explains why the fluid detaches from the structure at the rear of the CPA in previous simulations. This treatment seems to be lacking accuracy, thus the improvements proposed by Michel. In section 5.3.2 we have experimentally highlighted for the PCY4 case a flow directed towards the CPA in the rear region, and we can imagine that it is due to the fluid that stays attached to the tire when the latter leaves the ground. In the new flow separation model,

three criteria have to be fulfilled to authorize a particle to detach from the structure and cut its interaction with it. i) First the particle needs to be both at a minimum distance from the wall and at the free surface which might correspond to a possible separation point. ii) Second, a criterion on the pressure is considered :

$$P_s + P_i \leqslant 0 \tag{5.4}$$

Where P_s is the pressure extrapolated on the wall and P_i is the pressure of particle i. In this case, the particle and the wall are attracted to each other, and the detachment may be prevented. iii) Finally, a criterion on the relative velocity of the particle is introduced:

$$(\vec{v}_s + \vec{v}_i).\vec{n}_s \geqslant 0 \tag{5.5}$$

Where $\vec{v}_s$ and $\vec{v}_i$ are respectively the wall and the particle velocity and $\vec{n}_s$ is the normal to the wall pointing outwards. This last criterion authorizes only the particles that tend to detach from the structure to actually detach provided that the two above criteria are also fulfilled.

We give in Fig.5.29 the results obtained with the new treatment. We also give an overall view of the B groove in the XZ plane in Fig.5.30.
First, we can see in both Figues 5.29(a) and 5.30 that at the rear of the CPA ($x \approx -100mm$), we have succeeded in capturing a positive velocity as observed experimentally which has never been fulfilled before. Second, in Fig.5.29(a) we represent the new values of V_x^* plotted along with the experimental profile (black curve) as well as the results obtained with the fully coupled model with the old no-stick treatment (dashed blue profile). We observe that the values of V_x^* inside the WB with the new treatment become very close to the one experimentally measured, especially for Z_3 and Z_4. It is possible that because the particles stay attached to the tire, their velocity decreases and reaches the value measured experimentally. Furthermore, we can see that from one interpolation plane to another, $|V_x^*|$ increases with the plane altitude which was not the case in the fully coupled model, creating a $\frac{\partial V_x}{\partial z} \neq 0$. We give a zoom inside the CPA to highlight this shearing in Fig.5.29(b). However, the velocity profile inside the CPA i.e. $170mm \leqslant x \leqslant 210mm$ has become uniform inside each interpolation plane ($\frac{\partial V_x}{\partial x} \approx 0$), while experimentally it follows a rather linear increasing tendency. This is also a different result from the one obtained with the fully coupled model.

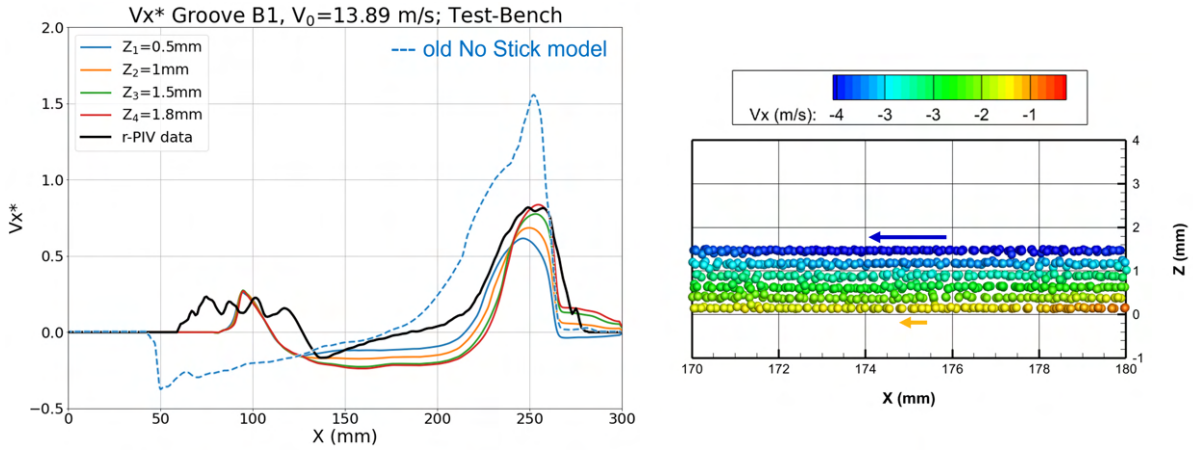

(a) (b)

Figure 5.29 – (a) Comparison between V_x^* from experimental data and over different interpolation planes' altitudes from the Test-Bench. The profile corresponding to the fully coupled model is also given (blue dashed). (b) Zoom inside B1 to highlight the shearing along Z-axis that appeared in the Test-Bench simulation.

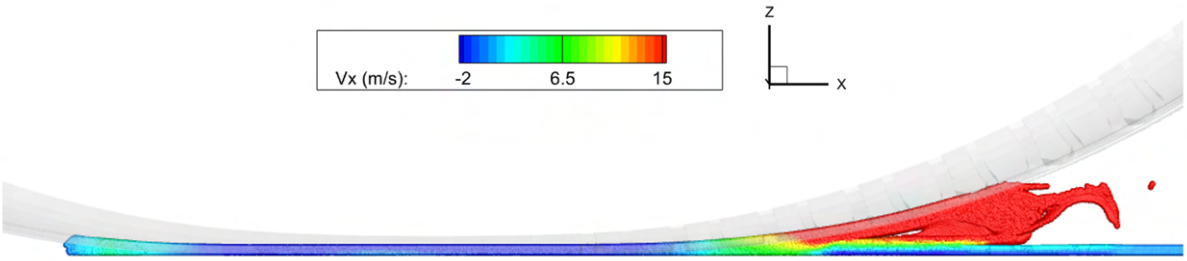

Figure 5.30 – XZ view of B-groove with the new flow separation treatment on the Test-Bench.

Returning to the examination of the suction effect in the rear of the CPA, we give in Fig.5.31 an enlarging view of this region. Figures 5.31(a) and 5.31(b) are extracted from a calculation with the old flow separation configuration, and Figures 5.31(c) and 5.31(d) are from the new model. Velocity components V_x and V_z are outlined in each flow separation configuration. We can clearly see how the particles stay attached to the tire (represented in transparency) when it leaves the ground in the case of the new flow separation model. This is what we physically expect to happen when an object leaves the surface of a fluid, it drags with him the free surface before it detaches. This results in a velocity $V_z \neq 0$ as depicted in Fig.5.31(d) while we can see that $V_z = 0$ in Fig.5.31(b).

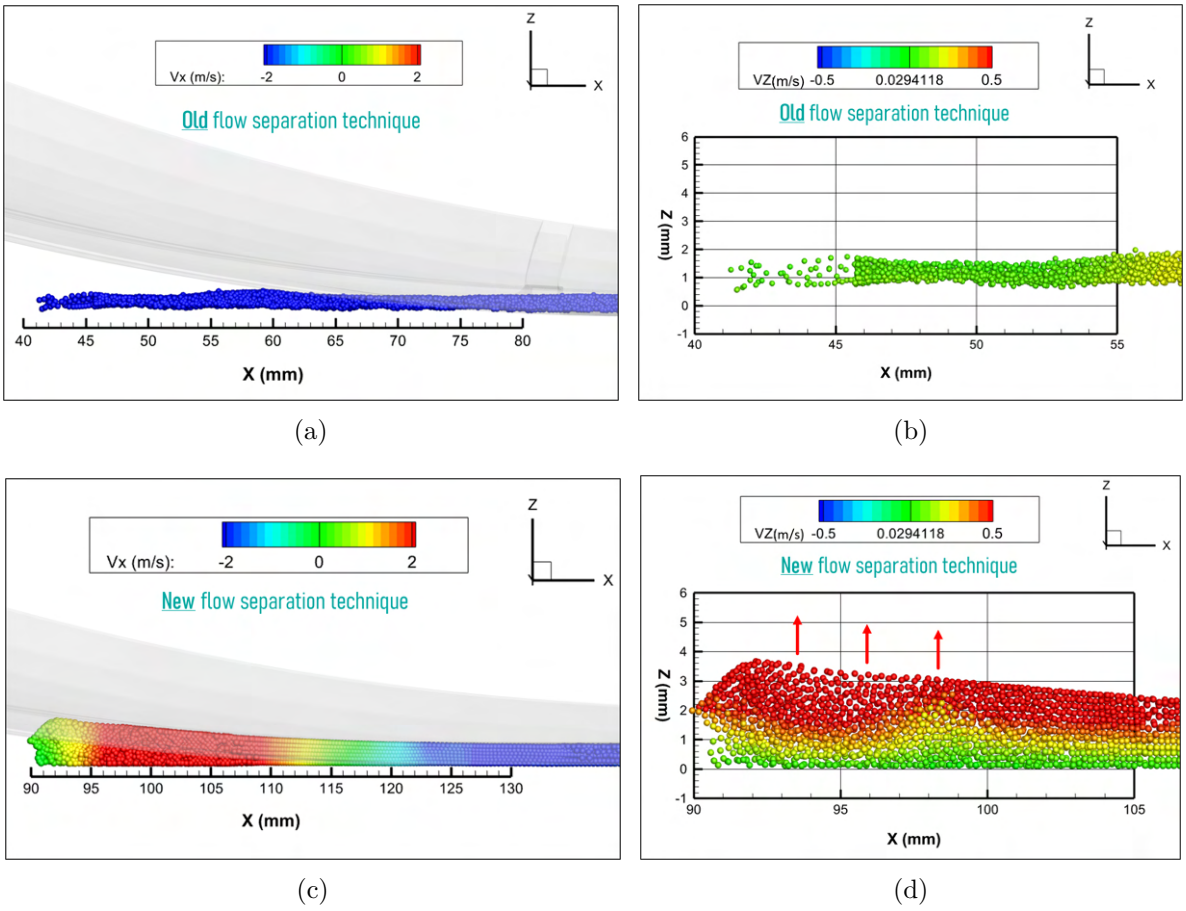

(a) (b)

(c) (d)

Figure 5.31 – Highlight on the back area of Groove B1 between $Y = 17mm$ and $Y = 18mm$ (middle width of Groove B1). In (a) and (c) we represent the V_x component of velocity adding the tire in transparency. In (b) and (d) the V_z component is shown. The configuration in (a) and (b) is the initial flow separation model obtained with the fully coupled simulation, while in (c) and (d) it corresponds to the results of the new proposed model obtained with the Test-Bench.

5.7 Conclusion and discussions

This chapter was dedicated to the analysis of the water flow in the WB and inside the longitudinal groove of a summer tire in its worn state. A self-similarity appeared inside the groove in the CPA when the vehicle speed increased as the direction of the flow ejection and the regions of high and low velocity are preserved. The numerical results showed a good agreement with the r-PIV measurements, however, thanks to this comparison some limitations of our numerical model have been pointed out, especially the importance of modeling the suction effect. Indeed, the velocity inside groove B and in front of it seemed

to be very dependent on the velocity at the rear of the CPA. Numerical tests on the Test-Bench have been conducted with a model taking into account the suction effect and the results are very encouraging. Not only the velocity in the rear region has been improved but also the WB velocity matches better the experimental value. Nevertheless, the proposed treatment should be tested on a fully coupled SPH-FE model to verify its relevance and its impact on the full fluid domain as we can expect modifications in C grooves as well.

Moreover, a parametric study has been conducted to validate some numerical and physical parameters chosen and quantify their impact on the hydroplaning application in particular the sound speed, the spatial resolution, and the $R/\Delta x_{SPH}$ ratio. These tests complement the work of Hermange [51] and Michel [84] and consolidate the numerical initialization of the SPH-FE coupling.

Last but not least, by generating the streamlines in the PCY4 case, some similarities appeared in front of the ribs with the WB of the Slick225, whereas inside the longitudinal grooves, the streamlines penetrated with a clear disparity between A and B grooves.

Chapter 6

Segmentation analysis in directional treads

In the current chapter, we focus on directional treads. Usually, the analysis of this type of tread is more complex than for the longitudinal one mainly due to the multiple changes in the grooves' direction. We give in Fig.6.1 an example of a directional tread (MICHELIN Alpin 6 case). The direction of a directional groove is highlighted with the dotted red line. To analyze the flow circulation inside such tread, the method previously used (ensemble averaging) in the case of a longitudinal tire is not well adapted for at least two reasons i) even if the position of the CPA in the field of view was identical for independent runs, the location of the directional grooves inside the CPA is random and the flow inside such a groove can possibly depend of its position, and ii) the geometry and the spacing between adjacent grooves is not constant. Therefore, we use the so-called segmentation method (Cabut [10],Ben Khodja et al. [8]).
The main idea is to define a new local referential ($\vec{u}$,$\vec{v}$) that follows the direction of the grooves and then to express the velocity field in this referential. Cabut [10] already proposed a velocity averaged parameter for a given transverse groove, and plotted it as a function of the longitudinal location of this groove (barycenter of the integration domain). Such a result shows how water ejection from the CPA is dependent on the location of the groove inside the CPA during the rolling process. This major result is carried on in the current chapter as the local average parameter defined in [10] is applied for the analysis of all grooves during the drainage process from the CPA zone to outside for different types of tire treads.

First, we present the segmentation process and how we apply it to different tread tires. We try to determine if there is a similarity when changing the vehicle speed. Moreover, a comparison is established between different tire treads to see if a common circulation scheme exists in the shoulder region. In addition, a numerical/experimental comparison is presented highlighting the shortcomings of our numerical model.

Figure 6.1 – Details of the Alpin 6 tread design with a highlight on a unique directional groove and its directions with respect to the horizontal axis.

6.1 Method of segmentation

The motivation here is to determine if the flow is sucked inside or pushed outside a portion of a segment, depending on its X position along the CPA, and to access the global circulation scheme inside the network of grooves of a given tire model. For that purpose, in the first step, we define the local referential $(\vec{u}, \vec{v})$ bound to the groove of interest (Fig.6.2). We split each directional groove inside the CPA into three straight segments following roughly their change in direction from the shoulder to the central part of the CPA. This operation is manually done by the user by giving to the algorithm the number of segments n_s defining the groove and then by manually selecting the vertices of the groove, i.e. $2(n_s + 1)$ points to select for each groove (Fig.6.3(a)). The longitudinal direction $\vec{u}$ of each segment is calculated as the mean between the directions of the two lines defined by respectively the first and second vertices, and the third and fourth vertices. For example, in Fig.6.3(b), the unit vector $\vec{u}$ is calculated as the mean direction between the green line (AB) and the blue line (CD):

$$Abss_{\vec{u}} = \frac{1}{2}[(X_B - X_A) + (X_C - X_D)] \tag{6.1}$$

$$Ordon_{\vec{u}} = \frac{1}{2}[(Y_B - X_A) + (Y_C - Y_D)] \tag{6.2}$$

therefore:

$$cos(\theta) = \frac{Abss_{\vec{u}}}{\sqrt{(Abss_{\vec{u}}{}^2 + Ordon_{\vec{u}}{}^2)}} \tag{6.3}$$

$$sin(\theta) = \frac{Ordon_{\vec{u}}}{\sqrt{(Abss_{\vec{u}}{}^2 + Ordon_{\vec{u}}{}^2)}} \tag{6.4}$$

where θ is the angle between $\vec{u}$ and the horizontal axis (Fig.6.3(b)). Then, since the segments have a parallelogram shape, the third selected point defines the segment's width (Fig.6.3(c)). We can see that for the upper segment, our approximation makes that some parts of its area are outside the groove. To avoid introducing some errors in the calculation of the mean velocity inside the segment, we consider masked fields from the start. In this way, the points outside the groove (hidden when using the mask) are not taken into consideration.

We give in Fig.6.4(a) the segments' definition for one of the directional grooves in the case of the A6 tire ($n_s = 3$) and we note $\vec{u}_k$ ($k = 1, 2, 3$) the vector defining the orientation of segment k. From now on we call simply $\vec{u}$ the unit direction vector of the groove, and we focus on the velocity component V_u as:

$$V_u = \vec{V}.\vec{u} = V_x\ cos(\theta) + V_y\ sin(\theta) \tag{6.5}$$

As shown in Fig.6.4(a), we have five directional grooves for each run. We call Groove 1 the directional groove near the end of the CPA till Groove 5 the directional groove near the water-bank following the X-axis orientation. A similar segmentation of the zigzag central groove is performed using $n_s = 9$ elementary straight segments (Fig.6.4(b)). In a second step, we define inside each segment a characteristic fluid velocity $V_{u_{mean}}$ as the value of V_u spatially averaged along its width and length:

$$V_{u_{mean}} = \frac{1}{S_{segment}} \int_u \int_v V_u\ dS \tag{6.6}$$

where $S_{segment}$ is the area of the considered segment (Fig.6.2).

If we have in mind that every velocity vector measured with the r-PIV technique is in fact the result of seeding particles that are randomly located and illuminated at different Z altitudes, we can consider that $V_{u_{mean}}$ is a global indicator of the velocity inside the volume corresponding to a segment. Finally, in a third step, we define the location x of a segment as the x-value of the geometric barycenter of the segment under consideration.

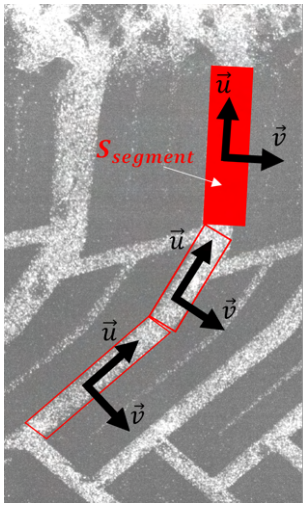

Figure 6.2 – Local referential $(\vec{u}, \vec{v})$ definition for three segments with highlight of the area $S_{segment}$ corresponding to segment 1.

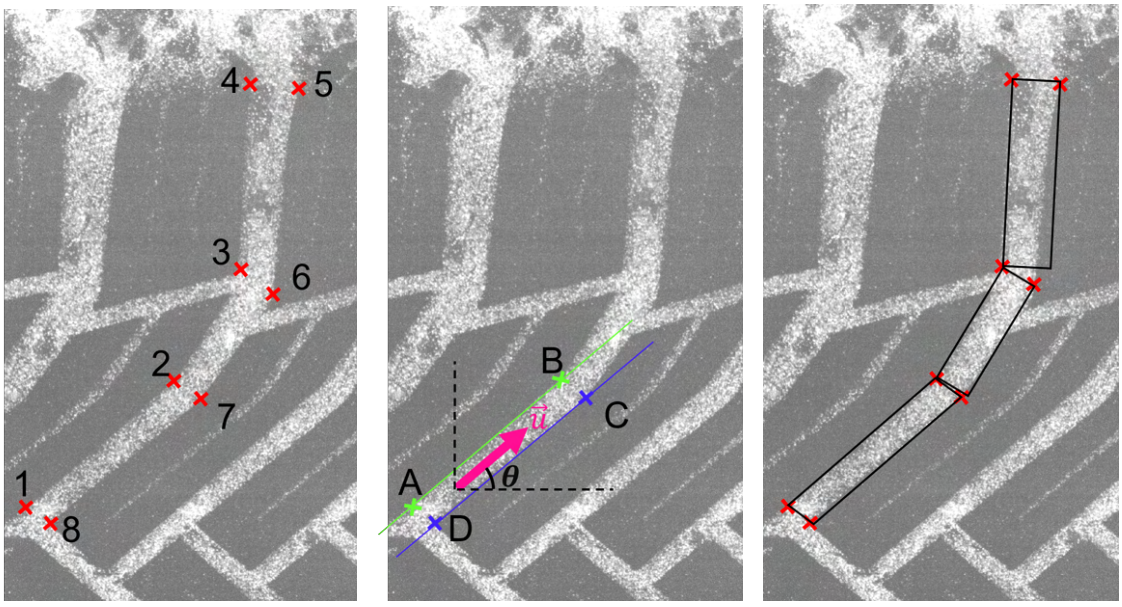

(a) step 1 (b) step 2 (c) step 3

Figure 6.3 – Example of segmentation of a directional groove (A6 case). On the left, the vertices of the directional grooves are highlighted by the red crosses. The user manually selects these points in the given order from 1 to 8. Then, in the center image, the unit vector $\vec{u}$ defining the segment's direction is calculated. Finally, the segments are depicted with the boxes with black edges in the image on the right.

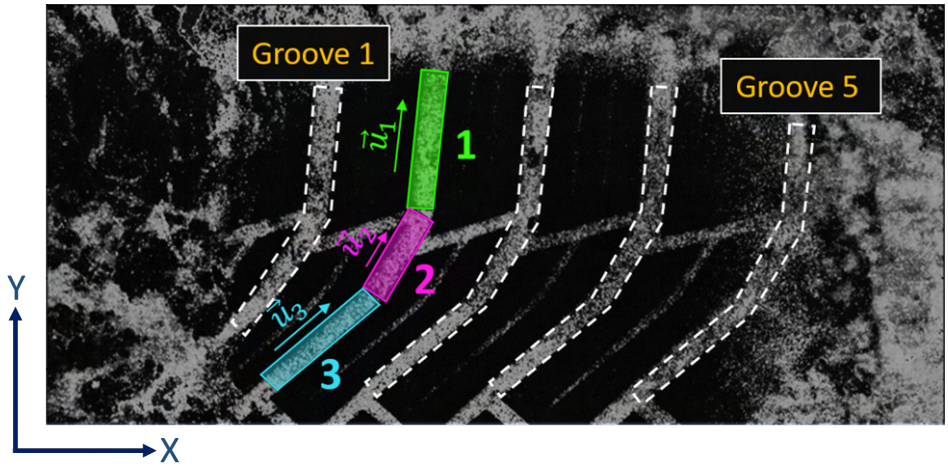

(a) Directional groove

(b) Central groove

Figure 6.4 – Definition of the segments cutting and highlight on the new referential axis in each segment in Groove 2 (a) and segmentation of the zigzag central groove (b): A6 tread

6.2 Alpin 6 case: analysis from r-PIV

We start, as an example of the way to proceed, by analyzing the MICHELIN Alpin 6 205/55 R17 (A6) case. We consider a worn state of the tire leading to a remaining tread depth of $h = 2mm$ (for a new tire it is about $8mm$). We give in Fig.6.5 a depiction of the A6 tread in both new and worn states with some dimensions to give the reader an order of magnitude concerning the tread design. The central groove has a zigzag shape connected to directional grooves extending from the center to the shoulder of the tire and segmented into three nearly straight segments. Note that for acoustic issues the actual width and spacing of directional grooves are not strictly equal for all of them, and the dimensions given in Fig.6.5 are averaged typical values. Moreover, some segments of the directional grooves have a worn indicator producing periodically a local geometric restriction of the flow in the groove as the car is rolling. Nevertheless, these indicators do not appear to influence the flow inside the central groove and are rarely located in the directional grooves in our database. In comparison, such indicators are of first-order importance inside

longitudinal grooves for summer tires as the one investigated by Cabut et al. [11]. The third kind of grooves of interest are the ones between two adjacent directional grooves, herein after simply identified as “connecting grooves”. Finally, the tire has what is known as an “evolving" tread, which results in the progressive appearance of sipes during the wear process among other modifications. Nevertheless, the spatial resolution of our r-PIV measurements is not sufficient for capturing the flow inside these sipes because of their reduced width. We only focus on the flow circulation in the central and directional grooves. A part of the results in this section has already been presented in [8].

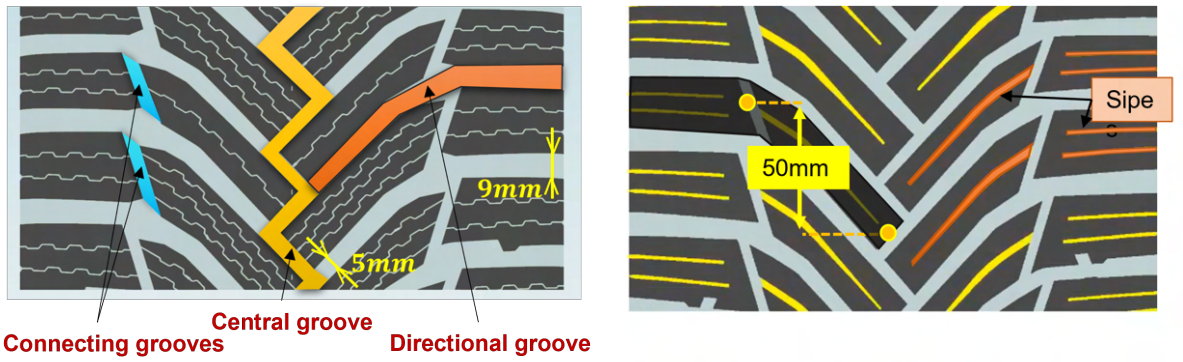

(a) New state (b) Worn state

Figure 6.5 – Details of the A6 tread design at new (a) and worn (b) state respectively.

6.2.1 Analysis in the central and directional grooves

The evolution of $V^*_{u_{mean}} = V_{u_{mean}}/V_0$ with X/L_x inside the CPA is shown in Fig.6.6, for directional grooves (Figures 6.6(a), 6.6(b) and 6.6(c)), and for the central zigzag groove (Fig.6.6(d)). In these figures, the position $X = 0$ corresponds to the entrance of the CPA, and $X/L_x = -100\%$ to the exit of the CPA. The results are remarkable, mainly for segment 1 of the directional grooves. Despite the small number of runs, the characteristic fluid velocity $V^*_{u_{mean}}$ of the fluid inside segment 1 is clearly correlated with X/L_x. The flow is pushed out of the groove at the beginning of the CPA, and sucked inside the segment at the end of the CPA; the maximum value of $V^*_{u_{mean}}$ is around 0.6 which is lower than the Slick tire where $V^*_y \approx 1$ near the shoulders (Fig.4.23), highlighting the effect of the grooves in the water distribution during the drainage. Such a correlation between the fluid velocity inside a transverse groove and its location inside CPA has previously been established by Cabut et al. [11] considering the analysis of transverse type C-type grooves

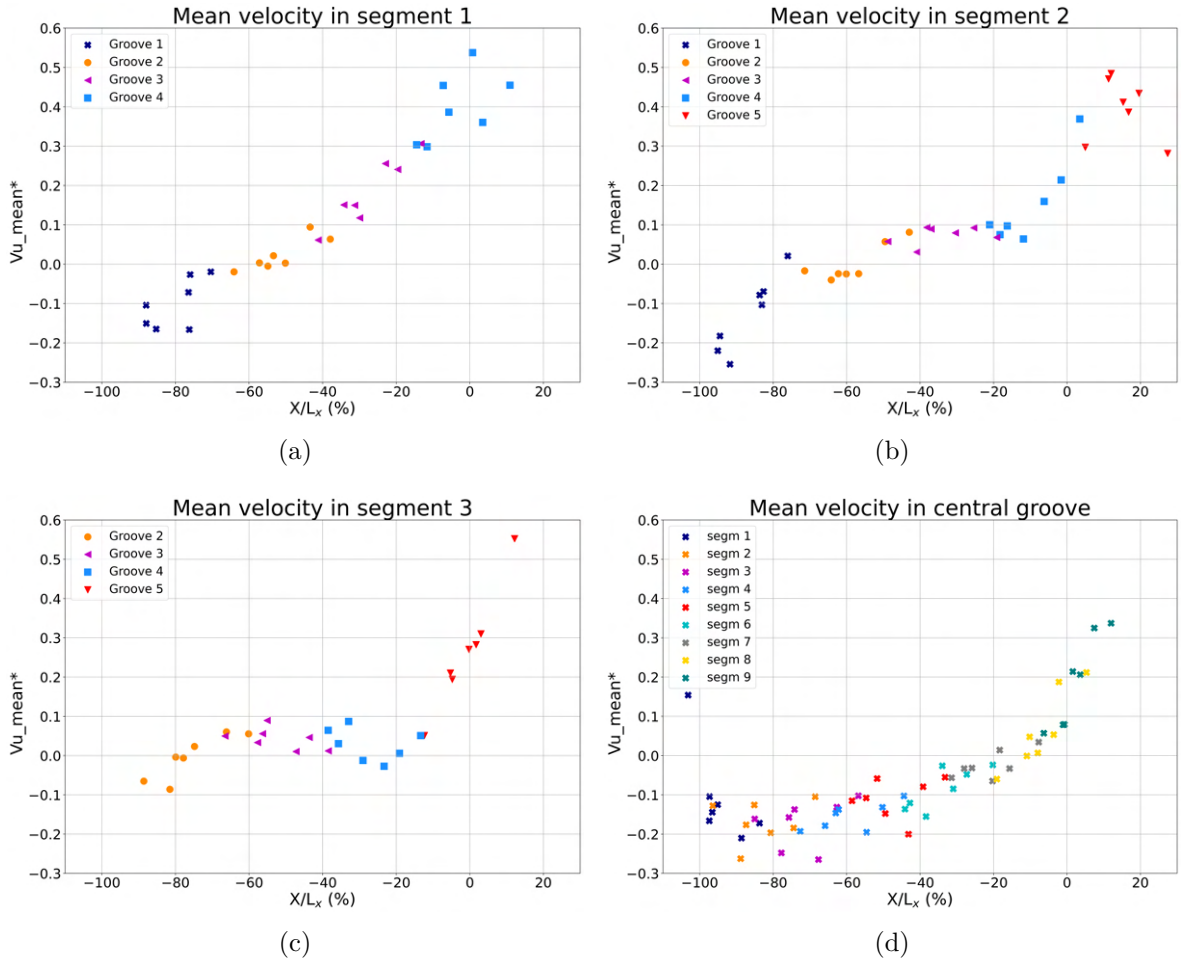

Figure 6.6 – Evolution of $V^*_{u_{mean}}$ over the grooves in the CPA in segment 1 (a), segment 2 (b), segment 3 (c) and zigzag groove (d) for N=7 runs, $V_0 = 11.11m.s^{-1}$ and $H_w = 1.5mm$

of a summer tire with four longitudinal grooves (PCY4). In that case, the correlation was nearly linear, there was no suction for grooves located at the end of the CPA, and the maximum normalized velocity was around 0.2, a value much smaller than the present one. The authors linked this behavior with the compression and relaxation of the rubber in the inlet and the outlet of the CPA, highlighting a parabolic distribution of the pressure at the shoulder (Heinrich and Klüppel [47]). A correlation between $V^*_{u_{mean}}$ and X/L_x is also clear for segments 1 and 2. For the central zigzag groove, the evolution of $V^*_{u_{mean}}$ with X/L_x shows a monotonic variation illustrating the accumulation of water from the front end of the CPA until its rear end. We give in Fig.6.7 a scheme of the upper half of the CPA with the flow drainage directions inside the grooves represented with arrows.

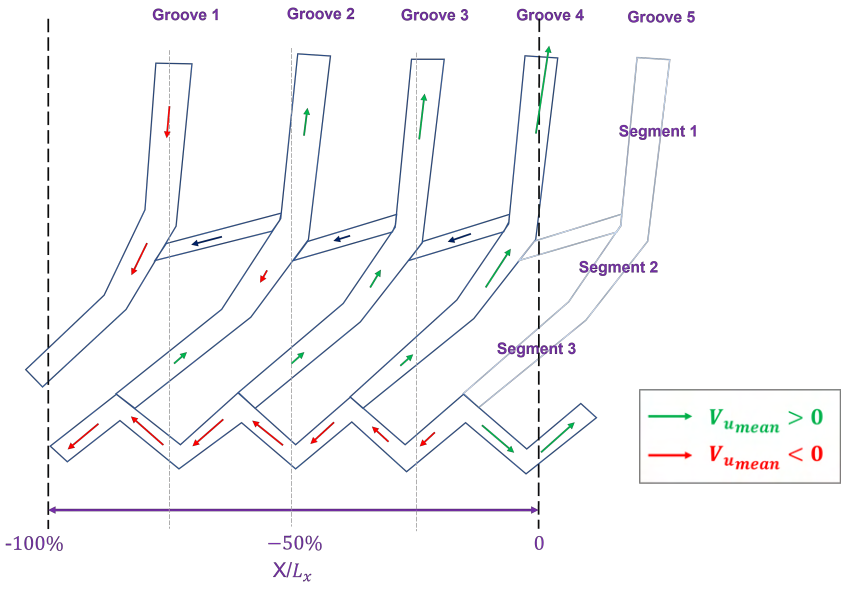

Figure 6.7 – Flow circulation scheme for the A6 at $V_0 = 11.11 m.s^{-1}$. The arrows depicted in the connecting grooves are given for general guidance purposes only and are based on the velocity field of a single run. A dedicated analysis should be conducted for more accurate results in these connecting grooves.

6.2.2 Effect of V_0

The previous results concerning the A6 tire were obtained for a single value of V_0 fixed at $11.11 m.s^{-1}$. In the current section, we aim to study the evolution of $V_{u_{mean}}$ for V_0 increasing from $8.33 m.s^{-1}$ to $19.44 m.s^{-1}$.

6.2.2.1 Inside the central groove

Fig.6.8 presents the results concerning $V^*_{u_{mean}}$ inside each segment of the central groove. The same segmentation into 9 sub-areas of the central groove previously used (Fig.6.4(b)), is also adopted for all V_0 values studied.
We can see that the shape of the $V^*_{u_{mean}}$ profiles is nearly the same for all V_0 values, and the correlation between the position of the segment with its corresponding $V^*_{u_{mean}}$ is preserved. We give also in these figures the standard deviation inside each segment in order to construct tendency profiles (Fig.6.8(f)) inside the envelopes of error.

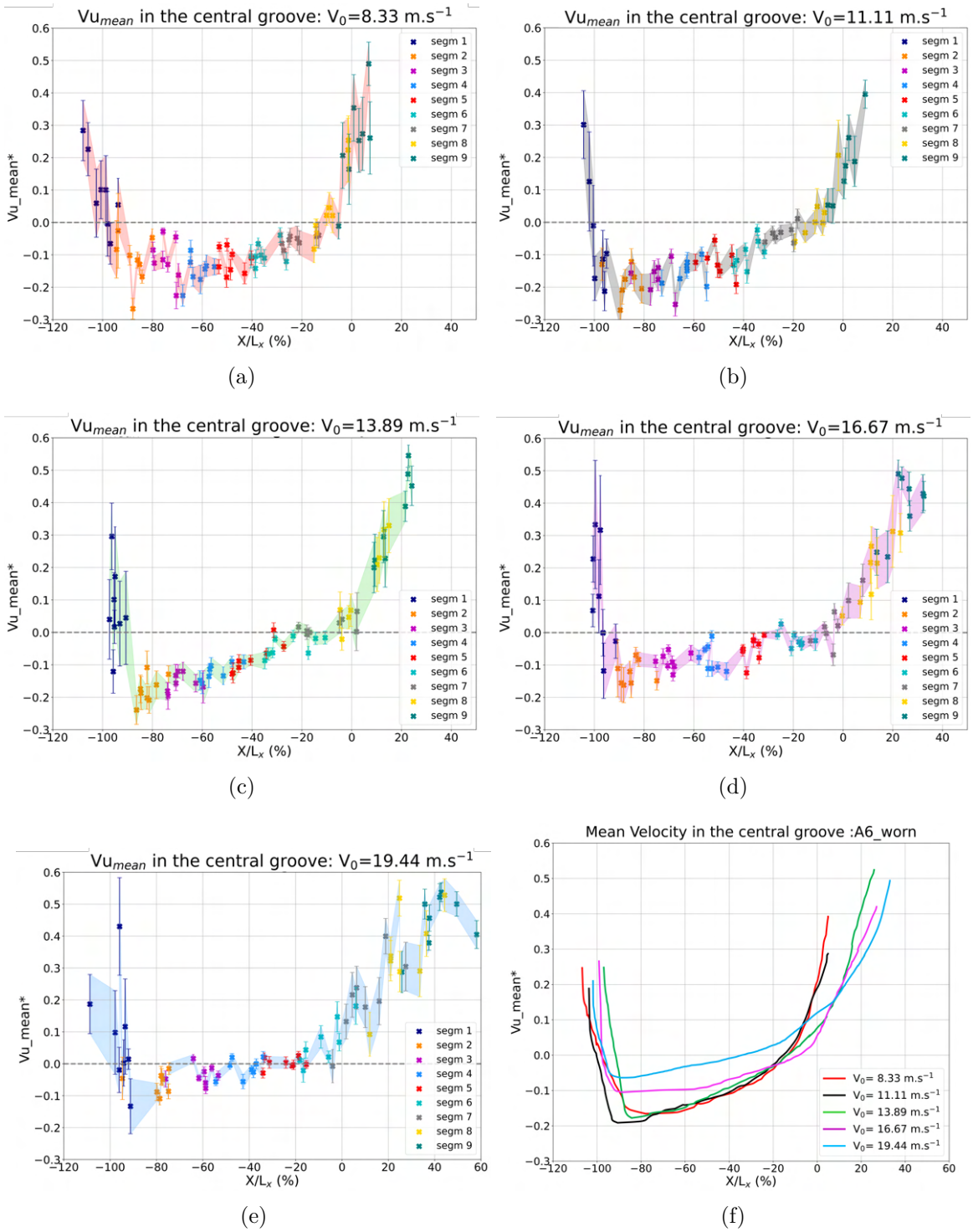

(a) (b) (c) (d) (e) (f)

Figure 6.8 – Evolution of $V^*_{u_{mean}}$ in the central groove of the A6 worn at respectively $8.33m.s^{-1}$ (a), $11.11m.s^{-1}$ (b), $13.89m.s^{-1}$ (c), $16.67m.s^{-1}$ (d) and $19.44m.s^{-1}$ (e). The error bars represent the standard deviation inside each segment, N=8 runs and $H_w = 1.5mm$. The X-axis is normalized by the respective CPA length L_x corresponding to each V_0 value. In (f) we represent a tendency profile for each V_0.

From case $V_0 = 16.67m.s^{-1}$ to $V_0 = 19.44m.s^{-1}$ we clearly see that profiles do not collapse indicating a change in the flow regime. Indeed, we can observe that $V^*_{u_{mean}}$ decreases when V_0 increases, and for $V_0 = 19.44m.s^{-1}$, the circulation inside the central groove does not exceed $0.05V_0 \approx 1m.s^{-1}$ inside the CPA, as if a certain limit of water evacuation has been achieved and the groove is only playing a role of storage. This change in regime corresponds to the sudden acceleration in the CPA reduction when V_0 increases given in Fig.6.9. This indicates that the establishment of the hydroplaning phenomenon follows different regimes with a sudden hype around a certain value of V_0 that depends on the tread height and the global parameter S/S_0 (relative CPA loss with S_0 the CPA surface when the vehicle is at rest) supports this observation. Therefore, the local parameter $V^*_{u_{mean}}$ would also follow this change in the regime when V_0 increases.

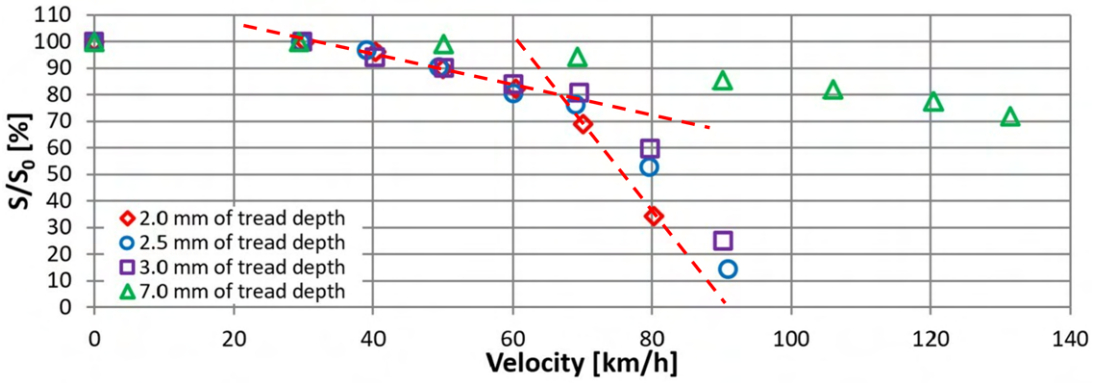

Figure 6.9 – Evolution of the relative contact surface with the vehicle velocity (extracted from Hermange et al. [50]). The slopes in dashed lines are added to the original figure.

6.2.2.2 In the shoulder area

We give in Fig.6.10(b) the evolution of $V^*_{u_{mean}}$ in the shoulder region of the A6 worn (segment 1 highlighted in Fig.6.10(a)). The profiles presented are the tendency curves over the N runs constructed as in Fig.6.8(f). We can clearly see that there is not any self-similarity in the $V^*_{u_{mean}}$ profiles when increasing V_0 as long as L_x is chosen to normalize the X-axis. We observe that the slope of the curves decreases with V_0 with a rather important gap between $V_0 = 19.44m.s^{-1}$ and the other lower velocities. Moreover, in the rear of the CPA, we see that $V^*_{u_{mean}} > 0$ for $V_0 = 19.44m.s^{-1}$, in opposition to the other cases where V_0 is negative. This means that the flow is not sucked anymore towards the CPA in the rear area, but it is expelled outside the CPA no matter the position of the groove. It looks

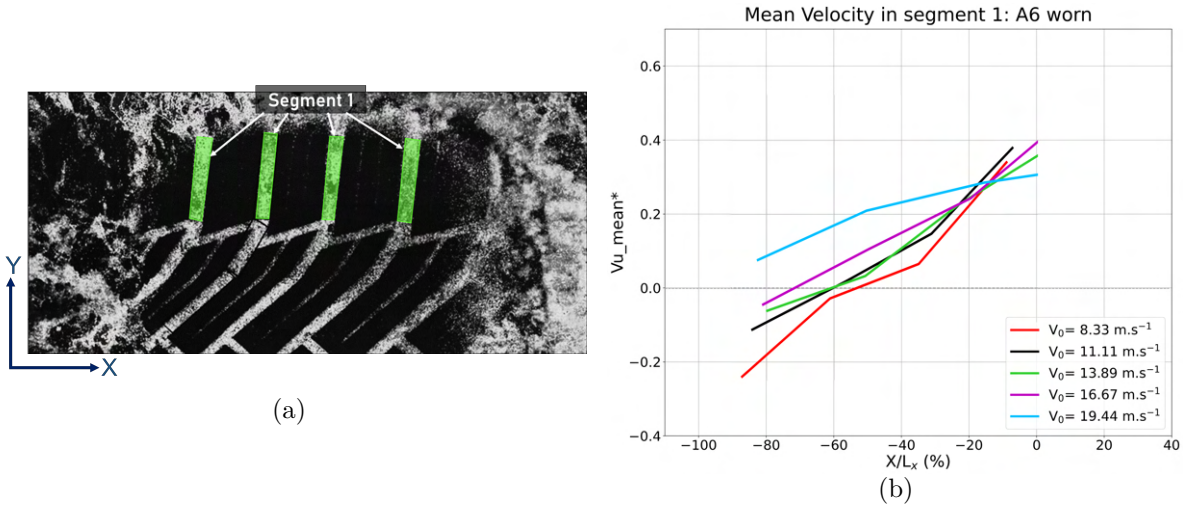

(a) (b)

Figure 6.10 – Highlight of the shoulder area (Segment 1 over the four grooves) on the left image, and tendency profiles of $V^*_{u_{mean}}$ for all V_0 values studied on the right part.

like at each value of V_0, a balance between low pressures at the rear of the CPA sustaining the water suction and high pressures inside the WB leading to the water ejection outside the CPA is established. Both phenomena intensify when V_0 is increased, but the high pressures in the WB seem to increase faster than the low pressures at the rear of the CPA. Segments 1 located in the rear of the CPA cannot suck water anymore, they either store it in the case of $V_0 = 16.67 m.s^{-1}$ or eject it if V_0 is increased even more. A unique regime in segments 1 tends to be reached where they play a similar role as we see slopes of $V^*_{u_{mean}}$ decreasing with V_0 in Fig.6.10(b).

6.3 Comparison at the shoulders with the PCY4 with the evolution of V_0

In this section, we aim to compare the behavior of a summer tire (PCY4) versus a winter type (A6) regarding the drainage of the water in the shoulder region. In his work, Cabut [10] presented results about the velocity in the C-type grooves (transverse grooves highlighted in Fig.6.11(a)) for the PCY4 comparing a new and a worn tire. For a worn tire, as we can see in Fig.6.11(b), there is a rather linear increase of $V^*_{u_{mean}}$ with the position of the groove inside the CPA for all V_0 values. However, the water is expelled outside the CPA no matter the position of the type-C groove, which is not the case for the PCY4

in a new state, and neither for the A6 worn when $V_0 < 19.44 m.s^{-1}$ (Fig.6.10(b)). What

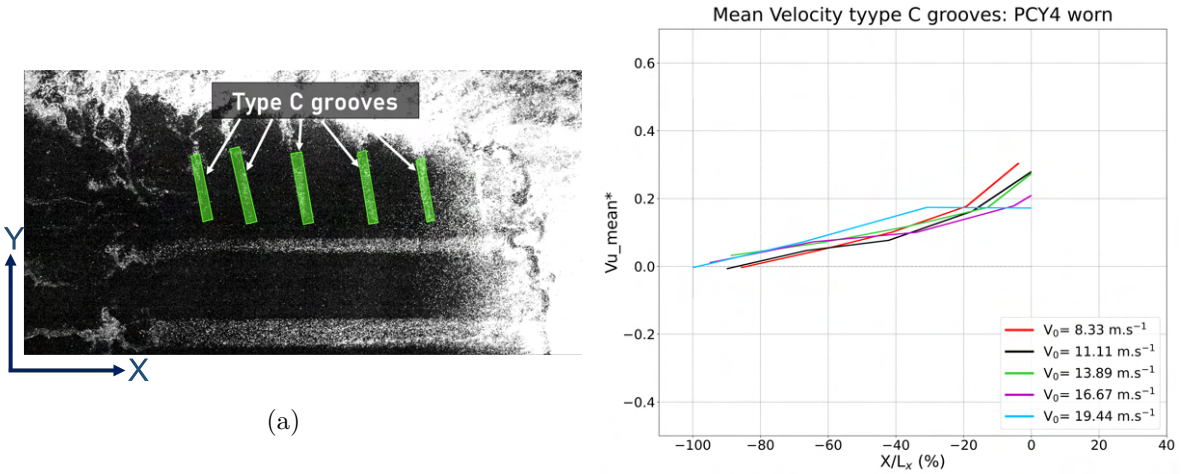

(a) (b)

Figure 6.11 – Highlight of the C-type grooves on the left image for the PCY4 worn, and tendency profiles of $V^*_{u_{mean}}$ for all V_0 values studied on the right part.

differentiates the PCY4 worn tread is the non-connection of C grooves with neither an A groove nor another segment of the same directional groove which is the case of the PCY4 new and the A6. The storage limit of these C grooves is therefore reached faster. It seems that for the suction to happen, a connection of the C grooves is needed with other channels of the tread. Moreover, the values of $V^*_{u_{mean}}$ are lower in the case of the PCY4 tire than for the A6, and a similarity in the C-type grooves is noticed as the profiles for different V_0 are rather overlapped. The post-treatment in the case of the A6 tire is more complicated than for the PCY4, and it is possible that normalizing the X-axis with L_x is not well adapted for such a directional tread pattern.

6.4 CCP case: comparison between numerical and experimental results

The MICHELIN Cross Climate+ 205/55 R16 (CCP) is an all-season tire presenting like the A6 a zigzag central groove and directional grooves connected to the center one (Fig.6.12). The segmentation method is applied to this tire as we did for the A6. The segmentation of the CCP tread is presented in Fig.6.13. Each directional groove inside the CPA is divided into three segments following the change of direction of the groove. The

Figure 6.12 – 3D sculpture of the CCP

central zigzag groove is divided into 9 segments. This allows us to cover approximately all the CPA locations longitudinally. The segmentation is similar between the numerical and experimental data and is manually done by the user as it has been detailed in 6.1.

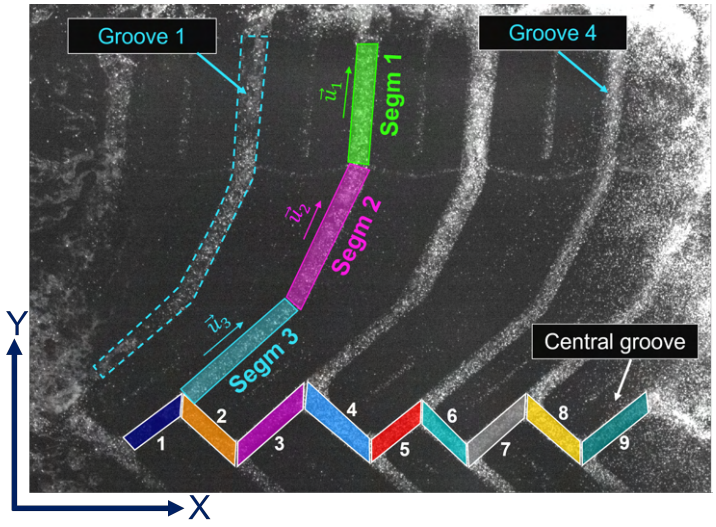

Figure 6.13 – Definition of the segments cutting and highlight of the new referential axis in each segment in CCP tire displayed here in Groove 2. The segmentation of the zigzag central groove is also represented.

6.4.1 Sources of discrepancies

Before presenting the results inside the segmented grooves of the CCP, we would like to highlight the different sources of errors and discrepancies that exist in our analysis:

- Since the segmentation of the groove's boundaries is done manually both experimentally and numerically, we introduce an error in the selection of the segment area and therefore in the calculation of its orientation vector $\vec{u}$ and its surface S_{segm}. We add that it is due to the irregularities in the tread design that an automatic segmentation is rather difficult, especially experimentally. These irregularities are further discussed in the following points.

- In a real CCP model, the tread design is not a circular repetition of a unique pattern but rather a repetition of a given number of patterns that differ in the distance between the directional grooves and also in their width. This is a commonly used technique by tire manufacturers to reduce noise ([68]). The experimental results are consequently impacted by these irregularities. However, the numerical model of the tire does not take into consideration this subtlety because it is largely difficult to reproduce each pattern individually in the FE mesh. Indeed, a unique pattern is used and with a circular repetition, the tread mesh is generated as described in Section 2.4.1.

- There is a rather important discrepancy in the experimental results between one run and the other and it is not only due to this existing irregularity in the tread design. As stated before, the tire studied is in a worn state which is obtained by reducing the tread depth of a new tire, and the process to obtain the wanted depth introduces inevitably an added irregularity in the shape of the grooves.

- Another source of discrepancy in the experimental results is the slight variation of the water depth from one run to another, those oscillations are generally around $\pm 0.1mm$ for $H_w = 1.5mm$ [10].

For all these reasons, we choose to focus on only one run from the experimental database in order to establish the comparison with the numerical results. The absolute values obtained experimentally may evolve from one run to another but not the general tendency in the circulation scheme inside grooves, and this is what we are going to focus on.

6.4.2 Numerical inputs and post-processing

We give in Fig.6.14 a 3D view extracted from coupled SPH-FE simulation. We choose $H_w = 1mm$ in the numerical model against $H_w = 1.5mm$ in the r-PIV, to limit the computing time mainly due to the complex 3D mesh of the CCP which has been generated for this specific application. This difference in H_w is inevitably a source of discrepancies between numerical and experimental results. The input parameters for the numerical model are given in Table 6.1.

The total number of SPH particles was around 3.3M particles. The FE mesh has 435

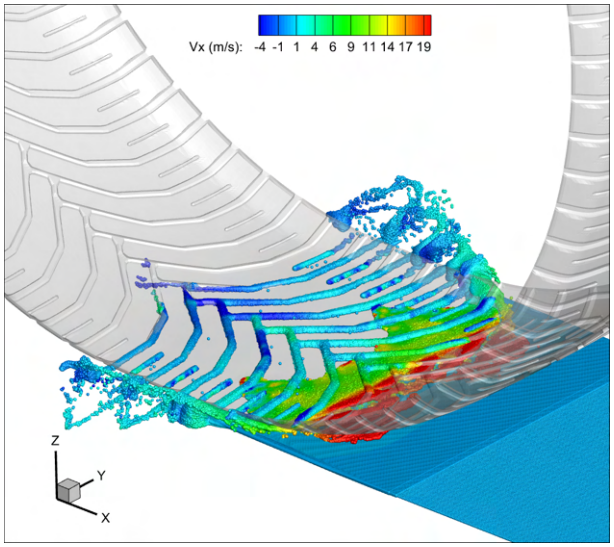

Figure 6.14 – Snapshot from simulation result: velocity field V_x for the CCP at $V_0 = 13.89m.s^{-1}$ and $H_w = 1mm$. Only the tire tread is represented (in transparency).

Physical parameter	Value
Puddle dimensions (XY) plane	L_x=1500mm L_y =200mm
H_w	$1mm$
V_0	$13.89m.s^{-1}$
ρ_{water}	$1000kg.m^{-3}$
g	$9.81\ m.s^{-2}$
P_{tire}	$2.4bars$
Load	$380daN$

Numerical parameter	Value
$\Delta x_{SPH_{min}}$	$0.25mm$
$R/\Delta x_{SPH}$	2.11
C_0	$250m.s^{-1}$
k_{CFL}	0.375

Table 6.1 – Physical and numerical parameters

780 solid elements, and a lot of work was been done to lighten the model especially by

reducing the refined region of the tread (Fig.2.9). The simulation was run on 48 CPUs for the SPH solver, 20 CPUs for the FE solver, and 1 CPU for the coupling algorithm. The computation time was around 670h which is very high for a water depth of for $H_w = 1mm$. This is due to the CCP tread mesh and its connection with the rest of the tire architecture. The tread mesh was generated using specific software (ICEM) and the major drawback was the incompatibility between the mesh nodes of the tread and the mesh nodes of the architecture. The calculation of this connection is very expensive in terms of computational costs than a model where the mesh nodes of the tread and the architecture perfectly match as is the case of the PCY4 mesh (Fig.6.15).

Furthermore, as a post-treatment, we choose to generate a 2D velocity field in the (XY)

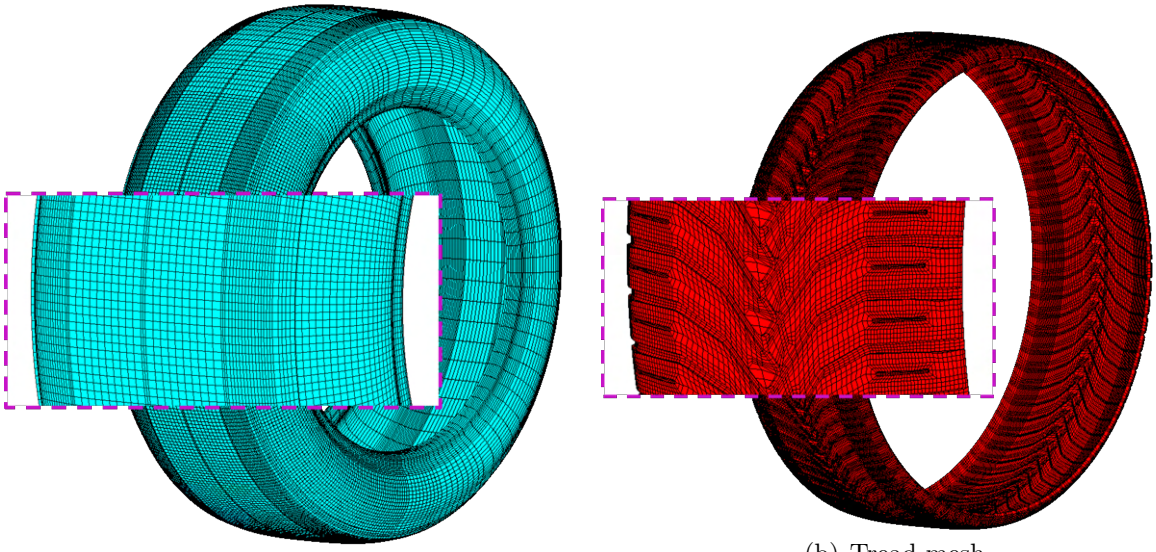

(a) Architecture mesh

(b) Tread mesh

Figure 6.15 – The CCP architecture (a) and tread (b) 3D meshes are given with a highlight on the difference in the nodes' positions in each of them.

plane at $Z = 0.5mm$ for the numerical/experimental comparison. Therefore, a slice is created at this altitude, on which velocity fields of the surrounding particles are interpolated (Fig.6.16).

6.4.3 Flow circulation scheme

To better grasp the full flow circulation in the CPA, we give in Fig.6.17 a scheme of the upper half of the CPA with the flow drainage directions inside the grooves represented with arrows. To facilitate the reading of the next paragraphs, the reader may refer to

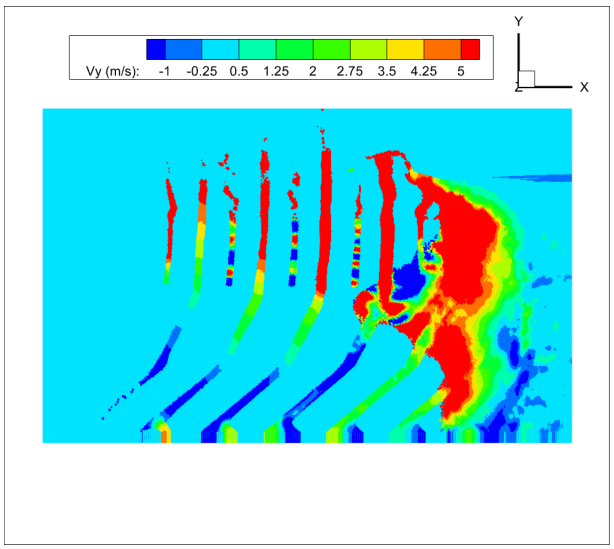

Figure 6.16 – Numerical solution of the CCP tire: Post-treatment result for the 2D velocity field in the (XY) plane at $Z = 0.5mm$. The interpolation plane focused on the upper half of the CPA region. This slice is used for the directional grooves segmentation.

these schematics. An important observation here is the opposite directions of the flow inside Groove 3 in segments 1 and 2 observed experimentally. Conservation considerations impose that such a situation can only occur if the fluid can escape from Groove 3 between segments 1 and 2 which is the case due to the presence of connecting grooves (highlighted in red in Fig.6.12). We can also see these grooves appear on an r-PIV image in Fig.6.13. However, such tread details were not taken into consideration in our numerical model due to their small thickness. Indeed, the spatial resolution of the fluid domain should be reduced significantly so that a minimum of SPH particles penetrate inside these connecting grooves and describe rather accurately the flow circulation. We would like to emphasize the difficulty to simulate such flow inside directional tread patterns where all grooves are connected to each other through a complex network. The tread geometry needs to be modeled very carefully so that the FSI coupling leads to satisfactory results.

6.4.4 Inside the directional grooves

Inside the CPA, at $V_0 = 13.89m.s^{-1}$ we usually capture 4 directional grooves. As stated before, each groove is divided into three segments numbered as in Fig. 6.13 where segm 1 is the outer one and segm 3 is the closest one to the central groove. The directional grooves are also numbered in the same figure, we note Groove 1 the rear groove (X-axis

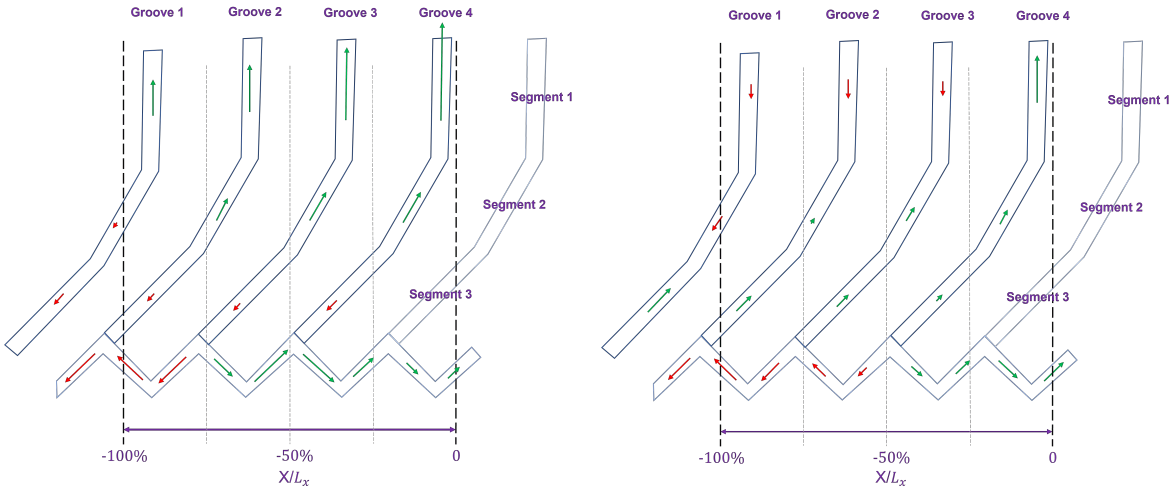

(a) Numerical (b) r-PIV

Figure 6.17 – Comparison between the flow circulation scheme over the directional grooves and the central zigzag groove from (a) numerical results and (b) experimental results, for the CCP at $V_0 = 13.89 m.s^{-1}$. The arrows in green represent a $Vu_{mean} > 0$ and in red $Vu_{mean} < 0$ inside each segment of interest. The connecting grooves are not represented here due to their very small width and lack of information on the flow inside them.

given in Fig.6.13) and Groove 4 the front one. The numerical and experimental results of the flow velocity inside each segment are given in Fig.6.18(a) and Fig.6.18(b) respectively. We see that there is not a good agreement in the absolute values of the flow velocity in the first instance. However, we have the right increasing dynamic in segment 1 and segment 2. But most importantly, we focus on the sign of Vu_{mean} in segment 1. We can see that experimentally $Vu_{mean} < 0$ until X/L_x is around 50%, meaning that the flow is entering the CPA in the rear region and is expelled in the front. This is not observed numerically. In Fig.6.18(a) we can see that the water flow is drained outside the CPA from $X/L_x = -100\%$. We note that the basic flow separation technique is used here. The water expulsion outside the CPA in the numerical model is rather similar to the one observed with the PCY4, in the rear of Groove B1 presented Section5.3.3. In both cases, we are unable to capture the entrance of the flow in the rear region of the CPA. And as long as this phenomenon is not well represented numerically, we cannot await a good agreement with the experimental results since it is expected to be a rather major driver of the flow circulation inside the CPA. Unfortunately, no further tests were conducted to estimate the effect of the new flow separation technique on the numerical results in the present work due to the lack of time.

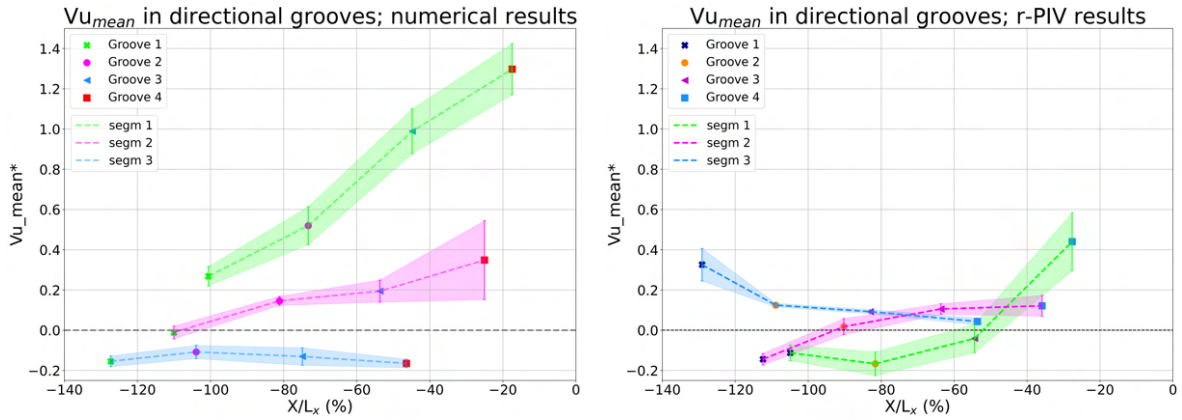

(a) Numerical (b) r-PIV

Figure 6.18 – (a) Vu_{mean} in the directional grooves for the CCP worn at $T = 11.4ms$: numerical results. The interpolation plane altitude is $Z = 0.5mm$. (b) Vu^*_{mean} in the directional grooves for the CCP worn at $H_w = 1.5mm$: experimental results. One run is considered here. In both (a) and (b), the envelope and the error bars represent the standard deviation of $Vu = \vec{V}.\vec{u}$ inside each segment.

6.4.5 Inside the central groove

We give in Fig.6.19 the results of the flow velocity inside the central zigzag groove. We can see that in both cases there is a position from which the flow is turned back and Vu_{mean} changes sign, we note it x_b. Experimentally,x_b is around -45% and numerically -75%, meaning that a major part of the drainage is done towards the front of the CPA in the numerical model, while experimentally it is rather evenly distributed between the expulsions to the front and to the rear. And while the evolution is close to linear in Fig.6.19(b), we can observe that there is a jump from $Vu^*_{mean} = -0.3$ to $Vu^*_{mean} = 0.2$ between segment 3 and segment 4. However, the circulation of the flow inside the central groove is most certainly affected by the flow drainage inside the directional grooves and further analysis of the central groove requires first a better acknowledgment of the circulation in the directional grooves.

Further comparison tests are conducted below to better understand the water drainage in the central groove during the rolling of the tire in the reverse direction to force a modification in the orientation of the directional grooves while keeping the same geometry. This can help analyze the impact of the circulation inside the directional grooves on the central one.

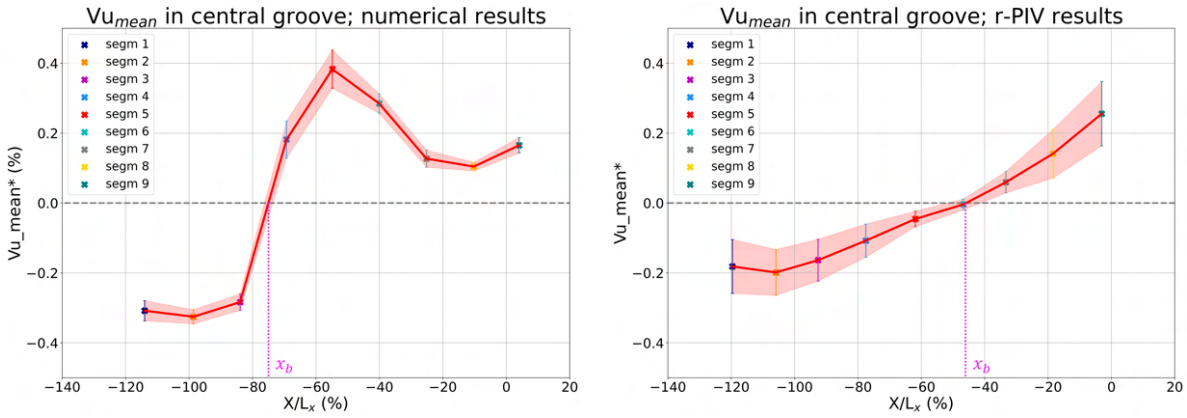

(a) Numerical

(b) r-PIV

Figure 6.19 – (a) Vu_{mean} in the central groove for the CCP worn at $T = 11.4ms$: numerical results. The interpolation plane altitude is $Z = 0.5mm$. (b) Vu_{mean} in the central groove for the CCP worn: experimental results. One run is considered here. The envelope and the error bars represent the standard deviation of Vu_{mean} inside each segment in both (a) and (b).

6.5 Comparison between the CCP in the direct and invert configurations

Directional tires, as mentioned before, have a tread pattern designed to rotate in only one direction. The grooves on both sides of the tread are made to run like two waterfalls joining from opposite sides forming a "V" shape (Fig.6.20(a)). Indeed, in this way, the grooves follow the natural direction of water ejection. However, Okano and Koishi [99] tested the configuration of a V-shape tread with a reverse rotation and compared it to the same tire rotated normally. It has been observed that the hydroplaning velocity of the reversed tread is lower. Therefore, we wanted to reproduce such a test and compare the results of the segmentation in particular in the shoulder region in the case of the CCP in a normal rotation configuration (Fig.6.20(a)) and a reverse one (Fig.6.20(b)).

The r-PIV measurements are conducted for the CCP worn at $H_w = 1.5mm$ and for three vehicle speeds: $8.33m.s^{-1}$, $11.11m.s^{-1}$ and $13.89m.s^{-1}$. The tendency profiles of $V^*_{u_{mean}}$ in the shoulder region (segment 1 as defined in Fig.6.13) are given in Fig.6.21. The full data are given in Appendix F.

Given the low number of repetitions $N = 3$, there is a rather important dispersion in the results, however, we will focus on one observation, in particular, that is always

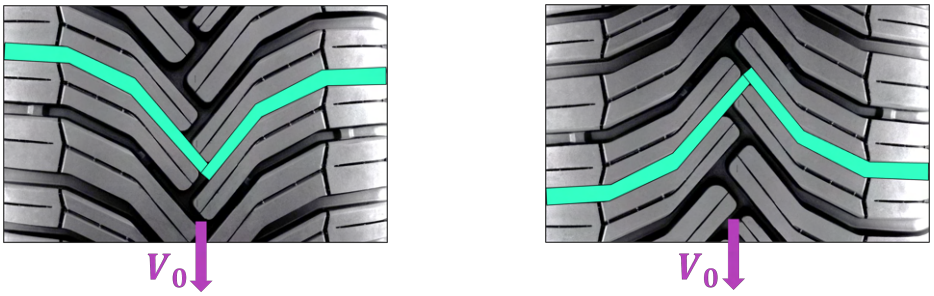

(a) Normal (b) Reverse

Figure 6.20 – Scheme of the CCP tire tread in a normal rotation configuration (a) and in a reverse rotation configuration (b). The vehicle moving direction is towards the bottom.

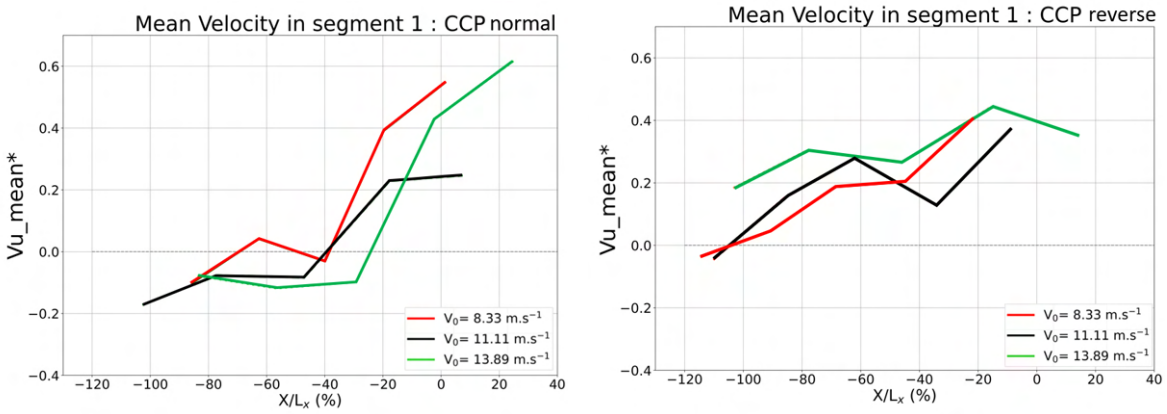

(a) Normal (b) Reverse

Figure 6.21 – tendency profiles of $V^*_{u_{mean}}$ for three V_0 values for the CCP in respectively normal (a) and invert (b) configurations.

respected. We see that for the reverse rotation, $V^*_{u_{mean}} > 0$ meaning that the water is expelled outside the CPA whatever the position of the groove. Meanwhile for the normal rotation, in the rear of the CPA, we observe that $V^*_{u_{mean}} < 0$. The water is therefore sucked up towards the CPA. This behavior when $V^*_{u_{mean}} < 0$ in the rear then $V^*_{u_{mean}} > 0$ in the front of the CPA is common to these cases:

- The A6 worn when V_0 is lower than $19.44 m.s^{-1}$
- The PCY4 new for $V_0 = 13.89 m.s^{-1}$ and $H_w = 8mm$ (Cabut [10])
- The CCP worn in a normal rotation configuration

While we found that $V^*_{u_{mean}} > 0$ no matter the position of the groove in the CPA for the following cases:

- The A6 worn at $V_0 = 19.44 m.s^{-1}$
- The PCY4 worn for all V_0 values ([10] and present work)
- The CCP worn in a reverse rotation configuration

Based on these observations, it seems that the water suction in the shoulder region at the rear of the CPA appears in overall better conditions than the expulsion all along the CPA i.e. lower V_0, new tire, normal rotation. The water suction from the shoulders towards the CPA looks like a drainage mechanism that can only be activated when certain conditions are fulfilled regarding the tread depth, the vehicle speed, and the whole tread pattern orientation. In addition, the connection of the transverse grooves' extremities to other parts of the tread channels (A grooves or other segments of the same directional groove), seems to be a major condition to the appearance of the suction effect. However, further measurements should be conducted to validate this observation, integrating the modification of the water height while keeping the same tread depth for example, and also covering a wider range of vehicle speeds to ensure that the tendency does not change for very high V_0.

6.6 Conclusion

In the current chapter, we presented some elements of a local investigation of the velocities involved during the rolling of a directional tire over a water film. The r-PIV measurement technique as well as the SPH-FE simulations have proven their efficiency in front of a rather complex tread design with inclined directional grooves and a central zigzag groove. The numerical results still need to be improved especially by testing the treatment proposed in section 5.6.3 to be able to generate a suction effect in the shoulders. Additional simulations should also be carried out with the exact same water depth as the experimental value. Connecting grooves should be taken into consideration in the tread mesh as well, as their impact on the overall flow circulation has been pointed out.
A segmentation of the directional and central zigzag grooves into elementary straight segments has been performed and allowed to deduce, for each element, and for every run, a dimensionless characteristic velocity $V_{u_{mean}}$. Results highlighted a clear correlation between $V_{u_{mean}}$ inside an elementary segment and its position in CPA. This correlation is particularly clear for the segments of the grooves close to the shoulders. Two different behaviors have been observed, either i) a water expulsion whatever the position of the groove, or ii) a region where the water is first sucked up towards the CPA in the rear

zone and then expelled outside the CPA in the front. Comparisons at different vehicle velocities, different tire treads, and different rolling configurations have been presented concluding on the parameters that seem to drive the appearance of one behavior over the other. Further investigations should be conducted to assert these observations. Last but not least, a change in regime in $V_{u_{mean}}$ in the central groove has been pointed out when increasing V_0 that has been correlated to the sudden change in slopes in previously published measurements about S/S_0 evolution. However, the normalizing variable L_x should be adapted to such directional tires.

Conclusion and perspectives

Major findings

The aim of this thesis was to improve the understanding of the hydroplaning phenomenon by means of r-PIV measurements and coupled SPH-FE numerical simulations. These tools have already been used separately in previous studies and the objective was to achieve a complementary analysis that will not only advance our comprehension of such a complex phenomenon as hydroplaning, but also pursue the validation of the numerical tool.

The post-processing phase of experimental results was first discussed and several offsetting strategies were proposed to collapse the recorded images into a common referential. The efficiency of these offsetting methods was shown to be tread-dependent, and quantification of the offsetting quality was proposed.

Furthermore, the complexity of the water-bank structure has been shown based on the divergence of the 2D experimental velocity field which gave valuable information on the important 3D flow circulation. Also, the proposed mass budget analysis quantified the effect of increasing the water depth or enlarging the tire. Different regimes were detected when the water depth increased and the presence of a secondary structure whose creation mechanism could be similar to the so-called "horseshoe vortex" for fixed semi-immersed bodies, was assumed in front of the tire. TR-PIV measurements were also conducted for the first time in a hydroplaning application, and relevant results about the unsteady nature of the flow were obtained demonstrating that further studies with such a tool are very promising.

After focusing on this simplified and near-analytical case, a longitudinal tire tread was studied as a more realistic condition for daily usage. Comparisons with numerical simulations have shown rather good agreement and encouraging results, however, the actual numerical model did not take into account suction effects which have been highlighted as an important phenomenon. Indeed, r-PIV measurements exhibited the significant impact of the suction at the rear on the water drainage inside the longitudinal grooves. Numerical tests on the Test-Bench where a new flow separation technique has been included showed

promising improvements compared to the fully coupled model and allowed us to consider further parametric studies to outline some major guidelines. With the Test-Bench, we were able to quantify the impact of C_0 on the numerical solution as well.
Last but not least, complex directional treads were studied. Based on the segmentation technique, a correlation between the groove's position and the velocity inside it has been presented. We showed that it is a powerful tool to demonstrate similar behavior and change in regime. The comparison with numerical results showed the importance of taking into account the connecting grooves in our tire model, as a directional tread is a complex network of water channeling, and simplifying it numerically degrades necessarily the results. Nevertheless, the comparison in the shoulder region between different directional and longitudinal treads at increasing vehicle speed exposed a common water circulation. It was shown that when the segments positioned at the limit of the shoulders are connected to other grooves or grooves' segments, water suction appeared at the rear of the CPA. This highlighted once more the importance of developing a numerical model that could reproduce such effects.
However, in some cases, experimental data suffered from a rather low number of repetitions, in part due to the limited number of exploitable images despite a high total number of images recorded (presence of WI, CPA trimmed, low illumination, H_w far from the target) but also due to adverse weather conditions during some testing campaigns. In addition, the variability of the flow in specific applications was not previously known and the number of repetitions was therefore underestimated.

Perpectives

The work provided in this thesis covered some effects of hydroplaning which involves various other phenomena leading to a large range of possible research. The numerical/experimental comparisons exhibited some limitations in our numerical model that are certainly simplifying the simulations and reducing the computational costs but at the expense of the solution accuracy. Therefore, the simplifying assumptions in our numerical model should be qualified depending on the case studied (tread geometry) and the user's need (global/local analysis). The introduction of the fluid viscosity should be considered if very local effects such as the possible development of vortices in front of the slick tire are studied. At a smaller geometric scale and for more relevant daily usage, studying tires like the PCY4 and the possible link between viscosity and vortex generation in front of

ribs at the inlet of longitudinal grooves remains an open scientific question and a challenge for both simulation and experiment. Moreover, the new flow separation technique should be tested on a fully coupled model, and if the results are in good agreement with r-PIV measurements, this new treatment should be taken into account to capture accurately the suction effects in the shoulders and behind the tire. In addition, increasing the spatial resolution and taking into account tread details as the connecting grooves in directional treads should be taken into consideration. Indeed, even if global parameters such as the loss of contact patch area are in good agreement with experimental results, the local velocity field inside the grooves is not well captured. The Test-Bench allowed us, given some simplifying hypotheses, to recover the important flow trends. Due to a lack of time, we have not completely finished testing such a tool for various types of tire treads. It seems now also important to pursue such development by adding the above-cited elements, then implementing them into the fully coupled simulations. We also briefly discussed the impact of wear indicators and a two-phase flow at the beginning of this thesis. It is the next challenge of this numerical tool to account for these elements.

These additional parameters will obviously increase the computational costs of the fully coupled SPH-FE simulations, which are already high, especially in an industrial context. Therefore, further optimizations should be investigated such as the use of an explicit FE solver. Also, we have pointed out the importance of a detailed tread geometry, but the relevance of such complex tire architecture in our numerical model was not studied. Further tests on simplifying the architecture model should be conducted and a trade-off should be found between computational costs and the accuracy of the results. In addition, increasing the regularity of pressure fields obtained with the SPH method would be useful for stability issues, and the question of switching to ISPH naturally arises. As it has been shown, based on the Test-Bench simulations, the value of C_0 is critical, and the acoustic effects inevitably generated by the particles' squashing are detrimental to the solution. This inevitably brings us to the ISPH approach and its relevancy to answering these two issues.

From another point of view, experiments provided results that did not describe directly and quantitatively the 3D domain. It is clear that in the future, more elaborate tools used by the LMFA should be tested allowing us to obtain the full time-resolved 3D-3C information. Some 3D PTV measurements could be conducted as those done by Lacassagne et al. [64]. Having in mind also the direct determination of both 3D velocity and pressure fields which constitute a very challenging objective for comparisons with numer-

ical simulations. Such an experimental strategy could include preliminary estimates of 2D pressure fields using r-PIV measurements. Furthermore, the TR-PIV measurements could allow more exhaustive comparisons with time-resolved numerical simulations and thus possible new joint parameters to help ultimately tire conception. Even if the first trials were not completely satisfactory for extra-scientific reasons (weather conditions), it is of first importance to pursue such time-resolved measurements. Moreover, different post-processing tools developed initially for the analysis of the flow in the case of a slick tire could be improved and used more systematically for different tire geometries with an in-depth analysis of the splitting process of the mass fluxes around the shoulder and inside grooves.

Different interrogations certainly remain concerning hydroplaning, as the effect of the gas phase, the presence or not of cavitation, and the influence of turbulence and few attempts have been made to study them. An extension of the present work is needed to cover these complex physics and quantify their impact on tire performance.

Appendices

Appendix A

Slick tires: measurements summary

Tire model	$\mathbf{H_w}(mm)$	$\mathbf{V_0}(\mathbf{m/s})$	N	$\sigma(\mathbf{H_w})(mm)$	$\sigma(\mathbf{V_0})(m.s^{-1})$
Slick 205	8	8.33	8	0.19	0.08
Slick 225	1.5	8.33	8	0.10	0.04
	2	8.33	3	0	0.19
	3	8.33	3	0	0.11
	4	8.33	3	0	0.13
	5	8.33	3	0	0.12
	6	8.33	3	0.01	0.11
	7	8.33	10	0.11	0.05
	8	8.33	8	0.42	0.11
Slick 275	8	8.33	8	0.20	0.18
Slick 315	8	8.33	8	0.07	0.04

Table A.1 – Summary of measurements parameters for the Slick tires

Appendix B

Taylor expansion for mass budget expression

Let us consider the Taylor series at first order applied to d_1 to estimate the integral along Z-axis:

$$V_x(x = x_1, y, z) - V_0 = V_x(x = x_1, y, z = z_0) - V_0 + (z - z_0)\frac{\partial V_x}{\partial z}(x = x_1, y, z = z_0) \quad \text{(B.1)}$$

Therefore we obtain:

$$\begin{aligned}\int_{z_0-\frac{\varepsilon}{2}}^{z_0+\frac{\varepsilon}{2}} \rho[V_x(x = x_1, y, z = z_0) - V_0]dz = \rho\int_{z_0-\frac{\varepsilon}{2}}^{z_0+\frac{\varepsilon}{2}} \underbrace{[V_x(x = x_1, y, z = z_0) - V_0]}_{=f(y)}dz + \\ \rho\frac{\partial V_x}{\partial z}(x = x_1, y, z = z_0)\underbrace{\int_{z_0-\frac{\varepsilon}{2}}^{z_0+\frac{\varepsilon}{2}}(z - z_0)\,dz}_{=0}\end{aligned} \quad \text{(B.2)}$$

We can then write d_1 in the form:

$$d_1 = \rho\varepsilon\int_{y_2}^{y_3}[V_x(x = x_1, y, z = z_0) - V_0]dy \quad \text{(B.3)}$$

In the same way, we can approximate the other mass fluxes in the way:

$$d_2 = -\rho\varepsilon\int_{x_1}^{x_4}[V_y(x, y = y_2, z = z_0)]dx \quad \text{(B.4)}$$

$$d_3 = \rho\varepsilon\int_{x_1}^{x_4}[V_y(x, y = y_3, z = z_0)]dx \quad \text{(B.5)}$$

$$d_4 = -\rho\varepsilon\int_{y_2}^{y_3}[V_x(x = x_4, y, z = z_0) - V_0]dy \quad \text{(B.6)}$$

Concerning d_5 and d_6, when applying the Taylor series to the first order we find:

$$V_z(x,y,z=z_0-\frac{\varepsilon}{2}) = V_z(x,y,z=z_0) - \frac{\varepsilon}{2}\frac{\partial V_z}{\partial z}(x,y,z=z_0) \tag{B.7}$$

therefore, the sum of d_5 and d_6 gives:

$$d_5 + d_6 = \rho\varepsilon \int_{x_1}^{x_4}\int_{y_2}^{y_3} \frac{\partial V_z}{\partial z}(x,y,z=z_0)dxdy \tag{B.8}$$

and giving that the considered flow is incompressible, we have:

$$div_{3D}(\vec{V}) = \underbrace{\frac{\partial V_x}{\partial x} + \frac{\partial V_y}{\partial y}}_{div_{2D}(\vec{V})} + \frac{\partial V_z}{\partial z} = 0 \tag{B.9}$$

consequently, eq. (B.8) becomes:

$$d_5 + d_6 = -\rho\varepsilon \int_{x_1}^{x_4}\int_{y_2}^{y_3} div_{2D}(\vec{V})(x,y,z=z_0)dxdy \tag{B.10}$$

Finally, the mass budget is written in the form:

$$\rho\varepsilon(\int_{y_2}^{y_3}(V_x - V_0)d_y - \int_{y_2}^{y_3}(V_x - V_0)dy + \int_{x_1}^{x_4} V_y dx - \int_{x_1}^{x_4} V_y dx + \int_{x_1}^{x_4}\int_{y_2}^{y_3}\frac{\partial V_z}{\partial z}dxdy) = 0 \tag{B.11}$$

Therefore the final mass budget performed in a closed 2D control domain is of course independent of ε; since the measured 2D velocity map is not divergence-free in the (X, Y) plane, an additional term including velocity V_z vertical gradients appears.

Appendix C

Mass budget: Effect of Dy_{23}

We give hereafter the evolution of the different mass budget contributions over the sections S_1 to S_6 for different x_4 positions. The effect of Dy_{23} is studied here.

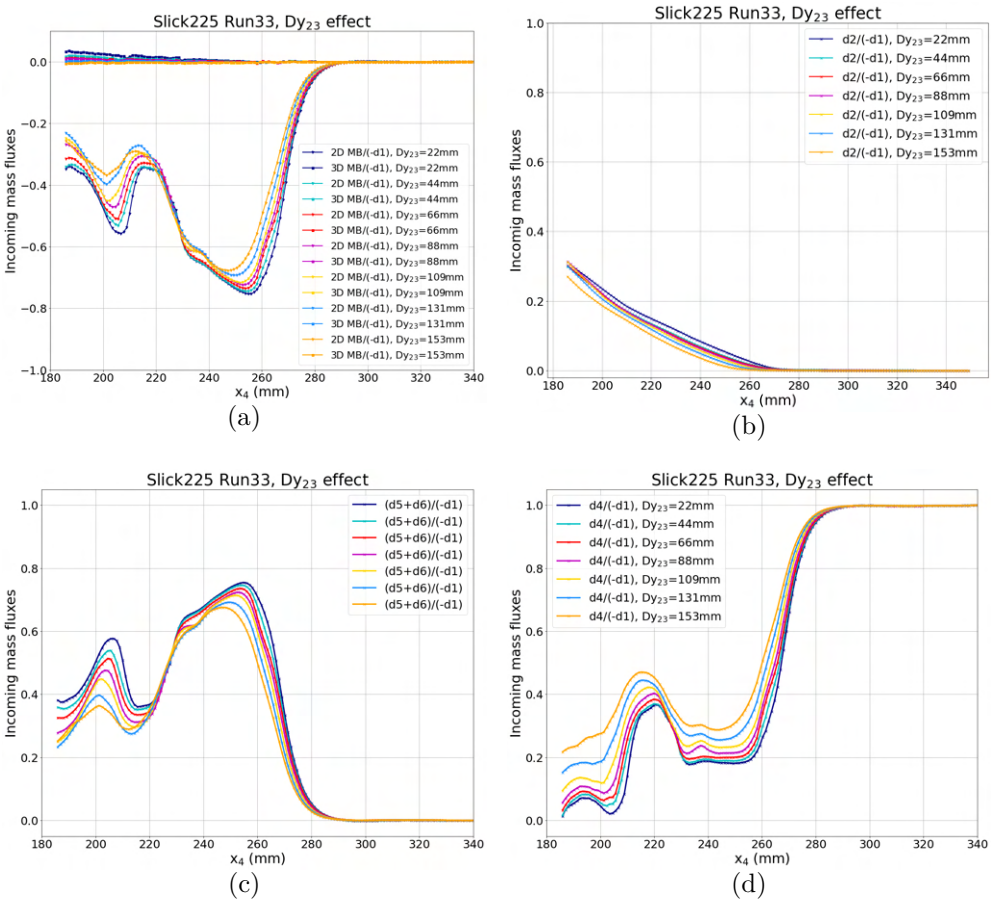

Figure C.1 – Evolution of the 2D and 3D mass budgets profiles (a), d_2 (b), $(d_5 + d_6)$ (c) and d_4 (d) for different values Dy_{23}. All quantities are normalized by $(-d_1)$.

Appendix D

Mass budget: Effect of H_w

We give hereafter the evolution of the different mass budget contributions over the sections S_1 to S_6 for different x_4 positions. The effect of H_w is studied here.

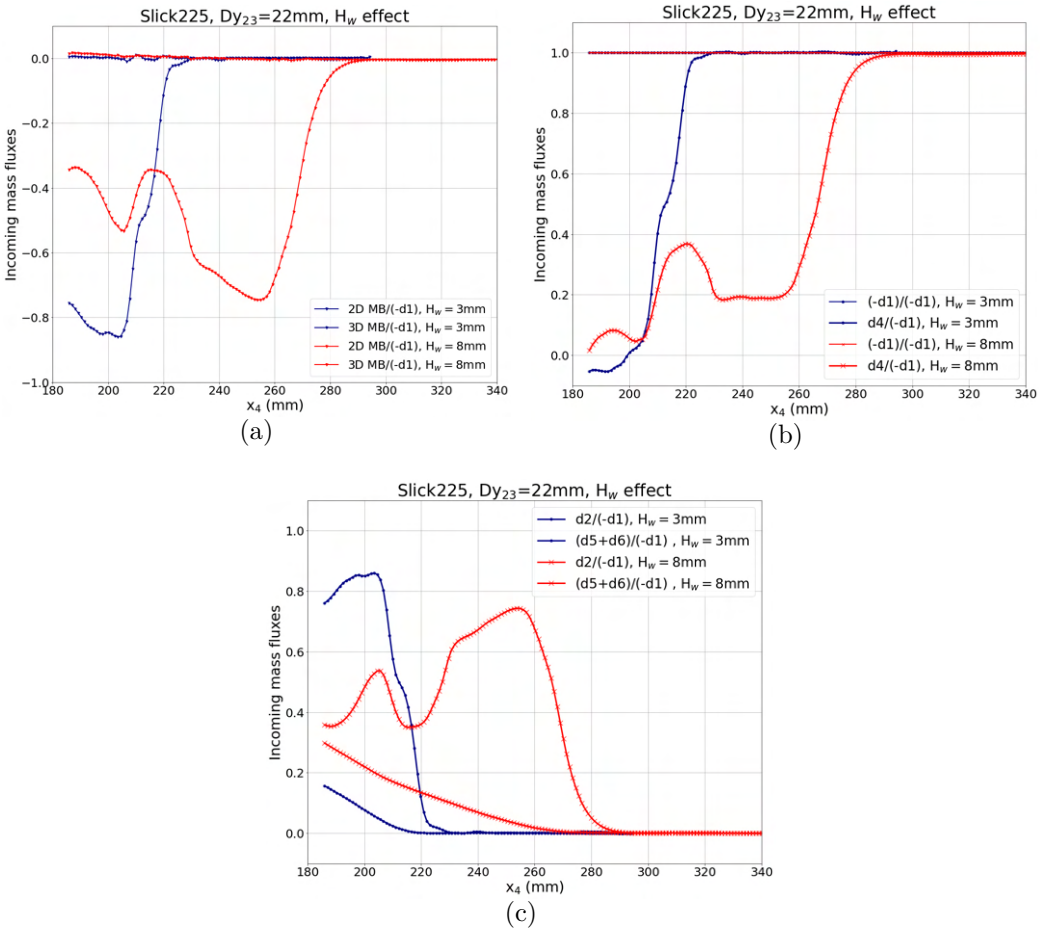

Figure D.1 – Evolution of the 2D and 3D mass budgets profiles with x_4 position (a) and decomposition of the mass budget contributions on the sections S_1 to S_6 (b and c) for $H_w = 3mm$ and $H_w = 8mm$ normalized by $(-d_1)$. The results for $H_w = 8mm$ correspond to the Run33 and are previously presented in Fig.4.25. The results for $H_w = 3mm$ belong to Run178.

Appendix E

Mass budget: Effect of tire width

We give hereafter the evolution of the different mass budget contributions over the sections S_1 to S_6 for different x_4 positions. The effect of the tire width is studied here.

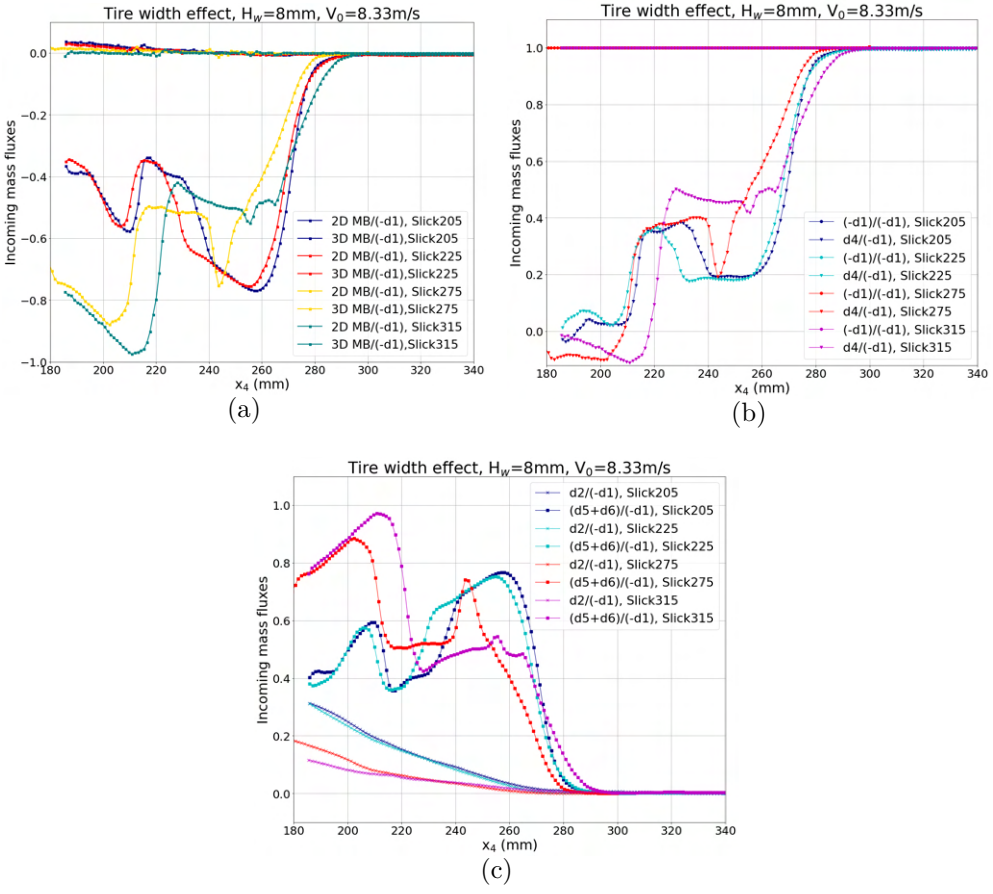

Figure E.1 – Evolution of the 2D and 3D mass budgets profiles with x_4 position (a) and decomposition of the mass budget contributions (b) and (c) for $H_w = 8mm$, $V_0 = 8.33m/s$ and four tire widths. All contributions are normalized by $(-d_1)$. The quantities belonging to the same tire are plotted in the same color on each graph. The results for the Slick205 correspond to the Run25, the Slick225 Run33, for the Slick275 Run119, and the Slick315 Run63.

Appendix F

CCP WORN: SEGMENTATION NORMAL VS REVERSE

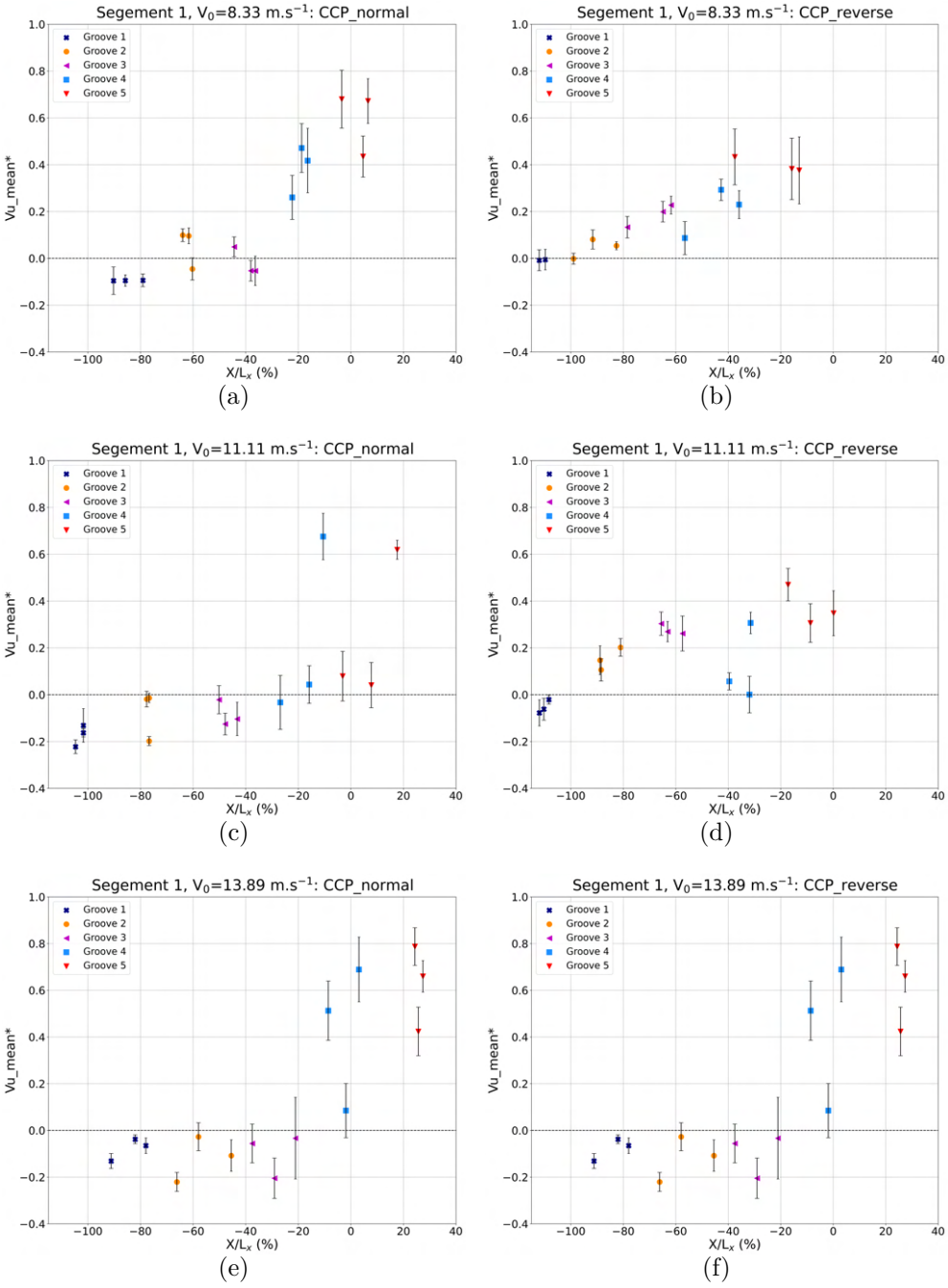

Figure F.1 – (Vu_{mean} in the segment 1 for the CCP worn, $N = 3$ (r-PIV measurements). The error bars represent the standard deviation of Vu inside each segment. Respectively for V_0 equal to $8.33 m.s^{-1}$ (a and b), $11.11 m.s^{-1}$ (c and d) and $13.89 m.s^{-1}$ (e and f) for both the normal and the reverese rotation.

BIBLIOGRAPHY

[1] M. A. Ahammed and S. L. Tighe, « Asphalt pavements surface texture and skid resistance—exploring the reality », *in*: *Canadian Journal of Civil Engineering* 39.*1* (2012), pp. 1–9.

[2] B. Allbert, « Tires and hydroplaning », *in*: *SAE Transactions* (1968), pp. 593–603.

[3] C. Antoci, M. Gallati, and S. Sibilla, « Numerical simulation of fluid–structure interaction by SPH », *in*: *Computers & structures* 85.*11-14* (2007), pp. 879–890.

[4] M. Antuono, A. Colagrossi, and S. Marrone, « Numerical diffusive terms in weakly-compressible SPH schemes », *in*: *Computer Physics Communications* 183.*12* (2012), pp. 2570–2580.

[5] C. Baker, « The turbulent horseshoe vortex », *in*: *Journal of Wind Engineering and Industrial Aerodynamics* 6.*1-2* (1980), pp. 9–23.

[6] D. A. Barcarolo, D. Le Touzé, G. Oger, and F. De Vuyst, « Adaptive particle refinement and derefinement applied to the smoothed particle hydrodynamics method », *in*: *Journal of Computational Physics* 273 (2014), pp. 640–657.

[7] D. A. Barcarolo, « Improvement of the precision and the efficiency of the SPH method: theoretical and numerical study », PhD thesis, École Centrale de Nantes, France, 2013.

[8] A. Ben Khodja, S. Simoëns, M. Michard, D. Le Touzé, C. Hermange, C. Poncet, and G. Oger, « R (refracted)-PIV measurements of water film flow: application to flow under a rolling tire », *in*: *Journal of Visualization* (2022), pp. 1–17.

[9] F. Biesse, « Analysis of wet road usage with a driving safety concern », *in*: *VDA Technischer Kongress*, 2019.

[10] D. Cabut, « Characterisation of the flow in a water-puddle under a rolling tire with refracted PIV method », PhD thesis, Université de Lyon, École Centrale de Lyon, France, 2020.

[11] D. Cabut, M. Michard, S. Simoëns, L. Mees, V. Todoroff, C. Hermange, and Y. Le Chenadec, « Analysis of the water flow inside tire grooves of a rolling car using refraction particle image velocimetry », *in*: *Physics of Fluids* 33.*3* (2021), p. 032101.

[12] D. Cabut, M. Michard, S. Simoëns, V. Todoroff, C. Hermange, and Y. Le-Chenadec, « PIV measurements using refraction at a solid–fluid interface », *in*: *Measurement Science and Technology* 32.*3* (2020), p. 035205.

[13] D. Cabut, M. Michard, S. Simoëns, V. Todoroff, J. Lemaıtre, C. Hermange, and Y. Le Chenadec, « Particle Image Velocimetry (PIV) measurements in a water film, application to a tire rolling through a puddle », *in*: *Mechanics & Industry* 20.*8* (2019), p. 811.

[14] V. Cerezo, M. Gothié, M. Menissier, and T. Gibrat, « Hydroplaning speed and infrastructure characteristics », *in*: *Proceedings of the Institution of Mechanical Engineers, Part J: Journal of Engineering Tribology* 224.*9* (2010), pp. 891–898.

[15] L. Chiron, M. De Leffe, G. Oger, and D. Le Touzé, « Fast and accurate SPH modelling of 3D complex wall boundaries in viscous and non viscous flows », *in*: *Computer Physics Communications* 234 (2019), pp. 93–111.

[16] L. Chiron, « Couplage et améliorations de la méthode SPH pour traiter des écoulements à multi-échelles temporelles et spatiales », PhD thesis, École Centrale de Nantes, France, 2017.

[17] L. Chiron, G. Oger, M. De Leffe, and D. Le Touzé, « Analysis and improvements of Adaptive Particle Refinement (APR) through CPU time, accuracy and robustness considerations », *in*: *Journal of Computational Physics* 354 (2018), pp. 552–575.

[18] J. Cho, H. Lee, J. Sohn, G. Kim, and J. Woo, « Numerical investigation of hydroplaning characteristics of three-dimensional patterned tire », *in*: *European Journal of Mechanics-A/Solids* 25.*6* (2006), pp. 914–926.

[19] A. Colagrossi, M. Antuono, and D. Le Touzé, « Theoretical considerations on the free-surface role in the smoothed-particle-hydrodynamics model », *in*: *Phys. Rev. E* 79 (5 May 2009), p. 056701, DOI: 10.1103/PhysRevE.79.056701, URL: https://link.aps.org/doi/10.1103/PhysRevE.79.056701.

[20] A. Colagrossi, M. Antuono, A. Souto-Iglesias, and D. Le Touzé, « Theoretical analysis and numerical verification of the consistency of viscous smoothed-particle-hydrodynamics formulations in simulating free-surface flows », *in*: *Phys. Rev. E* 84 (2 Aug. 2011), p. 026705, DOI: 10.1103/PhysRevE.84.026705, URL: https://link.aps.org/doi/10.1103/PhysRevE.84.026705.

[21] E. Commission, « Regulation (EU) 2020/740 of the European Parliament and on the labelling of tyres with respect to fuel efficiency and other parameters, amending Regulation (EU) 2017/1369 and repealing Regulation (EC) No 1222/2009 », *in*: *Official Journal of the European Union L* 177 (2020).

[22] S. J. Cummins and M. Rudman, « An SPH projection method », *in*: *Journal of computational physics* 152.*2* (1999), pp. 584–607.

[23] M. De Leffe, « Modelisation d'écoulements visqueux par methode SPH en vue d'application à l'hydrodynamique navale », PhD thesis, École Centrale de Nantes, France, 2011.

[24] M. Dehnad and A. Khodaii, « Evaluating the effect of different asphalt mixtures on hydroplaning using a new lab-scale apparatus », *in*: *Petroleum Science and Technology* 34.*20* (2016), pp. 1726–1733.

[25] L. Delorme, A. Colagrossi, A. Souto-Iglesias, R. Zamora-Rodriguez, and E. Botia-Vera, « A set of canonical problems in sloshing, Part I: Pressure field in forced roll—comparison between experimental results and SPH », *in*: *Ocean Engineering* 36.*2* (2009), pp. 168–178.

[26] J.-B. Deuff, « Extrapolation au réel des mesures de pression obtenues sur des cuves modèle réduit », PhD thesis, École Centrale de Nantes, France, 2007.

[27] M. Donatellis, E. Gelosa, R. Sangalli, M. Spinelli, and R. Vitali, « Virtual treaded tire simulation as a design predictive tool: Application to tire hydroplaning », *in*: *2009 SIMULIA Customer Conference*, 2009.

[28] M. Doring, « Développement d'une méthode SPH pour les applications à surface libre en hydrodynamique », PhD thesis, École Centrale de Nantes, France, 2005.

[29] D. L. Dwoyer, M. Y. Hussaini, and R. G. Voigt, *Finite Elements: Theory and Application Proceedings of the ICASE Finite Element Theory and Application Workshop Held July 28–30, 1986, in Hampton, Virginia*, Springer, 2013.

[30] J. Feldman and J. Bonet, « Dynamic refinement and boundary contact forces in SPH with applications in fluid flow problems », *in*: *International Journal for Numerical Methods in Engineering* 72.*3* (2007), pp. 295–324.

[31] J. Feldman, *Dynamic refinement and boundary contact forces in Smoothed Particle Hydrodynamics with applications in fluid flow problems*, Swansea University (United Kingdom), 2006.

[32] M. Ferrand, D. Laurence, B. D. Rogers, D. Violeau, and C. Kassiotis, « Unified semi-analytical wall boundary conditions for inviscid, laminar or turbulent flows in the meshless SPH method », *in*: *International Journal for Numerical Methods in Fluids* 71.*4* (2013), pp. 446–472.

[33] G. W. Flintsch, E. De León, K. K. McGhee, and I. L. AI-Qadi, « Pavement surface macrotexture measurement and applications », *in*: *Transportation research record* 1860.*1* (2003), pp. 168–177.

[34] G. Fourey, « Développement d'une méthode de couplage fluide-structure SPH-Eléments Finis en vue de son applicationa l'hydrodynamique navale », PhD thesis, École Centrale de Nantes, France, 2012.

[35] G. Fourey, C. Hermange, D. Le Touzé, and G. Oger, « An efficient FSI coupling strategy between smoothed particle hydrodynamics and finite element methods », *in*: *Computer Physics Communications* 217 (2017), pp. 66–81.

[36] T. Fwa, S. S. Kumar, K. Anupam, and G. P. Ong, « Effectiveness of tire-tread patterns in reducing the risk of hydroplaning », *in*: *Transportation research record* 2094.*1* (2009), pp. 91–102.

[37] T. Fwa, S. S. Kumar, G. P. Ong, and C. Huang, « Analytical modeling of effects of rib tires on hydroplaning », *in*: *Transportation Research Record* 2068.*1* (2008), pp. 109–118.

[38] B. Gallaway, D. Ivey, G. Hayes, W. Ledbetter, R. Olson, D. Woods, and R. Schiller Jr, « Pavement and geometric design criteria for minimizing hydroplaning », *in*: (1979).

[39] J. Gillard, « An Efficient Partitioned Coupling Scheme for Tire Hydroplaning Analysis », PhD thesis, Technische Universität München, Germany., 2019.

[40] R. A. Gingold and J. J. Monaghan, « Smoothed particle hydrodynamics: theory and application to non-spherical stars », *in*: *Monthly notices of the royal astronomical society* 181.*3* (1977), pp. 375–389.

[41] N. Grenier, « Modélisation numérique par la méthode SPH de la séparation eau-huile dans les séparateurs gravitaires », PhD thesis, École Centrale de Nantes, France, 2009.

[42] N. Grenier, M. Antuono, A. Colagrossi, D. Le Touzé, and B. Alessandrini, « An Hamiltonian interface SPH formulation for multi-fluid and free surface flows », *in*: *Journal of Computational Physics* 228.*22* (2009), pp. 8380–8393.

[43] H. Grogger and M. Weiss, « Calculation of the Hydroplaning of a Deformable Smooth-Shaped and Longitudinally-Grooved Tire », *in*: *Tire Science and Technology* 25.*4* (1997), pp. 265–287.

[44] P.-M. Guilcher, « Contribution au développement d'une méthode SPH pour la simulation numérique des interactions houle-structure », PhD thesis, École Centrale de Nantes, France, 2008.

[45] J. Hall, K. L. Smith, L. Titus-Glover, J. C. Wambold, T. J. Yager, and Z. Rado, « Guide for pavement friction », *in*: *Final Report for NCHRP Project* 1 (2009), p. 43.

[46] I. Hammani, « Improvement of the SPH method for multiphase flows application to the emergency water landing of aircrafts: application to the emergency water landing of aircrafts », PhD thesis, École Centrale de Nantes, France, 2020.

[47] G. Heinrich and M. Klüppel, « Rubber friction, tread deformation and tire traction », *in*: *Wear* 265.*7-8* (2008), pp. 1052–1060.

[48] C. Hermange, G. Oger, Y. Le Chenadec, and D. Le Touzé, « A 3D SPH–FE coupling for FSI problems and its application to tire hydroplaning simulations on rough ground », *in*: *Computer Methods in Applied Mechanics and Engineering* 355 (2019), pp. 558–590.

[49] C. Hermange, G. Oger, Y. Le Chenadec, M. de Leffe, and D. Le Touzé, « In-depth analysis of hydroplaning phenomenon accounting for tire wear on smooth ground », *in*: *Journal of Fluids and Structures* 111 (2018), pp. 552–575.

[50] C. Hermange, V. Todoroff, F. Biesse, and Y. Le-Chenadec, « Experimental investigation of the leading parameters influencing the hydroplaning phenomenon », *in*: *Vehicle System Dynamics* 60.*7* (2022), pp. 2375–2392.

[51] C. Hermange, « Simulation des interactions fluide-structure dans le problème de l'aquaplaning », PhD thesis, École Centrale de Nantes, France, 2017.

[52] C. Hermange, G. Oger, and D. Le Touzé, « Energy considerations in the SPH method with deformable boundaries and application to FSI problems », *in*: *Journal of Computational Physics: X* 1 (2019), p. 100008.

[53] T. E. Hoerner, *High performance concrete pavement: pavement texturing and tire-pavement noise*, US Department of Transportation, Federal Highway Administration, 2002.

[54] W. B. Horne, *Influence of the Tire Tread Pattern and Runway Surface Condition on Breaking Friction and Rolling Resistance of a Modern Aircraft Tire: Walter B. Horne and Trafford JW Leland*, National Aeronautics and Space Administration, 1962.

[55] W. B. Horne and R. C. Dreher, *Phenomena of pneumatic tire hydroplaning*, vol. 2056, National Aeronautics and Space Administration, 1963.

[56] W. B. Horne, T. J. Yager, and D. L. Ivey, « Recent studies to investigate effects of tire footprint aspect ratio on dynamic hydroplaning speed », *in*: *The tire pavement interface*, ASTM International, 1986.

[57] A. Hrennikoff, « Solution of problems of elasticity by the framework method », *in*: *Journal of applied mechanics* (1941).

[58] S. Idelsohn, J. Marti, A. Souto-Iglesias, and E. Oñate, « Interaction between an elastic structure and free-surface flows: experimental versus numerical comparisons using the PFEM », *in*: *Computational Mechanics* 43.*1* (2008), pp. 125–132.

[59] D. L. Ivey et al., « Truck tire hydroplaning—Empirical confirmation of Horne's thesis », *in*: *Mini-Tech Seminar on Tires, Service and Evaluation, Committee F-9, ASTM*, 1984.

[60] S.-T. Jenq, Y.-S. Chiu, et al., « Transient Hydroplaning Performance of Inflated Radial Tire with V-shape Grooved Tread Pattern Using LS-DYNA Explicit Interactive FSI Scheme », *in*: *Journal of the Chinese Society of Mechanical Engineers* 36.*2* (2015), pp. 135–144.

[61] M. Kane, M.-T. Do, V. Cerezo, Z. Rado, and C. Khelifi, « Contribution to pavement friction modelling: an introduction of the wetting effect », *in*: *International Journal of Pavement Engineering* 20.*8* (2019), pp. 965–976.

[62] M. Koishi, T. Okano, L. Olovsson, H. Saito, and M. Makino, « Hydroplaning simulation using fluid-structure interaction in LS-DYNA », *in*: *The 3rd European LS-DYNA Users Conference*, 2001.

[63] S. S. Kumar, K. Anupam, T. Scarpas, and C. Kasbergen, « Study of hydroplaning risk on rolling and sliding passenger car », *in*: *Procedia-Social and Behavioral Sciences* 53 (2012), pp. 1019–1027.

[64] T. Lacassagne, J. Vatteville, C. Degouet, M. El Hajem, and S. Simoëns, « PTV measurements of oscillating grid turbulence in water and polymer solutions », *in*: *Experiments in Fluids* 61.*7* (2020), pp. 1–15.

[65] M. G. Larson and F. Bengzon, *The finite element method: theory, implementation, and applications*, vol. 10, Springer Science & Business Media, 2013.

[66] G. Launay, « Etude expérimentale du tourbillon en fer à cheval au pied d'un obstacle émergent dans un roulement laminaire à surface libre », PhD thesis, Université de Lyon, École Centrale de Lyon, France, 2016.

[67] A. Leroy, D. Violeau, M. Ferrand, and C. Kassiotis, « Unified semi-analytical wall boundary conditions applied to 2-D incompressible SPH », *in*: *Journal of Computational Physics* 261 (2014), pp. 106–129.

[68] T. Li, « Literature review of tire-pavement interaction noise and reduction approaches », *in*: *Journal of Vibroengineering* 20.*6* (2018), pp. 2424–2452.

[69] Z. Li, J. Leduc, J. Nunez-Ramirez, A. Combescure, and J.-C. Marongiu, « A non-intrusive partitioned approach to couple smoothed particle hydrodynamics and finite element methods for transient fluid-structure interaction problems with large interface motion », *in*: *Computational Mechanics* 55.*4* (2015), pp. 697–718.

[70] L. D. Libersky, A. G. Petschek, T. C. Carney, J. R. Hipp, and F. A. Allahdadi, « High Strain Lagrangian Hydrodynamics: A Three-Dimensional SPH Code for Dynamic Material Response », *in*: *Journal of Computational Physics* 109.*1* (1993), pp. 67–75, ISSN: 0021-9991, DOI: https://doi.org/10.1006/jcph.1993.1199, URL: http://www.sciencedirect.com/science/article/pii/S002199918371199X.

[71] K. Lim and P. Ku, « Computational study for tyre tread performance on hydroplaning », *in*: *AIP Conference Proceedings*, vol. 2233, 1, AIP Publishing LLC, 2020, p. 020018.

[72] S. J. Lind, R. Xu, P. K. Stansby, and B. D. Rogers, « Incompressible smoothed particle hydrodynamics for free-surface flows: A generalised diffusion-based algorithm for stability and validations for impulsive flows and propagating waves », *in*: *Journal of Computational Physics* 231.*4* (2012), pp. 1499–1523.

[73] C. Liu, H. Meng, S. Lu, A. Li, C. Xu, Y. Sun, and G. Wang, « Design of Nonsmooth Groove Tire Bioinspired by Shark-Skin Riblet Structure », *in*: *Applied Bionics and Biomechanics* 2022 (2022).

[74] J. Löwer, P. Wagner, H.-J. Unrau, C. Bederna, and F. Gauterin, « Physical model of tire-road contact under wet conditions », *in*: *Tribology Letters* 68.*1* (2020), pp. 1–14.

[75] L. B. Lucy, « A numerical approach to the testing of the fission hypothesis », *in*: *The astronomical journal* 82 (1977), pp. 1013–1024.

[76] J.-C. Marongiu, « Méthode numérique lagrangienne pour la simulation d'écoulements à surface libre: application aux turbines Pelton », PhD thesis, Université de Lyon, École Centrale de Lyon, France, 2007.

[77] S. Marrone, M. Antuono, A. Colagrossi, G. Colicchio, D. Le Touzé, and G. Graziani, « δ-SPH model for simulating violent impact flows », *in*: *Computer Methods in Applied Mechanics and Engineering* 200.*13-16* (2011), pp. 1526–1542.

[78] S. Marrone, A. Colagrossi, D. Le Touzé, and G. Graziani, « Fast free-surface detection and level-set function definition in SPH solvers », *in*: *Journal of Computational Physics* 229.*10* (2010), pp. 3652–3663.

[79] M. Matilainen and A. Tuononen, « Tyre contact length on dry and wet road surfaces measured by three-axial accelerometer », *in*: *Mechanical Systems and Signal Processing* 52 (2015), pp. 548–558.

[80] G. Maycock, « Second paper: studies on the skidding resistance of passenger-car tyres on wet surfaces », *in*: *Proceedings of the Institution of Mechanical Engineers: Automobile Division* 180.*1* (1965), pp. 122–157.

[81] J. M. P. Mayora and R. J. Piña, « An assessment of the skid resistance effect on traffic safety under wet-pavement conditions », *in*: *Accident Analysis & Prevention* 41.*4* (2009), pp. 881–886.

[82] A. Mayrhofer, M. Ferrand, C. Kassiotis, D. Violeau, and F.-X. Morel, « Unified semi-analytical wall boundary conditions in SPH: analytical extension to 3-D », *in*: *Numerical Algorithms* 68.*1* (2015), pp. 15–34.

[83] J. Michel, A. Vergnaud, G. Oger, C. Hermange, and D. Le Touzé, « On Particle Shifting Techniques (PSTs): Analysis of existing laws and proposition of a convergent and multi-invariant law », *in*: *Journal of Computational Physics* 459 (2022), p. 110999.

[84] J. Michel, « Développements numériques de la méthode SPH couplée aux Eléments Finis appliqués au phénomène de l'hydroplanage. », PhD thesis, École Centrale de Nantes, France, 2020.

[85] C. Michler, S. Hulshoff, E. Van Brummelen, and R. De Borst, « A monolithic approach to fluid–structure interaction », *in*: *Computers & fluids* 33.*5-6* (2004), pp. 839–848.

[86] J. Monaghan, « On the problem of penetration in particle methods », *in*: *Journal of Computational physics* 82.*1* (1989), pp. 1–15.

[87] J. J. Monaghan, « Smoothed particle hydrodynamics », *in*: *Annual review of astronomy and astrophysics* 30.*1* (1992), pp. 543–574.

[88] J. J. Monaghan, « Smoothed particle hydrodynamics », *in*: *Reports on progress in physics* 68.*8* (2005), p. 1703.

[89] D. Moore, « A review of squeeze films », *in*: *Wear* 8.*4* (1965), pp. 245–263.

[90] R. P. Nelson and J. C. Papaloizou, « Variable smoothing lengths and energy conservation in smoothed particle hydrodynamics », *in*: *Monthly Notices of the Royal Astronomical Society* 270.*1* (1994), pp. 1–20.

[91] A. J. Niskanen and A. J. Tuononen, « Three 3-axis accelerometers fixed inside the tyre for studying contact patch deformations in wet conditions », *in*: *Vehicle System Dynamics* 52.*sup1* (2014), pp. 287–298.

[92] G. Oger, S. Marrone, D. Le Touzé, and M. De Leffe, « SPH accuracy improvement through the combination of a quasi-Lagrangian shifting transport velocity and consistent ALE formalisms », *in*: *Journal of Computational Physics* 313 (2016), pp. 76–98.

[93] G. Oger, « Aspects théoriques de la méthode SPH et applications à l'hydrodynamique à surface libre », *in*: *École Centrale de Nantes, France* (2006).

[94] G. Oger, M. Doring, B. Alessandrini, and P. Ferrant, « An improved SPH method: Towards higher order convergence », *in*: *Journal of Computational Physics* 225.*2* (2007), pp. 1472–1492.

[95] G. Oger, M. Doring, B. Alessandrini, and P. Ferrant, « Two-dimensional SPH simulations of wedge water entries », *in*: *Journal of computational physics* 213.*2* (2006), pp. 803–822.

[96] G. Oger, D. Le Touzé, D. Guibert, M. De Leffe, J. Biddiscombe, J. Soumagne, and J.-G. Piccinali, « On distributed memory MPI-based parallelization of SPH codes in massive HPC context », *in*: *Computer Physics Communications* 200 (2016), pp. 1–14.

[97] C.-W. Oh, T.-W. Kim, H.-Y. Jeong, K.-S. Park, and S.-N. Kim, « Hydroplaning simulation for a straight-grooved tire by using FDM, FEM and an asymptotic method », *in*: *Journal of Mechanical Science and Technology* 22.*1* (2008), pp. 34–40.

[98] T. Okano and M. Koishi, « A new computational procedure to predict transient hydroplaning performance of a tire », *in*: *Tire Science and Technology* 29.*1* (2001), pp. 2–22.

[99] T. Okano and M. Koishi, « Hydroplaning simulation using MSC. dytran », *in*: *Proceedings of the 3rd European LS-DYNA users conference*, 2001.

[100] G. P. Ong and T. Fwa, « Prediction of wet-pavement skid resistance and hydroplaning potential », *in*: *Transportation Research Record* 2005.*1* (2007), pp. 160–171.

[101] G. P. Ong and T. Fwa, « Wet-pavement hydroplaning risk and skid resistance: modeling », *in*: *Journal of Transportation Engineering* 133.*10* (2007), pp. 590–598.

[102] A. N. Parshikov, S. A. Medin, I. I. Loukashenko, and V. A. Milekhin, « Improvements in SPH method by means of interparticle contact algorithm and analysis of perforation tests at moderate projectile velocities », *in*: *International Journal of Impact Engineering* 24.*8* (2000), pp. 779–796.

[103] B. Persson, N. Prodanov, B. Krick, N. Rodriguez, N. Mulakaluri, W. Sawyer, and P. Mangiagalli, « Elastic contact mechanics: percolation of the contact area and fluid squeeze-out », *in*: *The European Physical Journal E* 35.*1* (2012), pp. 1–17.

[104] B. N. Persson, « Theory of rubber friction and contact mechanics », *in*: *The Journal of Chemical Physics* 115.*8* (2001), pp. 3840–3861.

[105] T. Praisner, D. Sabatino, and C. Smith, « Simultaneously combined liquid crystal surface heat transfer and PIV flow-field measurements », *in*: *Experiments in Fluids* 30.*1* (2001), pp. 1–10.

[106] Q. Qu, T. Liu, P. Liu, and R. K. Agarwal, « Simulation of water spray generated by pneumatic aircraft tire on flooded runway », *in*: *Journal of Aircraft* 55.*4* (2018), pp. 1700–1708.

[107] Y. Reyes López, D. Roose, and C. Recarey Morfa, « Dynamic particle refinement in SPH: application to free surface flow and non-cohesive soil simulations », *in*: *Computational Mechanics* 51.*5* (2013), pp. 731–741.

[108] J. G. Rose and B. M. Gallaway, « Water depth influence on pavement friction », *in*: *Transportation Engineering Journal of ASCE* 103.*4* (1977), pp. 491–506.

[109] Z. El-Sayegh and M. El-Gindy, « Sensitivity analysis of truck tyre hydroplaning speed using FEA-SPH model », *in*: *International Journal of Vehicle Systems Modelling and Testing* 12.*1-2* (2017), pp. 143–161.

[110] C. Schäfer, S. Riecker, T. I. Maindl, R. Speith, S. Scherrer, and W. Kley, « A smooth particle hydrodynamics code to model collisions between solid, self-gravitating objects », *in*: *Astronomy & Astrophysics* 590 (2016), A19.

[111] E. Seta, Y. Nakajima, T. Kamegawa, and H. Ogawa, « Hydroplaning analysis by FEM and FVM: effect of tire rolling and tire pattern on hydroplaning », *in*: *Tire Science and Technology* 28.*3* (2000), pp. 140–156.

[112] S. Shao and E. Y. Lo, « Incompressible SPH method for simulating Newtonian and non-Newtonian flows with a free surface », *in*: *Advances in water resources* 26.*7* (2003), pp. 787–800.

[113] D. Shepard, « A two-dimensional interpolation function for irregularly-spaced data », *in*: *Proceedings of the 1968 23rd ACM national conference*, 1968, pp. 517–524.

[114] R. L. Simpson, « Junction flows », *in*: *Annual Review of Fluid Mechanics* 33 (2001), p. 415.

[115] J. F. Sinnamon, *Hydroplaning and tread pattern hydrodynamics*, tech. rep., 1974.

[116] F. Spitzhüttl, F. Goizet, T. Unger, and F. Biesse, « The real impact of full hydroplaning on driving safety », *in*: *Accident Analysis & Prevention* 138 (2020), p. 105458.

[117] P. Sun, A.-M. Zhang, S. Marrone, and F. Ming, « An accurate and efficient SPH modeling of the water entry of circular cylinders », *in*: *Applied Ocean Research* 72 (2018), pp. 60–75.

[118] P. Sun, A. Colagrossi, S. Marrone, M. Antuono, and A.-M. Zhang, « A consistent approach to particle shifting in the δ-Plus-SPH model », *in*: *Computer Methods in Applied Mechanics and Engineering* 348 (2019), pp. 912–934.

[119] T. Suzuki and T. Fujikawa, *Improvement of hydroplaning performance based on water flow around tires*, tech. rep., SAE Technical Paper, 2001.

[120] T. Tang, K. Anupam, C. Kasbergen, A. Scarpas, and S. Erkens, « A finite element study of rain intensity on skid resistance for permeable asphalt concrete mixes », *in*: *Construction and Building Materials* 220 (2019), pp. 464–475.

[121] A. Taniere, B. Oesterle, and J. Monnier, « On the behaviour of solid particles in a horizontal boundary layer with turbulence and saltation effects », *in*: *Experiments in Fluids* 23.*6* (1997), pp. 463–471.

[122] V. Todoroff, S. Paupy, F. Biesse, and Y. Le Chenadec, « The mechanisms involved during the wet braking of new and worn tires », *in*: *Vehicle system dynamics* 57.*11* (2019), pp. 1601–1620.

[123] A. Tuononen and L. Hartikainen, « Optical position detection sensor to measure tyre carcass deflections in aquaplaning », *in*: *International Journal of Vehicle Systems Modelling and Testing* 3.*3* (2008), pp. 189–197.

[124] A. J. Tuononen and M. J. Matilainen, « Real-time estimation of aquaplaning with an optical tyre sensor », *in*: *Proceedings of the Institution of Mechanical Engineers, Part D: Journal of Automobile Engineering* 223.*10* (2009), pp. 1263–1272.

[125] B. Turnbull and J. N. McELWAINE, « Potential flow models of suspension current air pressure », *in*: *Annals of Glaciology* 51.*54* (2010), pp. 113–122.

[126] R. Vacondio, B. Rogers, P. K. Stansby, P. Mignosa, and J. Feldman, « Variable resolution for SPH: a dynamic particle coalescing and splitting scheme », *in*: *Computer Methods in Applied Mechanics and Engineering* 256 (2013), pp. 132–148.

[127] R. Vacondio et al., « Grand challenges for Smoothed Particle Hydrodynamics numerical schemes », *in*: *Computational Particle Mechanics* 8.*3* (2021), pp. 575–588.

[128] G. Van Es, « Hydroplaning of modern aircraft tires », *in*: (2001).

[129] A. Vergnaud, G. Oger, D. Le Touzé, M. DeLeffe, and L. Chiron, « C-CSF: Accurate, robust and efficient surface tension and contact angle models for single-phase flows using SPH », *in*: *Computer Methods in Applied Mechanics and Engineering* 389 (2022), p. 114292.

[130] J. Vila, « On particle weighted methods and smooth particle hydrodynamics », *in*: *Mathematical models and methods in applied sciences* 9.*02* (1999), pp. 161–209.

[131] S. Vincent, A. Sarthou, J.-P. Caltagirone, F. Sonilhac, P. Février, C. Mignot, and G. Pianet, « Augmented Lagrangian and penalty methods for the simulation of two-phase flows interacting with moving solids. Application to hydroplaning flows interacting with real tire tread patterns », *in*: *Journal of computational physics* 230.*4* (2011), pp. 956–983.

[132] D. Violeau and A. Leroy, « On the maximum time step in weakly compressible SPH », *in*: *Journal of Computational Physics* 256 (2014), pp. 388–415.

[133] H. Wendland, « Piecewise polynomial, positive definite and compactly supported radial functions of minimal degree », *in*: *Advances in computational Mathematics* 4.*1* (1995), pp. 389–396.

[134] B. Wies, B. Roeger, and R. Mundl, « Influence of pattern void on hydroplaning and related target conflicts », *in*: *Tire Science and Technology* 37.*3* (2009), pp. 187–206.

[135] T. J. Yager, W. P. Phillips, W. B. Horne, and H. C. Sparks, *A comparison of aircraft and ground vehicle stopping performance on dry, wet, flooded, slush-, snow-, and ice-covered runways*, tech. rep., National aeronautics and Space Administration Hampton va Langley Research Center, 1970.

[136] R. W. Yeager, « Tire hydroplaning: testing, analysis, and design », *in*: *The Physics of Tire Traction*, Springer, 1974, pp. 25–63.

[137] R. W. Yeager and J. L. Tuttle, « Testing and analysis of tire hydroplaning », *in*: *SAE Transactions* (1972), pp. 1601–1611.

[138] L. Zhang, G. P. Ong, and T. F. Fwa, « Developing an analysis framework to quantify and compare skid resistance performance on porous and nonporous pavements », *in*: *Transportation research record* 2369.*1* (2013), pp. 77–86.

[139] S. Zhu, X. Liu, Q. Cao, and X. Huang, « Numerical study of tire hydroplaning based on power spectrum of asphalt pavement and kinetic friction coefficient », *in*: *Advances in Materials Science and Engineering* 2017 (2017).

Titre : Méthodologies numériques et expérimentales pour la compréhension et la prédiction du phénomène d'hydroplanage des pneumatiques par simulations numériques couplées SPH-Éléments Finis et mesures PIV

Mot clés : Hydroplanage, couplage fluide-structure, SPH-EF, PIV, sculpture de pneumatique

Résumé : L'adhérence mouillée des pneumatiques est une performance essentielle touchant à la sécurité des passagers. Dans cette situation, le contact pneu/sol devient plus complexe à comprendre et modéliser, faisant intervenir des mécanismes physiques non triviaux tels que le couplage fluide-structure et les écoulements turbulents. Dans le but d'améliorer la compréhension de l'hydroplanage des pneumatiques, la présente thèse vise à mettre en place un plan de comparaison entre les simulations numériques couplées SPH- Éléments finis et les résultats de tests r-PIV. En effet, la méthode SPH présente de nombreux avantages de par sa nature Lagrangienne et sans maillage pour modéliser le domaine fluide. De plus, son couplage avec la méthode des Éléments finis est relativement aisé. Par ailleurs, sur le plan expérimental, la r-PIV a été introduite récemment pour étudier le roulage d'un pneumatique sur une flaque d'eau. Cette nouvelle approche constitue un puissant outil pour valider les simulations numériques sur la base de comparaisons locales de la circulation de l'eau pour une sculpture donnée. Enfin, les simulations numériques constituent également un moyen d'évaluation de la r-PIV grâce à une vision 3D du phénomène et à l'accès à des données encore inaccessibles expérimentalement.

Title: Numerical and experimental methodologies for understanding and predicting the hydroplaning phenomenon of tires by numerical coupled SPH-Finite Elements simulations and PIV measurements

Keywords: Hydroplaning, FSI, coupling SPH-FE, PIV, tire tread

Abstract: The wet grip performance of tires is an essential criterion affecting the safety of passengers. In this situation, the tire/ground contact becomes more complex to understand and model, involving non-trivial physical mechanisms such as fluid-structure coupling and turbulent flows. In the vision of improving our understanding of tires' hydroplaning, this thesis aims to set up a comparison strategy between the SPH-Finite Elements coupled numerical simulations and the r-PIV test results. Indeed, the SPH method has many advantages due to its Lagrangian and meshless nature to model the fluid part. Moreover, its coupling with the finite element method is relatively easy. In addition, the r-PIV was recently introduced for experimental investigations of a tire rolling over a water puddle. This new approach performed effectively as a powerful tool for validating numerical simulations based on local comparisons of the water circulation for a given tire tread. Finally, numerical simulations also evaluate r-PIV thanks to a 3D vision of the phenomenon and access to data that are still inaccessible experimentally.